



**HAL**  
open science

# Traversée d'une interface liquide-liquide par une goutte sous l'effet centrifuge pour un procédé de micro-encapsulation

Hassan El Itawi

► **To cite this version:**

Hassan El Itawi. Traversée d'une interface liquide-liquide par une goutte sous l'effet centrifuge pour un procédé de micro-encapsulation. Dynamique des Fluides [physics.flu-dyn]. Institut National Polytechnique de Toulouse - INPT, 2020. Français. NNT : 2020INPT0039 . tel-04164451

**HAL Id: tel-04164451**

**<https://theses.hal.science/tel-04164451>**

Submitted on 18 Jul 2023

**HAL** is a multi-disciplinary open access archive for the deposit and dissemination of scientific research documents, whether they are published or not. The documents may come from teaching and research institutions in France or abroad, or from public or private research centers.

L'archive ouverte pluridisciplinaire **HAL**, est destinée au dépôt et à la diffusion de documents scientifiques de niveau recherche, publiés ou non, émanant des établissements d'enseignement et de recherche français ou étrangers, des laboratoires publics ou privés.



Université  
de Toulouse

# THÈSE

En vue de l'obtention du

## DOCTORAT DE L'UNIVERSITÉ DE TOULOUSE

**Délivré par :**

Institut National Polytechnique de Toulouse (INP Toulouse)

**Discipline ou spécialité :**

Dynamique des fluides

---

**Présentée et soutenue par :**

M. HASSAN EL ITAWI

Le mercredi 24 juin 2020

**Titre :**

CROSSING OF A LIQUID-LIQUID INTERFACE BY A DROPLET IN  
CENTRIFUGAL FIELD FOR A MICRO-ENCAPSULATION PROCESS

---

**Ecole doctorale :**

Mécanique, Energétique, Génie civil, Procédés (MEGeP)

**Unité de recherche :**

Laboratoire de Génie Chimique (LGC)

**Directeur(s) de Thèse :**

Mme. NATHALIE LE SAUZE (Directrice)

Mme. GLADYS MASSIERA (co-Directrice)

**Rapporteurs :**

M. NICOLAS BREMOND, ESPCI PARIS

M. BENOIT SCHEID, UNIVERSITE LIBRE DE BRUXELLES

**Membre(s) du jury :**

M. JACQUES MAGNAUDET, TOULOUSE INP, Président

Mme. PIERRETTE GUICHARDON, ECOLE CENTRALE MARSEILLE, Membre

Mme. NATHALIE LE SAUZE, TOULOUSE PAUL SABATIER, Membre

Mme. GLADYS MASSIERA, UNIVERSITE DE MONTPELLIER, Membre

M. BENJAMIN LALANNE, TOULOUSE INP, Invité

M. OLIVIER MASBERNAT, TOULOUSE INP, Invité

**This thesis is dedicated to my father, my mother, my uncle, my two sisters, my brother, and Khouloud the love of my life.**

---

# Acknowledgements

First, I would like to thank the reviewers, the examiners and the invited members of the jury for my PhD defense, M. Jacques Magnaudet, Mme. Pierette Guichardon, M. Nicolas Bremond, M. Benoit Scheid. Thank you for reading, correcting and helping me to improve my manuscript with your positive criticism.

During my three years of the PhD, I have shared my time between two labs: Laboratoire de Génie Chimique and Laboratoire Charles Coulomb in Montpellier. I would like to thank the directors of both labs Pierre Aimar and Pierre Lefebvre. Thank you for giving me this great opportunity. It was an honor to be a part of LGC and L2C.

I would like to show my gratitude to the people who made the success of this PhD possible, my supervisors and the participating scientific team: Mme. Nathalie Le Sauze the nice personality and the friendly supervisor, the woman who never refused to help me on a professional or personal level, Mme. Gladys Massiera, the supportive and friendly advisor who accompanied me in my research period in Montpellier and did not hesitate to help him solve many communication problems I had in the beginning of my PhD when I didn't speak French. M. Olivier Masbernat the smartest person I ever met, the one who comes with the strongest ideas, he was tuff sometimes but I am pretty sure now that it was in the favor of this successful work, M. Benjamin Lalanne, the person from whom I acquired all my skills in numerical simulations, the friendly guy who's never tired from showing his support, and the person with the best teaching skills I've ever met (P.S.: this is also what his students said about him when I met them), and last but not least, M. Martin In the researcher I worked with during my stay in Montpellier, thank you for the very interesting scientific and non-scientific discussions we had. Thank you all for these years of my PhD, without you this would have never been possible. I am grateful for your continuous support, patience, motivation, and immense knowledge. I would like also to thank the four people who supported me with technical help in order to develop my complicated experimental pilot: From LGC: Alain Pontier the gentleman and sympathetic engineer who is always smiling when working, and Emmanuel Cid, the king of optics, lasers, and high speed camera technology. From L2C: Jean-Marc Fromental and Ty Phou, the kind and supportive person who accompanied me with the very first steps of the development of the experimental setup. Thanks for the support you gave me, I appreciate it very much.

I am also grateful to the funders of this project: The National Research Agency of France (ANR). I would also like to thank the administrative staff of both the labs Mme. Daniele Bouscary, Mme. Patricia Uliana, Mme. Maria Escobar Munoz, Mme. Claudine Lorenzon and M. Jean-Luc Labeyrie at LGC and Mme Béatrice Tomberli from L2C, thank you for your kindness and availability, the infinite help and your smiles. I would like also to thank

M. Alain Phillipe from LGC. A great thanks goes to "Service Analyses et Procédés" at LGC especially Mme. Marie-Line Pern for helping with the Tensiometer and Rheometer analysis. During my time in LGC, I was a part of two departments: STPI and GIMD. Thanks for the responsible of both departments: M. Michel Meyer and Mme. Séverine Camy from STPI and M. Sébastien Teychené from GIMD and to all members of both teams, it was a pleasure for me to learn about your scientific interest and to present my research work to you.

Now, it is the time of my colleagues. I dedicate the first thanks for the three people who accompanied me in the first days in LGC when I didn't speak French. They were there to help me integrate and to translate whenever I fail to understand French: Omar Yala, Fatine Berdouzi, and my office colleague Kevin Lachin. Thank you very much guys, without you I couldn't put my first steps in LGC. A great thanks also for Hélène Labauze, Robbie Radjagubalo, and Astrid Novella, the three colleagues who did not hesitate to help me when I needed. Carlos, Sid Ahmed, Samba, Antonin, Mahmoud, Robbie, Sergio, Juliano, Marco, thank you for enjoying Football with you after work. It was my pleasure to be a part of the Alambic team in 2018-2019, I made a part in the participation of activities I enjoyed before and I was happy to get to know: Thibaut, Milad, Florent, Michelle, Ranine, Elise, Ali, Mei, and all the other members. I would like also to thank my colleagues whom I was pleased to know Marwa, Garima, Mahmoud, Mohamad, Yousef, Nouha, Alexandre, Hanbin, Benoit, Kyliani, Adriana, Carlos, Konstantina, Yosra, Mariem, Mercedes, Lauren, and Emmanuel, thank you for the interesting discussions we had and the very good times at LGC, it was a great pleasure to know you guys.

A great thank to Sid Ahmed Kessas and Thomas Esteve, I was lucky to know you guys.

Thanks for my parents who made me who I am, and the two people whom I owe my success. I am grateful for my uncle, Mohammed, the one who funded me and made my dream to continue my studies in France possible and the one who always treated me as his son, and even more. Thanks to my brother and my two sisters who were physically far but always close. Thanks to every member of my big family. Thanks for my best friend, who was always beside me during the last nine years, the one who I never lost the daily contact with, and the one who was always there to hear me and help me solve my problems, the one and only Hassan Ahmad. I will be always proud to say my famous sentence "It is not easy to be Hassan Ahmad". Thanks to my childhood friend since 19 years, Hassan Atwi, I hope that our friendship continues. Thanks also to my friend who arrived to France with me in the same year, Hassan Mohanna and to the person I got to know more in France, Hassan Bou Ibrahim, thank you for your discussions which enriched my culture (We all have the same first name, it is a coincidence only, believe me) and last and not least Hussein Milany and Daniel Sayegh. I won't forget Rasha Seblany and Ranin Atwi, two of the most friendly people I've ever met. Thanks to my travel partners: Aly, Omar, Hamza, Maryam, Hala, Ali, Sarah, Imad, Hassan, Hassan, Hussein, Zeinab, Ghiwa thank you guys for the best time we spent discovering new places and cultures. Thanks to my close friend Kamar

(which means moon), the intelligent girl, she is a moon, believe me. Thanks to the people from my school class who I never lost contact with them: Ali, Ali, Mariam, and Sarah who never meet unless I come back home where the hajj hears everything. Thanks for Aly (aka Alexandre, Adrien as a French citizen) and Omar (aka Marc), and Hamza (the funniest person you meet in France) for being the gang I most spent time with in Toulouse. Thanks for the people from the French-Lebanese association “Amis du Liban – Toulouse” especially, Paul, Anthony, Farid, Maen, Iman, Andrea, Georgio and Ali. It was my pleasure to be one of you guys, thank you for all good times in Toulouse, and for the opportunity which made meeting the love of my life possible. Speaking about that, thank you Georgio for letting me take care of the new girl arriving to Toulouse: Khoulood.

My last words are for the love of my life, Khoulood, the girl who changed my life to the best. The one who became in a short period of time, my safest place whenever worried, anxious, or sad. Thank you for being beside me providing me with love, affection and attention during the last and most difficult stage of my PhD. You are the best event happened during these three years of PhD, and absolutely during my life. You know well that I belong to you and that my life will never be complete without you. I dedicate this work for you and for our love that I hope to be forever. Hoping for a beautiful future bringing us together, thank you very much for the past and for the present. You are wonderful. I love you.

**Abstract:**

The applications concerned by microencapsulation are constantly growing and cover sectors of industrial activities as varied as agriculture, pharmacy, food industry and even cosmetics. This work is a part of the development of a microencapsulation process based on sub-millimeter-sized drops crossing a liquid-liquid (L-L) interface under the influence of an external force, in this case centrifugal force. The objective of this work is to understand the hydrodynamics and interface mechanisms before, during and after the passage of a drop through a L-L interface, and leading to its coating. For this purpose, numerical and experimental approaches have been combined and complemented by theoretical models. A numerical method solves the Navier-Stokes equations for this three-phase flow by a finite volume discretization combined with the Level-Set and ghost-fluid methods to capture the interface dynamics and to deal with the discontinuities at the interfaces; it allows to compute the velocity field around the deformable droplets during the interface crossing. An experimental device for forming aqueous drops of sizes (100-1400  $\mu\text{m}$ ) and forcing their passage through a L-L interface using a centrifugal force of magnitude up to  $\approx 2500g$  was designed to observe all stages of the process by a high-speed camera synchronized with the rotation of the encapsulation cell, and to analyze the crossing conditions and the different fluid entrainment regimes. The crossing or the rebound of a droplet at the interface is a result of the competition between interfacial forces, the weight of the drop and its inertial force, and is due to complex phenomena involving non-dimensional numbers. The two approaches made it possible to define the crossing conditions as a function of the relevant non-dimensional numbers:  $\frac{\xi_{12}}{\xi_{13}}$  and  $Bo_{13}$ , and to develop a scaling law of the maximum length of the column formed during crossing, and the resulting drop coating volume. This work has thus made it possible to determine the optimal conditions, on the scale of a single drop, to encapsulate a liquid droplet by using this process, a necessary step prior to the design of an industrial pilot operating at a continuous production rate.

**Keywords:** Encapsulation, multiphase flow, interface crossing, level-set method, droplet.

**Résumé :**

Les applications concernées par la micro-encapsulation ne cessent de croître et couvrent des secteurs d'activités industrielles aussi variés que l'agriculture, la pharmacie, l'industrie alimentaire ou encore la cosmétique. Ce travail s'inscrit dans le développement d'un procédé de micro-encapsulation basé sur des gouttes de taille submillimétrique traversant une interface liquide-liquide sous l'influence d'une force extérieure, ici la force centrifuge. L'objectif de ce travail est de comprendre les mécanismes hydrodynamiques et la dynamique des interfaces avant, pendant et après la traversée d'une interface liquide par une goutte, conduisant à son enrobage. Dans ce but, des approches numériques et expérimentales ont été combinées et complétées par des modèles théoriques. Une méthode numérique résout les équations de Navier-Stokes, discrétisées par une approche en volumes finis, en se basant sur les méthodes « Level-Set » et « Ghost Fluid » pour capturer la dynamique des interfaces en présence et gérer les discontinuités aux interfaces ; elle permet d'accéder au champ de vitesse autour de la goutte déformable lors de la traversée de l'interface. Un dispositif expérimental, permettant de former des gouttes aqueuses de tailles (100-1400  $\mu\text{m}$ ) et de forcer leur passage au travers d'une interface liquide grâce à une force centrifuge pouvant atteindre  $\approx 2500g$ , a été conçu afin d'observer toutes les étapes du procédé grâce à une caméra rapide synchronisée avec la rotation de la cellule d'encapsulation, afin d'analyser les conditions de traversée et les différents régimes d'entraînement de fluide. La traversée ou le rebond d'une goutte à l'interface sont fonction de la compétition entre les forces interfaciales, le poids de la goutte et les forces inertielles, et relèvent de phénomènes complexes dépendant de nombreux paramètres adimensionnels. Les deux approches ont permis de définir les conditions de traversée en fonction des nombres adimensionnels pertinents  $\frac{\xi_{12}}{\xi_{13}}$  and  $Bo_{13}$ , et de développer une loi d'échelle de la longueur maximale de la colonne se formant pendant la traversée ainsi que du volume d'enrobage de la goutte en résultant. Ce travail a permis de déterminer les conditions optimales, à l'échelle d'une inclusion unique, pour encapsuler une goutte selon ce procédé, condition préalable au développement d'un pilote industriel associé à une production en continu.

**Mots-clés :** encapsulation, écoulement multiphasique, traversée d'interface, méthode « Level-Set », goutte.



# Table of Contents:

<b>Table of Contents:</b> .....	<b>7</b>
<b>Chapter 1: Introduction</b> .....	<b>11</b>
<b>Chapter 2: State of the art</b> .....	<b>16</b>
2.1. Introduction: .....	16
2.2. Motion of inclusions and their shapes inside a continuous liquid .....	19
2.2.1. Inclusion rising velocity.....	19
2.2.2. Droplet/Bubble shape during rising .....	22
2.2.3. Conditions at the interface .....	24
2.3. Crossing and coating .....	24
2.3.1. Rigid particles crossing a L/L interface: .....	25
2.3.2. Bubbles crossing a L/L interface: .....	35
2.3.3. Droplets crossing a L/L interface.....	39
<b>Chapter 3: Numerical Approach: Methods &amp; Validation</b> .....	<b>44</b>
3.1. Introduction .....	44
3.2. Numerical tool.....	46
3.2.1. Projection Method.....	48
3.2.2. The Level-Set method.....	49
3.2.3. Ghost-Fluid Method.....	52
3.2.4. Global algorithm and precisions on discretization schemes .....	53
3.3. Validation tests.....	55
3.3.1. Two-phase flow validation .....	55
3.3.2. Three-phase flow validation case.....	57
<b>Chapter 4: Numerical Approach: Results</b> .....	<b>65</b>
4.1. Introduction .....	65
4.2. Numerical method .....	70
4.3. Interface crossing in dynamic conditions.....	71
4.4. Crossing conditions with additional inertia.....	72
4.5. Dynamics of interface crossing .....	76
4.5.1. Phenomenology.....	76

4.5.2.	Crossing time .....	81
4.5.3.	Column maximal length.....	83
4.5.4.	Volume of the coating film .....	84
4.5.5.	Decrease in kinetic energy during crossing .....	89
4.6.	Concluding remarks and prospects .....	92
<b>Chapter 5: Experimental Approach: Material &amp; Methods .....</b>		<b>96</b>
5.1.	Description of the experimental prototype.....	96
5.1.1.	The two cells and the spin coater .....	96
5.1.2.	The role of pressure regulator .....	98
5.1.3.	Image Acquisition.....	100
5.2.	Image Processing Methodology .....	103
5.2.1.	Trajectory Detection: Hough transform and frame of reference .....	104
5.2.2.	Contour Processing: Size and Form Determination.....	108
5.2.3.	Velocity Calculation: By Image Cross-correlation function .....	110
5.2.4.	Calculation of droplet frequency .....	113
5.2.5.	The detection of Plane Interface position .....	114
5.2.6.	Calculation of the maximum column length.....	115
5.3.	Chemical Products.....	116
<b>Chapter 6: Experimental Approach: Results.....</b>		<b>120</b>
6.1.	Introduction .....	120
6.2.	Range of physical and non-dimensional parameters.....	121
6.3.	Droplets injection .....	123
6.3.1.	Influence of rotation speed.....	125
6.3.2.	Influence of capillary diameter .....	126
6.3.3.	Influence of surfactants.....	127
6.3.4.	Scaling law for droplet size.....	129
6.4.	Droplet trajectory before crossing.....	130
6.4.1.	Description of droplet motion in the centrifugal cell.....	130
6.4.2.	Modelling of droplet motion.....	132
6.4.3.	Droplet shape .....	136
6.5.	Interfacial Crossing .....	140
6.5.1.	Conditions for crossing (“Crossing or not crossing?”).....	141

6.5.2.	Droplet crossing configurations:.....	144
6.5.3.	Effect of surfactants on crossing.....	150
6.5.4.	Numerical predictions versus experimental data .....	158
6.6.	Conclusion.....	164
<b>Chapter 7: Conclusion &amp; Perspectives: .....</b>		<b>168</b>
<b>Appendix A: Experimental device and measuring methods.....</b>		<b>173</b>
A1.	A 3D scheme of the experimental device.....	173
A2.	Spin Coater and its modifications .....	174
A.2.1.	The Spin Coater .....	174
A.2.2.	The Assembly replacing the Mandrel .....	175
A.2.3.	The bottom and top supports.....	176
A.2.4.	The rotating base.....	177
A.2.5.	The cells .....	178
A3.	High-Speed Camera: Phantom Miro 320.....	178
A4.	Microscope: LEICA M651.....	179
A5.	Pressure Controller: ELVEFlow OB1 MK3 .....	179
A6.	PHLOX LED Pannel.....	180
A7.	Gardasoft RT 200-20.....	181
A8.	Anton Paar DMA 38 Density Meter .....	181
A9.	TA instrument AR 2000ex Rheometry .....	182
<b>Appendix B: Surfactants mass transfer calculation .....</b>		<b>184</b>
B.1.	The transfer of surfactants from phase 1 to the droplet interface.....	184
B.2.	The transfer of SDS from the inner part of droplet to the interface.....	186
B.3.	The stagnant cap regime at interface mentioned in section 2.2.3 .....	188
<b>References:.....</b>		<b>189</b>

# Chapter 1:

Introduction

# Chapter 1: Introduction

Microencapsulation brings together all the technologies enabling the coating or trapping of active ingredients in solid, liquid or gaseous phase within individualized particles whose size ranges varies from a few microns to a few millimeters (Richard & Benoît, 2000). It is the process by which an active ingredient is isolated from the external environment within a shell in order to protect it, trigger and control its release in time and space. The reasons of encapsulation are various such as: protecting an ingredient from external environment, before its targeted release, modifying the physical characteristics of a material, mixing incompatible components in one capsule, masking a taste or odors of an active ingredient through an isolator shell, handling harmful or toxic material safely. Encapsulation represents a wide range of applications in numerous fields (pharmaceutical, alimentation, cosmetics...) as well described in the reviews (Dubey et al., 2009; Mishra, 2015). The contribution of microencapsulation, for instance, for the controlled release of fertilizers or pesticides or even for pharmaceuticals, meets a strong societal requirement in terms of environmental preservation and progress in the field of public health. Microcapsules can be classified according to three parameters: size, morphology, and physico-chemical characteristics. Microcapsules range in size from sub-micrometers to few millimeters, however it is possible to have capsules with size down to 10 nm, that are often called nano-capsules (Mishra, 2015). The morphology of microcapsules is classified according to distribution of the core material, mono-cored/mononuclear microcapsules in which the active ingredient is found as one core with one shell around it, and can have a spherical or irregular shape, polycored/polynuclear microcapsules having a number of different sized cores within the shell, and matrix type capsule with homogeneous distribution of active ingredient (core material) within the shell material. According to applications needs, microcapsules can be oil-in-water (O/W) where the core material is an organic compound and the shell is aqueous, and water-in-oil (W/O) inversely.

The choice of the most appropriate encapsulation technology based on technical and economic constraints as well as the targeted objectives should be made with care. The physicochemical properties of the shell depend on its composition, its size, and thickness, all being fixed by the parameters of the process used to develop it, and can be difficult to master. Microencapsulation processes are still at very variable stages of industrial development. Industrialized production processes operate on a large scale (ink, dyes, pigments, etc...). Some of these processes offer a high rate of capsules production, yet the size distribution of the capsules is not narrow as in atomization techniques. Other processes such as microfluidic processes offer a very good size control but with a lower production rate. For applications of liquids microencapsulation, the processes used are still sequential and/or consumers of raw materials, in particular of carrier phases. Moreover, developed processes do not cover all morphologies and size ranges at an industrial production scale, precisely W/O mono-core microcapsules of sizes ranging between 100 and 300  $\mu\text{m}$ .

Current research for the production of this type of capsule is largely directed towards microfluidic inspiration processes, which allow perfect control of the coated volume and the thickness of the capsule.

In the framework of the EPIC (Encapsulation process by interfacial crossing) project funded by the National Research Agency of France (ANR), we develop a novel process based on a patent developed by one of the project partners (Laboratoire Charles Coulomb (L2C), patent EP2456550 A1, July 2010). The process is based on the continuous aqueous drops formation and crossing of a liquid-liquid interface by these deformable drops. Inspired by microfluidics, the process includes an external force driving the crossing. The same principle can also be used at lower inertia (i.e. low Bond number) in presence of amphiphilic molecules in the organic phase to form a specific capsule: a vesicle. In this case, the crossing mechanism relies on the zipping of two surfactant monolayers present at both the droplet and the planar interface, leading to a coating of the drop by a bilayer. The potentiality of the concept has been successfully explored at low inertia to produce giant unilamellar vesicles of sizes range between 10 and 50  $\mu\text{m}$  (PhD thesis of Etienne Loiseau, and Abkarian et al., 2011). Contrary to the cDICE process, the droplet is at a higher Reynolds and Bond numbers in the EPIC process, and the crossing is driven by inertia instead of Van de Waals attraction. The interface significantly deforms in order to favor the entrainment of the oil phase instead of excluding it as in the zipping of monolayers mechanism. So, the development of the process for higher Reynolds and Bond numbers will allow to encapsulate aqueous droplets of size range  $100 < d < 300 \mu\text{m}$  inside an organic shell (W/O monocoreshell capsule), for the high rate production of mono-dispersed capsules controlled in content and size and constituted of a shell with tunable thickness, mechanical strength and permeability. Given the targeted size range of the droplets, the crossing of the interface requires a large external force superior to the gravity force, to operate in inertial regime. The driving force is the centrifugal force varying up to 2400g experimentally. The process developed during this project includes four steps (Figure 1):

- injection of an aqueous droplet in an organic phase and their migration towards the interface,
- droplet coating by crossing an organic phase-aqueous phase interface,
- rising of the coated drop in the continuous aqueous phase.
- recovery of the coated drops in order to ensure the hardening of the coating phase.

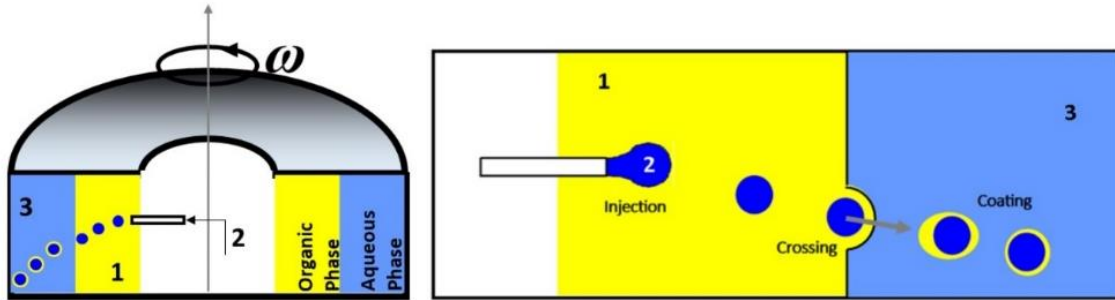


Figure 1: (A) The encapsulation centrifugal cell. (B) The steps of the encapsulation process.

This PhD work is dedicated to the three first steps of the process, and mainly on the step of interface crossing, crucial for the proper coating and thus capsule production. The capsule recovery step and the shell solidification are beyond this PhD work but is also as part of the EPIC project.

My PhD objectives are thus:

- to characterize the droplet size, shape, and trajectory towards, across and after the liquid-liquid interface,
- to determine the interface crossing conditions depending on the physical and physico-chemical parameters at one droplet scale, and to quantify the coating volume.

The development of this encapsulation process at a single droplet scale opens the doors for a potential scaling up to industrial scale through the conception of a pilot. This requires defining the physical and chemical parameters governing droplet interface crossing and coating and how these parameters can be transposed taking into account all the technical requirements. Numerical and experimental approaches will be combined in order to quantify the influence of the process parameters on the final physical characteristics and functionalities of the capsules. We will thus design a setup that allows the injection of droplets at a controlled size in a centrifugal chamber and the recording of the droplet rise and interface crossing in these rotating chamber. We will also develop a numerical method to simulate the interface crossing in absence of surfactants. In the following, we present the numerical and experimental methods employed with their respective results. This introduction is followed by six other chapters:

**Chapter 2. State of the art.** In this chapter we describe the physical problem of inclusions (bubble, droplet, or solid particle) rising in a stagnant liquid and crossing a liquid-liquid interface, and we propose a literature review of previous works focused on the subject.

**Chapter 3. Numerical Approach: Method & Validation.** This part is devoted to the presentation of the numerical method employed. First, we discuss briefly different methods used to simulate multi-phase flows. Then, we detail the numerical approach with its different numerical methods employed for simulation performed throughout this research work. Finally, we perform validation tests in the cases of two-phase and three-phase flows.

**Chapter 4. Numerical Approach: Results.** This chapter is written in the form of an article. It presents the results of numerical simulations of solid-like (non-deformable and viscous) and deformable droplets crossing a liquid-liquid interface. We explain the phenomenology observed during the rise and the crossing, then we give scaling laws for pertinent process parameters such as: the crossing time, the length of column entrained, and the encapsulation volume as a function of system non-dimensional parameters.

**Chapter 5. Experimental Approach: Material & Methods.** This chapter constitutes three parts. In the first part, we present the conception of the experimental pilot developed during this work. In the second part, we explain the image processing method employed to analyze the experimental results. And in the last part, we give the different chemical products used in the experiments with their description and range of physical parameters.

**Chapter 6. Experimental Approach: Results.** In this chapter, we give a synthesis of the experimental results regarding the three steps of the process: injection, rising and crossing. We give a scaling law of the injected droplets size as a function of pertinent physical parameters. We characterize the droplet trajectory during its rise in the stagnant liquid. Then, we present results regarding interface crossing for different systems of fluids and rotation speeds, and we describe and characterize different crossing regimes. We compare numerical and experimental approaches and we present comparisons in terms of the scaling of column length and coating volume.

**Chapter 7: Conclusion and Perspectives.** A summary of the main results obtained is presented, as well as various possible perspectives for this work in terms of: (i) the extension of present study to target wider range of parameters, (ii) the technological improvements which can be made on the present prototype, and (iii) the results obtained that will contribute to the process scaling-up to an industrial scale



# Chapter 2:

State of the art

# Chapter 2: State of the art

## 2.1. Introduction:

The encapsulation process studied is based on the crossing of an interface by a droplet (diameter of the order of hundred microns) at high inertia (Droplet Reynolds number  $Re > 1$ ). In the interest of studying the crossing of an interface by an inclusion, we observe the type of images shown in Figure 1: under the action of an external force (gravity, centrifugal force) the droplets, here formed at the end of a capillary tip, rise in a first continuous phase towards an interface, which they will be able to cross when the conditions are favorable (Figure 2.a). The crossing, requiring a time to be determined, is accompanied by the coating of the drop by phase 1 (Figure 2.a and 2.b), with the formation of a tail behind the drop (Figure 2.c and 2.d), As the drop moves away from the interface, the tail thins until it breaks (Figure 2.e). According to the way in which the coating will be carried out and the amount of entrained volume, the characteristics of the future capsule will be determined. It is therefore essential to completely understand the phenomena linked to crossing conditions. Few authors have studied the crossing of an interface with an inertial drop. Such an investigation is complex because it involves more parameters as compared to the case of particles or bubbles, due to the droplet viscosity and deformability. In order to identify this problem, we therefore made the choice to widen the bibliography elements on the crossing of an interface by inclusions (not only drops but also bubbles and rigid spheres), and to synthesize the results obtained in all regimes studied in the literature (Stokes and Inertial regimes).

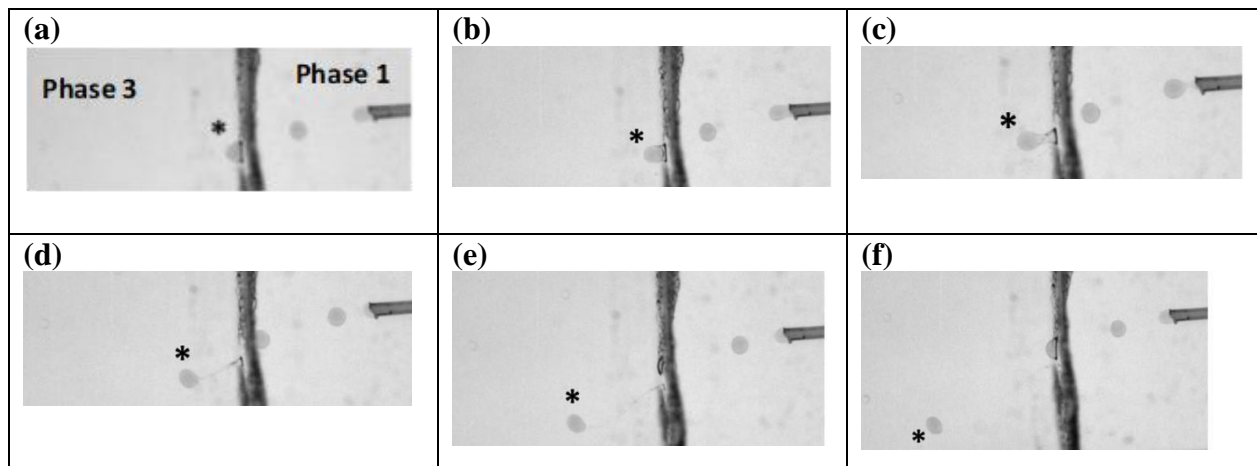


Figure 2: The sequence of images of a droplet crossing a liquid-liquid interface. The droplet is constituted from a sucrose solution of mass concentration 25% and density  $\rho_2 = 1081 \text{ Kg.m}^{-3}$  and of viscosity  $\mu_2 = 0.0024 \text{ Pa.s}$ . The first continuous phase is Silicone oil of density  $\rho_1 = 960 \text{ Kg.m}^{-3}$  and of viscosity  $\mu_1 = 0.0024 \text{ Pa.s}$ . The second continuous phase (phase 3) is water with SDS surfactants at concentration 10 mM with  $\rho_3 = 997 \text{ Kg.m}^{-3}$  and of viscosity  $\mu_3 = 0.001 \text{ Pa.s}$ .

To provide a physical description of the rise of an inclusion and of its coating after crossing a liquid/liquid interface, one needs to define the physical parameters and the associated non-dimensional numbers of the problem. The three-phase systems involving Newtonian fluids are characterized by their physical properties, namely densities ( $\rho_i$  with  $i= 1, 2,$  and  $3$ ), dynamic viscosities ( $\mu_i$  with  $i= 1, 2,$  and  $3$ ) and the interfacial tensions between phases 1 and 2 ( $\gamma_{12}$ ) and between phases 1 and 3 ( $\gamma_{13}$ ), assuming that phases 2 and 3 will never be in contact in this problem. Moreover, it is supposed in general that the physical parameters (densities, viscosities, and surface tension) are constant. In particular, the presence of surfactants in the system is characterized by the static surface tensions at a given surfactant concentration. Other parameters of importance in this configuration are the droplet diameter  $d$  or radius  $R$ , the position of the initially plane interface  $r_i$ , the centrifugal acceleration ( $a_c = r_i \omega^2$ ) at the position of this plane interface, and  $r_0$  the initial position of the droplet centroid with respect to the axis of rotation. In such a system, the normal gravity acceleration ( $g$ ) is neglected compared to the centrifugal one because of the very high rotation velocities which are considered. As these ten mentioned quantities involve three fundamental units (mass, time and length), the theorem of Vaschy-Buckingham states that the problem may be characterized with  $10 - 3 = 7$  independent dimensionless parameters. The following non-dimensional numbers may be chosen:

- The density ratio between phase 1 and phase 2:  $\xi_{12} = \frac{\rho_2}{\rho_1} - 1$
- The density ratio between phase 1 and phase 3:  $\xi_{13} = \frac{\rho_3}{\rho_1} - 1$
- The viscosity ratio between phase 1 and 2:  $\lambda_{12} = \frac{\mu_2}{\mu_1}$
- The viscosity ratio between phase 1 and 3:  $\lambda_{13} = \frac{\mu_3}{\mu_1}$
- The Bond number of the droplet immersed in phase 1 which describes its deformability by comparing inertial effects applied on the droplet to the interfacial tension:  $\mathbf{Bo}_{12} = \frac{|\rho_2 - \rho_1| r_0 \omega^2 R^2}{\gamma_{12}}$
- The Bond number of the interface which describes its deformability by comparing inertial to interfacial effects at the position of the interface:  $\mathbf{Bo}_{13} = \frac{|\rho_3 - \rho_1| r_i \omega^2 R^2}{\gamma_{13}}$
- The Archimedes number which describes the flow regime of the droplet rise in phase 1, and which is merely a Reynolds number based on centrifugal velocity  $(\xi_{12} r_i \omega^2)^{\frac{1}{2}}$

$$\mathbf{Ar} = \frac{\rho_1 (\xi_{12} r_i \omega^2)^{\frac{1}{2}} R^3}{\mu_1}$$

Two instantaneous non-dimensional numbers describing the droplet rise and deformability in phase 1 can be additionally defined: The Reynolds number ( $Re$ ) which describes the flow regime and the Weber number ( $We_{12}$ ) of the droplet which compares the inertial stress applied to the droplet and responsible for its deformation ( $\rho_1 u(t)^2$ ) over its interfacial tension that resists to deformation ( $\gamma_{12}/d$ ):

- $Re(t) = \frac{\rho_1 u(t) d}{\mu_1}$
- $We_{12}(t) = \frac{\rho_1 u(t)^2 d}{\gamma_{12}}$ ; where  $u(t)$  is the instantaneous velocity of the droplet center of mass.

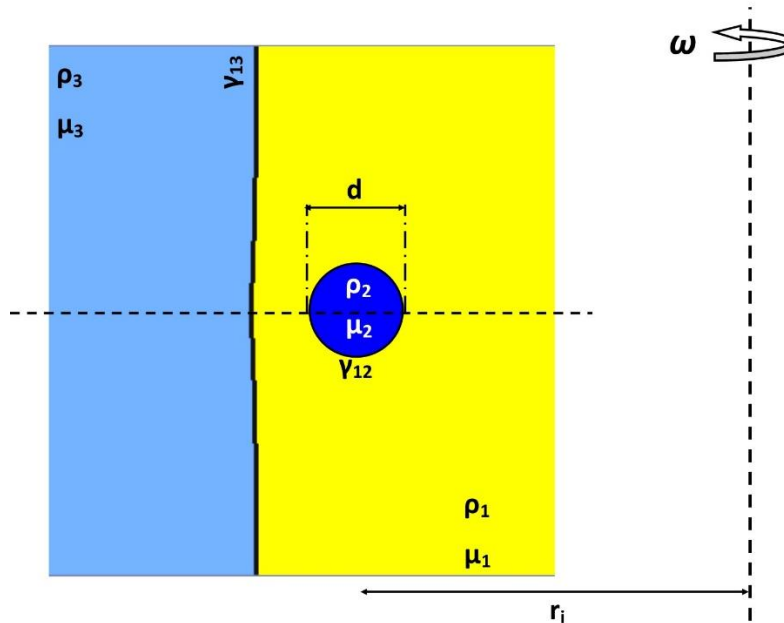


Figure 3: The scheme of physical problem of three phases with the labels and physical parameters corresponding to each phase.

Some of above physical parameters are fixed, which reduces the number of varying physical parameters and therefore of non-dimensional numbers:

- When the dispersed phase is a rigid sphere, its viscosity is infinite and so is  $\lambda_{12}$ , and the particle is non deformable ( $Bo_{12} = 0$ ).
- When the dispersed phase is a gas bubble  $\xi_{12}$  is -1 and  $\lambda_{12}$  is 0.

The case of the deformable droplet treated in this thesis is the case involving the highest number of physical parameters and non-dimensional numbers.

## 2.2. Motion of inclusions and their shapes inside a continuous liquid

The shape and velocity of an inclusion before arriving to the interface plays a significant role in the dynamics of crossing. So, before delving into the topic of L/L interface crossing by an inclusion, we would like discuss their motion and shapes while rising in phase 1. In this part, we discuss the available models to characterize the motion of inclusions inside a stagnant liquid in terms of settling velocity and shape (deformation and conditions at its interface).

### 2.2.1. Inclusion rising velocity

The motion of an inclusion whether it is a rigid particle, a drop, or a bubble inside a continuous phase can be described by a model based on the application of the fundamental principle of dynamics. Under the influence of an acceleration field (gravity), the forces acting on a rising body are the buoyancy force due to gravity  $F_G$ , the drag force  $F_D$ , the force of added mass  $F_M$  and a history force  $F_H$ . However, in a rotating system, the centrifugal acceleration  $a_{cc}$  dominates and gravity is negligible, the buoyancy force becomes due to the centrifugal acceleration instead of gravity. As a consequence of the inertia due to centrifugal acceleration, the Coriolis force  $F_C$  appears when characterizing the motion from a rotating frame. This force is responsible of a deflection of the trajectory of the body. Based on Newton's second law in a rotating frame, the following expression of forces acting on the spherical body presented in the scheme of Figure 4 is derived:

$$\vec{F}_G + \vec{F}_C + \vec{F}_D + \vec{F}_M + \vec{F}_H = m_2 \frac{d\vec{u}}{dt} \quad (1)$$

Where  $\vec{u}$  is the inclusion velocity, and  $m_2$  is the mass of the spherical body. More details on the derivation of the expression of the forces can be found in the handbook of (Clift et al., 1978).

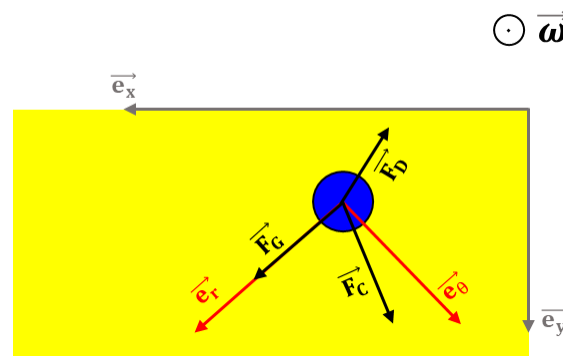


Figure 4: A scheme of the forces acting on the a spherical inclusion in a centrifugal cell. The Cartesian coordinates are  $e_x$  and  $e_y$ , and the polar coordinates are  $e_r$  and  $e_\theta$ .

The contribution of the centrifugal and Coriolis force will be studied explicitly in Chapter 6. The force of added mass is a force of inertia due to the acceleration of the body which deflects some volume of the continuous phase as it moves inside it. It is simply modeled as some volume of the phase 1 moving with the object. So, it only depends on the shape of inclusion. The history force term describes the force due to the lagging boundary layer development with the change in acceleration of bodies moving through a fluid, it accounts for unsteady viscous effects. Although it can be large for an accelerated body, no general expressions are available for all cases and it is often neglected for practical reasons. The drag force acts on the inclusion as it moves inside the continuous phase, it represents all stresses (viscous and pressure) acting by the fluid on the inclusion (excluding the Archimedes force); this force being opposite to the particle motion. It has the following expression:

$$\vec{F}_D = \frac{-\pi R^2}{2} C_D \rho_1 \mathbf{u} \vec{u}$$

With  $u$  being the magnitude of the inclusion velocity.

The magnitude of this force depends on the value of the drag coefficient  $C_D$  which is a non-dimensional number. The drag coefficient of a rigid sphere or a non-deformed gas bubble depends only on the instantaneous Reynolds number. For a liquid non-deformable droplet, the coefficient  $C_D$  depends on  $\lambda_{12}$  additionally to  $Re$ . For deformed shapes, a parameter describing the deformation is added to the two effective parameters  $Re$  and  $\lambda_{12}$  determining the drag coefficients. Several expressions for the coefficient  $C_D$  were developed in the literature after the oldest analytical solution of Stokes for a rigid sphere at a very low Reynolds number ( $Re \ll 1$ ) and its correction by Oseen that is valid for  $Re \leq 1$  (Oseen, 1913). In Table 1, we present the expressions found for  $C_D$  in the literature with their respective limits of validity and references. In Figure 5, we plot  $C_D$  as a function of  $Re$  for the Stokes expression and its correction by Oseen, together with three expressions for rigid spheres, liquid droplet, and gas bubbles in inertial regime. For all Reynolds numbers, the drag coefficient for a rigid sphere is larger than for bubbles and droplets. For  $Re < 0.1$ , bubbles and droplets have close values of  $C_D$ , but in inertial regimes, the drag coefficient of a droplet becomes significantly larger than that of the bubble. Since this work is done in inertial regime where differences are significant, the choice of  $C_D$  must be as relevant as possible when modeling the rise of the droplet.

The drag coefficients expressions are valid for liquid drops and gas bubbles remain valid as long as the interface is not contaminated, i.e. in absence of surfactants and impurities. Surfactants increase  $C_D$  as shown in Myint et al., 2007. Actually, surfactants tend to damp both the tangential velocity at the interface and the internal motion inside the droplet, which is often referred as interface immobilization, as we will see in the section 2.3.3.

	Correlation	Limit of validation	Reference
1	$C_D = \frac{24}{Re} \left(1 + \frac{3}{16} Re\right)$	Rigid sphere $Re \leq 1$	(Oseen, 1913) verified experimentally by (Maxworthy T., 1965) for $Re \leq 0.45$
2	$C_D = \frac{24}{Re} (1 + 0.15 Re^{0.687})$	Rigid sphere $1 < Re < 800$	(Schiller & Nauman, 1933) through experimental work
3	$C_{DS} = \frac{24}{Re} \left(1 + 0.15 Re^{0.687} + \frac{0.0175}{1 + 4.25 * 10^4 Re^{-1.16}}\right)$	Rigid sphere $1 < Re < 3.7 * 10^5$	(Clift et al., 1978)
4	$C_{DB} = \frac{48}{Re} \left[1 - 2.211 Re^{-\frac{1}{2}} + O(Re^{-\frac{5}{6}})\right]$	Non-deformed bubble Clean interface $Re > 50$	(Moore, 1962)
5	$C_D = \frac{16}{Re} \left[1 + \left(\frac{8}{Re} + \frac{1}{2} \left(1 + \frac{3.315}{Re^{0.5}}\right)\right)^{-1}\right]$	Non-deformed bubble Clean interface	(Mei et al., 1994)
6	$C_D = \frac{1}{1 + \lambda_{12}} \left[\lambda_{12} \left(\frac{24}{Re} + 4 Re^{-\frac{1}{3}}\right) + 14.9 Re^{-0.78}\right]$	Non-deformed liquid drop Clean interface $Re < 200$	(Rivkind V. Ya.M. & Ryskin G., 1976)
7	$C_D = \frac{1}{1 + \lambda_{12}} \left[\lambda_{12} \left(\frac{24\chi^{-1/3}}{Re} + 4 Re^{-\frac{1}{3}}\right) + 14.9 Re^{-0.78} \chi^{-0.26}\right]$ $\vec{F}_D = \frac{\pi R^2 \chi^{2/3}}{2} C_D \rho_1 u \vec{u}; (1)$	Deformed droplet Clean interface $Re < 200$	(Helenbrook & Edwards, 2002) (Clift et al., 1978) Correction of the above expression by taking the major axis of a deformed droplet as a characteristic length

Table 1: The drag coefficients of inclusions rising in an immiscible liquid. (1)  $\chi$  is the droplet aspect ratio defined at the ratio between the major and the minor axis of an ellipsoidal deformed droplet.

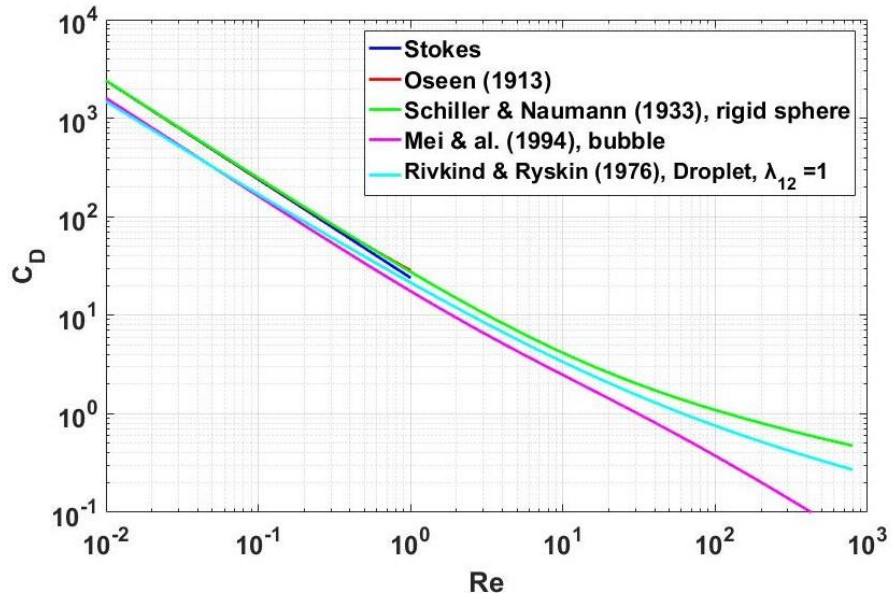


Figure 5: The plots of drag coefficients derived in literature as a function of Reynolds number.

The resolution of equation (1) with the suitable coefficients, gives the velocity evolution in time for an inclusion immersed in a stagnant liquid. Under gravity, a falling or rising object released from rest accelerates, its velocity increases and so does the drag acting on it (the acceleration regime). After some time, once viscosity has diffused momentum

around the inclusion, the wake develops, and the drag force balances the buoyancy force. The droplet acceleration becomes null since the net force acting on the object is zero (stationary regime). In the case of motion driven by the centrifugal acceleration as in our study, even if the speed of rotation is constant, the centrifugal acceleration still increase linearly with the droplet position, meaning that an object acceleration never becomes null, a pseudo steady state is reached instead (See figure 7 in the article).

### 2.2.2. Droplet/Bubble shape during rising

Unlike rigid spheres, bubbles and droplets in a liquid phase may experience deformation when moving into a fluid, either rising or falling. The parameter characterizing the deformation is the aspect ratio defined as the equatorial diameter divided the polar diameter of the bubble or droplet  $\chi = \frac{a}{b}$  (Figure 6).

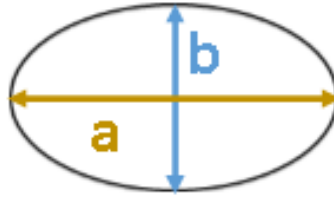


Figure 6: A scheme of the ellipsoidal deformed droplet/bubble with the two axis characterizing the aspect ratio  $\chi = \frac{a}{b}$ .

The aspect ratio of a bubble can be characterized using the Clift diagram (Clift et al., 1978) of Figure 7 as a function of both  $Re$  and  $Bo_{12}$ . The diagram shows also the iso-curves depending on the Morton number,  $Mo = \frac{g\mu_1^4}{\rho_1\gamma_{12}^3}$ , which strongly depends on the external liquid viscosity  $\mu_1$ . In addition, other studies in the inertial regime (Taylor, T. Acrivos, 1964, Bhaga & Weber, 1981, Shopov et al., 1990, and Legendre et al., 2012) have shown that  $\chi$  is an increasing function of the Weber number  $We_{12}$ . In the latter study, the equation (2), valid up to an aspect ratio  $\chi=3$ , was derived to describe the bubble deformation in the stationary regime as a function of both  $We_{12}$  and  $Mo$ . The expression derived by Legendre & al. corrects the expression written by Moore long time before, in 1965, to describe the deformation of bubbles in low viscosity liquids. Shopov (Shopov & Minev, 1992) confirmed the non-deformation of the bubble at low Weber numbers ( $We_{12} \ll 1$ ), and showed that it will have the same shape when attaining the stationary regime at the same Weber number regardless of its initial shape.

$$\chi = \frac{1}{1 - \frac{9}{64} We(1 + 0.2Mo^{0.1}We)^{-1}} \quad (2)$$

where  $Mo = \frac{g\mu_1^4}{\rho_1\gamma_{12}^3}$  is the non-dimensional Morton number.



Concerning liquid drops, their deformation while rising in gas was studied by Helenbrook (Helenbrook & Edwards, 2002), and Clift (Clift et al., 1978) modelled droplets deformation in air in the limit of  $Bo_{12} < 2$ . Regarding droplets moving in stagnant liquids, Grace (Grace et al., 1976) derived the aspect ratio as a function of  $\lambda_{12}$  and  $Bo_{12}$  considering motion in water. Moreover, Wellek (Wellek et al., 1966) proposed a shape description for non-oscillating drops in contaminated immiscible liquids as a function of  $We_{12}$ , in addition to another proposed expression of  $\chi$  as a function of  $Bo_{12}$  respectively, both in the limit of low (Eq. 3) and moderate viscosity (Eq. 4) ratios. Myint (Myint et al., 2007) also proposed an expression for  $\chi$  as a function of the non-dimensional Tadaki number  $Ta = Re * Mo^{0.23}$  valid only for values of  $Mo$  in between  $2.5 * 10^{-12}$  and 0.126. Finally, the graph extracted from Clift (Clift et al., 1978) in Figure 7 maps the shapes of fluid particles as a function of  $(Bo_{12}, Re)$  or  $(Re, Mo)$  and is valid in the cases of either bubbles or liquid droplets in a liquid external phase.

$$\chi = 1 + 0.091We_{12}^{0.95} \quad (3)$$

$$\chi = 1 + 0.465Bo_{12}^{0.757} \quad (4)$$

The expressions mentioned above remain valid for droplets with clean interfaces. The presence of surfactants is expected to decrease the surface tension of the interface, leading to stronger deformations at the same inertia.

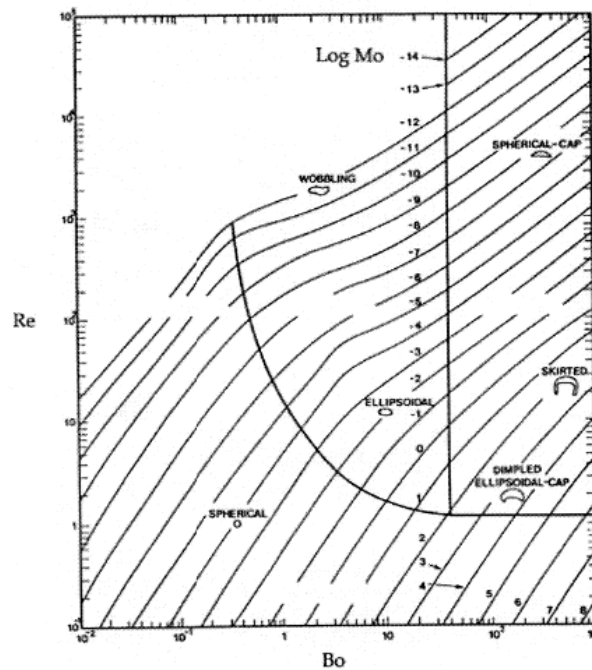


Figure 7: The mapping of the shape of a fluid particle as a function on non-dimensional numbers. Extracted from (Clift et al., 1978).

### 2.2.3. Conditions at the interface

During the rise of a deformable inclusion (bubble or drop) in a stagnant liquid, tangential stresses form at the interface. In case the interface is perfectly clean, there is a continuity of tangential stresses at its surface. The tangential velocity is non-zero and the fluid can slide freely on the surface. This condition is often called a mobile interface. However, this case is very difficult to carry out experimentally due to the presence of impurities that transfer to the surface of the interface by the flow.

Several studies were performed to investigate the effect of surfactants on the flow around bubbles (Bel Fdhila & Duineveld, 1996; Cuenot et al., 1997; V. Levich, 1962; Palaparthi et al., 2006) and droplets (Piedfert et al., 2018; Stebe & Maldarelli, 1994). It is well known that a residual amount of surfactants/impurities is sufficient to change drastically the dynamics of a bubble or droplet (Takagi & Matsumoto, 2011). When surfactants are swept towards the interface, gradients of concentration of surfactants along the surface are induced (for example, in the case of a drop that rises, the surfactants are all swept back by the flow), therefore gradients of interfacial tension develop along the interface. A new tangential force appears at the interface, the Marangoni stress which tends to oppose the constraint which was already exerted on the surface of the drop because of its upward movement. The consequence of these two stresses of opposite signs on the surface is that the tangential speed of the fluid becomes almost zero as in the case of a rigid particle. The overall speed of the drop becomes lower than that of a clean drop, and becomes the same as that of a solid particle of the same size. This effect, which is a consequence of the Marangoni effect, was shown theoretically by Levich (Levich & Tobias, 1963). This condition is often called an immobile interface.

Nevertheless, there is an intermediate regime between the "fully mobile" and the "fully immobilized" interface. It happens when the Marangoni effect is too weak, for example, when the local tangential speed of the fluid is zero on one part of the interface, while it is non-zero on the other part. This is what is called the "stagnant cap" regime, characterized by an angle of contamination between the two zones (See appendix B). However, this transition zone exists only over a very limited interval of concentration of surfactants (or even impurities).

## 2.3. Crossing and coating

After rising in phase 1, the next and most decisive step of the encapsulation process concerns the interface crossing and the droplet coating. In this section, the three cases of bubbles, drops, and particles are distinguished and a final summary of the state of the art is presented. The studies presented in this part are without the presence of surfactants and are based on gravity-driven motion, so in order to perform studies on large range of

Reynolds numbers, authors frequently varied the size of the inclusions and the viscosity of first phase.

### 2.3.1. Rigid particles crossing a L/L interface:

#### Film drainage when crossing

When an object is in contact with a L/L interface, a film of the continuous liquid forms between its pole and the deformed interface (Figure 8 (a)). Regardless of the mobility of the droplet interface (completely immobile in the case of rigid spheres), this film drains as the sphere continues to penetrate the interface. The draining film profile was first studied by Hartland (Hartland, 1968), its importance arise from its influence on the coating volume which will stay around the droplet after crossing. Figure 8 extracted from the same paper shows the thickness profile of the film forming around a sphere approaching the L/L interface. At low Reynolds number, this profile was found to be symmetrical with respect to the axis of sphere and thinnest at the outer edge with a possible secondary thickness minimum at the center, and with a decreasing thickness in time.

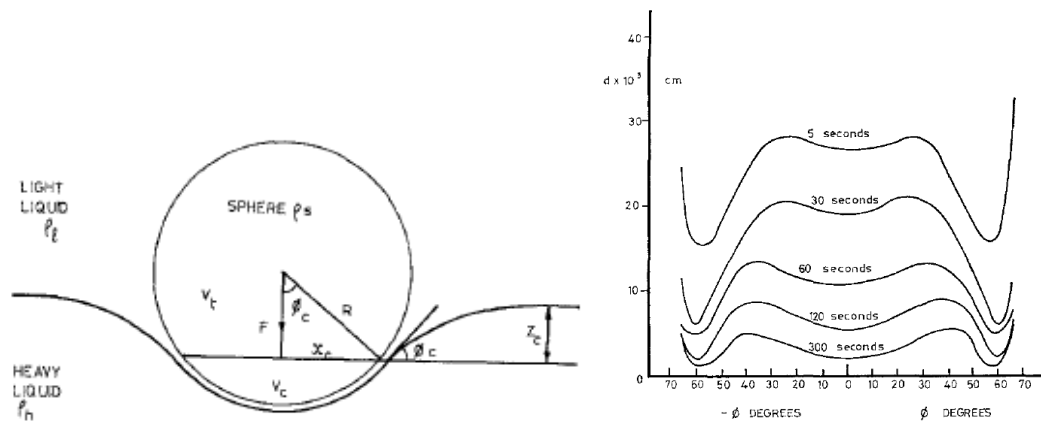


Figure 8: Extracted from (Hartland, 1968), The profile of the draining film thickness forming between the rigid sphere and the plane interface as a function of the angle  $\phi_c$  shown on the left hand side and for different instants.

#### Crossing conditions:

The rigid sphere standing on the interface may undergo two phenomena: crossing of the interface if inertial forces are stronger than the surface tension of the interface and Archimedes resisting force or floating otherwise (Maru et al., 1971). This implies two regimes of the interface deformation as defined by Geller (Geller et al., 1986): draining and tailing. Figure 9 (a) extracted from the study of Pierson (Pierson & Magnaudet, 2018) shows a sphere floating at the interface with a draining deformation regime at the interface

(film between the droplet and meniscus is very thin) while (b) shows a sphere crossing the interface which undergoes a tailing deformation.

For the purpose of determining the transition between the two regimes (crossing and floating), a theoretical model was developed based on a force balance applied to a rigid sphere settled at the interface with a partial wetting condition (Figure 10). The model was recently written in the study of Pierson (Pierson & Magnaudet, 2018) and has several parts in common with previous work (Maru et al., 1971, Vella et al., 2006, Bonhomme et al., 2012, and Malmazet et al., 2015). Under strict static conditions (Eq. (5)), the buoyancy force, which favors crossing is balanced with the interfacial tension force and the hydrostatic pressure force which acts in the direction opposite to droplet motion.

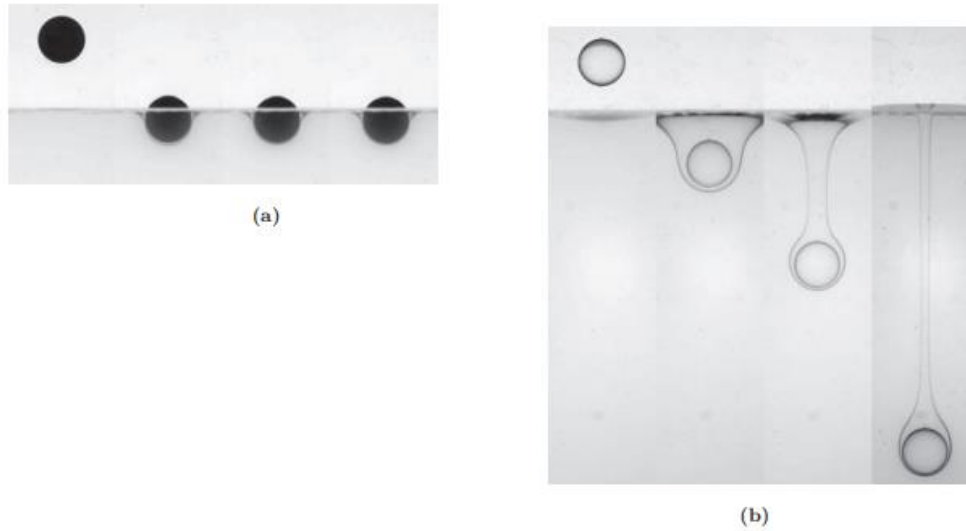


Figure 9: (a) Sequence of images illustrating the blockage of a rigid sphere at the interface. (b) Sequence of images showing a crossing and columnar entraining configurations. These two configurations correspond respectively to the release of a polyacetal and glass spheres of the same diameter (1cm) through the same pair of liquids (silicone oil/ water (21%) - glycerin (79%)). (Pierson & Magnaudet, 2018).

$$\mathbf{F}_B \geq \mathbf{F}_\gamma + \mathbf{F}_{PH} \quad (5)$$

$$\frac{\xi_{12}}{\xi_{13}} \geq \frac{3}{2Bo_{13}} \sin^2 \psi + \frac{1}{4} (2 - 3\cos\psi + \cos^3\psi) - \frac{3}{4} z_s^* \sin^2 \psi \quad (6)$$

Where  $\mathbf{F}_B = \rho_2 g V_2$  is the droplet weight with  $V_2$  being the volume of the droplet,  $\mathbf{F}_\gamma = 2\pi\gamma_{13}R \sin^2(\psi)$  is the interfacial tension force with  $\psi$  the contact angle of the fluid on the particle. To derive  $\mathbf{F}_{HP}$ , the force due to hydrostatic pressure, we consider two distinct parts of the droplet: a bottom zone with volume  $V_b$  that corresponds to the spherical cap in contact with the interface, and a top volume immersed in phase 1  $V_t = V_2 - V_b$ . The

surface separating these two volumes is a horizontal disk of radius  $r_s$  located at  $z = z_s$ .  $P_t$  and  $P_b$  are respectively the hydrostatic pressures at  $z = z_t$  and  $z = z_b$ . The hydrostatic pressure at  $z = z_s$  are respectively  $P_{S1}$  exerted by the first phase and  $P_{S3}$  exerted by the third phase. This yields to the following expressions:  $\mathbf{P}_{S1} = \mathbf{P}_t + \rho_1 \mathbf{g}(z_t - z_s)$  and  $\mathbf{P}_{S3} = \mathbf{P}_b - \rho_3 \mathbf{g}z_s$ . The hydrostatic pressure force is written now as a sum of two terms: the hydrostatic force exerted by phase 1 ( $F_{HP1}$ ) and that exerted by phase 3 ( $F_{HP3}$ ) both on the rigid sphere. To evaluate  $F_{HP1}$ , we consider that the volume  $V_t$  is totally immersed in phase 1 with the same hydrostatic pressure at the top. The sum of pressure forces exerted by phase 1 on the upper part of  $V_t$  and on the flat bottom is equal to the Archimedes push:  $\mathbf{F}_{HP1} + \pi r_s^2 \mathbf{P}_{S1} = \rho_1 V_t \mathbf{g}$ . In the same manner,  $\mathbf{F}_{HP3} - \pi r_s^2 \mathbf{P}_{S3} = \rho_3 V_b \mathbf{g}$ , which writes finally  $\mathbf{F}_{HP} = \rho_1 \mathbf{g} V_t - \pi R^2 \sin^2(\psi) \mathbf{P}_{S1} + \rho_3 \mathbf{g} V_b + \pi R^2 \sin^2(\psi) \mathbf{P}_{S3}$ .

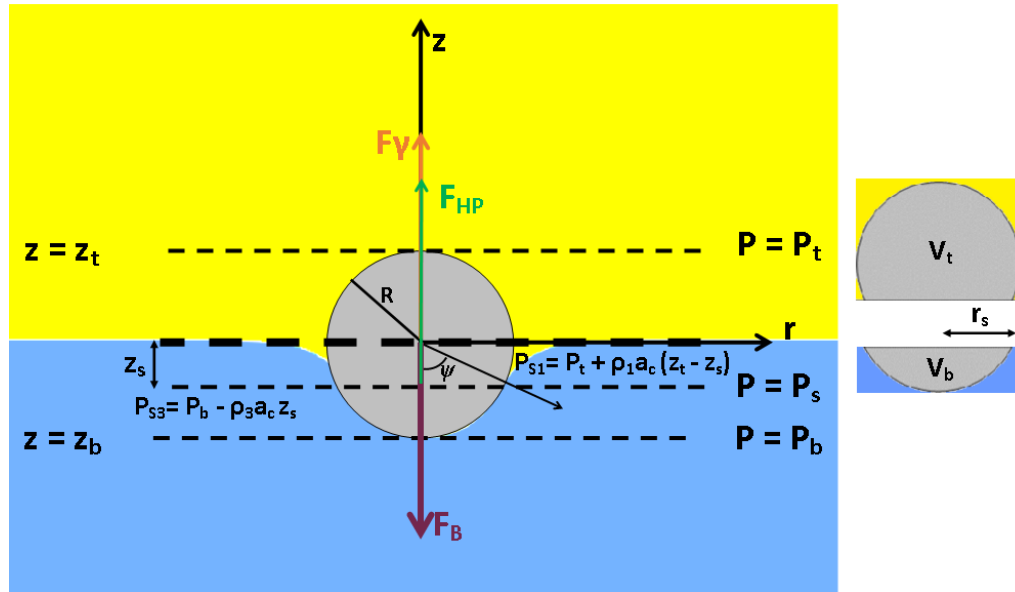


Figure 10: The scheme of a rigid sphere standing on the interface.

After substituting  $F_B$ ,  $F_{HP}$ , and  $F_\gamma$  in equation (5), we obtain the non-dimensional equation (6). In order to evaluate the right hand side of equation (6),  $z_s^*$  must be determined as a function of  $\psi$  from solving the Young-Laplace equation that allows computing the meniscus shape. For small Bond numbers ( $Bo_{13} \ll 1$ ), the problem was solved by O'Brien (O'Brien, 1996) using a matched asymptotic development similar to the procedure developed by (James, 1974) for a circular cylinder. Assuming total wetting, the results writes:

$$z_s^*(\psi) = \left( \gamma_E - \log \left( \frac{4}{\sqrt{Bo_{13}} (\sin \psi (1 + \cos \psi))} \right) \right) \sin^2 \psi + O \left( Bo_{13} [\log(\sqrt{Bo_{13}})]^2 \right) \quad (7)$$

Where  $\gamma_E \approx 0.577$  is the Euler constant. We take  $\psi = \pi/2$  because at this value the forces acting against the direction of particle motion (i.e.  $F_{HP}$  and  $F_\gamma$ ) are at the maximum value they could attain. Thus, in the limit of  $Bo_{13} \ll 1$ , crossing is possible for spheres approaching a L/L interface satisfying the following equation:

$$\frac{\xi_{12}}{\xi_{13}} \geq \frac{3}{2Bo_{13}} + \frac{1}{2} + \frac{3}{4} \left( \log \left( \frac{4}{\sqrt{Bo_{13}}} \right) - \gamma_E \right) \quad (8)$$

For  $Bo_{13} = 1$ , equation (8) overestimates  $z_s^*$  by 20%, which in turn overestimates the critical value of  $\frac{\xi_{12}}{\xi_{13}}$  by only 6% (Pierson & Magnaudet, 2018). For  $Bo_{13} \gg 1$ , the meniscus can only be determined by numerical simulations of the Young-Laplace equation. A rough model assuming that the meniscus takes a circular shape has been developed by Maru (Maru et al., 1971) and (Bonhomme et al., 2012); the maximal angle of contact computed is  $\psi_{max} = \pi - k$  with  $k = 2(2Bo_{13})^{-\frac{1}{4}}$ , writing  $z_s^*$  in the following form.

$$z_s^* = - \left( \frac{2}{Bo_{13}} \right)^{\frac{1}{2}} \quad (9)$$

Therefore, in the limit  $Bo_{13} \gg 1$  the condition of interfacial crossing is described by the following equation:

$$\frac{\xi_{12}}{\xi_{13}} \geq \frac{3}{2Bo_{13}} \sin^2(k) + \frac{1}{4} (2 + 3 \cos k - \cos^3 k) + \frac{3}{4} \left( \frac{2}{Bo_{13}} \right)^{\frac{1}{2}} \sin^2 k \quad (10)$$

The two expressions giving crossing condition (Equations (8) and (10)) were validated by Pierson (Pierson & Magnaudet, 2018) through experiments in inertial regime complemented with the results of Maru (Maru et al., 1971). In these experiments, inertia favors the crossing of the particle compared to the strict static conditions at which the model was developed. Figure 11 shows the two curves corresponding to Equations (8) and (10) showing a good agreement with the experimental results.

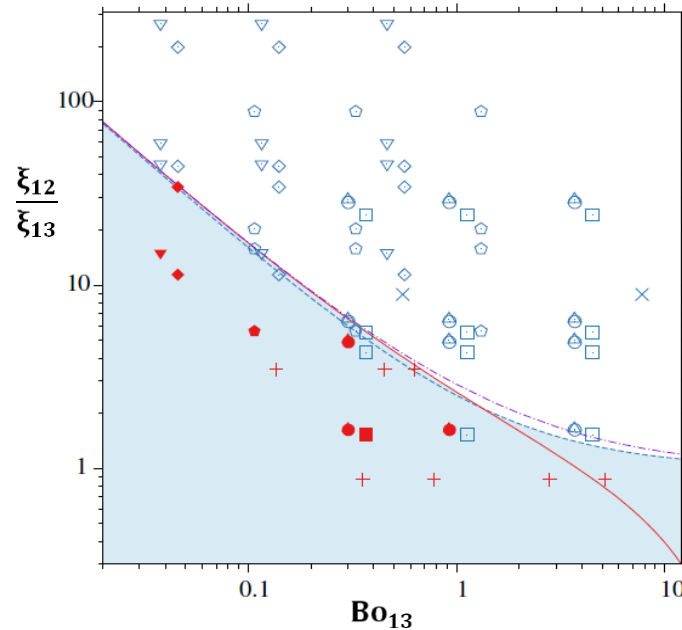


Figure 11: Extracted from (Pierson & Magnaudet, 2018), the validation of equations 8 (red line) and 10 (blue dotted line) through experimental data, in red: floating, and in blue: crossing.

### Crossing configurations:

Although all spheres respecting the criteria of equations (8) and (10) cross the interface, the crossing configuration strongly varies among the results presented in Pierson & Magnaudet, 2018. At a low inertia, barely sufficient to cross (close to the critical line in Figure 11), the column breaks directly after crossing rather than extending to a longer length inside phase 3. This configuration is called quasi-static detachment where the particle velocity vanishes while penetrating the interface. Far away from the critical line of Figure 11, a tailing configuration is observed, a long tail forms behind the droplet which may take an axisymmetric shape, a corollas shape, or a fragmented shape due to strong shearing around the tail where 3D effects appear (Pierson & Magnaudet, 2018b).

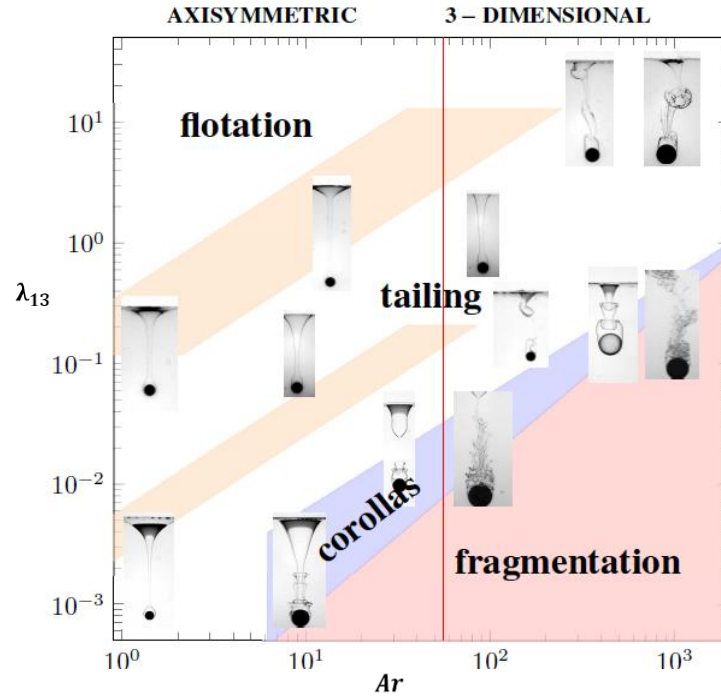


Figure 12: Extracted from (Pierson & Magnaudet, 2018), the map of tail configuration as a function of  $Ar$  and  $\lambda_{13}$  for cases where a tail is formed while crossing.

These tailing configurations were mapped as shown in Figure 12 according to the Archimedes number  $Ar$  describing the flow regime and the viscosity ratio between the two continuous fluids  $\lambda_{13}$ . Axisymmetric tails with different lengths are observed for particles inducing a flow with  $Ar < 55$ , the limit at which the particles do not follow a vertical path anymore and three dimensional effects appear according to Fabre (Fabre et al., 2012). Higher than this limit, a tail fragmentation is observed. For  $\lambda_{13} \ll 1$ , despite that Archimedes number in phase 3 (based on the properties of phase 3 instead of phase 1) is of order  $O(10^3)$ , we observe a tail with a corollas axisymmetric shape instead of fragmentation. This is due to the wake behind the particle, which develops inside the tail. As long as the sphere remains attached to the tail, the relevant parameter to identify the transition from axisymmetric to a fragmentation regime is  $Ar$  based on the properties of phase 1.

When the tail is not fragmented, it may detach in two different modes depending on the location of detachment along the column. The two modes classified by Aristoff (Aristoff & Bush, 2009) in their study of a sphere impacting an air/water interface are: (i) a shallow pinch-off from which detachment occurs in the close vicinity of the interface and (ii) a deep seal pinch-off for which detachment occurs close to the particle rear (Figure 13). According to the study of Maru (Maru et al., 1971) the height of column detachment decreases as the surface tension of the interface is increased. This maximum height was correlated to the Reynolds number of the sphere in phase 1 and that of phase 3 for a certain range of parameters in the study of Dietrich (Dietrich et al., 2011). After extending and detachment, the column may break into small droplets of first phase suspended in the third



phase, which return gradually to the initial position of the interface (Figure 14 and Figure 16). This condition happens when the two continuous phases have comparable viscosities. On the reverse, if a tail with a high viscosity compared to phase 3 ( $\lambda_{13} \gg 1$ ) detaches in a deep seal mode, it stays connected to the interface and retracts gradually to the initial position without breaking into small drops (Figure 15). The detachment of the column is independent of the height of immersion as shown in the study of Pitois (Pitois & Chateau, 2002).

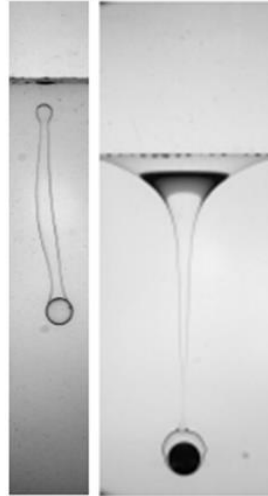


Figure 13: Extracted from (Pierson & Magnaudet, 2018b), left hand side: a shallow pinch-off detachment where the column breaks close to the initial position of the interface,  $\xi_{12} = 1.74$ ,  $\xi_{13} = 0.32$ ,  $\lambda_{13} = 18.3$ ,  $Bo_{13} = 1.1$ ,  $Ar = 164$ . Right hand side, deep seal pinch-off, where the column forms a neck behind the droplet rear and pinches-off at this position,  $\xi_{12} = 1.23$ ,  $\xi_{13} = 0.03$ ,  $\lambda_{13} = 1.9 \cdot 10^{-3}$ ,  $Bo_{13} = 0.24$ ,  $Ar = 2.3$ .

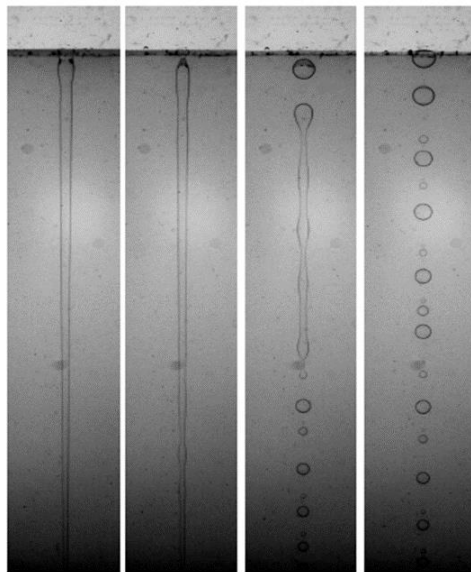


Figure 14: Extracted from (Pierson & Magnaudet, 2018b), the image sequence of the column breakage into small droplets after detachment. Non-dimensional parameters:  $\xi_{12} = 1.25$ ,  $\xi_{13} = 0.26$ ,  $\lambda_{13} = 1.7$ ,  $Bo_{13} = 1.9$ ,  $Ar = 23.1$ .

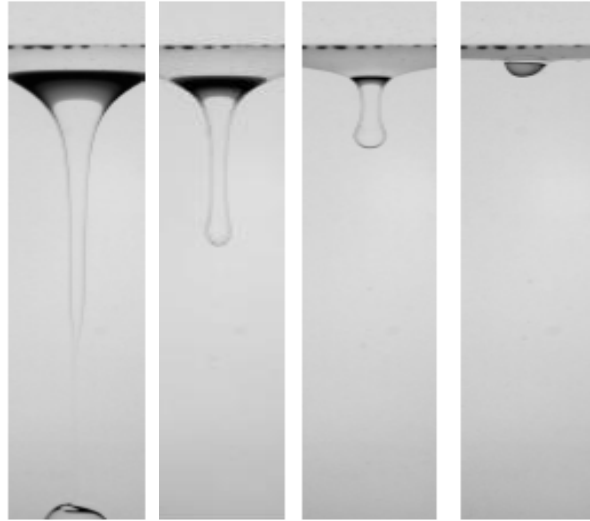


Figure 15: Extracted from (Pierson & Magnaudet, 2018b), the image sequence of the column retraction to the initial position of the interface without breaking into small droplets after detachment. Non-dimensional parameters:  $\xi_{12}= 1.23$ ,  $\xi_{13}= 0.03$ ,  $\lambda_{13}= 1.9 \cdot 10^{-3}$ ,  $Bo_{13}= 0.24$ ,  $Ar= 2.3$ .

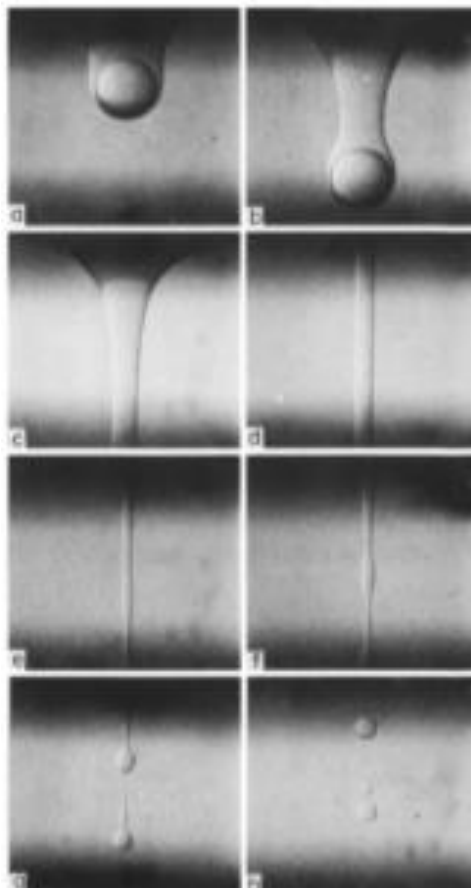


Figure 16: Extracted from (Maru et al., 1971), The sequence of images for the passage of a rigid sphere through a L/L interface. (a) Arrival of the rigid sphere, (b) crossing of the interface with column entrainment, (c) The base of the column, (d-e) The column which being stretched, (f-h) The breakage of the column into small droplets.

### Coating Volume:

When the fluid column is not fragmented, it extends until breakage occurs near the droplet rear. The sphere is then left suspended in phase 3 with a volume of phase 1 coating it as shown in Figure 17 also from Pierson & Magnaudet, 2018. We call this volume the coating volume  $V_f$ .

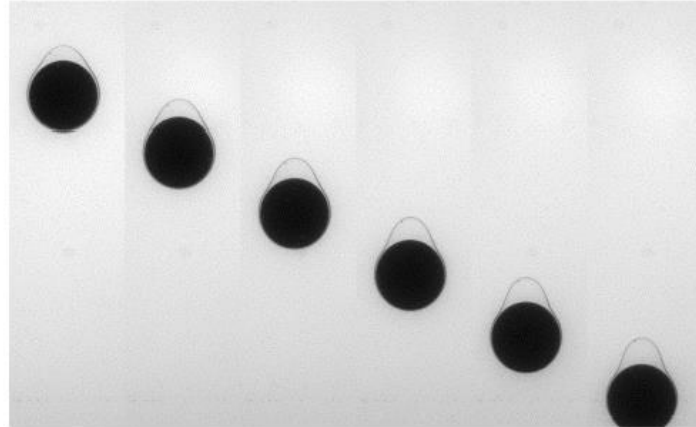


Figure 17: Post-pinch-off evolution of the volume covering a polyacetal sphere of radius  $R=7$  mm. The first phase is Silicone oil and the third phase is water-glycerin. Non-dimensional numbers:  $\lambda_{13}= 1.7$ ,  $\xi_{12}= 0.42$ ,  $\xi_{13}= 0.26$ ,  $Bo_{13}= 4$ ,  $Ar= 20$ . Extracted from Pierson & Magnaudet, 2018.

Few studies were performed to investigate this parameter. We cite the studies of Pitois et al., 1999 and Pierson & Magnaudet, 2018 where  $V_f$  normalized by the sphere volume was scaled as a function of the Bond number  $Bo_L = \left( \frac{\xi_{12}}{\xi_{13}} - 1 \right) Bo_{13}$ . Although a non-negligible scatter was observed on this plot, the volume seems to increase consistently with  $Bo_L$  in a linear manner as shown in Figure 18.

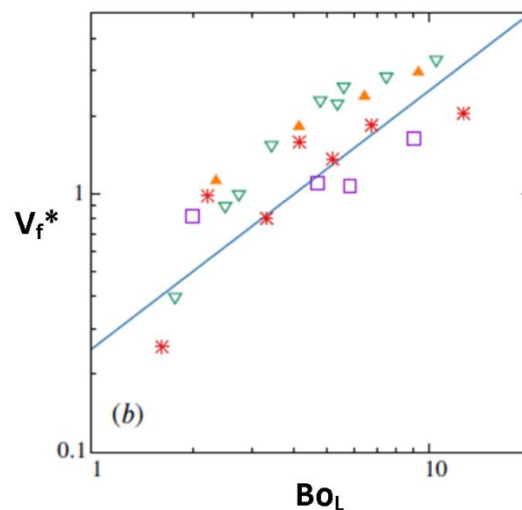


Figure 18: The variation of the normalized encapsulation volume as a function of  $Bo_L$ . Extracted from (Pierson & Magnaudet, 2018).

**Crossing time:**

This characteristic is not much documented in the bibliography. In the experimental study of Dietrich (Dietrich et al., 2011) at a moderate Reynolds number, the crossing time was defined as the time between the instant of first contact between the sphere and the interface and the instant of last contact between them (detachment). With a certain range of parameters, an empirical correlation to determine it was written as follows:

$$\frac{t_{cr}}{t_D} = 54.4 \left( \frac{Re_1}{Re_3} \right)^{0.35} \quad (11)$$

Where  $t_{cr}$  is the crossing time,  $t_D = D/u_{T1}$  is approximately the time spent by the sphere to travel an equivalent distance of its own diameter with  $u_{T1}$  being the terminal velocity in phase 1,  $Re_1$  and  $Re_2$  are the Reynolds numbers based on terminal velocities inside phase 1 and phase 3.

**Summary:**

- The profile of draining film between a sphere and the interface is thinner at the top during crossing.
- From the quasi-static force balance on the sphere, the crossing of the interface is a function of two non-dimensional parameters:  $\frac{\xi_{12}}{\xi_{13}}$  and  $Bo_{13}$ .
- The detachment of the column entrained is described as quasi-static at the critical crossing condition.
- There are three configurations of column entrainment: axisymmetric tailing, tail corollas, and tail fragmentation. The pertinent parameters predicting the configuration are  $Ar$  and  $\lambda_{13}$ .
- The coating volume  $V_f^*$  was found to vary linearly with respect to  $Bo_L$ .
- The crossing time correlates with the Reynolds numbers in the two continuous phases for a certain range of parameters.

**Comments:**

- The effect of the column and detachment configuration on the final coating volume remains an interesting question.
- For the development of the encapsulation process. It is important to scale the coating volume in a more rigorous correlation.
- The crossing time as defined in the study of Dietrich & al., 2011 is rather a detachment time. The extension of the column for a long time does not necessarily means a long time to cross.

### 2.3.2. Bubbles crossing a L/L interface:

#### Deformation due to the interface

We start by pointing out the shape of the bubbles and their deformation due to the interface which actually influences the film entrainment mechanism while crossing. The Weber number characterizes the bubble deformation, where for  $We_{12} \ll 1$  the bubble remains spherical. However, for the same  $We_{12}$ , when a bubble penetrates the interface, it may deform even if their shape during the rise was spherical. The simulations of Shopov (Shopov & Minev, 1992) in conditions with  $Re \ll 1$  and  $We_{12} \ll 1$  showed in Figure 19 (a) a prolate shape bubble at the interface. This prolate shape has a more elongated shape with sharpened edges when the bubble initial position is far away from the interface as in Figure 19 (b). In a simulation at higher Reynolds and Weber number displayed in Figure 19 (c), a dimple forms on the bubble rear while rising; when crossing the interface, surface tension at the rear become dominant and allows reducing the bubble concavity, leading to a spherical cap shape. At the position of the interface, a thin film forms ahead of the bubble while crossing the interface. The study of Debrégeas (Debrégeas et al., 1998) showed that the flow within the forming film has a plug-type profile. The thickness of this film decreases exponentially with time (Jones & Wilson, 1978). The same observation regarding the droplet shape can at the interface be extracted from the experimental and numerical study of Bonhomme (Bonhomme et al., 2012) for crossing of a gas bubbles in inertial regimes (Figure 20).

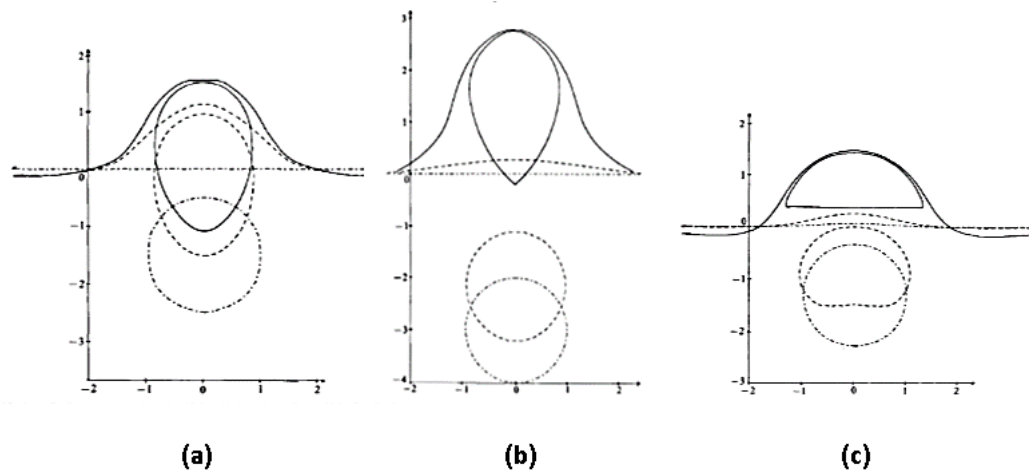


Figure 19: Extracted from (Shopov & Minev, 1992), (a) the droplet does not deform before arriving to the interface, and deforms into a prolate shape at the interface:  $Re = 0.078$ , (b) the droplet does not deform before arriving to the interface and deforms into a prolate shape with more elongation and sharp edge:  $Re = 0.078$ , (c) the droplet deforms while rising with a dimple forming at its rear, at the interface, concavity reduces due to the domination of surface tension and its shape becomes a spherical cap:  $Re = 60$ .

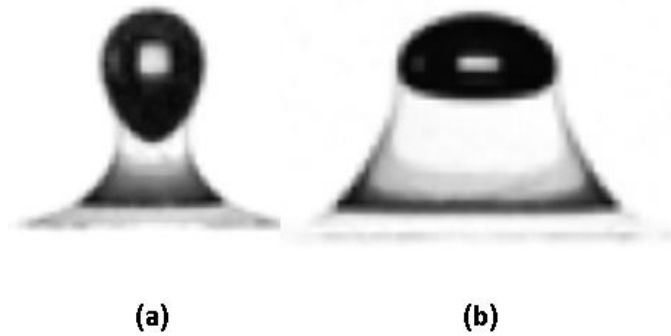


Figure 20: Extracted from (Bonhomme et al., 2012), (a) the bubble deforming into a prolate shape at the interface,  $Ar= 4.1$ , (b) The bubble deforming into an oblate shape and finally a spherical cap shape,  $Ar= 42.6$ .

### Crossing Conditions:

For a bubble standing at a L/L interface, Bonhomme (Bonhomme et al., 2012) identified to regimes of behavior: a trapped bubble at the interface (Figure 21.a), and a bubble crossing the interface with a columnar entrainment (Figure 21.b).

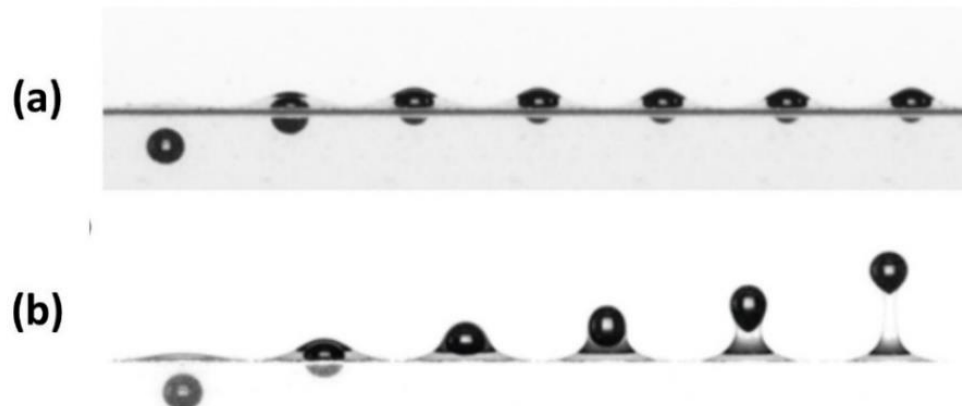


Figure 21: (a) Sequence of images illustrating the blockage of a gas bubble at the interface. (b) Columnar entraining of a bubble crossing the interface. These two configurations correspond to the rise of a gas bubble in a pair of fluids 95% glycerin+ water/ Silicone oil (Bonhomme et al., 2012).

A simple criterion to predict the conditions under which a bubble crosses the plane interface was derived by Green (Green et al., 1988) assuming the bubble has a spherical shape and based on the idea that the bubbles will not stop at the interface if the buoyancy force in first phase overcomes the maximum possible capillary force. This criterion is expressed by the following equation:

$$Bo_{13} > \frac{6s}{\xi_{13} + 1} \quad (12)$$

Where  $s = \frac{\gamma_{12}}{\gamma_{13}}$  is the ratio between the bubble surface tension and the surface tension of the plane interface.

Bubbles which do not respect the conditions of equation (12) will be trapped at the interface. On the other hand, bubbles respecting the same expression cross the interface in three probable configurations of crossing presented in Figure 22: shell formation, long tail formation, and shell rupture as classified in the recent experimental study of Emery (Emery et al., 2018).

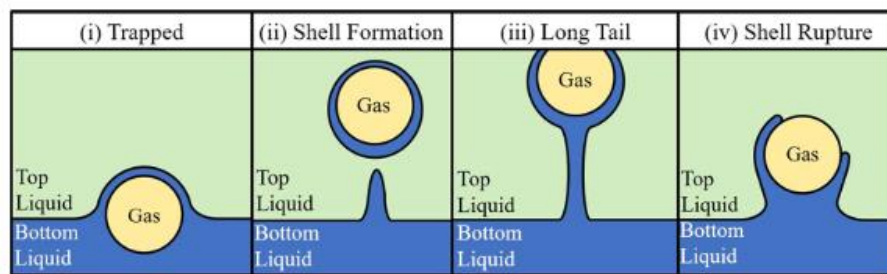


Figure 22: Extracted from (Emery et al., 2018), (i) a bubble trapped at the interface. The three interface crossing configurations: (ii) Shell formation, (iii) Long tail formation, (iv) Shell rupture.

### Crossing configurations:

The first configuration to discuss is the shell formation. It occurs when a liquid shell forms around the bubble as it crosses the L/L interface (Figure 23). As the bubble reaches the plane interface, it slows down and a thin film forms between the apex of the bubble and the plane interface. The film thins and stretches as the bubble continues its rise, forming a column behind it; beyond a certain length, the column forms a neck and eventually breaks. The coated bubble keeps on rising in the third phase. According to Emery (Emery et al., 2018), long tail configuration occurs under high inertial condition, a bubble crosses the interface with a slight decrease of its velocity. So, as the bubble passes through the interface, the first phase embraces the bubble and forms a long tail behind. This configuration may also occur with relatively high viscosity of the first continuous phase (phase 1) compared to phase 3. This high viscosity slows the entrained film drainage and delays the neck formation and shell rupture which allows the shell and column to be maintained even if the bubble moves a significant distance in phase 3. In other words, the contribution of viscosity is stronger than that of surface tension on the deformation of the column, which can be rationalized by computing of the Ohnesorge number  $Oh_{13} = \frac{\mu_1}{\sqrt{\rho_1 \gamma_{13} d}}$ . Long tail formation occurs in cases where  $Oh_{13}$  is important. As the bubble continues its rise, the tail thins and remains attached to the plane interface. In the study of

Emery (Emery et al., 2018), the tail extends until the bubble exits the observation window of the camera. The long tail regime was also observed by in the experiments of Bonhomme (Bonhomme et al., 2012).

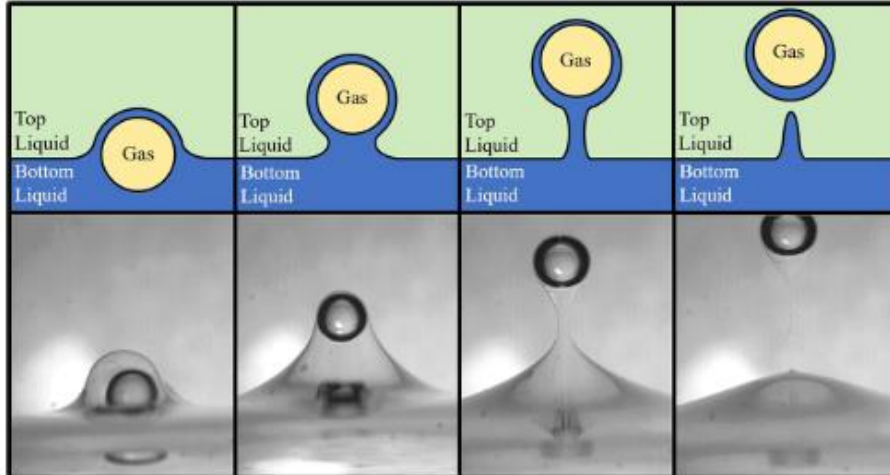


Figure 23: Extracted from (Emery et al., 2018), the steps of the shell formation regime shown using schemes and experimental results of Emery & al.

The last configuration presented in this part in the shell rupture. In the beginning of crossing, this configuration is similar to the shell formation configuration (first image of Figure 24). While crossing, a rupture point forms and grows as the bubble advances. The coating film forming around the droplet falls down to the column and the film retracts under the bubble. A possible reason for this is the appearance of surface instabilities due to the difference in surface tension acting on each side of the film as it retracts.

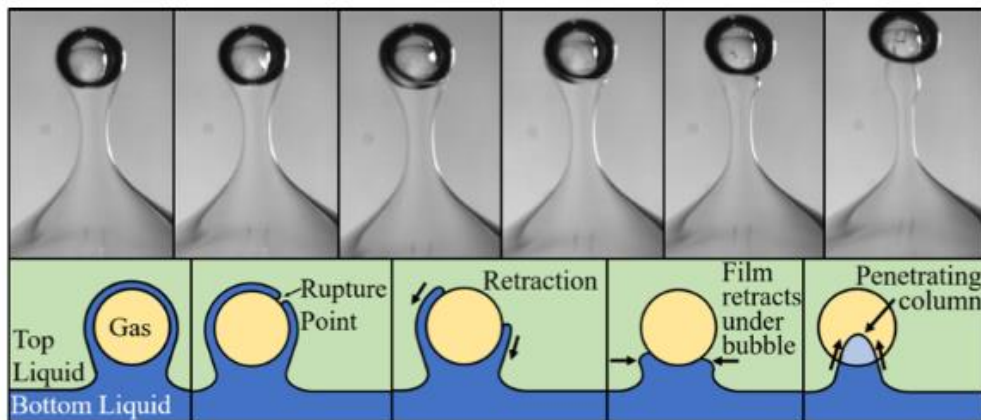


Figure 24: Extracted from (Emery et al., 2018), the steps of the shell rupture regime shown using schemes and experimental results of Emery & al.



### Crossing time:

In case of bubbles, a correction of the expression of crossing time for rigid spheres was proposed by Dietrich (Dietrich et al., 2011) by using the Morton numbers in each continuous phase. The new expression can be written as follows:

$$\frac{t_p}{t_c} = 9.6 \left( \frac{Re_1}{Re_3} \right)^{2.76} \left( \frac{Mo_1}{Mo_3} \right)^{1.27} \quad (13)$$

Where  $t_p$ ,  $t_c$ ,  $Re_1$ , and  $Re_2$  are as defined in the rigid particles section,  $Mo_1 = \frac{\mu_1^4 g}{\rho_1 \gamma_{12}^3}$  and  $Mo_3 = \frac{\mu_3^4 g}{\rho_3 \gamma_{13}^3}$ .

### 2.3.3. Droplets crossing a L/L interface

This case is more complex as the droplet internal viscosity plays a role in the dynamics as well as the drop deformability.

### Film drainage while crossing

For a liquid droplet with an internal viscosity, all studies are limited to non-inertial regimes ( $Re \ll 1$ ); their objectives were generally to investigate the droplet coalescence at a plane interface. Chi (Chi & Leal, 1989) studied numerically the motion of viscous deformable droplets towards a L/L interface and determined three distinct modes of drainage of the thin film forming between the droplet and the interface: rapid drainage, uniform drainage, and dimpled drainage. Rapid drainage was observed when the internal viscosity of the droplet was less than the continuous phase ( $\lambda_{12} = 0.1$ ) with a minimum thickness reached at the top of the droplet, uniform drainage occurred when  $\lambda_{12} = 1$ , and finally the dimpled drainage occurred when the droplet is more viscous than the first phase  $\lambda_{12} = 10$ . These results were qualitatively compared to the experiments of Hartland (Hartland, 1967, 1969) as shown in Figure 25. Similar modes of drainage were observed upon varying the concentration of surfactants in the studies of Hodgson (Hodgson & Woods, 1969) and Burrill (Burrill & Woods, 1973).

The observation of Figure 25 was validated by the parametric study of Manga (Manga & Stone, 1995) in the Stokes regime, through experiments and numerical computations by the boundary integral method. The simulations of the crossing of deformable droplets have shown that the amount of volume entrained by the crossing increases with the viscosity ratio  $\lambda_{12}$ . This result was validated through experiments on bubbles ( $\lambda_{12} = 0$ ) and rigid spheres ( $\lambda_{12} = \infty$ ) crossing the L/L interface, where the entrained volume by the rigid sphere was much more than that entrained by a bubble crossing the L/L interface.

The effect of viscosity ratio  $\lambda_{12}$  on the deformation was discussed, and the results showed that the deformation of the droplet, while crossing the interface increases with the decrease of  $\lambda_{12}$  as shown in Figure 26. According to the same figure, the drainage of the film forming between the top of the droplet and the interface is faster for smaller values of  $\lambda_{12}$ .

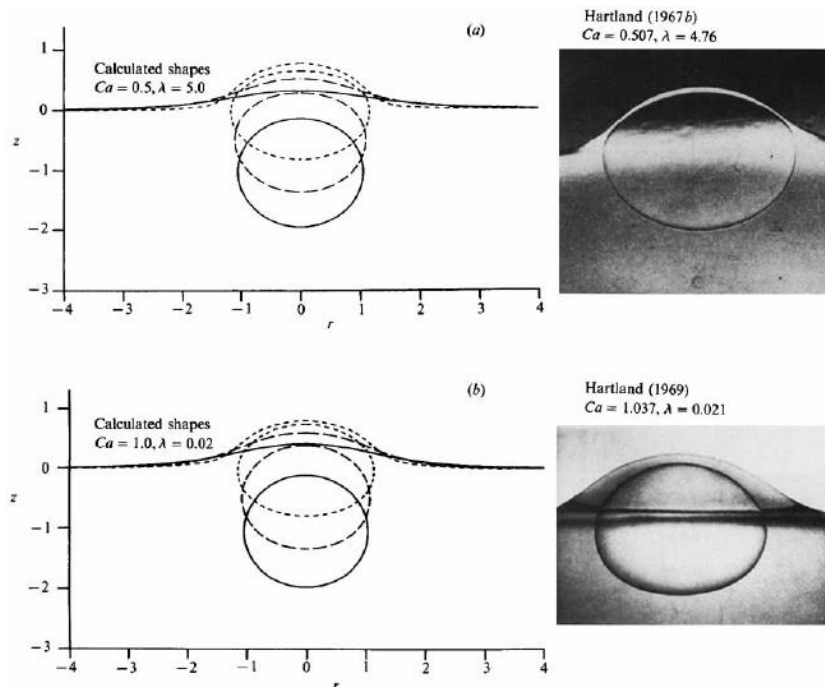


Figure 25: Extracted from (Chi & Leal, 1989), comparison of Chi & Leal numerical results to the left with the experimental results of Hartland to the right. At the top, a dimpled drainage with more important film thickness than the case of rapid drainage at the bottom of the figure.

The effect of  $\lambda_{13}$  was also studied in Manga & Stone, 1995. As seen in Figure 27, the rate of deformation of the droplet increases when it enters a less viscous fluid ( $\lambda_{13} = 0.1$ ) as it accelerates strongly, whereas when it enters to a low viscosity fluid, it deaccelerates ( $\lambda_{13} = 10$ ), and its deformation is weaker. Looking carefully at the same figure, images reveal that for a given  $\lambda_{12}$ , the volume of phase 1 entrained increases with decreasing  $\lambda_{13}$ . Unsurprisingly, the rise speed of the droplet decreases when  $\lambda_{13}$  increases.

According to this paper, the drainage of the film volume is influenced by the viscosity ratios  $\lambda_{12}$  and  $\lambda_{13}$  and independent from the Bond numbers  $Bo_{12}$  and  $Bo_{13}$ .

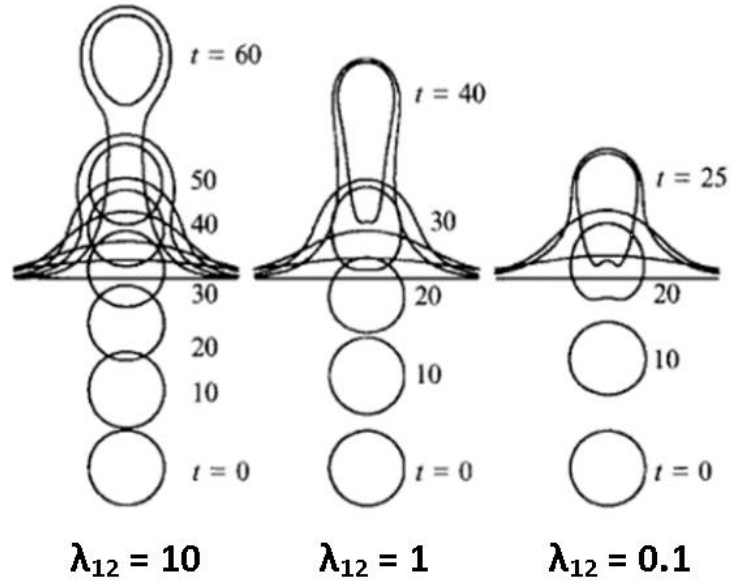


Figure 26: Extracted from (Manga & Stone, 1995), a comparison between three simulations showing the effect of  $\lambda_{12}$  where all other parameters are identical. Non-dimensional parameters:  $\xi_{12}/\xi_{13} = 5$ ,  $\lambda_{13} = 0.1$ ,  $B_{012} = 20$ ,  $B_{013} = \infty$ .

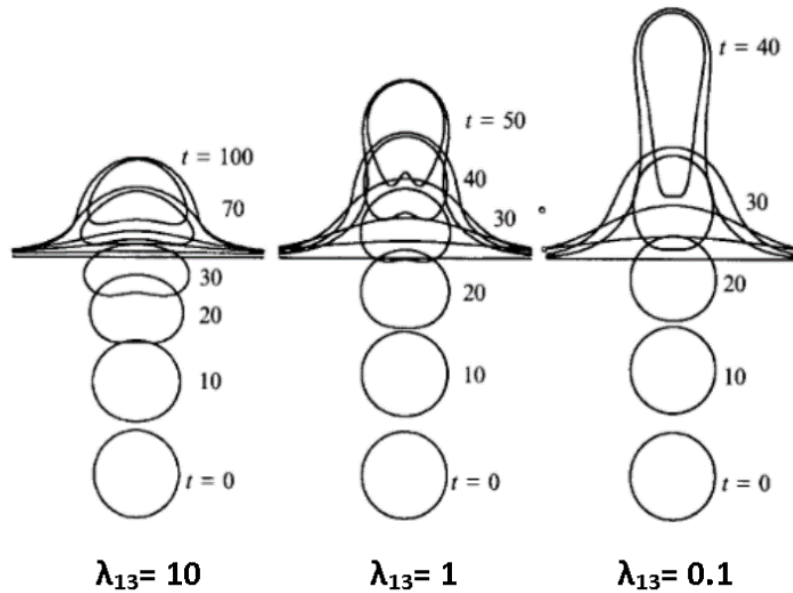


Figure 27 Extracted from (Manga & Stone, 1995), a comparison between three simulations showing the effect of  $\lambda_{13}$  where all other parameters are identical. Non-dimensional parameters:  $\xi_{12}/\xi_{13} = 5$ ,  $\lambda_{13} = 1$ ,  $B_{012} = 20$ ,  $B_{013} = \infty$ .

**Summary:**

- There exists no correlation to predict crossing conditions for a liquid droplet.
- From results in the Stokes regime, the volume of entrained fluid increases in the condition where  $\mu_2 > \mu_1 > \mu_3$ .
- The rise speed of the droplet increases when decreasing  $\lambda_{12}$  and/or  $\lambda_{13}$
- The drainage of film volume between the top of the droplet and the interface is independent from  $Bo_{12}$  and  $Bo_{13}$  at low Reynolds number.

**Comments:**

- The correlation to determine crossing conditions for solid particles may serve as a base to find a similar one for liquid droplets.
- Majorly, studies in this part are done in Stokes regime, where the influence of the physical parameters was determined.
- The work is novel as it concerns non-deformable droplets crossing a liquid-liquid interface in inertial regime.

At our knowledge, there exists no results for droplets crossing a L-L interface at high Reynolds numbers regimes. The originality of this work reveals in performing the study in this regime where the objectives are to characterize the critical crossing conditions, to investigate the dynamics of crossing as a function of all system parameters including  $\lambda_{12}$  and  $\lambda_{13}$  that play an important role at low Reynolds number as proved by Manga & Stone, 1995, and finally to scale the film volume of the coating of the droplet where no results are available.

# Chapter 3:

Numerical Approach:  
Methods & Validation

# Chapter 3: Numerical Approach: Methods & Validation

In this project, simulations of the crossing of a liquid-liquid interface by a droplet inside a centrifugal field will be performed, with the objective of computing the drop rise motion and deformation before, during and after the crossing step, which leads to the formation of a coating film around the droplet after rupture of the covering interface. Such simulations require efficient numerical methods able to solve the Navier-Stokes equations for a three-phase flow with implementing the appropriate physical parameters (densities, viscosities, surface tensions of the three phases and droplet size) and the driving force. In the case of rotating systems, the driving force is the centrifugal force accompanied with the Coriolis force. The simulations are axisymmetric, so the Coriolis force is neglected (otherwise the case will be fully three-dimensional, with a high computational cost). We will see later in the experimental results of chapter 6 that this force is not negligible. The range of Reynolds numbers is  $1 < Re < 200$ .

In this chapter, first, we briefly review different approaches allowing to simulate a multiphase flow with dispersed objects (bubbles, droplets or particles); then, we detail the numerical methods employed for the simulations carried out in the next chapter, by presenting some validation cases both in the case of a two-phase flow and a three-phase flow involving deformable liquid-liquid interfaces.

## 3.1. Introduction

In order to study dispersed multiphase flows through Direct Numerical Simulations, several approaches are available. Methods could be classified as Lagrangian methods, Eulerian methods or a coupling between both approaches. Figure 28 shows a scheme of a Lagrangian mesh and an Eulerian mesh.

Methods classified as Lagrangian can be based on boundary-fitted grids, i.e. grids that follow the geometry of the interface, the latter begin one boundary of the simulation domain. These methods are well-suited to impose the interface boundary conditions, and to accurately capture the boundary layers around a particle or a bubble, giving a high precision on interface quantities. However, in case of deformable interfaces, an issue associated to these methods is that the mesh has to be built at each time step, making the approach expensive in terms of computational time, complex for simulating high deformations and incompatible with rupture and coalescence phenomena. All the methods

which use markers to track the interface lye also in this category, the markers being carried by the flow in the simulation. In particular, this is the case of the front-tracking method (Unverdi & Tryggvason, 1992), which combines Lagrangian interface markers with an Eulerian mesh grid to compute the flow around the object. In the latter, highly deformed interfaces can be handled, even though special treatments are required in order to maintain a good marker distribution along the interface in case of intense stretching by the flow. Simulation of breakup and coalescence phenomena is possible, but requires a high computational cost due to the changes of topology of the bubbles and the necessity to move the interface markers.

An alternative consists in using Eulerian methods, for which the grid is fixed and does not follow the interface geometry, making possible to capture the dynamics of complex interface shapes (highly deformed interfaces, including breakup and coalescence phenomena). Then, a method is employed to implicitly capture the interface by the use of a marking function. The most known types of marking functions are the Volume-Of-Fluid (VOF) function, mentioned by several authors including Hirt (Hirt & Nichols, 1981), and the Level-Set function, introduced by Osher (Osher & Sethian, 1988). In the VOF method, a step marking function ranging from 0 to 1 corresponds to the fraction of fluid inside the grid cell, an interface being present for cells which have an intermediate value between 0 and 1. In the Level-Set method, a signed distance function is used as marking function, corresponding to the minimal distance between the cell center and the interface, the different phases being distinguished by the sign of the distance function. Note that either fluid-fluid or solid-fluid interfaces can be captured by such methods.

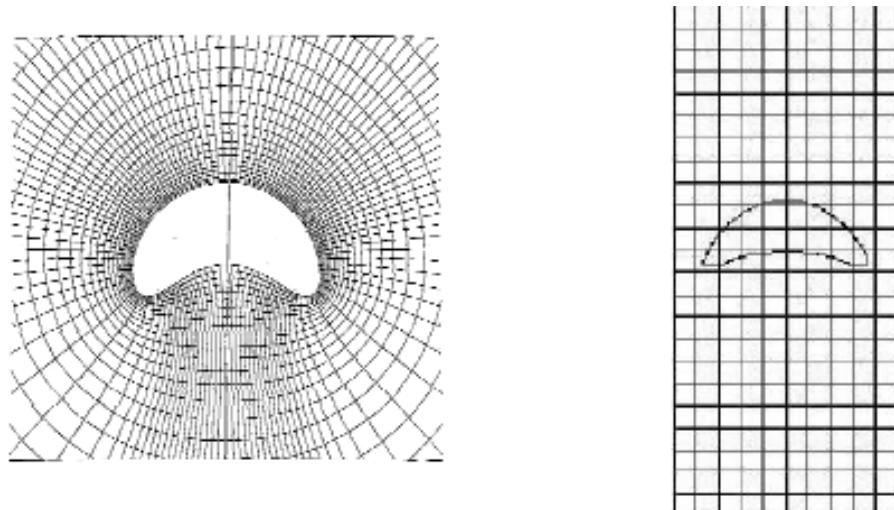


Figure 28: Left hand side, a Lagrangian mesh adapted to an interface of a droplet. Right hand side, a scheme of a fixed Eulerian mesh where the image is extracted from Bonometti PhD thesis (2005) (Bonometti, 2005).

In such Eulerian approaches, the interface boundary conditions have to be included without having any mesh points on the interface. In the case of solid interfaces, the fluid velocity

at the interface has to be set to zero, a condition that can be imposed through different methods such as the immersed boundary method (IBM), first developed by Peskin (Peskin, 1972) to simulate fluid-structure (fiber) interactions. The IBM method imposes the fluid velocity as an elastic forcing term in the Navier-Stokes equations. In other approaches, such as with a Ghost-Fluid Method, the boundary condition is directly included during the discretization of velocity gradients across the interface. In the case of fluid-fluid interfaces, the capillary force has to be imposed in order to satisfy the normal stress balance, with conditions of continuity of velocity (in the absence of phase change) and viscous tangential stresses (in the absence of Marangoni stresses at the interface). Among the classical methods, the capillary force can be imposed through the continuum surface force approach (CSF), which adds a surface force term to the Navier-Stokes equations, discretized over several mesh cells around the interface by using a numerical approximation of the Dirac distribution (Brackbill et al., 1992). Alternatively, sharp methods can be employed, like for example the Ghost Fluid method that imposes the capillary force as a jump condition in pressure in between both sides of the interface, during discretization of pressure derivatives, a method originally developed by Fedkiw (Fedkiw et al., 1999).

In the numerical method employed in our study, involving deformable droplets, we make use of a Eulerian mesh grid combined with a Level-Set function to capture the interfaces, and a Ghost-Fluid method to treat the discontinuities at the interfaces. In what follows, we explain the numerical method in details.

## 3.2. Numerical tool

The numerical tool used in this study is the in-house DIVA code, created at IMFT to simulate two-phase flows involving bubbles and drops (Lalanne, Villegas, et al., 2015; Tanguy et al., 2007), and extended for the case of three-phase flows during this ANR project at LGC.

The objective is to simulate an axisymmetric configuration sketched by Figure 29, with two interfaces: that separating the first and second phase  $\Gamma_{12}$  (droplet interface) and that separating the first and third phase  $\Gamma_{13}$  (initially planar interface).

In our numerical approach, we solve the Navier-Stokes equations, written in a one-fluid formulation, (equations (1) and (2)), with the appropriate jumps of densities, viscosities, and normal stresses at both interfaces (equations 4-9), by using the DIVA code.



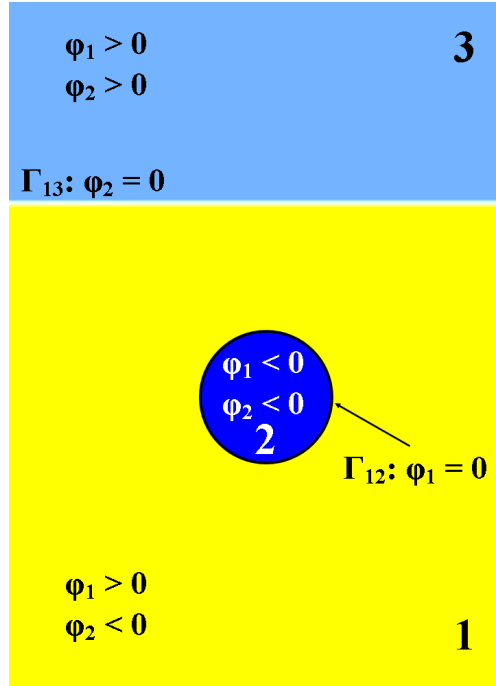


Figure 29: A scheme of the three phase system where: the yellow color corresponds to the first phase, dark blue corresponds to the third phase, and the light blue circle correspond to the droplet, with the signs of the signed distances in each part of the system.

$$\frac{\partial \vec{u}}{\partial t} + (\vec{u} \cdot \nabla) \vec{u} = -\frac{\nabla P}{\rho} + \frac{1}{\rho} \nabla(2\mu \mathbf{D}) + \vec{F} \quad (1)$$

$$\nabla \cdot \vec{u} = 0 \quad (2)$$

$$\mathbf{D} = \frac{\nabla \vec{u} + \nabla \vec{u}^T}{2} \quad (3)$$

Equation (1) represents the momentum equation written in the framework of one fluid approach, where  $\vec{u}$  is the velocity field and  $P$  the pressure field,  $\rho$  and  $\mu$  respectively the fluid density and viscosity at a considered mesh point,  $\mathbf{D}$  is the rate of deformation tensor defined in equation (3),  $\vec{F}$  is a volume force that will be either gravity ( $\vec{F} = \vec{g}$ ) or the inertial forces when considering a centrifugal field; in the latter case, the force is divided into a centrifugal force expressed as  $\vec{\omega} \times \vec{\omega} \times \vec{r}$ , where  $\vec{\omega}$  is the rotation vector and  $\vec{r}$  is the position vector, and the Coriolis force component expressed as  $2\vec{\omega} \times \vec{u}$ , leading to  $\vec{F} = \vec{\omega} \times \vec{\omega} \times \vec{r} + 2\vec{\omega} \times \vec{u}$ . Equations (4) to (7) represent the jumps in density and viscosity on the droplet and L/L interface. In equation (8) and (9),  $\gamma_{12}$  is the surface tension between the droplet and phase 1,  $\gamma_{13}$  is the surface tension of the plane interface,  $\kappa_i$  is the curvature of each interface, and  $u_n$  is the normal velocity at a given point on the interface. This numerical method is the three-phase flow extension of the one described in the paper of Lalanne (Lalanne, Villegas, et al., 2015).

$$[\rho]_{\Gamma_{12}} = \rho_2 - \rho_1 \quad (4)$$

$$[\rho]_{\Gamma_{13}} = \rho_3 - \rho_1 \quad (5)$$

$$[\mu]_{\Gamma_{12}} = \mu_2 - \mu_1 \quad (6)$$

$$[\mu]_{\Gamma_{13}} = \mu_3 - \mu_1 \quad (7)$$

$$[\mathbf{p}]_{\Gamma_{12}} = \gamma_{12} \kappa_{12} + 2[\mu]_{\Gamma_1} \frac{\partial \mathbf{u}_n}{\partial \mathbf{n}} \quad (8)$$

$$[\mathbf{p}]_{\Gamma_{13}} = \gamma_{13} \kappa_{13} + 2[\mu]_{\Gamma_2} \frac{\partial \mathbf{u}_n}{\partial \mathbf{n}} \quad (9)$$

In this system of equations, the unknowns are the pressure and velocity fields  $(\mathbf{P}, \bar{\mathbf{u}})$ , which are computed by solving the Navier-Stokes equation thanks to a projection method detailed in the next sub-section. Moreover, the two interfaces immersed in the fixed mesh need to be captured at each time step, in order to locate the different phases and to know which value of density and viscosity has to be used in a given mesh cell. To such a purpose, the Level-Set function, presented after, is used.

### 3.2.1. Projection Method

The projection method allows solving the Navier-Stokes equations (equations 1 and 2) of an incompressible flow and computing the velocity and pressure independently. This method is based on a temporal discretization of the momentum balance, given by equation (1), by explicitly treating the viscous, convective and volume source terms:

$$\frac{\mathbf{u}^{n+1} - \mathbf{u}^n}{\Delta t} + (\mathbf{u}^n \cdot \nabla) \mathbf{u}^n + \frac{\nabla P^{n+1}}{\rho} = \frac{\nabla \cdot (2\mu \mathbf{D}^n)}{\rho} + \vec{\mathbf{F}} \quad (10)$$

We choose an intermediate velocity  $\mathbf{u}^*$ , calculated by using the explicit terms of equation (10), which does not respect the zero-divergence condition.

$$\mathbf{u}^* = \mathbf{u}^n - \Delta t \left( (\bar{\mathbf{u}}^n \cdot \nabla) \bar{\mathbf{u}}^n - \frac{\nabla \cdot (2\mu \mathbf{D})}{\rho} \right) + \vec{\mathbf{F}} \quad (11)$$

By replacing the term  $\mathbf{u}^n$  of equations 11 inside equation 10, we obtain the following equation:

$$\mathbf{u}^* = \mathbf{u}^{n+1} + \Delta t \frac{\nabla P^{n+1}}{\rho} \quad (12)$$

Finally, by using equation (12) and considering the incompressibility condition ( $\text{div}(\mathbf{u}^{n+1}) = 0$ ), we obtain the Poisson equation applied on pressure:

$$\nabla \left( \frac{\nabla P^{n+1}}{\rho} \right) = \frac{\nabla \cdot \vec{u}^*}{\Delta t} \quad (13)$$

Then, in practice, this method is used with the following three steps. First, the intermediate velocity  $\mathbf{u}^*$  is computed through equation (11). Then, we are able to calculate the pressure field by solving the Poisson equation (13), through discretizing it into a linear system. Finally, we calculate the zero-divergence velocity field  $\mathbf{u}^{n+1}$  thanks to equation (12). In the code, temporal derivatives are discretized by a two order Runge-Kutta scheme. Spatial derivatives of the velocity in the nonlinear advection term  $(\vec{u}^n \cdot \nabla) \vec{u}^n$  are discretized by a fifth order modified WENO scheme, while the discretization of the viscous terms is performed through a second order centered scheme, convective and viscous terms being explicitly treated.

### 3.2.2. The Level-Set method

#### Two phase flows

The level-set method permits the manipulation of topology changes such as deformation, rupture, or reconnection of interface. The objective of the level set method is to capture the interface in order to know which phase is presented in a mesh point which allows the adjustment of the physical parameters corresponding to the cell. Its principle is to define a continuous function  $\phi(x,t)$  as a signed distance between a mesh point and the interface at a certain time instant; it is chosen negative if the mesh point is inside the droplet and positive outside and the contour line 0 corresponds to the drop interface (Figure 30).

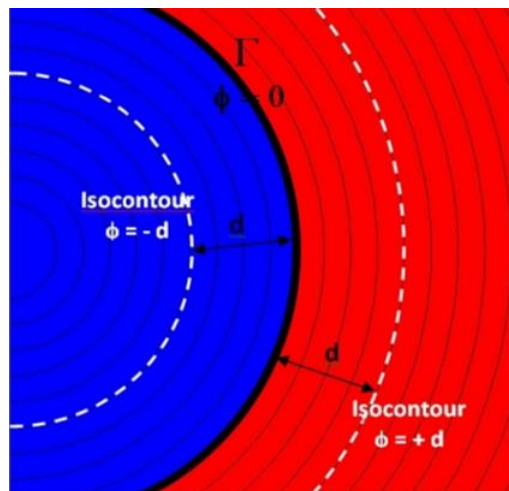


Figure 30: The iso-contours of the level-set method

The convection equation (14) is solved to calculate the evolution of the  $\phi$  function, which allows to implicitly determine the interface location. Then, we can compute the interface geometrical properties such as the normal vector and the curvature (equations 15 and 16), that are necessary for solving the balance of normal stress at the deformable interface.

$$\frac{\partial \phi}{\partial t} + \vec{u} \cdot \nabla \phi = 0 \quad (14)$$

$$\vec{n} = \frac{\nabla \phi}{|\nabla \phi|} \quad (15)$$

$$K(\phi) = \nabla \cdot \vec{n} \quad (16)$$

During the advection of the Level-Set function by the local velocity field, in case of intense shearing or stretching, the mathematical properties of the Level-Set function (distance function) can be altered: the different isocontour lines can be transported with different velocities, whereas only the transport velocity of the interface is physical. Then, a redistance algorithm is applied, as proposed by Sussman (Sussman et al., 1994), in order to reorganize the different contour lines around the interface and to maintain  $\phi$  as a distance function, without altering the zero contour position.

### From two-phase to three-phase flows

In order to develop the numerical model from a two-phase flow model to a three-phase flow model, in the Level-Set framework, we define a new signed distance function  $\phi_2(\mathbf{x}, \mathbf{t})$  of which the contour line 0 is the interface  $\Gamma_{13}$  separating phases 1 and 3; values of  $\phi_2(\mathbf{x}, \mathbf{t})$  have a negative sign for mesh points located in phase 1 and phase 2 and a positive sign for mesh points located in phase 3 (see Figure 29).

The evolution of  $\phi_2$  (equation (17)) is computed through a similar transport equation as equation (14), and the same re-distance algorithm is then applied.

$$\frac{\partial \phi_2}{\partial t} + \vec{u} \cdot \nabla \phi_2 = 0 \quad (17)$$

Once the two Level-Set functions are known,  $\rho$  and  $\mu$  have to be given properly in the resolution of Navier-Stokes equations. We use the value of one of the liquids or of the drop according to the phase in which a grid cell is located (known from the local signs of  $\phi_1$  and  $\phi_2$ ). In the cells crossed by the interface, we define a harmonic mean of the different densities or viscosities, weighted by the position of the interface in the mesh cell. The position of the interface in sub-grid is obtained from the Level-Set functions values. Note that it can be shown that, in case of a two-phase flows, this choice of harmonic mean

between viscosities of both phases satisfies the continuity of viscous tangential stresses in the cell crossed by the interface. For this purpose, based on Figure 31 where the interface  $\Gamma_{12}$  is present between nodes  $i$  and  $i+1$ , we define the parameter  $\delta_1 = \frac{|a_1|}{|a_1|+|a_2|}$  in order to locate the interface, where  $a_1$  is the value of  $\varphi_1$  at node  $i$  and  $a_2$  the value of  $\varphi_1$  at node  $i+1$ .  $\delta_1$  is then used as weighting for the harmonic mean between the densities or viscosities, for this mesh cell. The same harmonic average is defined when the interface  $\Gamma_{13}$  crosses a mesh cell. Some examples are shown in Table 2.

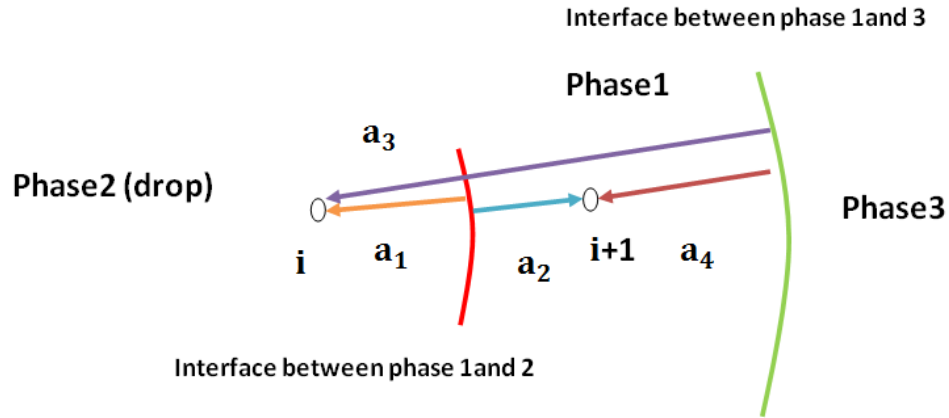


Figure 31: Sub-grid position of an interface, between the mesh points  $i$  and  $i+1$ : in this example,  $a_1 < 0$ ,  $a_2 > 0$  for the interface between phases 1 and 2  $\Rightarrow$  the interface  $\Gamma_{12}$  is present in the cell and we use  $\delta_1$  as weighting between the viscosities; nevertheless,  $a_3 < 0$  and  $a_4 < 0$  so the interface  $\Gamma_{13}$  between phases 1 and 3 is not present in the cell between nodes  $i$  and  $i+1$ .

$a_1$	$a_2$	$a_3$	$a_4$	Value of density in the cell (Figure 31)
+	+	+	+	$\rho_{\text{mean}} = \rho_3$
-	+	-	-	$\rho_{\text{mean}} = \frac{\rho_1 * \rho_2}{\rho_1 * \delta_1 + \rho_2 * (1 - \delta_1)}$
+	+	+	-	$\rho_{\text{mean}} = \frac{\rho_1 * \rho_3}{\rho_1 * \delta_2 + \rho_3 * (1 - \delta_2)}$

Table 2: Examples on the harmonic function,  $\delta_2$  being a weighted parameter defined in a similar way as  $\delta_1$  based on values of  $a_3$  and  $a_4$  of Figure 31.

Note that, if the mesh resolution is sufficient for the simulation of a drop passing through a liquid-liquid interface, the drainage film should be captured in more than one grid cell, so we would not have a grid cell containing simultaneously the two interfaces. Nevertheless, in case of a coarse grid, this situation will happen and a harmonic mean between the densities and viscosities of the three phases will be used, based on both the weightings  $\delta_1$  and  $\delta_2$ .

### 3.2.3. Ghost-Fluid Method

The Ghost fluid method deals with the discontinuities of pressure in between both sides of the different interfaces (equations 8 and 9), which are taken into account when writing the discretization of the pressure derivatives around the interface. Here, we illustrate the principle of the method. First, ghost values of the pressure are defined, based on extensions by continuity of the real values on each side of the interface. Then, these ghost values are employed to obtain a robust approximation of the derivative in the mesh points close to the interface.

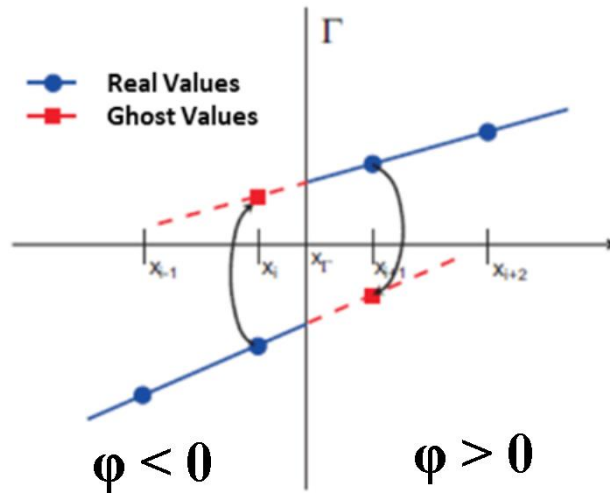


Figure 32: The principle of the Ghost fluid method, figure extracted from B. Lalanne PhD thesis [9].

In this way, the pressure field has to be derivate when solving the Poisson equation (equation 13, written here as equation 18), whereas this variable is discontinuous at an interface (due to surface tension and the discontinuity of normal viscous stresses). Here, we note  $a(x_\Gamma)$  the jump of pressure at an interface localized at  $x_\Gamma$  (equation 19):

$$\Delta P = f \quad (18)$$

$$[P]_\Gamma = a(x_\Gamma) \quad (19)$$

In 1D, at node  $i$ , we can write the finite volume discretization of (18) as follows:

$$\frac{\left| \frac{\partial P}{\partial x} \right|_{i+\frac{1}{2}} - \left| \frac{\partial P}{\partial x} \right|_{i-\frac{1}{2}}}{\Delta x} = f_i \quad (20)$$

leading to

$$\frac{P_{i+1}^+ - P_i^-}{\Delta x^2} - \frac{P_i^- - P_{i-1}^-}{\Delta x^2} = f_i$$

where the - index corresponds to a point located before the interface ( $\phi < 0$ ), and + index corresponds to a point located after the interface ( $\phi > 0$ ).

Nevertheless, when an interface lies between the points  $x_i$  and  $x_{i+1}$  (as sketched in Figure 32), the derivative of the pressure is not well defined for  $i + \frac{1}{2}$ . Consequently, the previous discretization will be modified. With this objective, the Ghost Fluid method helps in avoiding mixing the + and - indices, i.e. avoids to use discontinuous variables: the value  $P_{i+1}^+$  is replaced by its corresponding ghost value, defined by applying the jump value  $a(x_\Gamma)$ :

$$P_{i+1}^{(g)-} = P_{i+1}^+ - a(x_\Gamma)$$

During calculation, the jump value at the interface,  $a(x_\Gamma)$ , is interpolated from the values  $a(x_i)$  and  $a(x_{i+1})$  at points  $i$  and  $i+1$ , computed from equation (8) or (9), because curvature is only known at the mesh point location.  $a(x_\Gamma)$  is then obtained by using the location of the interface, given by the Level-Set function at points  $i$  and  $i+1$ :

$$a(x_\Gamma) = \frac{a(x_i)|\phi_{i+1}| + a(x_{i+1})|\phi_i|}{|\phi_i| + |\phi_{i+1}|}$$

Finally, the Ghost value  $P_{i+1}^{(g)-}$  can be included in the discretization, leading to a modified numerical scheme:

$\frac{P_{i+1} - P_i}{\Delta x^2} - \frac{P_i - P_{i-1}}{\Delta x^2} = f_i + \frac{a(x_\Gamma)}{\Delta x^2}$ . In the same way, the Ghost-fluid method modifies the discretization at mesh  $i+1$ :

$$\frac{P_{i+2} - P_{i+1}}{\Delta x^2} - \frac{P_{i+1} - P_i}{\Delta x^2} = f_i - \frac{a(x_\Gamma)}{\Delta x^2}$$

Thus, the Ghost Fluid method is equivalent to modify the discretization only at the two mesh points  $i$  and  $i+1$  around the interface, where the jump condition  $a(x_\Gamma)$  appears as a source term in the right hand side. It is a method easy to combine with the Level-Set approach, since the location of the interface in sub-cell needs to be known.

### 3.2.4. Global algorithm and precisions on discretization schemes

Figure 33 shows the complete algorithm of the code.

The discretization used the code, for all the Partial Differential Equations, is of finite volume type. A staggered grid is used, where the scalars (pressure, level set function...) are

centered in the control volume and the velocity vector components are defined shifted from half of a mesh cell, depending on the direction concerned.

The spatial derivatives of the viscous terms are discretized with a centered scheme of order 2, whereas all the advection terms are discretized by a WENO scheme of order 5. The temporary derivatives are discretized by a Range-Kutta scheme of order 2.

As convective, viscous and volume force terms are treated explicitly, as well as the surface tension term in the pressure jump, several time steps constraints are necessary to ensure the stability of the numerical method, like in (Kang et al., 2001). The following table shows the constraints on the time step imposed by each physical phenomenon.

The global time step ( $\Delta t$ ) is then calculated according to the following equation:

$$\Delta t \left( \frac{1}{\Delta t_{\text{visc}}} + \frac{1}{\Delta t_{\text{cap}}} + \frac{1}{\Delta t_{\text{conv}}} + \frac{1}{\Delta t_{\text{acc}}} \right) = 1$$

Physical Phenomenon	Constraint on time step	Value of $\alpha_i$
Viscosity	$\Delta t_{\text{visc}} \sim \alpha_{\text{visc}} \frac{\Delta x^2}{\max(v)}$	0.25
Capillarity	$\Delta t_{\text{cap}} \sim \alpha_{\text{cap}} \sqrt{\frac{\rho \Delta x^3}{\gamma}}$	0.25
Convection	$\Delta t_{\text{conv}} \sim \alpha_{\text{conv}} \frac{\Delta x}{\max(u_x, u_y, u_z)}$	1
Acceleration	$\Delta t_{\text{acc}} \sim \alpha_{\text{acc}} \sqrt{\frac{\rho \Delta x}{r \omega^2}}$	0.5

Table 3: The constraint of each physical phenomenon on the time step



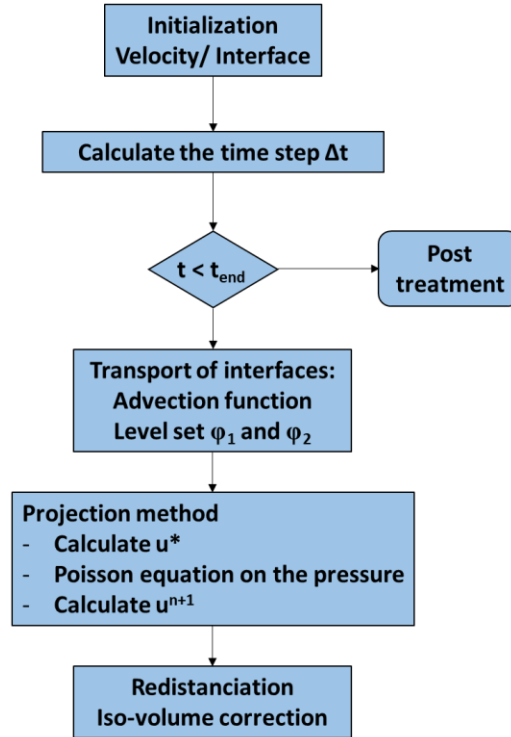


Figure 33: The general algorithm resolution.

### 3.3. Validation tests

In this section, we validate the results and the convergence of the global numerical method through (i) a gravity driven two-phase flow simulation and (ii) a simulation of a three-phase flows. Results are compared to theoretical predictions or existing correlations when they are available, and mesh convergence studies are performed in order to validate the use of the code for the problem of interface crossing, by characterizing the accuracy of the method.

#### 3.3.1. Two-phase flow validation

We simulate the rise of a droplet in a stagnant liquid at two different Reynolds numbers ( $Re_T = \frac{\rho_1 u_T d}{\mu_1}$ ) where  $u_T$  is the terminal velocity:  $Re_T = 20$  (case 1) and  $Re_T = 180$  (case 2). The terminal velocity can be predicted through a force balance between the drag force and the buoyancy force in the steady state regime (equation 21).

$$\frac{1}{2} \pi R^2 \rho_1 C_D u_T^2 = (\rho_2 - \rho_1) \frac{\pi d^3}{6} g \quad (21)$$

The Weber number  $We_{12}$  (defined in section 2.2 of chapter 2) is chosen low enough to work with a non-deformable droplet ( $We_{12} < 1$ ).

Since the droplet is spherical with a clean interface, the drag coefficient  $C_D$  is given by the expression issued from the simulations of Rivkind & Ryskin  $C_D = \frac{1}{1+\lambda_{12}} \left[ \lambda_{12} \left( 24Re + 4Re^{-\frac{1}{3}} \right) + 14.9Re^{-0.78} \right]$  (Rivkind & Ryskin, 1976), valid with maximal error of 7% for moderate Reynolds numbers, lower than 200. For each case, the implemented value of gravitational acceleration  $g$  is adjusted so as to reach the desired  $u_T$  based on the prediction of equation (21).

Table 4 shows the physical parameters of the simulation. The computation is axisymmetric, the mesh is uniform in both cases and the grid resolution is varied between 8, 16, 32 nodes per drop radius  $R$ . Figure 34 shows the Reynolds number evolution corresponding to each case for the different mesh resolutions. For both cases, the numerical code shows a very good convergence for the approximation of the terminal velocity from 16 points per radius, where the Reynolds number curve converges towards the same value of  $Re_T$ . For case 1, the prediction of  $u_T$  is perfectly consistent with the results of numerical simulations (discrepancy of 0.4%), and for case 2, the discrepancy is around 9%, showing a good agreement in this range of Reynolds number that is close to the range that will be investigated in the following.

Case	$\rho_1$ [Kg.m <sup>-3</sup> ]	$\rho_2$ [Kg.m <sup>-3</sup> ]	$\mu_1$ [Pa.s]	$\mu_2$ [Pa.s]	$\gamma_{12}$ [N.m <sup>-1</sup> ]	$a_c$	$d$ [μm]
1	850	1100	0.01	0.0033	2	3070g	200
2	850	1100	0.002	0.0033	2	3070g	200

Table 4: The physical parameters of simulation presented in Figure 34.

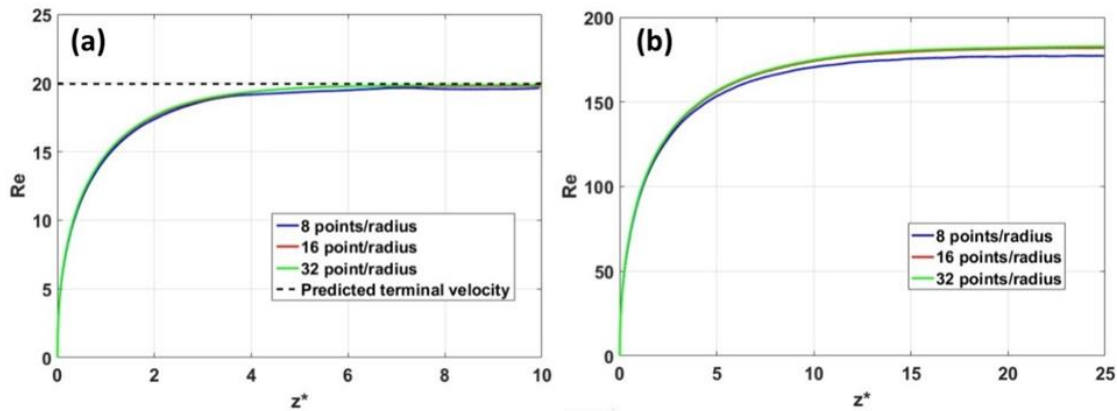


Figure 34: The Reynolds number evolution as a function of normalized distance covered by the droplet  $z^* = z/d$  for different mesh resolutions for: (a) Case 1,  $Re_T = 20$ ,  $We_{12} = 0.11$ , simulation domain:  $8R \times 16R$ , (b) Case 2,  $Re_T = 180$ ,  $We_{12} = 0.31$ , simulation domain:  $6R \times 12R$ .

### 3.3.2. Three-phase flow validation case

In this part, we validate the numerical method on three-phase flow configurations for two cases: the first one is the case of the crossing of an interface by a droplet in static conditions, i.e. in the case of a droplet initially released at the interface with zero velocity, for which a static force balance is able to predict the crossing condition, and the second one is a similar case but in dynamic conditions, i.e. for a droplet initially released far from the interface in an acceleration field, for which mesh convergence studies are presented on the quantities of interest.

All simulations are performed under the axisymmetric assumption, in a domain of size  $6R \times 19R$ , and in the frame of the droplet. This choice is made to keep the droplet centered in the domain, and to use non-uniform meshes with a higher density of mesh cells in the droplet area with the objective to capture accurately the dynamics close to the drop interface.

#### Static case of interface crossing: “crossing or no crossing?”

In the literature, there exists a force balance model predicting crossing conditions in quasi static conditions for a rigid particle. The model derived in chapter 2 (section 2.4.1) gives the critical condition for crossing in a non-dimensional form, by considering the balance between the force favoring the crossing (apparent weight) and the resisting forces (surface tension and hydro-static pressure). We recall the critical conditions of crossing in equations (22) and (23) where the non-dimensional numbers are as defined in section 2.2 of chapter 2.

For  $Bo_{13} \ll 1$ :

$$\frac{\xi_{12}}{\xi_{13}} \geq \frac{3}{2Bo_{13}} + \frac{1}{2} + \frac{3}{4} \left[ \log_{10} \left( \frac{4}{\sqrt{Bo_{13}}} \right) - 0.577 \right] \quad (22)$$

For  $Bo_{13} \gg 1$ :

$$\frac{\xi_{12}}{\xi_{13}} \geq \frac{3}{2Bo_{13}} \sin^2(k) + \frac{1}{4} (2 + 3 \cos(k) - \cos^3(k)) + \frac{3}{4} \left( \frac{2}{Bo_{13}} \right)^{\frac{1}{2}} \sin^2(k) \quad (23)$$

With  $k = 2(2Bo_{13})^{-\frac{1}{4}}$

In order to adapt with the numerical tool being used in our simulations, which is suitable for droplet or bubble simulations (assuming continuity of velocities of the fluids between each part of the interface), we mimic a particle by a solid-like droplet, i.e. a very viscous and non-deformable droplet by using a high viscosity ratio ( $\lambda_{12} = 50$ ) and a vanishing droplet Bond number ( $Bo_{12} \sim O(10^{-2})$ ).

Three crossing configurations of a liquid-liquid interface by a solid-like droplet corresponding to three different density ratio  $\xi_{12}/\xi_{13}$  are considered in Table 5 and Table 6 presenting respectively the physical parameters and non-dimensional numbers of the simulations in static conditions. The Bond number  $Bo_{13}$  is varied through changing the centrifugal acceleration (configuration 1 and 2) or the surface tension (configuration 3), in order to validate the model predicting the condition of interface crossing. The physical parameters and non-dimensional numbers of the simulations are given in. Simulations are carried out in the droplet frame, with a mesh grid of high resolution of 48 points/radius (see Figure 35). These simulations are done under the effect of a constant acceleration (higher than normal gravity by 2 to 3 orders of magnitude) which is varied in order to reach the crossing value  $Bo_{13}$  based on the theoretical prediction for a droplet of size  $d = 200 \mu\text{m}$  chosen to be compatible with the targeted size range of capsules in the process.

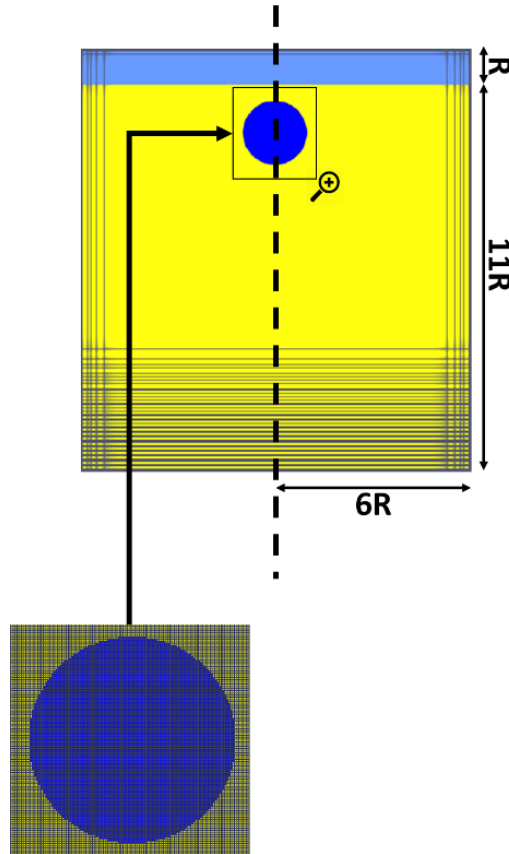


Figure 35: The mesh employed in the simulations for the static crossing cases.

Configuration	$\rho_1$ [Kg.m <sup>-3</sup> ]	$\rho_2$ [Kg.m <sup>-3</sup> ]	$\rho_3$ [Kg.m <sup>-3</sup> ]	$\mu_1$ [Pa.s]	$\mu_2$ [Pa.s]	$\mu_3$ [Pa.s]	$\gamma_{12}$ [N/m]	$\gamma_{13}$ [N/m]	ac	d [ $\mu$ m]
1	995	1100	1000	0.001	0.05	0.001	1	0.01	1430g	200
									1630g	
									2850g	
2	980	1100	1000	0.001	0.05	0.001	1	0.01	1325g	200
									1735g	
									2550g	
3	930	1080	1000	0.002	0.1	0.002	1	0.01	1360	200
							0.84	0.0084		
							0.715	0.00715		
							0.715	0.0045		

Table 5: The physical parameters of the simulation presented in Figure 36.

Configuration	$\xi_{12}$	$\xi_{13}$	$\xi_{12}/\xi_{13}$	$\lambda_{12}$	$\lambda_{13}$	Bo <sub>12</sub>	Bo <sub>13</sub>	Ar
1	0.105	0.005	21	50	1	0.014	0.07	38
						0.017	0.08	41
						0.03	0.14	54
2	0.12	0.02	6	50	1	0.015	0.26	39
						0.02	0.34	44
						0.03	0.5	54
3	0.161	0.075	2.14	50	1	0.02	0.93	22
						0.023	1.11	
						0.028	1.3	
						0.028	2.08	

Table 6: The non-dimensional numbers of the simulation presented in Figure 36.

In Figure 36, we presents the results for the three configurations compared to equation 21 (the red line) and equation 22 (the green line). As the blank squares correspond to non-crossing result and colored ones correspond to a crossing one, it is observed on the diagram that the crossing condition is accurately reproduced for each value of  $\xi_{12}/\xi_{13}$ , as compared to the theory. These simulation results validate both the three-phase flow extension of the numerical code and the use of the solid-like droplet approximation to mimic the dynamics of a solid particle for this interface crossing configuration. After examining the conditions of crossing in static condition, we examine more finely the crossing in terms of velocity and film characterization.

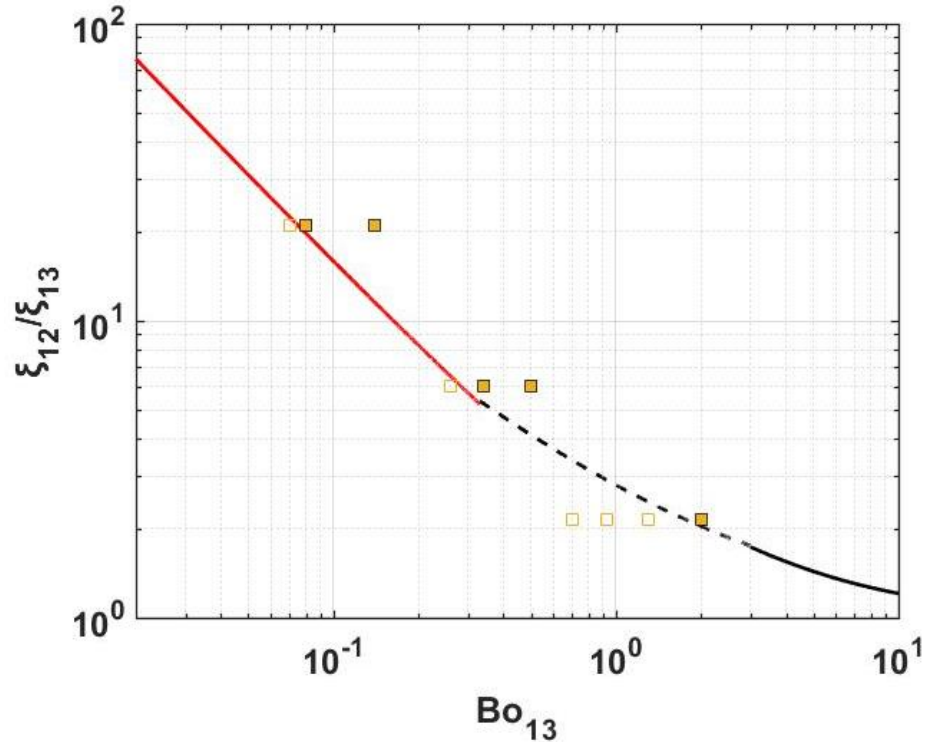


Figure 36: Mapping of the crossing configuration. The red line corresponds to the expression of equation 22 and the green line corresponds to the expression of equation 23. The dashed black line connects the two theoretical predictions. Filled diamonds correspond to a result of interfacial crossing in static case, while non-filled diamonds correspond to a point corresponding to a droplet which failed to cross the interface.

### Dynamic case of interface crossing: Droplet velocity and film characterization

In this subsection, the simulations are also performed in the frame of droplet, which is released at an initial distance of  $6R$  of the interface and acquires a non-zero velocity when arriving at the interface because of an acceleration field. Indeed, a linearly increasing acceleration is used to mimic a centrifugal force driving the motion of the droplet, the characteristic acceleration value at the interface position being given by  $F = a_c = r_i \omega^2$  with  $r_i$  the position of the interface with respect to the axis of rotation. This configuration is thus equivalent to a droplet in a centrifugal device with neglecting the Coriolis force. Contrary to the previous validation case, the interface crossing will take place in dynamic conditions because of the kinetic energy of the droplet when arriving at the interface.

Figure 37 shows the calculation domain with mesh in the vicinity of the droplet. We perform the simulations at three different mesh resolutions: 48, 72, and 96 points/radius in order to test the convergence of the mesh for the three phase case. This simulation case is that of a droplet, all the physical parameters of the simulation being reported in Table 7 and the non-dimensional numbers given in Table 8.

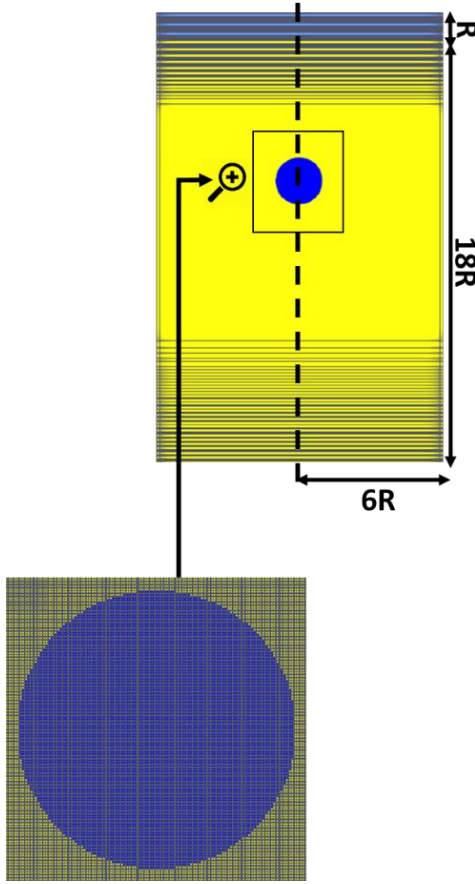


Figure 37: The mesh employed for the simulations of the dynamic crossing cases.

$\rho_1$ [Kg.m <sup>-3</sup> ]	$\rho_2$ [Kg.m <sup>-3</sup> ]	$\rho_3$ [Kg.m <sup>-3</sup> ]	$\mu_1$ [Pa.s]	$\mu_2$ [Pa.s]	$\mu_3$ [Pa.s]	$\gamma_{12}$ [N/m]	$\gamma_{13}$ [N/m]	<b>N</b> [rpm]	<b>d</b> [ $\mu$ m]
995	1100	1000	0.001	0.005	0.001	0.01	0.01	7000	200

Table 7: The physical parameters of the simulation presented in this part.

$\xi_{12}$	$\xi_{13}$	$\xi_{12}/\xi_{13}$	$\lambda_{12}$	$\lambda_{13}$	<b>Bo<sub>12</sub></b>	<b>Bo<sub>13</sub></b>	<b>Ar</b>
0.105	0.005	21	5	1	2.8	0.134	53

Table 8: The non-dimensional numbers of the simulation presented in this part.

The physics of this case will be mainly described in the next chapter. It is observed that the droplet reaches a velocity close to its terminal value before arriving at the interface. Then, it slows down due to the presence of the liquid-liquid interface and continues its crossing by entraining a column of fluid. Finally, the droplet is accelerated again when entering in the new continuous phase, and the column finishes to be detached, leaving the droplet encapsulated (see a sequence of images on figure 6 and 8 of chapter 4). Here, the numerical accuracy of this case is presented and discussed.

Figure 38 shows the results of the simulation for the three resolutions in terms of droplet velocity throughout the simulations and the screenshots at the instant of film detachment. The curves of the time evolution of the drop center of mass along the trajectory are superimposed between the three different meshes; we observe that the curves converge towards the same evolution for all steps, i.e. before, during, and after the interface crossing. Moreover, the drop deformation is shown to be the same in all calculations, as well as the geometry of the column at the instant of detachment. The encapsulated volume around the droplet varies only by 0.67% between the three different meshes. Then, the results of such a simulation case can be considered as converged regarding the quantities of interest for this project, the smaller grid resolution (i.e. 48 points/radius) being sufficient to obtain reliable results.

According to the screenshots of Figure 38, the film around of the droplet is not uniform: at the instant of column rupture, the film is very thin at the top, with less than one mesh point in the top part of the droplet as it can be seen on Figure 39(a). This occurs because the film is composed of a lighter fluid, which is attracted towards the rear of the droplet due to gravity effects. Only high viscosity ratio (between the droplet and the first phase and/or between the film phase and the third phase) could resist to such a fast drainage, by changing the interface conditions from mobile to immobile interfaces. As an example, let us consider Figure 39 (b), which is a different case with a larger viscosity ratio  $\lambda_{12} = 50$  (instead of 5 previously) and smaller viscosity ratio  $\lambda_{13} = 0.1$  (instead of 1 previously), where the film was not totally drained at the instant of detachment, leading to a simulation which is well-resolved with several grid points all around the drop contour.

Note that the presence of very thin film at the top, similar to Figure 39 (a), happens in the majority of the simulations presented in this work (see next chapter), and the simulations become thus under-resolved in this part of the film after a given time; nevertheless, the mesh resolution required to capture accurately this film is probably unaffordable today, due to the huge difference of scales between its thickness and the relevant scales for the droplet motion. This example of multiscale phenomena remains a more general limitation of Eulerian simulations today, like in the problem of drop coalescence, and as also explained by (Bonhomme et al., 2012). However, in such cases, the contribution of the film at the top of the drop to the total coating volume is clearly negligible, all the volume being attached to the drop rear where the grid resolution is sufficient. In order to give an estimate, if we add a contribution on the film volume from the top half of the droplet, artificially considered with a thickness equal to the size of the mesh cell ( $\approx 3 \mu\text{m}$ ), we obtain only around 3 to 5% of additional volume, confirming that it is a negligible contribution.

This allows us to be confident in the computed values of the encapsulated film, even in these unfavorable conditions of fast drainage for a simulation. The perfect agreement on the film volume value between the three different meshes confirms this statement.



All these validation tests allow us to conclude that the whole numerical approach, based on the Level-Set and Ghost-Fluid method, captures accurately the drop dynamics, both in a configuration of rise motion and of crossing of a liquid-liquid interface. In the range of Reynolds numbers considered in this study (less than 200 in the next chapter), a resolution of 48 grid points per radius has been shown to be accurate enough to obtain mesh converged results on drop velocity, deformation, crossing critical condition and crossing dynamics, with reliable quantities of interest like the volume of the coating film.

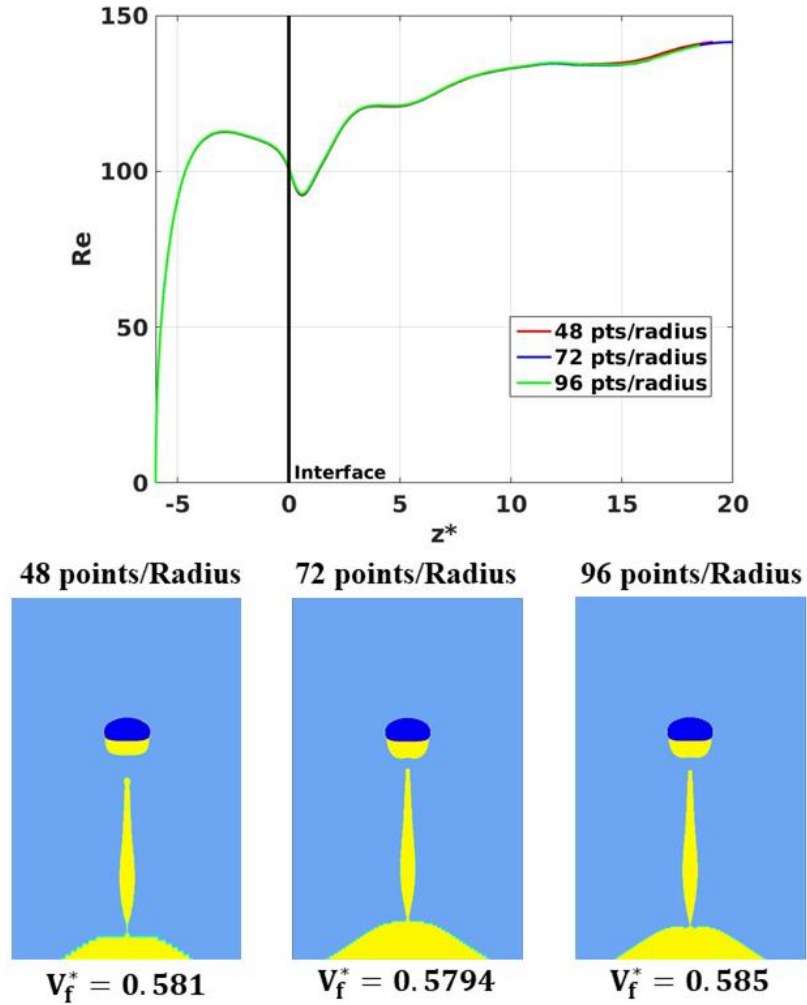


Figure 38: The velocity evolution of the simulation for three different resolutions alongside with the screenshot at the instant of film detachment at which the volume of the film is evaluated.  $V_f^* = \frac{V_f}{V_d}$ , with  $V_f$  being the volume of the coating film and  $V_d$  is the volume of droplet.

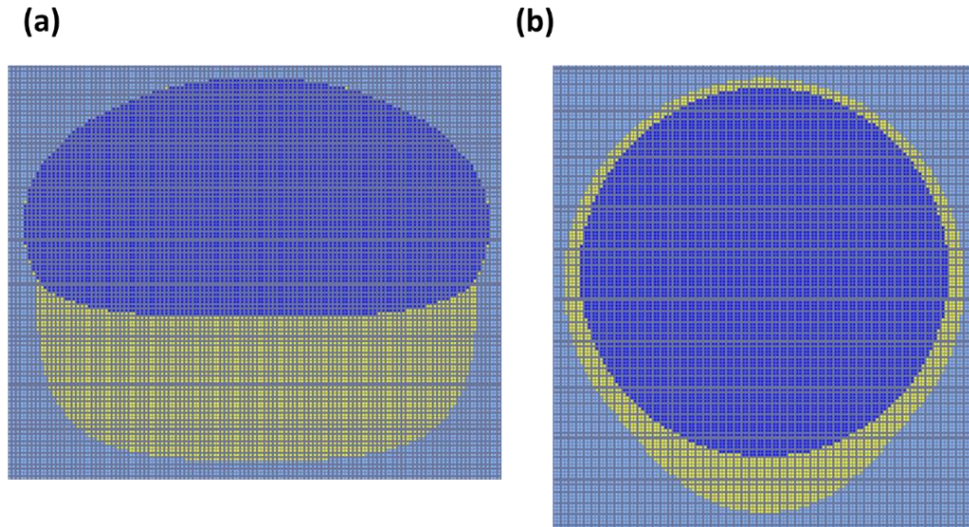


Figure 39: The screenshots showing the mesh points inside the droplet and the coating film at the instant of film detachment for two different cases. (a) A case where the film is totally drained to the rear and very thin in the rest regions with less than one mesh point inside the film. (b) A case where the film is not totally drained to the rear with more than one mesh point inside the coating film. Simulation resolution: 48 points/radius. Non dimensional numbers: (a)  $\xi_{12}=0.105$ ,  $\xi_{13}=0.005$ ,  $\lambda_{12}=5$ ,  $\lambda_{13}=1$ ,  $Bo_{12}=2.8$ ,  $Bo_{13}=0.134$ ,  $Ar=53$ ; (b)  $\xi_{12}=0.294$ ,  $\xi_{13}=0.176$ ,  $\lambda_{12}=50$ ,  $\lambda_{13}=0.1$ ,  $Bo_{12}=0.06$ ,  $Bo_{13}=3.75$ ,  $Ar=10$ .

# Chapter 4: Numerical Approach: Results

Numerical simulations of a drop crossing a plane liquid-liquid interface in a centrifugal field have been performed by using the Level-Set method. The objective is to characterize, at high inertia, the hydrodynamics parameters controlling the coating volume of the droplet, which results from the rupture of the liquid tail of lighter phase entrained by the droplet during the crossing of the interface. The numerical method has been first validated in two-phase flow simulations of a drop rising in a stagnant liquid, then in three-phase flow configurations to reproduce the theoretical critical condition for a drop to cross an interface in static conditions (crossing driven by the drop apparent weight). Then, in inertial conditions, extensive simulations of crossing droplets have been performed in a wide range of flow parameters and phase properties, for two types of drop: solid-like droplets (mimicking rigid particles) and deformable drops. For each studied case, crossing time, maximum length of the column of liquid pulled by the droplet and the volume coating the drop after crossing have been computed and scaled as a function of inertia parameters deduced from the analysis of drop velocity and shape evolution during the crossing.

## 4.1. Introduction

Encapsulation is a process by which an active ingredient is isolated from its external environment within a shell, in order to protect it, trigger and control its release in time and space. Several encapsulation processes already exist in the industry (pharmaceutical, food industry, cosmetics...) (Dubey et al., 2009; Mishra, 2015). The context of this work is the development of a microfluidic encapsulation process allowing the coating of submillimeter-sized droplets (the target diameter  $d$  being of order  $O(100 \mu\text{m})$ ) by a liquid phase immiscible with the droplet phase, by crossing of a liquid-liquid (typically oil/water) interface in a centrifugal field (Massiera et al., 2012). The same principle was applied at very low inertia for the production of giant vesicles (Abkarian et al., 2011). However, in the latter investigation, the crossing of the interface and the encapsulation process were driven by a different mechanism: the zipping of two amphiphilic monolayers adsorbed both on the droplet surface and the plane interface. In the present study, inertia forces, such as apparent weight or dynamic pressure force, are responsible for the crossing of droplets and result in the entrainment of a lighter liquid column into the heavier fluid (tailing regime) (Dietrich et al., 2011) which, after rupture, leaves the droplet coated.

The development of a process at high Reynolds number regime is thought to enhance the production rate of encapsulated droplets, with a possibility to tune the film thickness according to flow parameters and phase properties. The development of such a process first

requires to investigate the physics of the crossing of a liquid-liquid interface by a droplet in inertial regime, including the determination of the crossing conditions and of the mechanism of encapsulation.

In the considered process, a centrifugal field drives the droplet (phase 2) towards an interface separating two immiscible liquids, phases 1 and 3 (liquid 1 being the lighter phase), as sketched in Figure 40. In order to ensure an inertial regime for sub-millimeter sized drops and ordinary liquids, centrifuge accelerations as large as 5000g are considered.

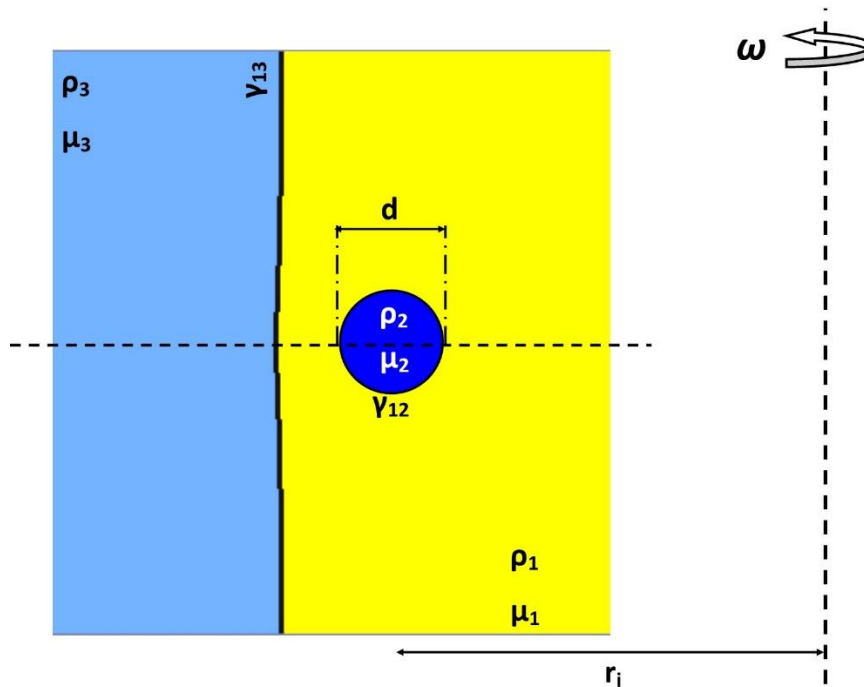


Figure 40: Scheme of the studied three-phase system in a centrifuged cell ( $\omega$  is the angular speed). Phase 1: lighter (organic) continuous phase; phase 2: droplet (aqueous); phase 3: heavier (aqueous) continuous phase.

The system is composed of ten physical parameters which are the densities of the three phases ( $\rho_i$ ,  $i= 1, 2, 3$ ), their dynamic viscosities ( $\mu_i$ ,  $i= 1, 2, 3$ ), the surface tensions ( $\gamma_{12}$  and  $\gamma_{13}$ ) respectively between phases 1 and 2 and phases 1 and 3 (assuming that phases 2 and 3 will never be in direct contact allows to disregard  $\gamma_{23}$ ), the droplet diameter  $d$  (or radius  $R$ ), and the centrifugal acceleration  $a_c=r_i\omega^2$  evaluated at the interface position,  $r_i$  being the radial position of the interface in the cylindrical coordinate system centered on the axis of rotation as sketched in Figure 40 and  $\omega$  the angular speed of rotation. As these ten quantities involve three fundamental units (mass, time and length), the theorem of Vaschy-Buckingham states that the problem can be described with seven independent

dimensionless parameters. In this study, we chose: the density ratios  $\xi_{12}=\rho_2/\rho_1-1$  and  $\xi_{13}=\rho_3/\rho_1-1$ , the viscosity ratios  $\lambda_{12}=\mu_2/\mu_1$  and  $\lambda_{13}=\mu_3/\mu_1$ , the Bond number  $Bo_{12}=(\rho_2-\rho_1)a_cR^2/\gamma_{12}$  of the droplet immersed in phase 1 which describes its deformability by comparing the centrifugal force applied on the droplet to its interfacial tension, the Bond number  $Bo_{13}=(\rho_3-\rho_1)a_cR^2/\gamma_{13}$  of the interface, and the Archimedes number  $Ar=\rho_1(\xi_{12}a_c)^{1/2}R^{3/2}/\mu_1$  which describes the flow regime in phase 1, which is merely a Reynolds number based on the gravitational velocity  $(\xi_{12}a_cR)^{1/2}$ . Other useful non-dimensional numbers can be used, like the drop Reynolds number in phase 1,  $Re(t)=\rho_1V(t)d/\mu_1$  where  $V(t)$  is the velocity of the droplet center of mass at a given time, and its Weber number in phase 1 which compares the inertial stress responsible for its deformation over the interfacial tension stress,  $We(t)=\rho_1V^2(t)d/\gamma_{12}$ .

The problem of a sphere settling through a liquid-liquid interface (with  $\rho_1$  and  $\rho_3$  of same order of magnitude, contrary to the problem of splashing where a sphere impacts a free surface) was addressed in the literature through theoretical models, numerical simulations and experiments, gravity being generally the driving force in most of the studies. The different investigations have generally addressed one of the following questions: (i) the film drainage problem, which corresponds to a sphere standing at the interface in a quasi-static equilibrium, or (ii) the tailing regime leading to the entrainment of a column of fluid, where the sphere crosses the interface with a finite velocity, its crossing being possible even though the film drainage process is not achieved.

In the case of solid particles, the two configurations of (i) film drainage mode (see the study of Hartland (Hartland, 1968)) or (ii) tailing mode (see the study of Dietrich et al., 2011) were reproduced in the simulations of Geller et al., 1986, and presented in a regime diagram experimentally obtained by Jarvis et al., 2019 and depending on both the interface Bond number  $Bo_{13}$  and the viscosity ratio  $\lambda_{13}$ . Generally, small and light spheres remain trapped at the interface. To analyze the quasi-static problem, Maru (Maru et al., 1971) proposed a force balance model, between the particle weight, driving its crossing, and surface tension and buoyancy forces opposing to it, leading to the prediction of a minimal sphere radius as crossing condition, validated by experimental observations. A similar critical condition was established by (Pierson & Magnaudet, 2018) in the form of a minimum relative density contrast  $\xi_{12}/\xi_{13}$  required to cross an interface under static conditions, at a given Bond number  $Bo_{13}$ . From experimental observations with several particles and pairs of fluids, these authors found that this relationship successfully predicted, in most of the cases, if a particle would cross the interface or be trapped on it. This criterion was validated in quasi-static regimes, where a settling particle is stopped for a long time at the interface, and in dynamic conditions where the sphere velocity remains finite during crossing. In only a few cases was the crossing possible thanks to dynamic effects whereas the quasi-static balance predicted that the particle should not cross, associated to a strong deceleration of the particle at the interface; the crossing mechanism was due in these cases to a supplementary

history force (Pierson & Magnaudet, 2018) issued from the collapse of the particle wake at the interface, which made it possible to overcome the resisting forces to crossing. In the tailing regime, (Pierson & Magnaudet, 2018) have shown that the entrained liquid column geometry strongly depends on  $\lambda_{13}$  and the Archimedes number  $Ar$  based on properties of phase 1, due to the fact that the column keeps the footprint of the wake developed in phase 1. The entrained tail stretches inside phase 3, and eventually breaks. Different column rupture modes have been classified by Aristoff & Bush, 2009 and characterized by Pierson & Magnaudet, 2018: deep seal pinch-off, corresponding to a column detachment close to the particle in the case where buoyancy effects are dominant, and shallow pinch-off where the column detachment first occurs close to the position of the interface when driven by the interfacial tension. Column axisymmetric is ensured provided that  $Ar < 55$  (Fabre et al., 2012). In very high inertial conditions ( $Ar > 55$ ), the development of instabilities has been observed (Jarvis et al., 2019; Pierson & Magnaudet, 2018) and leads to configurations of tailing with surrounding corollas, or even full three-dimensional tails with possible fragmentation due to the strong shearing from the boundary layer developing around the tail when  $Ar \sim O(100)$  and  $\lambda_{13} < 1$ .

In all cases, once the entrained column breaks up, a part of the fluid of phase 1 covers the settling particle. At small  $\xi_{13} \leq 0.1$  and with continuous phases of contrasted viscosities  $\lambda_{13} \leq 0.02$  the coating volume experimentally measured by Pitois et al., 1999 (particles falling in Stokes regime in phase 1) and Pierson & Magnaudet, 2018 scales linearly with a modified Bond number  $(\xi_{12}/\xi_{13}-1)Bo_{13}$  obtained from a force balance on the coated particle in the limit of small  $Ar$ ; note that, in these cases, the coating volumes are of same order of magnitude as that of the particle. At larger liquid density contrasts ( $\xi_{13} > 0.1$ ), the coating volume was observed to be highly sensitive to both  $Bo_{13}$  and  $\xi_{12}/\xi_{13}$  in a non-trivial way.

The crossing of a liquid-liquid interface by bubbles is more complex due to bubble deformation. Shopov (Shopov & Minev, 1992) performed numerical simulations of deformed bubbles crossing an interface, at small and moderate Reynolds numbers, focusing on the bubble and interface deformations and on the film drainage dynamics rather than on the tailing mode. They have shown that, at very low Weber and Reynolds numbers, a bubble can be deformed into a prolate shape (i.e. elongated in the direction of motion) during the passage through the interface in cases at low  $\lambda_{13}$ , a result confirmed by the simulations of Manga & Stone, 1995, whereas at higher Weber and Reynolds numbers, the action of inertial forces and the interaction with the interface lead to oblate bubbles with formation of a concavity at the rear and spherical cap shapes during the crossing. Interface crossing in inertial regimes was also experimentally investigated by Dietrich (Dietrich et al., 2011) who provided a relationship of the crossing time of the interface by a bubble as a function of the ratio of the terminal velocities inside the two continuous phases. Once the tail is formed, in the column, their PIV measurements have shown the coexistence of a

fluid motion entrained in the bubble wake and an opposite flow driven by gravity. The crossing in tailing mode in the case of a bubble was also considered by Bonhomme (Bonhomme et al., 2012), both experimentally and numerically under inertial conditions, in a wide variety of bubble shape configurations (from spherical to toroidal). A mapping of the bubble shapes and entrained column geometries was provided as a function of both  $Bo_{13}$  and  $Ar$ . Small bubbles are slowed down and even stopped at the interface without crossing (film-drainage configuration, the crossing being possible only provided that the drainage process is achieved), whereas larger spherical cap bubbles at larger  $Bo_{13}$  generally cross the interface easily. It has been found that the volume entrained is also larger with such spherical cap bubble shapes since they offer a larger cross-section to the interface than spheroidal bubbles, for a given gas volume. In the experiments of Emery (Emery et al., 2018), the crossing by a single bubble shows additionally that, in the tailing mode, the column of liquid entrained is longer in case where the bubble velocity does not change much during the crossing of the interface; the tail is observed to remain connected a long time before its rupture, in some cases the liquid shell covering the bubble breaking before the column. The latter study has investigated the crossing of a stream of bubbles, giving a map of the different flow regimes with the possible formation of clusters. The experimental results of Manga (Manga & Stone, 1995) also illustrates the case of vertically aligned bubbles, by showing that the following bubble in a train experiences less resistance during the crossing, leading to a more elongated shape as compared to the previous bubble.

Finally, the problem of droplets crossing a liquid-liquid interface is even more complex because it involves more parameters as compared to the case of particles or bubbles, due to the droplet viscosity and deformability. Only a few studies are available, most of them addressing the film drainage problem in the context of drop-interface coalescence under quasi-static conditions. In this configuration, Hartland (Hartland, 1967) studied experimentally the profile of the draining film beneath a droplet approaching a liquid-liquid interface and derived expressions of the drainage dynamics in case of either mobile or immobile interfaces, a more complete theoretical analysis being further provided by Jones & Wilson, 1978 who clarified the possible narrowing of the drainage film at its periphery (dimple formation). Simulations of Chi (Chi & Leal, 1989) at low Reynolds number were also able to consider the influence of the drop internal circulation on the film drainage dynamics, through the viscosity ratio  $\lambda_{12}$  ( $= \lambda_{13}$ ) in their particular conditions. They have confirmed that different types of film geometry can be observed upon the arrival of the drop at the interface: a film with a minimum thickness at the top indicating a rapid drainage at low  $\lambda_{12}$ , a film with a uniform thickness when  $\lambda_{12}$  is of the order of unity, and a film with minimum thickness at its periphery involving the formation of a dimple at high  $\lambda_{12}$ . When the droplet travels a distance of several radii beyond the interface, i.e. when it actually crosses the interface, Manga & Stone, 1995 did a parametric numerical study in low Reynolds number regimes in the first phase. The influence of four non-dimensional numbers,  $\lambda_{12}$ ,  $\lambda_{13}$ ,  $Bo_{13}$ , and  $Bo_{12}$  on the drop and interface deformations and film drainage rate, was addressed. As for bubbles, at low  $\lambda_{13}$  drops have been observed to undertake a

prolate shape during the interface crossing; at large  $Bo_{12}$ , they deform by developing either an elongated tail or a small cavity at the back. Concerning the film drainage, it has been found that the higher the droplet viscosity (the higher  $\lambda_{12}$ ) the thicker the coating film of phase 1 around the drop, the slowest drainage rate occurring when  $\lambda_{12} \gg 1 \gg \lambda_{13}$ . However, due to the limitation of the numerical approach, calculations could not capture the long tail dynamics and its rupture. To our knowledge, there is no study dedicated to investigate the tailing mode with droplets until breakup of the column.

In this chapter, the crossing of a liquid-liquid interface by a droplet submitted to a centrifugal field has been numerically investigated, by focusing in the tailing regime. Two types of drops have been considered, both solid-like drops mimicking rigid particles (with a high internal viscosity and surface tension) and deformable drops at different viscosity ratios  $\lambda_{12}$ , in a wide range of flow parameters and phase properties, which however correspond to common liquid phases and oil-water interfaces. In all cases, droplet motion lies in inertial regime ( $7 \leq Re \leq 160$ ), based on the settling velocity in phase 1).

The paper is structured as follows: in the next section (section 4.2), the numerical Level-Set method used in the three-phase system is briefly presented and some validation test cases are discussed to compute the terminal velocity of non-deformed droplets, the deformation of drops in inertial regimes, and, in three-phase configurations, the crossing criterion for solid-like drops in static conditions. Then, the results obtained in dynamic crossing conditions (i.e. with an impacting velocity) are presented and discussed in section 4.3 starting with the effect of the drop velocity at the interface on the condition for crossing, followed by an analysis of the drop shape and velocity during crossing. Finally, the length of the entrained column and the volume coating the droplet are scaled as a function of parameters characterizing drop inertia.

## **4.2. Numerical method**

Axisymmetric direct numerical simulations of droplets travelling through liquid-liquid interfaces are carried out using the numerical code DIVA. In view of solving a three-phase flow involving the dynamics of two interfaces, the numerical approach is based on a one-fluid formulation of the Navier-Stokes equations, and the Level-Set method is used to capture the two interfaces on a Cartesian grid that does not follow the complex interface shapes.

This numerical method is the natural extension for three phases of that described in Tanguy et al., 2014, Lalanne, Villegas, et al., 2015, and Rueda Villegas et al., 2016 in case of two-



phase flows, with several validation tests of the dynamics of deformed droplets and bubbles. The method is briefly presented here. The method consists in solving the Navier-Stokes equations for an incompressible flow (see section 3.2) to compute the velocity field  $\vec{u}$  and the pressure field  $P$ .

In the simulation of dynamic interface crossing resulting in drop encapsulation, the film volume covering the droplet is evaluated as post-treatment. The method consists in evaluating the volume  $V_e$  enclosed by the interface between phase 1 and 3 around the droplet (see Figure 49 for pictures from the simulation), based on the Level-Set function  $\varphi_2$ , to which the droplet volume  $V_{\text{drop}}$  is subtracted in order to obtain the film volume  $V_f = V_e - V_{\text{drop}}$ . As post-treatment,  $V_e$  is computed through the volume integration of a regularized Heaviside function  $H$ , equal to 1 inside the film contour defined by a minimum numerical thickness  $\varepsilon_0 = 1.5\Delta x$  (with  $\Delta x$  the smaller mesh cell size) as:

$$H(\varphi) = \begin{cases} 0 & \text{if } \varphi_2 < -\varepsilon_0 \\ \frac{1}{2} \left[ 1 + \frac{\varphi_2}{\varepsilon_0} + \frac{1}{\pi} \sin\left(\frac{\pi\varphi_2}{\varepsilon_0}\right) \right] & \\ 1 & \text{if } \varphi_2 > \varepsilon_0 \end{cases}$$

For most of the cases in dynamic crossing, the contribution to  $V_f$  from the bottom part of the droplet is generally dominant, which is a well-resolved zone, whereas the contribution at the top is of negligible thickness (see Figure 49 and Figure 50). In order to test the sensitivity on the film volume to the grid resolution, a mesh convergence study has been carried out, in the case  $D_2$  from Table 10, by using 48, 72 and 96 grid points per radius. The difference in volume computation was less than 1% between the different grids. Therefore, a grid resolution of 48 points per radius has been chosen for the following simulations.

### 4.3. Interface crossing in dynamic conditions

In this part, we consider axisymmetric simulations of interface crossing in inertial conditions by either solid-like droplets  $S_i$ , simulated as highly viscous ( $\lambda_{12} = 50$ ) and non-deformed droplets (both  $Bo_{12} \ll 1$  and  $We_{12} \ll 1$ ), or deformable droplets  $D_i$  with variable  $\lambda_{12}$ . As shown in Figure 40, the driving force is induced by a high acceleration, which increases linearly with the drop position like in a centrifugal field. Simulations are carried out in the frame moving with the droplet, of size  $6R^*13R$  or  $19R$ , with a resolution of 48 mesh points per radius based on the validation tests. In what follows, the conditions and dynamics of interface crossing and film entrainment have been investigated. In terms of non-dimensional parameters, several values of  $\xi_{12}/\xi_{13}$  are considered ( $1.67 \leq \xi_{12}/\xi_{13} \leq 21$ ), which correspond to  $0.0105 \leq \xi_{12} \leq 0.2941$  and  $0.0005 \leq \xi_{13} \leq 0.176$ . For each case, the Bond number  $Bo_{13}$  is taken to be high enough for interface crossing, the study being performed from moderate to high inertia  $5.3 \leq Ar \leq 70$  (maximal value of  $Ar$  is 55 for solid-like droplets). For deformable drops, the drop Bond number  $Bo_{12}$  lies in between 1.3 and 6.25,

and the viscosity ratio  $\lambda_{12}$  is varied in a wide range ( $0.1 \leq \lambda_{12} \leq 50$ ). In most cases,  $\lambda_{13} = 1$  and in a few cases  $\lambda_{13} < 1$  (down to 0.05). For solid-like droplets, it has been verified that the tangential velocity along the interface is always small compared to the drop rise velocity  $u_T$ , the maximal value never exceeds 10% of  $u_T$ , leading to a negligible fluid velocity at both the interface and inside the solid-like droplet. The physical parameters and non-dimensional numbers of all simulations are reported in Table 9 and Table 10 respectively.

**4.4. Crossing conditions with additional inertia**

Here, the effect of drop impact velocity on crossing condition is examined. In a quasi-static regime, the critical crossing condition is given by equations 22 and 23 of section 3.3.2 and in two limits  $Bo_{13} \ll 1$  and  $Bo_{13} \gg 1$ . In dynamic conditions, the droplet is released far from the interface (at a distance of 3 diameters in the simulations) and has time to develop its wake in phase 1, the drop motion being inertial in the studied conditions. When the droplet approaches the interface, it is decelerated due to the presence of the interface, reaching a minimum value  $U_{min}$  while crossing. For each case, the minimal Reynolds number  $Re_{min}$  computed from this velocity is reported in Table 10. In most cases,  $Re_{min}$  is positive but in some cases,  $Re_{min}$  falls to 0 when the drop (deformable or not) is stopped by the interface.  $U_{min}$  can even reach negative values for bouncing drops. For a non-crossing case in static conditions, inertia could be expected to favor the crossing. Then, Figure 41 compares the theoretical critical condition for crossing given by the static theory, with the simulation results in dynamic cases at different Ar values, for both solid-like and deformable droplets.

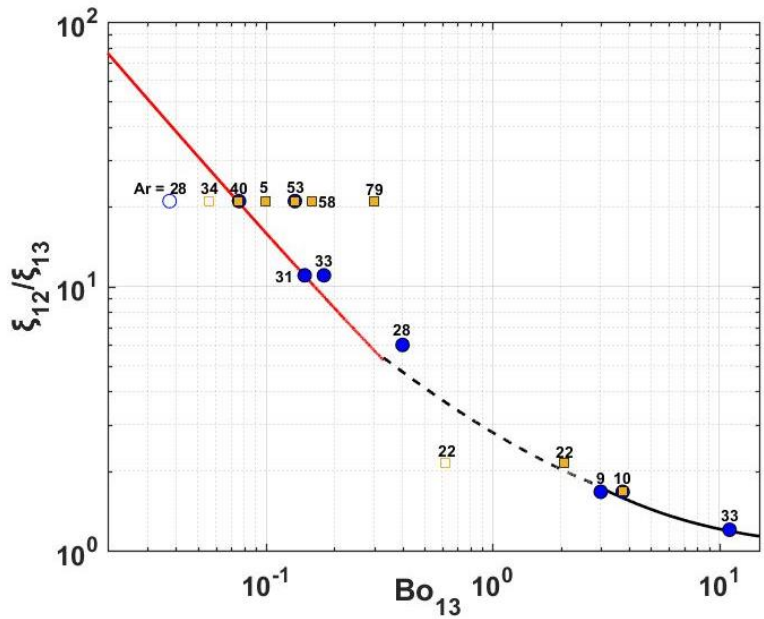


Figure 41: The diagram showing the crossing and no crossing zones as a function of static theory predictions (continuous lines): eq. 8 and 9. The squares and the circles correspond to simulations of solid-like droplets and deformable droplets respectively, in dynamic case, where the points are labeled by the Archimedes number Ar. Symbols are colored in case of crossing in the simulation, blank otherwise.

Droplet type	Sim	$\rho_1$	$\rho_2$	$\rho_3$	$\mu_1$	$\mu_2$	$\mu_3$	$\gamma_{12}$	$\gamma_{13}$	$a_c$
<b>Solid-like</b>	$S_1$	995	1100	1000	0.001	0.05	0.001	1	0.01	2740g
	$S_2$	995	1100	1000	0.002	0.1	0.002	1	0.01	1551g
	$S_3$	995	1100	1000	0.001	0.05	0.001	1	0.01	1551g
	$S_4$	995	1100	1000	0.001	0.05	0.001	1	0.01	2660g
	$S_5$	995	1100	1000	0.001	0.05	0.001	1	0.01	3262g
	$S_6$	995	1100	1000	0.0015	0.075	0.0015	1	0.01	1551g
	$S_7$	995	1100	1000	0.0007	0.035	0.0007	1	0.01	1551g
	$S_8$	930	1080	1000	0.002	0.1	0.002	1	0.0045	1359g
	$S_9$	850	1100	1000	0.01	0.5	0.001	2	0.02	5097g
	$S_{10}$	980	1100	1000	0.001	0.05	0.001	1	0.01	2548g
	$S_{11}$	980	1100	1000	0.001	0.05	0.001	1	0.01	1733g
<b>Deformable</b>	$D_1$	995	1100	1000	0.001	0.05	0.001	0.01	0.01	2740g
	$D_2$	995	1100	1000	0.001	0.005	0.001	0.01	0.01	2740g
	$D_3$	995	1100	1000	0.001	0.02	0.001	0.01	0.01	2740g
	$D_4$	995	1100	1000	0.01	0.05	0.01	0.01	0.01	2740g
	$D_5$	995	1100	1000	0.01	0.05	0.01	0.0134	0.0134	2740g
	$D_6$	995	1100	1000	0.001	0.05	0.001	0.01	0.01	1529g
	$D_7$	960	1200	1000	0.0017	0.0085	0.0017	0.01	0.01	1359g
	$D_8$	960	1200	1000	0.0007	0.0035	0.0007	0.01	0.01	1359g
	$D_9$	960	1200	1000	0.0017	0.085	0.0017	0.01	0.01	1359g
	$D_{10}$	960	1200	1000	0.0007	0.035	0.0007	0.01	0.01	1359g
	$D_{11}$	980	1200	1000	0.001	0.0005	0.001	0.006	0.006	503g
	$D_{12}$	850	1100	1000	0.01	0.01	0.001	0.02	0.02	4077g
	$D_{13}$	850	1100	1000	0.01	0.05	0.001	0.02	0.02	5097g
	$D_{14}$	913	1081	997	0.005	0.0024	0.001	0.036	0.011	898g
	$D_{15}$	930	1081	997	0.01	0.0024	0.001	0.036	0.011	923g
	$D_{16}$	950	1081	997	0.02	0.0024	0.001	0.036	0.011	926g

Table 9: The physical parameters of simulations presented in this paper. Density is in  $\text{kg.m}^{-3}$ , dynamic viscosity in Pa.s, surface tension in  $\text{N.m}^{-1}$ . The droplet size is  $d = 200 \mu\text{m}$  for all simulations.

Sim	$\xi_{12}$	$\xi_{13}$	$\frac{\xi_{12}}{\xi_{13}}$	$\lambda_{12}$	$\lambda_{13}$	$Bo_{12}$	$Bo_{13}$	$Ar$	$Oh_{12}$	$Oh_{13}$	$Re_{max}$	$Re_{min}$	$We_{max}$	$I_{ez}$	$\chi_{max}$	$\chi_{min}$	$\chi_{det}$
$S_1$	0.105	0.005	21	50	1	0.03	0.13	53	0.1	0.02	160	134	0.13	11	1	1	1
$S_2$	0.105	0.005	21	50	1	0.02	0.076	20	0.21	0.04	48	16	0.046	1.56	1	1	1
$S_3$	0.105	0.005	21	50	1	0.02	0.076	40	0.1	0.02	114	62	0.065	3.05	1	1	1
$S_4$	0.105	0.005	21	50	1	0.03	0.13	52	0.1	0.02	158	130	0.125	10.5	1	1	1
$S_5$	0.105	0.005	21	50	1	0.03	0.16	57	0.1	0.02	178	158	0.16	14.8	1	1	1
$S_6$	0.105	0.005	21	50	1	0.02	0.076	27	0.16	0.03	69	25	0.054	1.76	1	1	1
$S_7$	0.105	0.005	21	50	1	0.02	0.076	57	0.07	0.01	177	104	0.077	3.82	1	1	1
$S_8$	0.161	0.075	2.14	50	1	0.02	2.07	22	0.22	0.07	52	17	0.058	1.61	1	1	1
$S_9$	0.294	0.176	1.67	50	0.1	0.06	3.75	10	0.75	0.17	19	0	0.106	1.05	1	1	1
$S_{10}$	0.12	0.02	6	50	1	0.03	0.5	54	0.1	0.02	94	85	0.045	5.07	1	1	1
$S_{11}$	0.12	0.02	6	50	1	0.02	0.34	45	0.1	0.02	72	36	0.026	1.83	1	1	1
$D_1$	0.105	0.005	21	50	1	2.82	0.134	53	1.06	0.02	124	95	7.72	6.4	1.77	1.93	1.63
$D_2$	0.105	0.005	21	5	1	2.82	0.134	53	0.1	0.02	112	92	6.37	6.14	2.39	3.24	1.77
$D_3$	0.105	0.005	21	20	1	2.82	0.134	53	0.43	0.03	116	95	6.8	6.38	2.21	2.12	1.808
$D_4$	0.105	0.005	21	5	1	2.82	0.134	5	1.06	0.22	7	2.8	2.37	2.17	1.24	1.09	1.16
$D_5$	0.105	0.005	21	5	1	2.1	0.1	5	0.92	0.19	7	1.3	1.77	1.4	1.21	0.998	1.11
$D_6$	0.105	0.005	21	50	1	1.57	0.076	40	1.06	0.02	96	40	4.63	1.85	1.33	1.4	1.13
$D_7$	0.25	0.042	6	5	1	2.43	0.4	28	0.17	0.03	60	38	5.4	3.67	2.1	0.95	1.26
$D_8$	0.25	0.042	6	5	1	2.43	0.4	69	0.07	0.01	151	116	5.8	5	2.52	1.79	1.5
$D_9$	0.25	0.042	6	50	1	2.43	0.4	28	1.74	0.03	64	30	6.2	2.83	1.4	1.16	1.16
$D_{10}$	0.25	0.042	6	50	1	2.43	0.4	69	0.71	0.01	162	111	6.76	4.68	1.95	1.53	1.39
$D_{11}$	0.224	0.02	11	0.5	1	1.8	0.16	33	0.01	0.02	77	58	5	4.37	2.23	1.48	1.42
$D_{12}$	0.294	0.176	1.67	1	0.1	5	3	9	0.15	0.17	16	1.8	7.3	1	1.65	0.6	1.17
$D_{13}$	0.294	0.176	1.67	5	0.1	6.25	3.75	10	0.75	0.17	17	-2.5	8.3	1.05	1.83	0.72	1.1
$D_{14}$	0.184	0.092	2	0.48	0.2	1.37	2.25	18	0.02	0.08	48	37	4.76	4.7	1.82	1.39	1.31
$D_{15}$	0.162	0.072	2.25	0.24	0.1	1.44	2.09	10	0.02	0.16	22	17	3.5	3.96	1.43	1.13	1.33
$D_{16}$	0.138	0.049	2.78	0.12	0.05	1.36	1.6	5	0.02	0.3	8	6.5	1.97	5.14	1.21	0.92	1.76

Table 10: The non-dimensional numbers of all simulations.  $Re_{max}$ ,  $Re_{min}$  and  $We_{max}$  are based on properties of phase 1. Note that drop breakup occurs during the interface crossing for simulations  $D_{12}$  and  $D_{14}$ .

For the different values of  $\xi_{12}/\xi_{13}$  investigated, the critical condition for crossing is found to be consistent with the quasi-static theoretical predictions, and does not seem to be affected by the impact velocity. Actually, the value of  $Ar$  is probably not crucial to understand the role of additional inertia for crossing conditions. Indeed, the additional inertia force exerted by the particle or the drop on the interface is approximately equal to its apparent weight: whatever the value of  $Ar$ , the maximum force brought by inertia turns to simply double the particle weight. Hence the maximum effect is given by a drop having the same properties with a volume multiplied by 2, or a diameter multiplied by  $2^{1/3}$ . The corresponding equivalent Bond number  $Bo_{13eq}$  is then  $Bo_{13}$  multiplied by  $2^{2/3}=1.59$ , which remains a small factor. Making use of this equivalent apparent weight, the solid-like case at  $Ar=22$  in Figure 41, which is subcritical (i.e. non-crossing case), has a  $Bo_{13}$  approximately equal to 0.6. Multiplying  $Bo_{13}$  by 1.59 leads to  $Bo_{13eq}=0.95$  which still stands below the critical condition on the static crossing condition curve: the particle is not crossing. The same evaluation can be achieved for the deformable drop case at  $Ar=28$  and  $Bo_{13}$ , smaller than 0.04. In this case, equivalent  $Bo_{13eq}=0.06$ , which remains smaller than the critical value, close to 0.08: here again, the droplet is not crossing.

The case  $Ar=34$ , corresponding to a solid-like droplet, is interesting because its equivalent Bond number ( $Bo_{13eq}=0.087$ ) is close to - slightly above - the critical value (around 0.08) predicted by the static crossing theory. In this case, the drop is submitted to several oscillations and it did not cross the interface at the end of the simulation. Such a behavior indicates that this point is close to the critical condition of crossing as predicted by the equivalent Bond number. However, running a simulation over a longer time could have shown that crossing was possible, in particular if, after some time, the collapse of the drop wake is able to help it to overcome the resisting forces of the interface (Pierson & Magnaudet, 2018).

Finally, these different examples on crossing conditions in dynamic cases emphasize the strong interest of the static theory, which is shown to be able to predict quite well if a droplet succeeds or fails to cross the interface, even when the droplet arrives at the interface with a non-zero velocity. In this case, a rough approximation consists in shifting the theoretical curve (for crossing in a quasi-static regime) by dividing the Bond number  $Bo_{13}$  by a factor 1.59 ( $2^{2/3}$ ). Note that the effect of  $Ar$  discussed here only concerns the final state, i.e. crossing or non-crossing, and disregards the dynamics of the interaction of the drop with the interface, which naturally is strongly dependent on  $Ar$  and involves inertial forces as discussed by (Pierson & Magnaudet, 2018).

In the following section, simulations result of crossing cases  $S_i$  (solid-like drops) and  $D_i$  (deformable drops) are presented and discussed.

## 4.5. Dynamics of interface crossing

### 4.5.1. Phenomenology

For solid-like droplets, Figure 42 shows the evolution of the velocity of the particle centroid as a function of its travel distance across the interface, and the corresponding image sequence, for cases  $S_1$  ( $Ar=53$ ) and  $S_2$  ( $Ar=20$ ), with the same densities and viscosities ratios (Table 10). In both cases, the droplet accelerates in phase 1, and the droplet wake develops with recirculation, as expected (Johnson & Patel, 1999) at these Reynolds numbers (maximum values of the Reynolds number in phase 1,  $Re_{max}$ , are respectively 160 and 48). In these cases, the distance of drop release to the interface was not sufficient to reach the point where viscous effects are fully established (note that, even with a larger initial distance between the droplet and the interface, a steady state is not expected because the centrifugal acceleration increases linearly with the distance from the rotation axis: only a quasi-steady state could be reached, with the drop acceleration that becomes low but does not vanish). At a distance from the interface of the order of the drop radius (close to point 1), the droplet velocity reaches a maximum  $U_{max}$ , then decelerates due to the presence of the interface (point 2 corresponds to the drop arrival at the position of the plane interface). Between points 2 and 3, drainage of phase 1 develops in the thin film between the top of the droplet and the interface, giving rise to a lubrication flow in this film, as the droplet continues its rising motion, pulling a column of phase 1 in its wake. At point 3, the droplet velocity reaches a minimum value  $U_{min}$  (from which  $Re_{min} = \rho_1 U_{min} d / \mu_1$  is computed). In both cases, while the droplet velocity reaches an extremum ( $U_{max}$  and  $U_{min}$  close to point 1 and at point 3 respectively), all of the forces exerted on the droplet center of mass are at equilibrium. Then, from point 3 to point 5, the droplet accelerates inside phase 3 with a different rate in the two cases considered, entraining a liquid column of phase 1 which extends up to a maximum length  $L_{max}$  before it breaks. For the two cases considered here, the column first detaches at the bottom close to the interface position (point 6), then at the rear of the droplet (point 7), leaving the droplet coated by a volume of phase 1 rising in phase 3. Due to gravitational effects, the volume of the lighter phase 1, coating the droplet, moves towards its rear, thinning up strongly at the top. It can be noticed that  $L_{max}$  is larger in case  $S_1$  than in case  $S_2$ , i.e. when inertia is higher.

Let us now consider the case of deformable droplets at  $Ar= 53$  and same Bond number of the interface  $Bo_{13}= 0.134$ , similarly to  $S_1$  (solid-like droplet), for two different viscosity ratios:  $\lambda_{12} = 50$  (case  $D_1$ ) and  $\lambda_{12} = 5$  (case  $D_2$ ). Case  $D_1$  corresponds to a very viscous droplet but deformable, and case  $D_2$  corresponds to a deformable droplet of lower internal viscosity. The droplet dynamics during its rising motion towards the interface is first analyzed. Simulation results of cases  $D_1$  and  $D_2$  both in the presence of the liquid-liquid interface (three-phase system) and without the interface (two-phase system) are compared, in order to evaluate the coupling between the drop velocity and its shape.

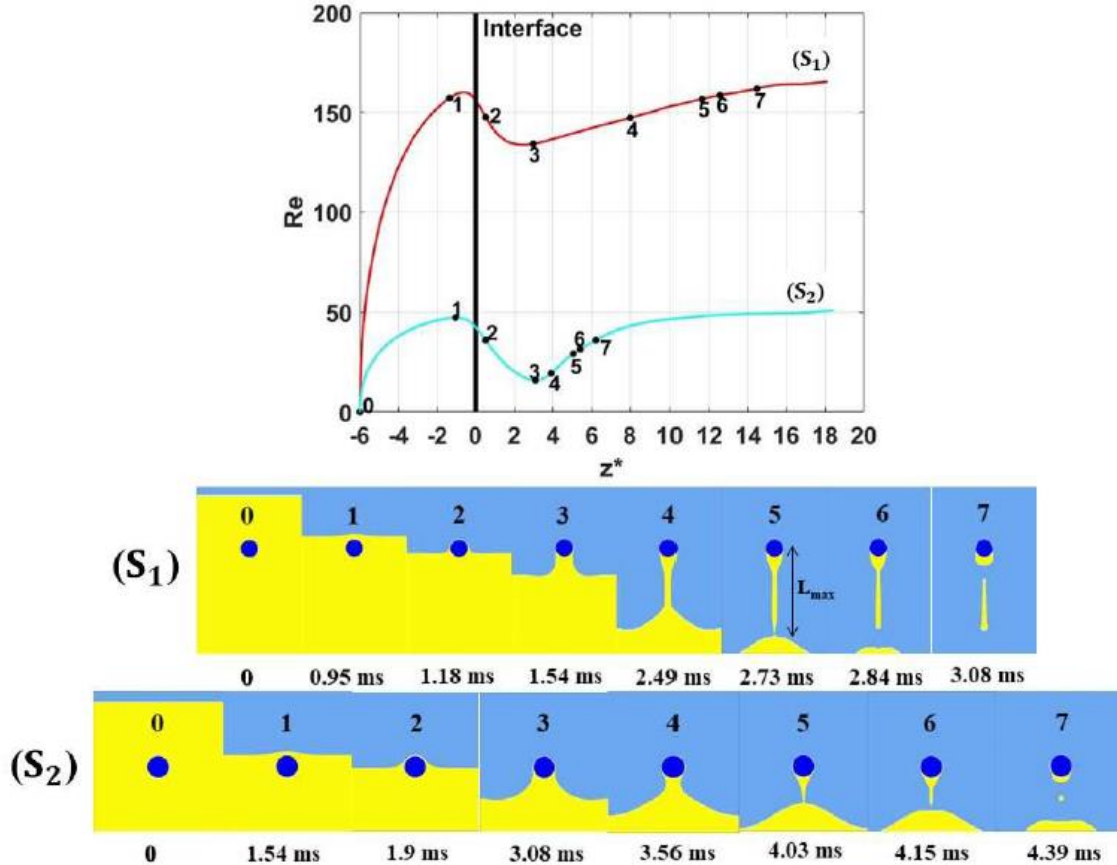


Figure 42: Evolution of the Reynolds number  $Re=\rho_1 U d/\mu_1$  ( $U$  is the instantaneous drop velocity) as a function of  $z^*$  (drop center of mass position normalized by  $R$ ), for cases  $S_1$  and  $S_2$ , alongside with screenshots of the phase indicator functions field issued from the simulations.  $z^*=0$  is the interface position. Figures appearing on the curves of the Reynolds number time signal are related to the image sequences.

Figure 43 displays the evolution of the instantaneous Reynolds number and aspect ratio of the two droplets. Quasi-steady conditions are not reached in the three-phase flow simulation before the liquid-liquid interface. In particular, if the velocity is close to its terminal value, the aspect ratio is still increasing, reaching a plateau value over longer distances based on the results from the two-phase flow simulations. The slow drop deformation dynamics is due to viscosity effects from both phases 1 and 2, in the same way as the damping rate of Eigen modes of drop shape oscillations (Miller & Scriven, 1968): for the same  $\mu_1$ , the higher the drop viscosity, the slower the drop shape response to the deforming stress.

By analyzing the steady-state conditions, the  $D_1$  droplet is found to have a larger velocity (larger  $Re$  and  $We_{12}$ ) but lower deformation than the  $D_2$  droplet. Indeed, as already emphasized in Figure 43, deformation of a viscous droplet in inertial conditions is not only a function of  $We_{12}$  but also of the viscosity ratio  $\lambda_{12}$ , which is ten times larger for  $D_1$ , resulting in a less flattened drop shape in quasi-steady conditions. Concerning the drop rising velocity, even if  $Ar$  is the same in both cases (same acceleration),  $D_1$  rises faster than  $D_2$ , a result which probably arises from two competing effects acting on the drag force: as  $\mu_2$  is higher for  $D_1$ , dissipation of the energy provided by gravity is increased for  $D_1$ ,

whereas the aspect ratio, of 2.4 for  $D_1$  lower than that of  $D_2$  (3.4), results in a larger drag on  $D_2$  than on  $D_1$ , the influence of drop shape being observed to dominate since the velocity of  $D_2$  is finally smaller. Note also that some velocity and shape oscillations are observed in the quasi-steady regime, of larger amplitude in case  $D_2$ , probably due to the fact that  $Ar$  is close to the critical value of 55 where a path instability appears (known for a solid particle motion (Fabre et al., 2012)), even though such a threshold could be different in a computation which assumes axisymmetry. All these comments make us understand that, when these droplets arrive close to the liquid-liquid interface in the three-phase flow simulation, their shape can strongly differ and can still be deforming despite close velocities.

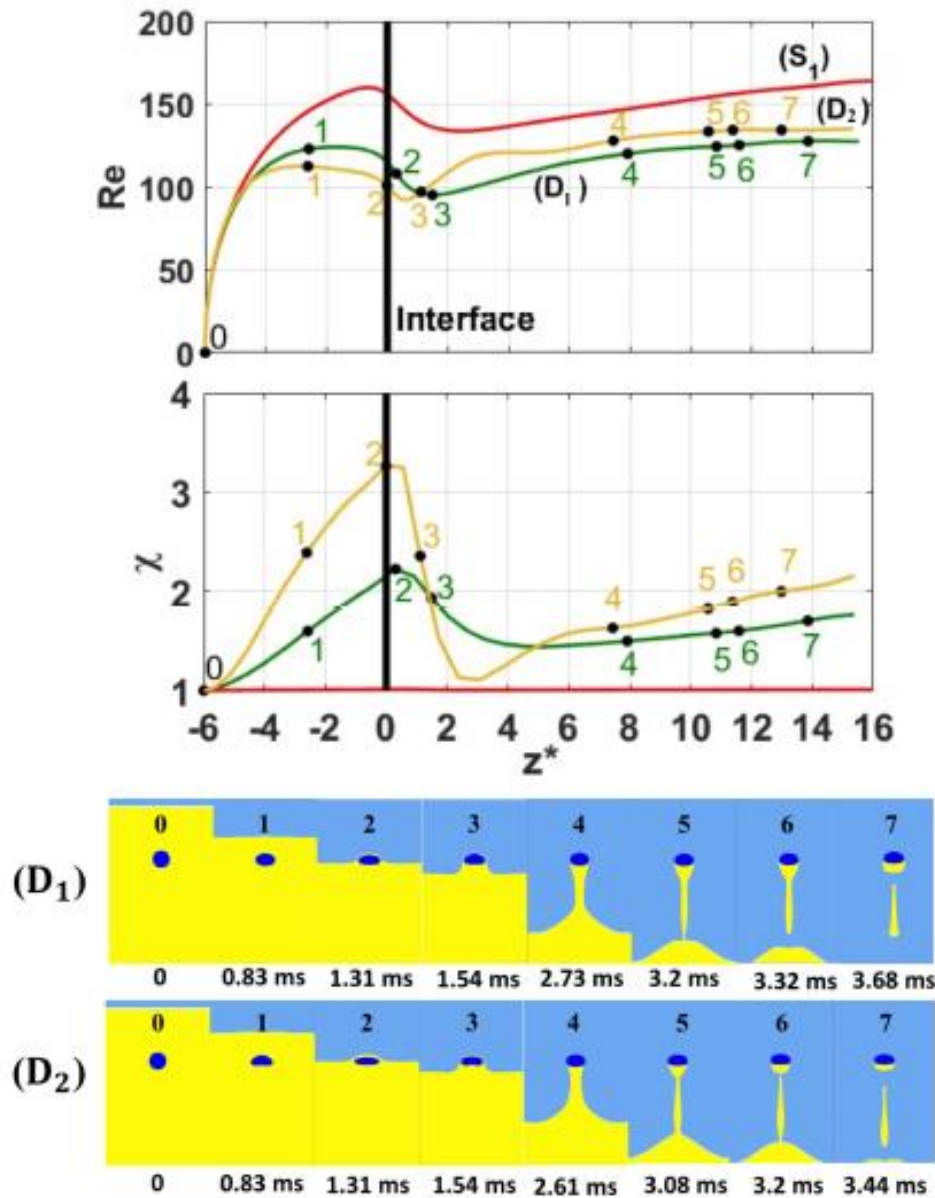


Figure 43: Evolution of the Reynolds number as a function of  $z^* = z / R$ , for two cases of deformable droplets  $D_1$  and  $D_2$  and the case  $S_1$  of a solid-like droplet at same  $Ar$  and  $Bo_{13}$ , alongside with screenshots of the simulations. The points indicated on the Reynolds number curve are relative to the shown images.



Now, in the presence of the liquid-liquid interface, Figure 43 shows the variation of the Reynolds number alongside with that of the drop aspect ratio as a function of the drop position, for cases  $D_1$  and  $D_2$  as well as for the solid-like droplet  $S_1$ .

Before the interface, due to the strong effect of deformation on the rise velocity, the highly deformed droplets  $D_1$  and  $D_2$  have both a smaller maximum velocity (at point 1) than the solid-like one  $S_1$ . Between points 1 and 3, the presence of the interface makes the velocity decrease at a distance of about  $1R$  before the interface, as clearly visible from the curves of Figure 44. The droplet shape continues flattening until point 2, at which external stresses action deform the droplet in the direction perpendicular to the acceleration, hence towards a spherical shape. At point 3, the interface is crossed and a column of phase 1 is entrained by the drop motion, like in the solid-like drop case. Between points 3 and 4, droplet  $D_2$ , which reacts faster in deformation to the external flow due to lower  $\mu_2$ , sees its deformation nearly vanishing (the minimum value of the aspect ratio is close to 1) before flattening again due to the acceleration in phase 3; the same dynamics is observed for  $D_2$ , except that the droplet has never retrieved a spherical shape during its deformation history. The drop acceleration at point 4 allows the column of phase 1 to be strongly extended.

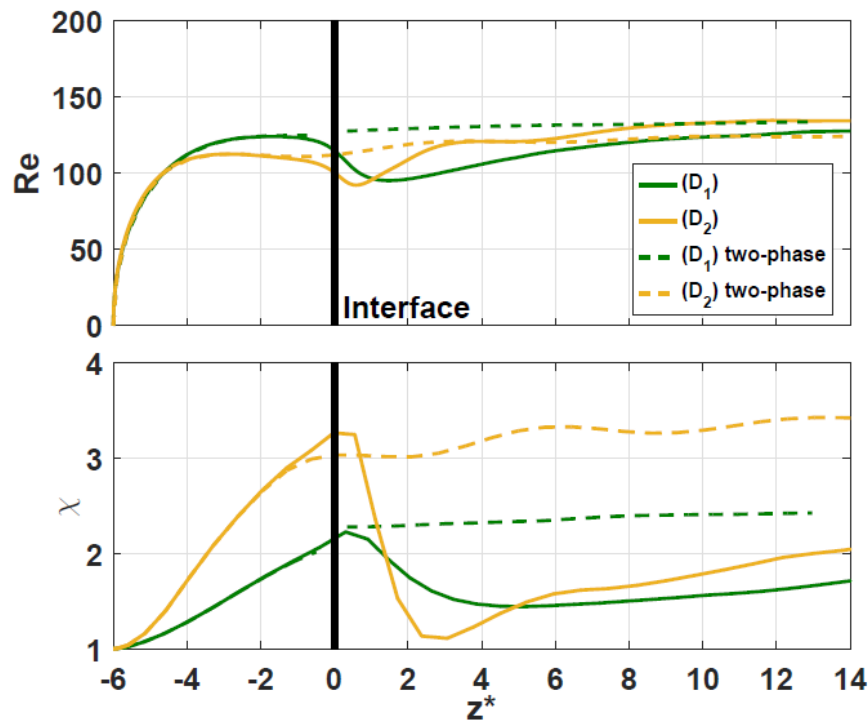


Figure 44: Evolution of the Reynolds number  $Re$  and aspect ratio  $\chi$  as a function of  $z^* = z/R$  for cases  $D_1$  and  $D_2$ . Dashed lines correspond to the two-phase flow simulations (without the interface), used as a base of comparison for the three-phase flow case.

Figure 45 shows the velocity fields of cases  $S_1$ ,  $D_1$ , and  $D_2$  at point 5, which is the last instant before the column breaks. In all cases, the entrained fluid column behind the droplet is lighter than the surrounding phase 3, so a part of the fluid in the column moves back towards the interface whereas another part is entrained in the droplet wake. This wake is

already developed from the drop rising in phase 1, and in these examples, it is not really modified by the presence of the interface because viscosities of phases 1 and 3 are the same ( $\lambda_{13}=1$ ). The column is stretched and thinned by an upward and a downward flow, which leads to the presence of a zero velocity point. The rupture takes place at point 6 for cases  $D_1$  and  $D_2$ . In case  $D_1$ , the detachment mechanism is similar to that described for cases  $S_1$  and  $S_2$  of Figure 42, taking first place at the column bottom then in the drop wake. However, in case  $D_2$ , the column detachment occurs first behind the droplet. In all cases, the encapsulated droplet, detached from the interface, rises in phase 3 and a part of column of phase 1 moves back to the interface, possibly breaking up into several droplets. The detachment in case  $S_1$ ,  $D_1$  is similar to the shallow pinch-off detachment mode, while that of case  $D_2$  is similar to deep seal detachment mode, both reported by Aristoff & Bush, 2009.

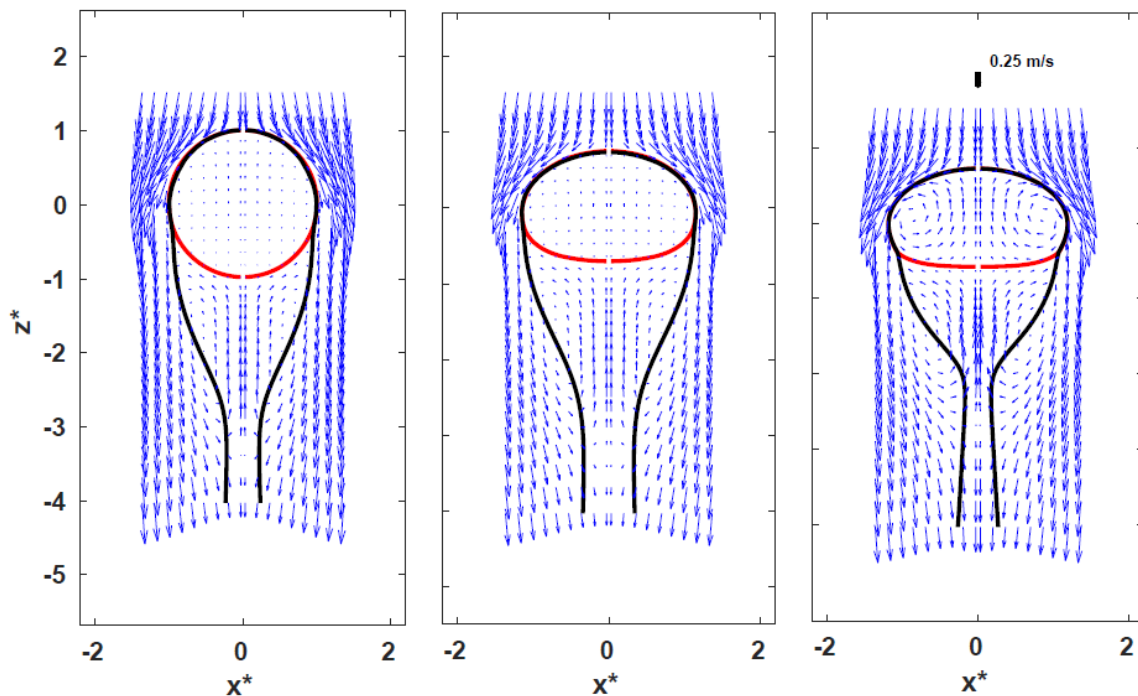


Figure 45: From left to right, velocity field of cases  $S_1$ ,  $D_1$  and  $D_2$  right before the column detachment. On the last image, the scaling velocity vector is indicated.  $x^*$  and  $z^*$  are the coordinates of the calculation domain normalized by the radius of the droplet. In all cases, the viscosities of the two continuous phases are identical ( $\lambda_{13}=1$ ).

The velocity field of case  $D_2$  shows a high internal circulation inside the droplet and a high tangential velocity at the interface comparable to the droplet velocity, which forces the interface to follow the deformation of the droplet and stay close to it up to a high separation angle. Such a high tangential velocity and drop internal circulation (lower value of  $\lambda_{12}$ ) favors a rapid film drainage along the interface and forces the column to detach earlier behind the droplet rear. In cases  $S_1$  and  $D_1$ , the droplet has a stronger internal viscosity leading to an approximately null tangential velocity and internal circulation, due to the continuity of tangential stresses at the interface. This does not favor the film detachment close to the droplet rear as in case  $D_2$ , and tends to increase the film volume finally coating

the droplet. In case  $D_2$ , the resulting film volume ( $V_f = 0.58V_{\text{drop}}$ ) is smaller than in case  $S_1$  ( $V_f = 0.67V_{\text{drop}}$ ) and much less than in case  $D_1$  where the film volume is approximately equal to the droplet volume.

Regarding the film drainage dynamics during the crossing, in the case where the drainage is slow (high values of  $\lambda_{12}$ ), the grid resolution is fine enough to capture the drainage flow (see points 2 and 3 in Figure 42 and Figure 43). Obviously, this is not the case when fast drainage occurs. This is a limitation of numerical simulations to study this multi-scale problem due to the spatial resolution required to solve both accurately the droplet dynamics and film drainage flow. Such a limitation of DNS is well known, as discussed in the study of Bonhomme et al., 2012. However, the film at the top of the droplet is expected to have a negligible influence regarding the interface crossing problem, since it has a very small thickness and the pressure across this film can be considered as constant - the vertical pressure gradient in the film is only hydrostatic based on the lubrication theory - thus which does not impact the force balance acting on the droplet, as already confirmed by the excellent agreement, in static conditions, between theoretical predictions of eq. 22 and 23 of section 3.3.2 (also neglecting the influence of the thin film) and experimental data with solid particles (Pierson & Magnaudet, 2018). This allows to be also confident on the results obtained by the simulations on the interface crossing problem in dynamic conditions.

To conclude on this part, in crossing conditions at same  $Ar$  and  $Bo_{13}$ , we observe that a very viscous droplet ( $\lambda_{12} \gg 1$ ), even deformed, has a behavior similar to a solid-like droplet regarding column entrainment during the crossing and further detachment that takes place at the bottom of the column, whereas a moderate  $\lambda_{12}$  results in a more deformed droplet and enhances the drainage rate in the film due to the non-vanishing tangential velocity at the interface, leading to a column detachment firstly occurring at the droplet rear and to a smaller volume coating the droplet.

#### 4.5.2. Crossing time

When the drop reaches the interface with a non-zero velocity, it is slowed down (sometimes significantly), as illustrated in Figure 42, due to the resistance of the plane interface to deformation. In view of the development of a continuous encapsulation process, this slowing time is an important quantity to take into consideration because it fixes an upper limit for the droplets frequency of arrival at the interface. Indeed, the time between two successive drops arriving at the interface must be significantly larger than a characteristic time related to the crossing dynamics.

In case where the condition of crossing is not achieved, i.e. when the resisting forces of the interface overcome the drop inertial forces, the drop will bounce and its velocity will become negative before cancelling, then the drop will finally stand below the interface. In such condition, we have observed that the distance travelled by the drop above the level of the plane interface is always smaller than its diameter. Then, we define a crossing time  $t_{cr}$  as the time required for the droplet to travel a distance equal to its diameter  $d$ , after its center of mass reached the interface position, as illustrated in Figure 46.

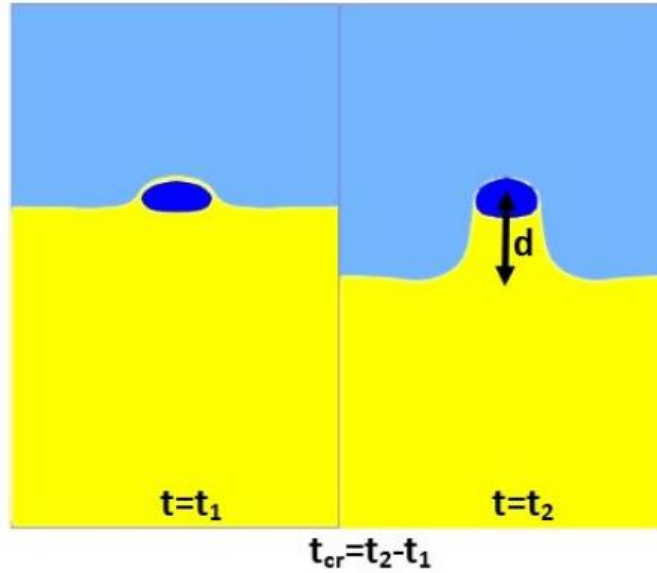


Figure 46: Illustration of crossing time criterion.

As shown in Figure 47, for either solid-like or deformable droplets, it is found that  $t_{cr}$  is well scaled by the arithmetic average of  $U_{max}$ , the drop maximal velocity prior to the interface (close to the terminal velocity in phase 1), and  $U_{min}$ , the minimal velocity reached after the slowing down when crossing the interface. This result turns to consider a linear behavior of the velocity in between the two extrema. The crossing time can therefore be predicted from the scaling of the two velocities  $U_{max}$  and  $U_{min}$ . This question will be addressed in section \ref{subsubsec:Dec\_Ekin}.

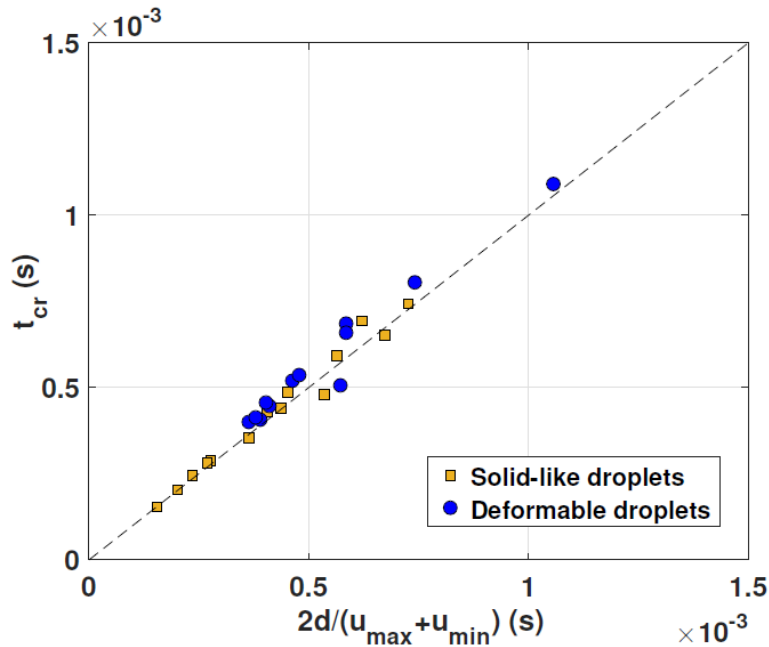


Figure 47: Crossing time  $t_{cr}^*$  as a function of  $2d/(U_{max}+U_{min})$  for both solid-like and deformable droplets.

### 4.5.3. Column maximal length

As clearly observed in Figure 42 and Figure 43, inertia modifies the extension of the entrained column of phase 1 in phase 3 during the droplet crossing: the higher the velocity at the interface, the larger the length of the entrained column. We define the maximal column length  $L_{max}$  as the distance between the droplet center of mass and the position of column detachment at the bottom of the column (see Figure 42) which always occurs even in cases for which the column rupture takes place before at the droplet rear. The scaling of this quantity is important because it scales the volume of phase 1 which doesn't stay attached to the drop when it comes to break, and is sent back to the interface under the form of drops. In real continuous process conditions, this phenomenon can be limiting since it leads to the formation of an emulsion that keeps on growing on the interface as the drops are continuously crossing the interface.

With the objective to characterize the driving force responsible for the film entrainment during drop crossing, two force ratios are defined. The first one,  $F^*$ , compares the importance of forces that push on the interface, which are both the drop apparent weight  $(\rho_2 - \rho_1) a_c \pi d^3/6$  and the dynamic pressure due to drop inertia  $\rho_2 U_{min}^2 \pi d^2$ , over the stress which tends to pull back the fluid entrained of phase 1 towards the 1-3 interface and defined by a gravity force at the scale of the drop volume  $(\rho_3 - \rho_1) a_c \pi d^3/6$ , leading to:

$$F^* = \frac{(\rho_2 - \rho_1)a_c d + 6\rho_2 U_{min}^2}{(\rho_3 - \rho_1)a_c d} = \frac{\xi_{12}}{\xi_{13}} \left[ 1 + 6 \frac{\rho_2}{\rho_2 - \rho_1} \frac{U_{min}^2}{a_c d} \right]$$

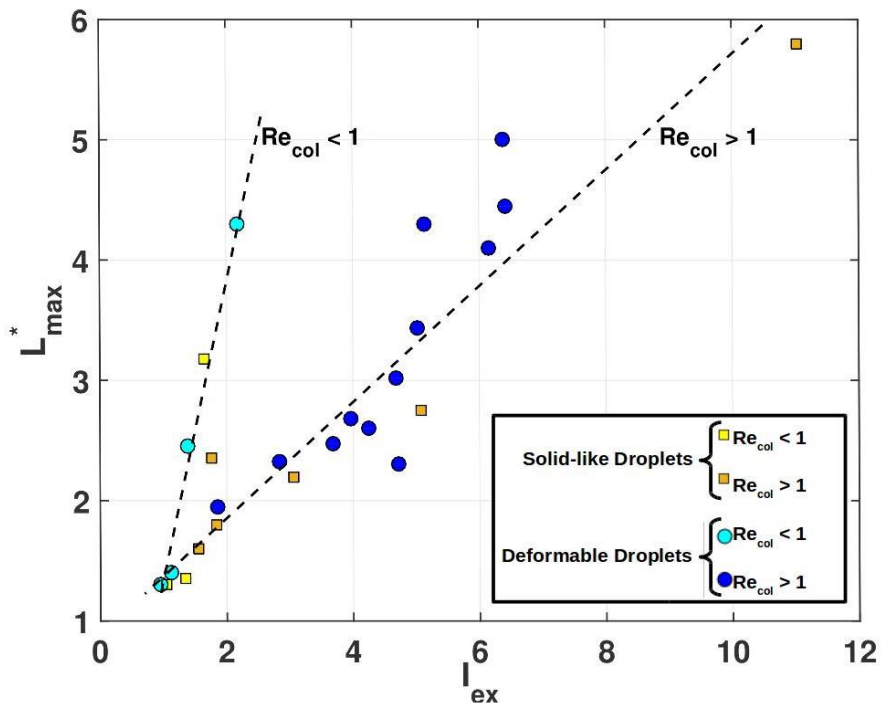


Figure 48: The mapping of non-dimensional maximal column length  $L_{max}^* = L_{max}/d$  as a function of the non-dimensional inertia excess  $I_{ex}$  for both non-deformable and deformable droplets. According to  $Re_{col}$ , two regimes of  $L_{max}^*$  are observed on the figure.

The parameter  $F^*$  is based upon  $U_{\min}$ , taken as the reference velocity in the film entrainment process in phase 3. It doesn't include any restoring surface tension force exerted by the film on the droplet, this force being assumed to be negligible once the crossing condition is achieved, which is fulfilled for all cases under consideration (i.e.  $\xi_{12}/\xi_{13} \geq f(Bo_{13})$ ). Once the drop (or particle) is reaccelerated in phase 3, the entrained film phase will unavoidably break due to the counter flow developing in the film, as evidenced by the velocity fields (see Figure 45). One part is entrained in the wake of the rising drop, one part is pulled back towards the plane interface due to gravity, leading to the column thinning and break-up and to the formation of a capsule of phase 1 around the drop. The second ratio represents the inertia excess with respect to the critical value for crossing in the static case, noted  $f(Bo_{13})$ :

$$I_{ex} = \frac{F^*}{f(Bo_{13})}$$

The normalized maximal column length  $L_{\max}^*$  is plotted against  $I_{ex}$  in Figure 48. For both drops and solid-like droplets,  $L_{\max}^*$  increases linearly with  $I_{ex}$ , and despite the scattering of the data (due to the limitation of the numerical resolution at the instant of film breakup), two distinct trends can be observed, which are not related to drop deformation but to the Reynolds number in the column flow ( $Re_{col}$  is based upon phase 1 properties, the drop velocity at the instant of detachment and the column average thickness). For cases with small values of  $Re_{col}$  (typically  $\leq 1$ ), the growth rate of  $L_{\max}^*$  is about 6 times larger than that observed with larger  $Re_{col}$  values, and this behavior is observed for both deformable and solid-like droplets. Even if  $Re_{col}$  is found to evolve linearly with  $Re_{\min}$ , it is not clear to understand how these two different regimes of film extension develop. In particular, at low inertia, the observation of a large growth rate of  $L_{\max}^*$  with  $I_{ex}$  is obviously due to a delay of the pinch-off formation behind the drop, possibly resulting from the viscous resistance of the column to deformation that would lead to longer and thinner columns before break-up. Such an effect is expected to be scaled by the film Ohnesorge number ( $Oh_{13}$  in Table 10): indeed,  $Re_{col}$  globally decreases with  $Oh_{13}$ . However, in all studied cases,  $Oh_{13}$  remains small (maximum value of  $Oh_{13}$  is 0.2), suggesting a limited influence of phase 1 viscosity on the deformation and breakup process of the column (added to the fact that, in most cases,  $\lambda_{13} = 1$ ). Moreover, the use of  $Oh_{13}$  to find a unique scaling law for  $L_{\max}^*$  was not successful, leading to exhibit these two different behaviors, which are both growing functions of the inertia excess  $I_{ex}$  and which depend on the flow regime in the column characterized by  $Re_{col}$ .

#### 4.5.4. Volume of the coating film

Whatever the column extension is, its breakage occurs at the rear of the droplet (even when column breakage first occurs at the bottom of the column, it is followed by a breakup event in the droplet wake region), leading to a volume  $V_f$  of film entrained around the droplet. This coating volume of phase 1 rapidly migrates towards the rear of the droplet due to buoyancy effects. The volume  $V_f^*$ , normalized by the droplet volume, has been determined for each case.

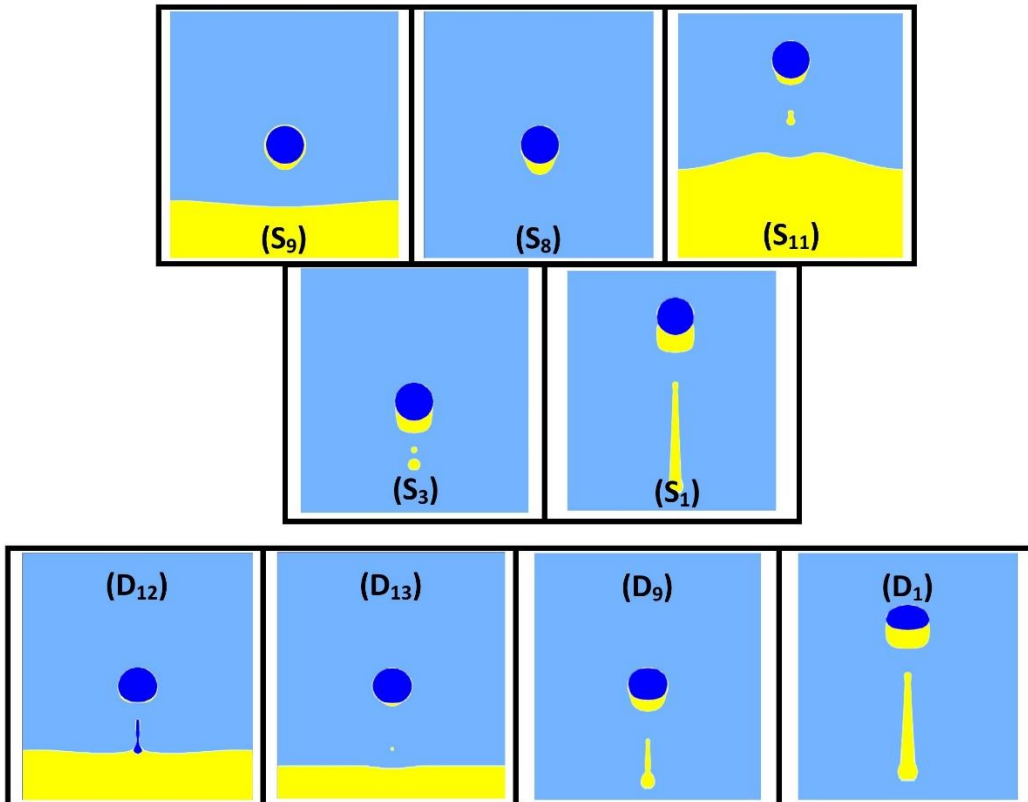
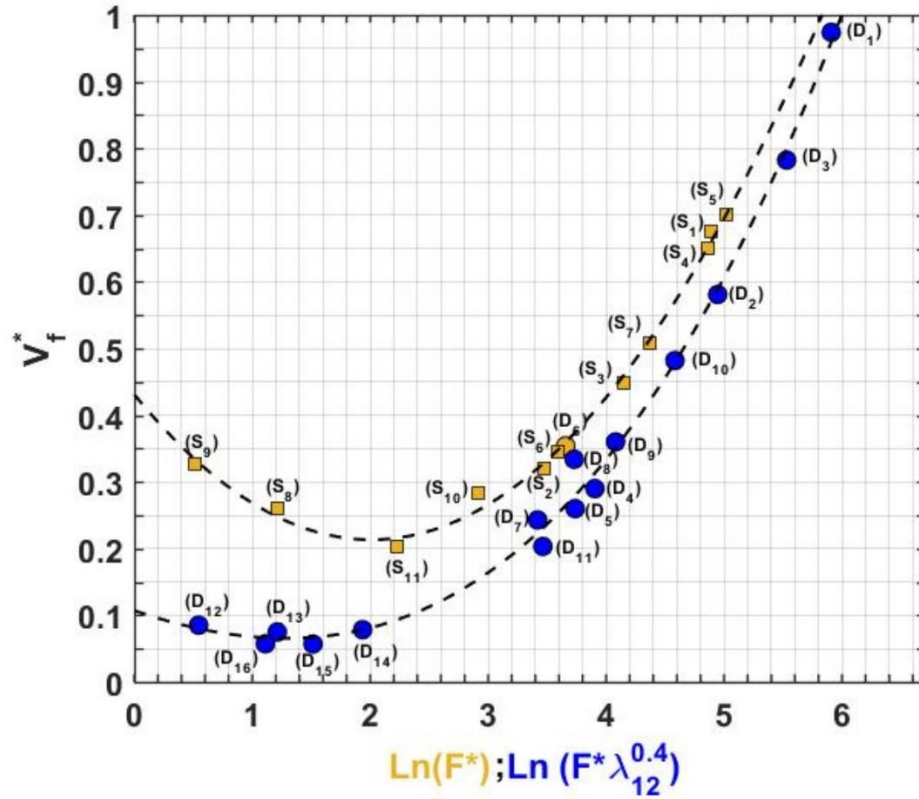


Figure 49: Dimensionless film volume  $V_f^* = V_f/V_{\text{drop}}$  as a function of parameter  $F^*$  in the case of solid-like droplets, and as a function of  $F^* \lambda_{12}^{0.4}$  in the case of deformable droplets. A series of screenshots of the phase indicator function at the instant of column detachment is also presented for some cases.

For solid-like droplets, Figure 49 reports the evolution of  $V_f^*$  as a function of  $\text{Ln}(F^*)$ . We first observe that film volume values are smaller than the particle or drop volume in the range of investigated parameters. These values remarkably well collapse on a single curve which can be fitted by a second order polynomial. It seems that the evolution goes through a minimum around  $\text{Ln}(F^*) \approx 2$ , with a sharp increase rate at high inertia and a slight decrease rate at low inertia. For deformable droplets, a similar trend is observed when plotting  $V_f^*$  as a function of the logarithm of  $F^*$  corrected by the viscosity ratio  $\lambda_{12}$  to the power 0.4. Such a correction is related to the film drainage rate kinetics around the droplet during rising: the higher  $\lambda_{12}$ , the slower the film drainage and the larger the remaining film volume at the instant of detachment. However, this effect of  $\lambda_{12}$  seems to be of importance for deformed droplets only. Indeed, one case of deformable droplet is not following this trend but that of solid-like droplets (case D<sub>6</sub>, orange circle symbol on the graph of Figure 49). This drop has a high viscosity ratio ( $\lambda_{12}=50$ ) but is weakly deformed at the time of column detachment (aspect ratio equal to 1.13), possibly explaining why this drop follows the trend of solid-like droplets. Therefore, the correction of  $F^*$  by  $\lambda_{12}^{0.4}$  probably reflects a more subtle coupling between film drainage and drop deformation. For both solid-like droplets and deformable drops, the film volume coating the drop seems to be controlled by inertia and not by surface tension forces. Of course, this is valid for particles or droplets crossing the interface, i.e. fulfilling the criterion  $\xi_{12}/\xi_{13} \geq f(\text{Bo}_{13})$ , and is confirmed by the fact that  $V_f^*$  is neither correlated to the interface Bond number,  $\text{Bo}_{13}$  or  $\text{Bo}_{13} (\xi_{12}/\xi_{13}-1)$ , nor to a droplet Weber number (based on  $\gamma_{13}$  and drop velocity at the minimum or at the film detachment). At high inertia, increasing inertia (i.e. increasing  $F^*$  or  $F^* \lambda_{12}^{0.4}$ ) favors the growth of the coating volume. It is interesting to note that the two curves of Figure 49 seem to merge in the limit of high inertia. At low inertia, but yet for crossing solid-like or deformable droplets, their respective behaviors diverge, the coating film being significantly smaller for deformed drops than for solid-like drops and the presence of a minimum is much less pronounced for deformable than for solid-like droplets. This observation calls for a deeper insight in the encapsulation process in this regime.

To that end, we have reported in Figure 49 some screenshots of the phase indicator functions field, immediately after that the film breakage occurred for a few cases corresponding to low and high inertia regimes, for deformable and solid-like droplets. The encapsulated volume can be visualized on these fields by the yellow ring around the blue droplet. Series S<sub>9</sub>, S<sub>8</sub> and S<sub>11</sub> correspond to increasing values of  $F^*$  for solid-like droplets in the low inertia regime ( $\text{Ln}(F^*) < 2$ ). For case S<sub>9</sub>, film volume is clearly composed of two significant contributions, one due to the film coating the top of the particle and one at the rear of the particle. With S<sub>8</sub>, the contribution of this film at the top has decreased compared to the bottom one and for case S<sub>11</sub>, the volume at the rear of the drop has increased due to increasing inertia, and keeps on increasing in cases S<sub>3</sub> and S<sub>1</sub> as  $F^*$  is increased. Hence, the presence of a minimum of  $V_f^*$  can be due to the relative weight of the film remaining at the top of the drop at the instant of detachment in low inertia conditions. This can be explained by the fact that the rate of film drainage coating the particle is an increasing function of inertia at the front of the droplet. Note that this effect is even emphasized in case S<sub>9</sub> due to the lower viscosity ratio  $\lambda_{13} = 0.1$ , compared to other solid-like drops case



series where  $\lambda_{13} = 1$ . To illustrate this effect of  $\lambda_{13}$  on the film drainage, we have reported in Figure 50 the axial velocity profile in the radial direction along the equator for the case  $S_9$ , at the instant of detachment. The continuity of tangential stresses at the interface imposes a strong gradient of velocity in phase 3 close to the interface (within the external boundary layer), making the velocity at the interface between the film and phase 3 to be quite small. This is a condition allowing a slow film drainage, in addition to the quasi null velocity at the drop surface.

Thus, a larger film thickness can be observed in cases where  $\lambda_{13} < 1$  (which is consistent with the results of Manga & Stone, 1995 at low Reynolds number).

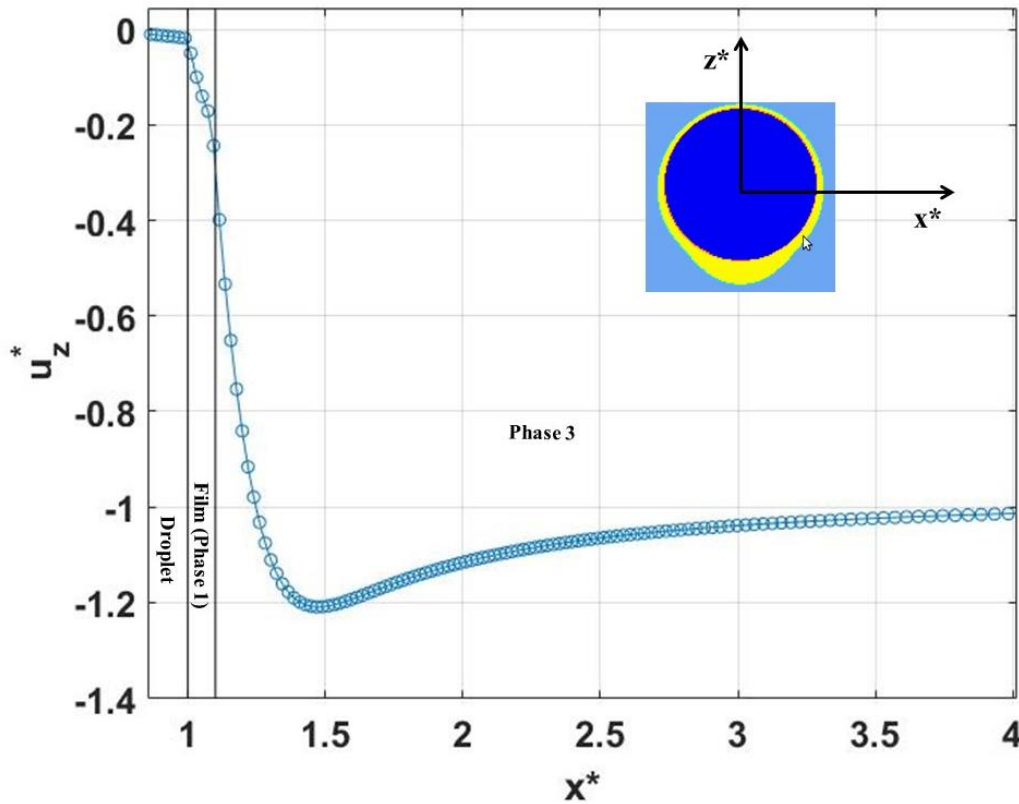


Figure 50: Profile of axial velocity (normalized by the instantaneous drop velocity) along the drop equator ( $z^* = 0$ ), for case  $S_9$ , in the droplet frame. Film thickness corresponds to 4 mesh points at this instant, still providing a reasonably accurate value for  $V_f^*$ .

In deformable drop cases ( $D_{12}$ ,  $D_{13}$ ,  $D_9$  and  $D_1$  series), such a contribution to  $V_f^*$  of the film coating the top of the drop seems to be strongly attenuated at low inertia, the film being drained to the rear of the drop before detachment occurred (see cases  $D_{12}$  and  $D_{13}$ ). Compared to the solid-like cases, smaller viscosity ratios  $\lambda_{12}$  (respectively equal to 1 and 5) accelerate the film drainage, leading to smaller encapsulation film volumes with a systematic small contribution of the drop top film. Note that for both cases  $D_{12}$  and  $D_{13}$ ,  $\lambda_{13} = 0.1$  as for  $S_9$ . However, deformation also seems to play a role in the film drainage at

low inertia. More precisely, the transition from an oblate to a prolate shape when the drop rises from the interface to the point of minimum velocity is thought to accelerate the drainage of the film from the top to the rear of the drop.

This effect induced by deformation can be observed for  $D_{13}$  in Figure 51, at  $Ar = 10$ , where the drop velocity falls to zero when crossing the interface, taking even small negative values due to the resistance force of the interface. Then, the droplet becomes elongated (prolate shape) when trapped at the interface, and even more elongated due to the strong reacceleration suddenly experienced in phase 3 (of lower viscosity than phase 1), until point 5 in the plot where it begins to flatten again (oblate shapes) during its rise in phase 3. Even though  $\lambda_{13} \ll 1$ , the screenshots clearly suggest that such a prolate shape will induce a strong downward flow inside the drop, which favors a faster drainage. Prolate shapes are always obtained in such cases of deformable droplets crossing the interface at low Reynolds number, which correspond to the lower values of  $F^*$  in Figure 51. Note that, in the simulations of Shopov & Minev, 1992 and in experiments of Bonhomme et al., 2012 in the case of bubbles trapped at a liquid-liquid interface, crossing regimes at low  $Re$  and  $Ar$  exhibited similar elongated shapes. On the contrary, at high values of  $F^*$  (cases  $D_9$  and  $D_1$  in Figure 49), the Reynolds and drop Weber number  $We_{12}$  being large, the drop is oblate before reaching the interface and during the crossing, as already discussed in Figure 44. Consequently, there is no acceleration of film drainage due to a change of shape and the evolution of film volume with inertia (corrected by  $\lambda_{12}^{0.4}$ ) is consistent to the trend observed with solid-like drops.

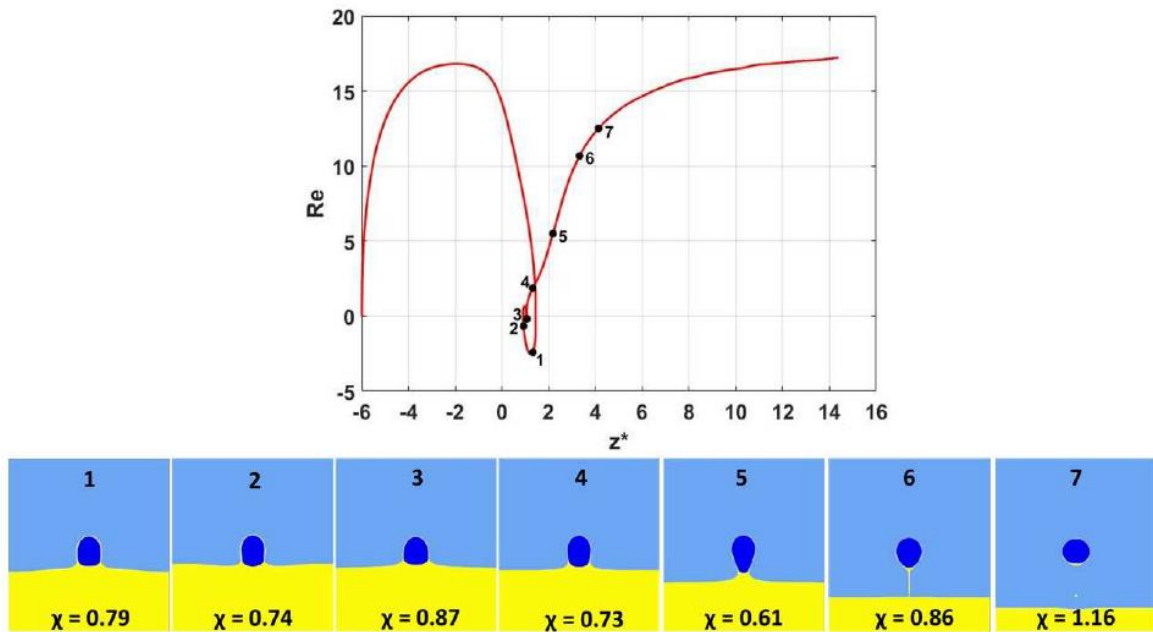


Figure 51: Evolution of the Reynolds number  $Re = \rho_1 u(t) d / \mu_1$  as a function of the centroid position for case  $D_{13}$ . Droplet deforms into a prolate shape when decelerating and reaccelerating in phase ( $\lambda_{13} = 0.1$ ). Screenshots correspond to the different positions indicated on the red curve with corresponding values of the aspect ratio.

4.5.5. Decrease in kinetic energy during crossing

Because the minimum velocity  $U_{\min}$  has been identified as a reference velocity for the scaling of film entrainment dynamics during crossing, the scaling of this quantity is requested. To this purpose, we have examined the normalized ratio  $\Delta E_k^*$  of kinetic energy variation between the minimum and maximum velocity values, accounting for the added mass coefficient dependence with deformation in the case of deformable droplets:

$$\Delta E_k^* = \frac{E_{k\max} - E_{k\min}}{E_{k\max}}$$

Where  $E_{k\max} = 1/2 (m_2 + C_{M\max} m_1) U_{\max}^2$  and  $E_{k\min} = 1/2 (m_2 + C_{M\min} m_1) U_{\min}^2$  are the total kinetic energy at the instant of respectively the maximal velocity and minimal velocity,  $C_{M\max}$  and  $C_{M\min}$  being the added mass coefficients at  $U_{\max}$  and  $U_{\min}$  for a displaced mass  $m_1$  of phase 1 and the mass  $m_2$  of the drop. For spherical droplets,  $C_M = 0.5$ , whereas for deformable droplets,  $C_M$  is a function of the instantaneous droplet aspect ratio (Lamb, 1932):  $C_M = \alpha_0 / (\alpha_0 - 2)$  with  $\alpha_0 = 2 (\zeta_0^2 + 1) (1 - \zeta_0 \cot^{-1}(\zeta_0))$  for prolate shapes and  $\alpha_0 = 2 (\zeta_0^2 + 1) \zeta_0 \cot^{-1}(\zeta_0) - \zeta_0^2$  for oblate shape, with  $\zeta_0 = (\chi^2 - 1)^{-1/2}$

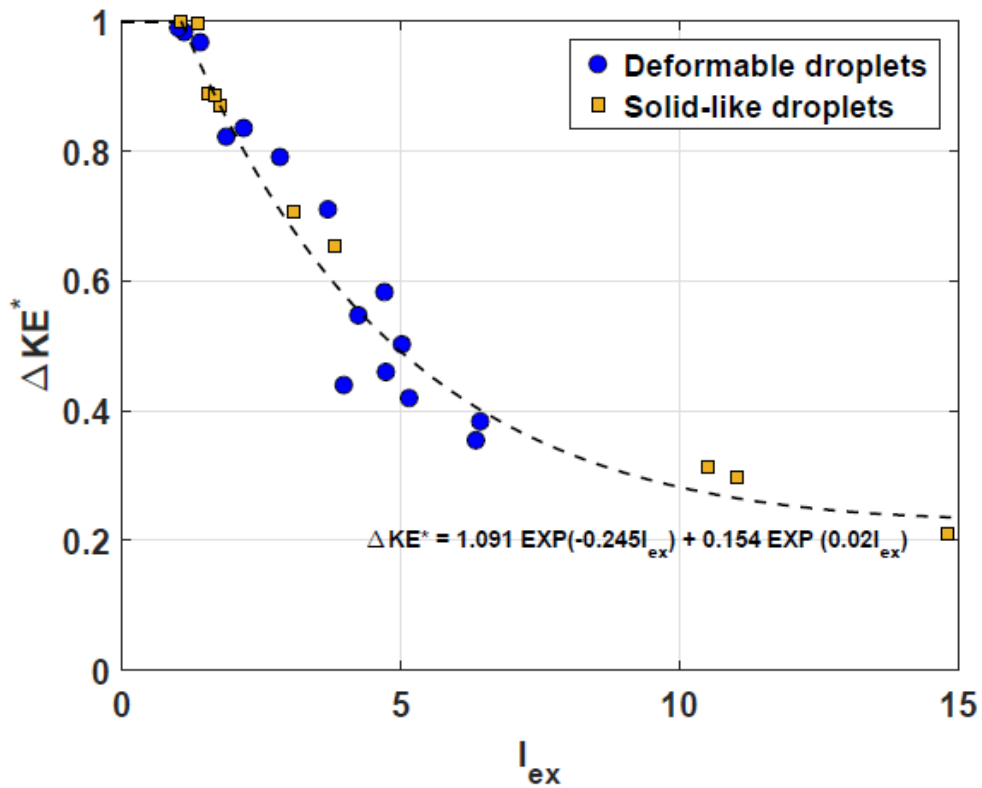


Figure 52: Kinetic energy variation ratio  $E_k^*$  as a function of inertia excess  $I_{ex}$ ; orange squares: solid-like droplets; blue circles: deformable droplets; dashed line is a double exponential fit of all points.

In Figure 52, the plot of the kinetic energy ratio  $\Delta E_k^*$  has been reported as a function of the excess of inertia  $I_{ex}$  for both rigid and deformable droplets. It can be observed that all points gather on a single master curve, which can be fitted by a double exponential decay, which tends to zero as the excess of inertia tends to infinity. This means that, as the inertia of the droplet increases with respect to the minimum needed to cross the interface, the droplet will not be slowed down at the interface ( $U_{min} \approx U_{max}$ ), the ratio  $\Delta E_k^*$  tends to vanish. On the contrary, at low  $I_{ex}$ , crossing dynamics will tend towards the static configuration (i.e.  $\Delta E_k^* = 1$ ), the initial kinetic energy of the drop motion below the interface being fully dissipated.

The fit of the curve of Figure 52 then provides an implicit relationship allowing to predict  $U_{min}$  for a given  $U_{max}$ . Note that it has not been considered that the added mass coefficient can increase depending on the distance between the drop and the interface (Milne-Thomson, 1962). However, the exact value of the added mass coefficient has only a small effect on the value of  $\Delta E_k^*$  here, because of the small density difference between the liquid phases. Finally, the maximum velocity  $U_{max}$  reached by the drop during its rising in phase 1 needs to be scaled, by being assumed to be the terminal velocity. For solid-like droplets, the force balance between buoyancy and drag sufficiently far from the interface leads to an implicit relation between  $Re_{max}$  and  $Ar$ :

$$Re_{max} \sqrt{\frac{3}{32} C_D(Re_{max})} = Ar \quad (1)$$

If we substitute in the equation (1) the Schiller and Naumann correlation (Schiller & Nauman, 1933) for the drag coefficient, we obtain:

$$Ar = \frac{3}{2} \sqrt{Re_{max}(1 + 0.15Re_{max}^{0.687})} \quad (2)$$

On Figure 53, the Archimedes number has been plotted as a function of right-hand side term of equation (2). It is a linear fit which deviates from the first bisector by a nearly constant factor of 14%. Even if Schiller and Naumann correlation (Schiller & Nauman, 1933) has some finite accuracy (a few percent), this deviation is more likely to be due to the fact that terminal velocity is not reached by solid-like droplets before interacting with the interface (the drops travel on a distance of  $3d$  in the simulations). A proof of that is given by case  $S_1$ , which has a maximum velocity below the interface of 0.8 m/s. When running the simulations on longer travel distances without the plane interface

(two-phase flow simulation), the terminal velocity found is 0.97 m/s and the corresponding  $Re_{max}$  value falls on the first bisector of Figure 53.

For deformable drops, the plot of  $Re_{max}$  as function of  $Ar$  displays a linear evolution in all range of parameters investigated (with a slope equal to 2.25). In this case, results cannot be compared with a well-known law of the drag coefficient inserted in equation (2). Moreover, because of viscous effects (from both internal and external phases), the response in deformation to the stress is always delayed and when the drop center of mass velocity reaches a plateau, the drop shape is not always steady and keeps on deforming, as already shown in Figure 43. However, the linear fit of Figure 54 suggests that the drag coefficient in equation (1) is nearly constant, as a consequence of two competing effects when increasing Archimedes number: increasing  $Re_{max}$  decreases  $C_D$  but also increases drop deformation which increases  $C_D$ . So the plateau reached by the drop velocity far from the interface corresponds to a regime where this balance between deformation and drag is reached, and seems to be independent of the instantaneous value of the deformation, which strongly increases during the drop rising until the interface. It is interesting to note that this linear behavior does not seem to be influenced by viscosity ratios  $\lambda_{12}$  or  $\lambda_{13}$ , and covers a wide range of drop deformation (aspect ratio varying between 1.2 and 2.5).

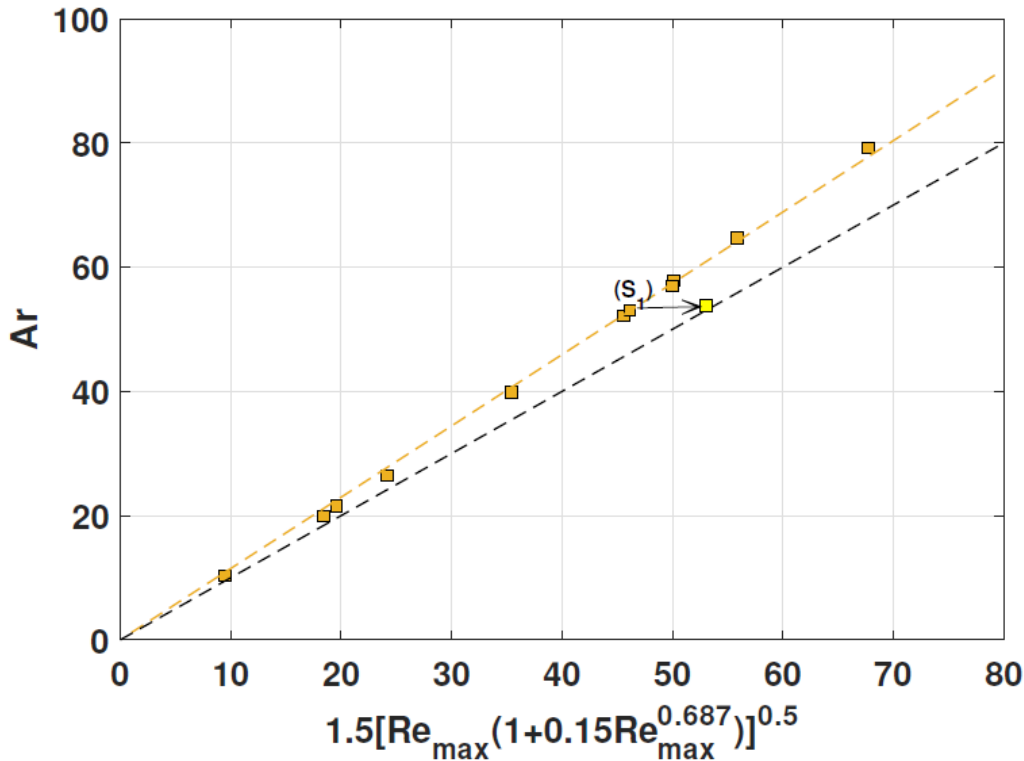


Figure 53: Archimedes number as a function of  $\frac{3}{2}\sqrt{Re_{max}(1 + 0.15Re_{max}^{0.687})}$  for solid-like droplets. Orange squares correspond to all solid-like droplets in the three-phase flow simulations, and the yellow square corresponds to  $S_1$  case in a two-phase flow simulation (i.e. without the interface) where the terminal velocity can be reached and fits with Schiller and Naumann's correlation (---).

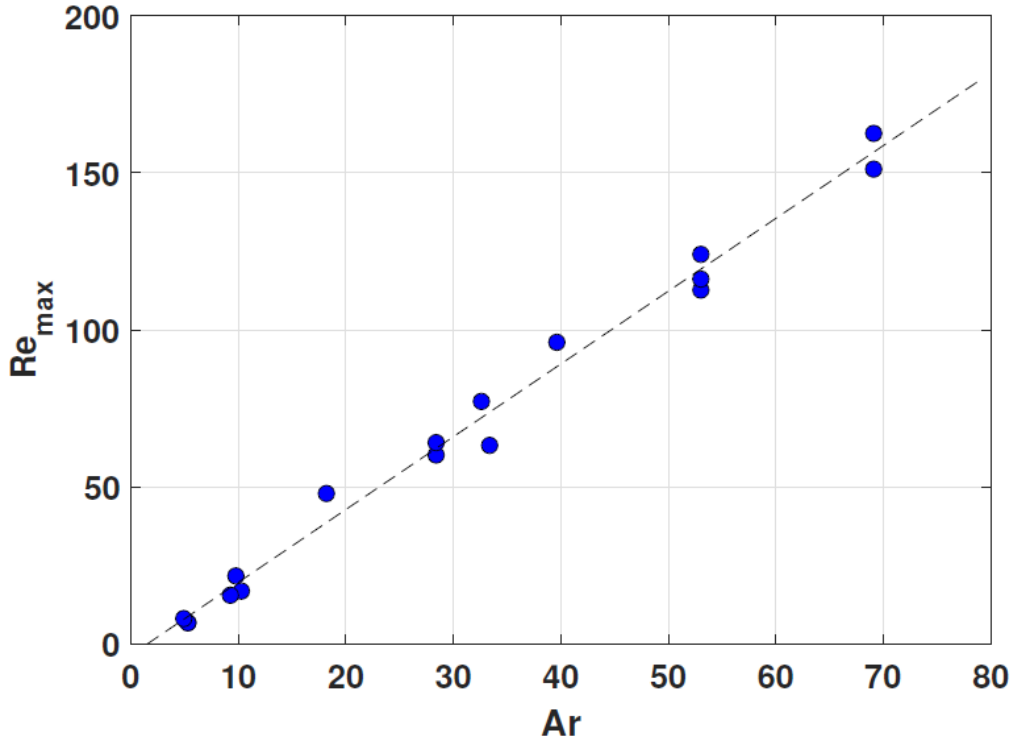


Figure 54: Maximum Reynolds number as a function of Archimedes number for deformable droplets. Dashed line represents a linear fit.

To summarize,  $U_{\max}$  can be scaled with Archimedes number  $Ar$  for both solid-like (Figure 53) and deformable droplets (Figure 54) and  $U_{\min}$  can be deduced from  $U_{\max}$  through a known function of  $I_{\text{ex}}$  (Figure 52). This scaling gives access to the prediction of the different quantities relevant for the encapsulating process in a wide range of flow parameters in inertial regime.

#### 4.6. Concluding remarks and prospects

In this work, the study of a drop crossing a liquid-liquid interface under the action of a centrifugal field has been undertaken by means of resolved numerical simulations. The investigated conditions for crossing correspond to an inertial regime in phase 1 ( $10 < Re_{\max} < 200$ ). Two types of drops have been studied: solid-like droplets with a high internal viscosity and surface tension, mimicking rigid particles, and deformable droplets. The Level-Set method used in the simulations has been first validated in two-phase flow configurations (i.e. without the planar interface) by comparing the computed terminal velocity of non-deformed drops at vanishing Weber number and the drop aspect ratio at higher Weber number with existing results in the literature. As three-phase flow validation, the crossing criterion of an interface by a solid-like droplet in static conditions (i.e. starting from the interface without initial velocity) have also been successfully compared to a

theoretical model based upon the balance between gravity and surface tension forces. Then, an extensive number of simulations have been run in crossing conditions for both solid-like and deformable drops, covering a wide range of the seven non-dimensional parameters describing this problem. The main results of this study can be summarized as follows:

- the influence of an impact velocity (maximum velocity  $U_{\max}$ ) of the drop, close to its terminal velocity, on the criterion for crossing the interface turns to double its apparent weight, resulting in a slight shift of the theoretical criterion in static conditions towards lower Bond numbers of the liquid-liquid interface ( $Bo_{13\text{eq}} = Bo_{13}/1.59$ ). As a consequence, the static condition criterion is still a relevant reference of the minimum inertia required for a drop to cross a liquid-liquid interface, for both solid-like and deformable droplets;

- in dynamic crossing conditions, the drop velocity during crossing always goes through a minimum velocity  $U_{\min}$  which is used as a reference velocity to scale inertia additional to the drop apparent weight;

- during crossing, film entrainment of the lighter phase by the drop leads to the formation of a column that extends and thins as it is pulled by the drop in phase 3, which ends to break behind the drop, leading to the formation of a volume coating the drop. The main mechanism responsible for the breakup of the entrained column is the competition between inertial force that makes the drop rise in phase 3 and the centripetal force acting on the lighter column phase that pulls it back in the opposite direction towards the interface. In order to characterize the film entrainment and the coating volume, these observations lead us to define two non-dimensional parameters: the first is based on the ratio of these two forces (noted  $F^*$ ) and the second corresponds to the first one rescaled by the criterion of crossing in static conditions (named inertia excess, and noted  $I_{\text{ex}}$ );

- the maximum column length at breakup linearly evolves with inertia excess, but with two distinct growth rates depending upon the Reynolds number in the film column, independently of deformation. Higher growth rate corresponds to viscous flows in the column. The transition between these two regimes is not yet elucidated;

- for solid-like droplets, the coating film volume  $V_f^*$  is remarkably well described by the force ratio  $F^*$ , exhibiting a minimum for increasing  $F^*$ , which originates from the contribution of the film volume on the top part of the particle which is non-negligible at low inertia. For deformable droplets,  $V_f^*$  is also very well described by  $F^*$  provided it is corrected by the viscosity ratio  $\lambda_{12}$  between the drop and the film phase to the power 0.4, which has a strong impact on the tangential velocity at the drop surface then on the film

drainage rate (in the range of investigated parameters with  $0.05 \leq \lambda_{13} \leq 1$ , note that the viscosity ratio  $\lambda_{12}$  has a greater influence on  $V_f^*$  than  $\lambda_{13}$ ). At low inertia, the coating volume is much smaller for deformable than for solid-like drops. This is promoted by two effects: first is the lower  $\lambda_{12}$ , second is the oblate-prolate shape transition observed during crossing between the interface level and the location of  $U_{\min}$ , both effects tending to accelerate the film drainage during the drop rising in phase 3, leading therefore to minimize the film volume attached to the drop;

- the ratio between  $U_{\max}$  and  $U_{\min}$  can be scaled by a unique function of  $I_{ex}$ .

The whole results make possible the prediction of the critical condition and dynamics of crossing, maximum column length entrained and coating volume for solid-like as well as for deformable droplets in a rather large range of flow parameters.

Prospects of this study will address the comparison of the numerical results with experimental data. Then, with the objective to develop an efficient encapsulation process based on interface crossing, surfactants are necessary to stabilize the encapsulated droplet, in order to make it resisting to breakup while the drop is rising in the phase 3. An analyze of the influence of surfactants, adsorbed at the liquid-liquid plane interface, on the crossing dynamics and encapsulation volume seems therefore to be highly relevant to continue this work.



# **Chapter 5:**

Experimental Approach:  
Material & Methods

# Chapter 5: Experimental Approach: Material & Methods

In this chapter, we first explain the conception of the experimental device and the methodology for image processing and analysis. Then, we give the chemical products that will be used in the experimental study with their corresponding characteristics and parameters.

## 5.1. Description of the experimental prototype

The experimental device (Figure 55-Figure 56) consists of two cells connected by a capillary tube: the encapsulation cell containing the two continuous phases (phase 1 and phase 3) and the reservoir cell containing the dispersed phase (phase 2) to be injected inside the encapsulation cell while rotating. In order to make the two cells rotate at a precise high speed of rotation securely, the whole assembly is inserted in the place of the mandrel of the bowl of a spin coater (SPIN150i) marketed by the company SPS. The experimental device consists also of a pressure regulator (OB1 MK3) supplied by ELVEFlow, a high speed camera (Miro Lab320) provided by Vision Research with a microscope (M651) supplied by LEICA, a PHLOX LED panel with Gardasoft RT lighting control technology which permits a precise pulsative overdriving of the LED lightening intensity in order to provide a sufficient amount of light especially at high speeds of rotation, and a delay generator capable of synchronizing image acquisition with the arrival of the cell to the camera observation window. Figure 1 shows a 2D scheme of the installation with all the mentioned elements, and figure 2 shows a zoom image which explains the circulation of fluids and presents more details.

### 5.1.1. The two cells and the spin coater

The two cells: reservoir and encapsulation are connected by a very small and very fine capillary fused Silica capillary tube supplied by Postnova (from 100 to 530  $\mu\text{m}$  inlet diameter), of length  $L= 12$  cm and with inlet and outlet diameters kept among values shown in Table 11. The capillary tube is very fragile and it must be handled with a lot of care. The spin coater holding the whole assembly permits a secured and controlled rotation, thanks to its rotation speed controller, at a speed up to 12000 rpm with an accuracy of  $\pm 0.1$  rpm. The assembly is fixed by screw and nuts and supports in the place of the mandrel found at the bowl of spin coater, so it is removable if needed for cleaning of cells change purposes, reader can refer to Appendix A for more construction details. Finally, given the high speeds of rotation, it is essential to have a balanced system. The two cells must have the same

mass, so we made the choice to use the balancing system with one cell (reservoir cell) being a feeder cell related to the encapsulation cell which in turn related.

	Tube 1	Tube 2	Tube 3	Tube 4
$D_i$ [ $\mu\text{m}$ ]	100	250	320	530
$D_o$ [ $\mu\text{m}$ ]	190	365	435	660

Table 11: Different capillary tubes used in experiments and their corresponding size.

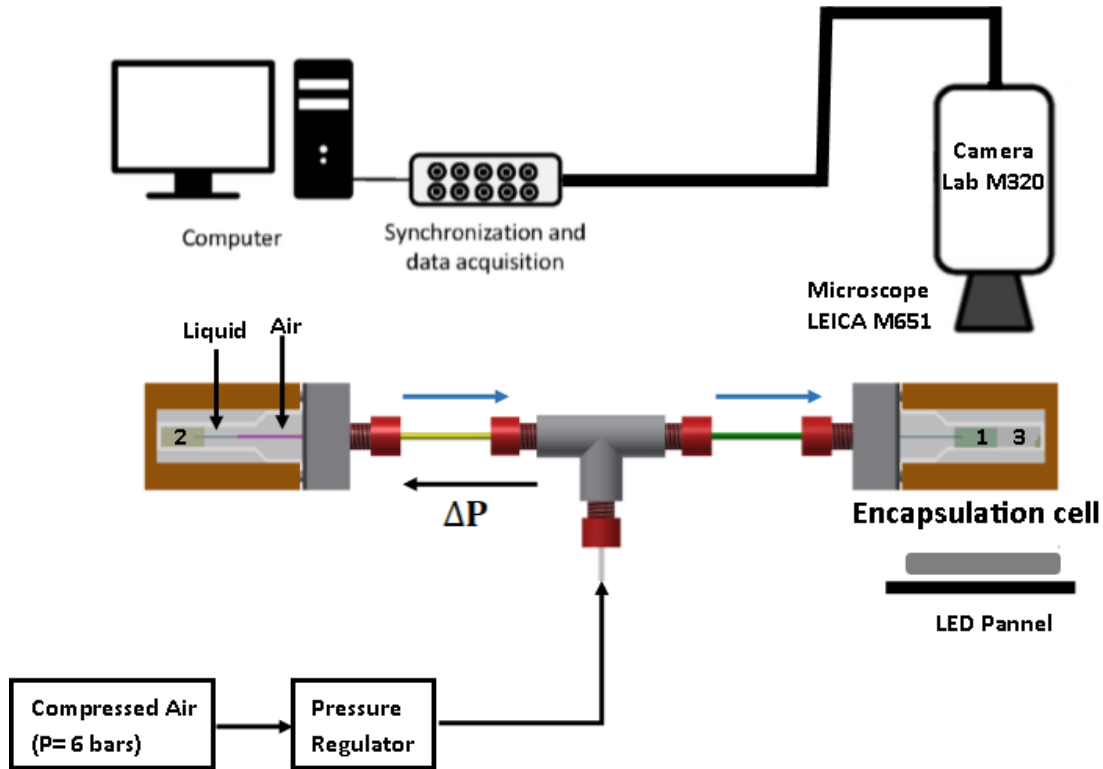


Figure 55: A scheme of the two cells connected by a capillary tube. The black arrow represents the flow of compressed air, while blue arrows shows the flow of phase 2 (phase to be injected). Air circulates through the purple capillary tube of the reservoir cell, and through the blue one, phase 2 circulates.

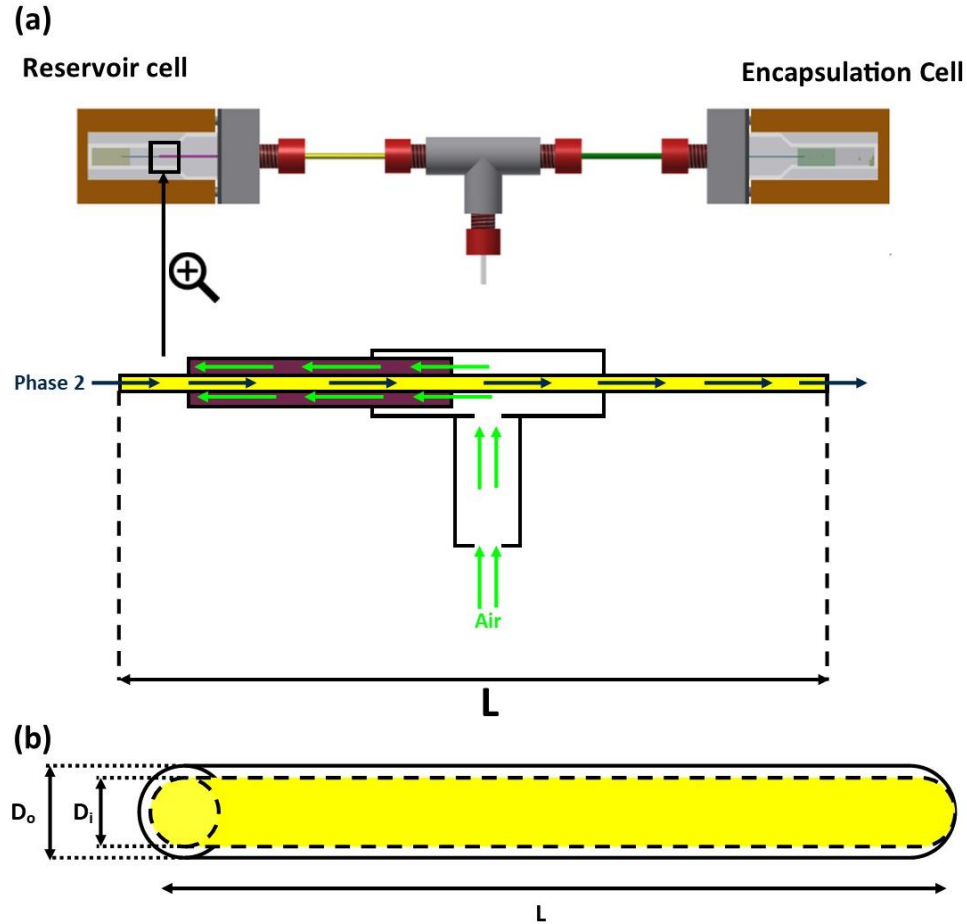


Figure 56: (a) A scheme showing the circulation of the compressed air from the axis of rotation to the capillary tube in purple and finally to the reservoir cell, and the circulation of phase 2 inside the capillary tube as an effect of overpressure from the reservoir cell through the capillary tube in yellow and finally to the encapsulation cell. (b) The dimensions of the capillary tubes.

### 5.1.2. The role of pressure regulator

The hydrostatic pressure balanced between the two cells, so in order to inject and form droplets of phase 2 (reservoir cell) inside the encapsulation cell and through the capillary tube, a slight overpressure must be generated in the reservoir cell. Starting from a speed of rotation  $N \approx 1530$  rpm, the pressure inside the cell becomes of the order of 1 bar, so the overpressure must have a higher value, yet very precise since the head loss which is necessary to overcome is small. However, despite the precision of the regulation of the flow, sometimes higher overpressure increases the flow rate inside the capillary tube to a limit the drop regime changes to a jet regime (Figure 57). A correlation for the critical flow rate at which the jet forms was derived in the study of Scheele (Scheele & Meister, 1968), in present notations it is expressed in equation (1). The small order of magnitude of the head loss makes it difficult to find the exact value of the overpressure which permits the circulation and dripping of the fluid at the same time, so finally we will find

this value by trial and error. In addition, a small leakage in the injection cell is necessary in order to avoid cell breakage due to increased pressure, which makes the pressure control more difficult.

$$Q_{jet} = 1.36 \sqrt{\frac{\gamma_{12} D_i^3}{\rho_2} \left(1 - \frac{D_i}{1.24 V_2^{1/3}}\right)} \quad (1)$$

$V_2 = \frac{\psi_H \pi D_i \gamma_{12}}{\Delta \rho_{12} a_c}$  is the volume of the droplet that would have formed if jetting did not occur, and  $\psi_H$  being the Harkin correcting factor with an empirical correlation (2) written in the papers Heertjes et al., 1971 and Lando & Oakley, 1967.

$$\psi_H = [0.92878 + 0.87638K - 0.261K^2]^{-1} \quad (0.6 < K < 2.4) \quad \dots (2)$$

$$\psi_H = 1 - 0.66023K + 0.33936K^2 \quad (0 \leq K \leq 0.6)$$

$$K = \frac{D_i}{V_2^{1/3}}$$

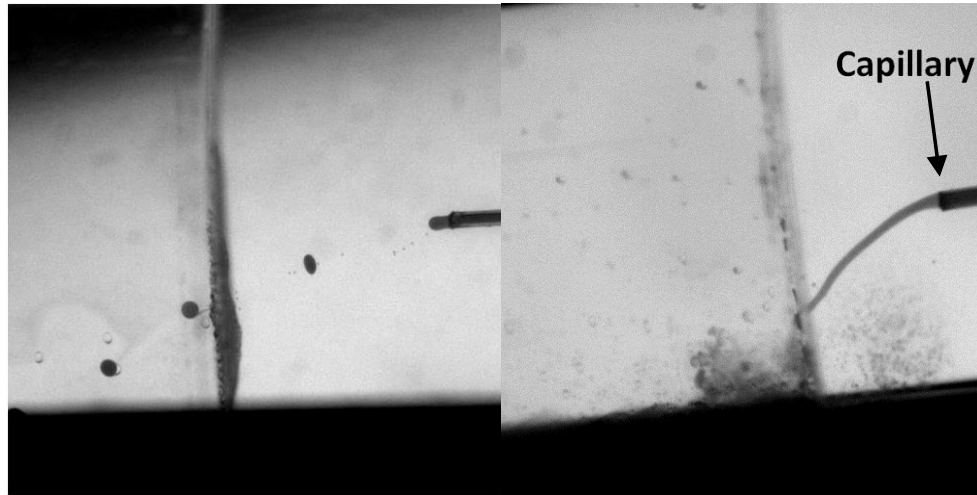


Figure 57: Left hand side, dripping regime of phase 2 by the capillary tube inside phase 1. Right hand side, jet injection regime of phase 2 by the capillary tube inside phase 1 due to high overpressure value. The black region corresponds to the support holding the cell, so the line between the black region and the grey one is the cell wall, and the line perpendicular to the cell wall is the interface.

The pressure regulator (ELVEFlow), connected to compressed air at 6 bars, allows a fine tuning of this overpressure: from 0 to 6 bars with an accuracy of 2 mbar. The value adjusted at the outlet will be the value of air pressure which arrives to the spin coater through the center of the rotating support (Figure 55 and Figure 56). The coaxial capillary tube colored in purple in Figure 56 (larger than the tube connecting the two cells), only connected to the reservoir cell through the T-junction assures the circulation of compressed air causing the overpressure. Finally, if the overpressure is optimized, droplets will be injected continuously inside the cell (Figure 57), and they will be filmed whenever the rotating cell

passes by the observation window of the fixed high speed camera. We note that, the injection cell contains a small leakage which allows venting and the exit of air during injection, which eliminates the pressure stress exerted on the encapsulation cell during injection. However, as injection continues and air continues in exiting the cell at some point a volume of phase 1 will exit the cell which will displace the initial position of the plane interface (Figure 58).

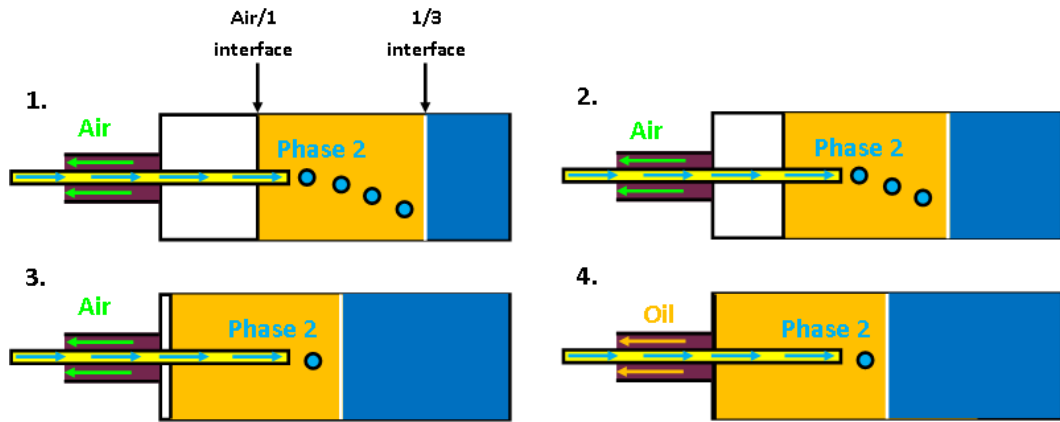


Figure 58: Scheme of the evolution of the displacement of the Air/phase1 interface (Air/1), and the L/L interface (1/3) as droplets are injected inside the encapsulation cell. 1. The first injections with the interfaces are not shifted yet, 2. After certain number of droplets injected, the interface is shifted while air exits the cell through the venting of a larger coaxial capillary which shifts the air/1 interface. 3. Injection continues and the shift of the interfaces continues in the same manner as 2, with a small quantity of air still inside the cell. 4. No more air inside the cell and the oil starts exiting the cell.

### 5.1.3. Image Acquisition

The device is equipped with a high speed camera (Miro Lab 320) installed perpendicular to the plane of the spin coater, which allows to observe what happens in real time inside the encapsulation cell during manipulation, and thus to record with high precision and images quality, the four steps of the process. Since the camera is fixed and the cells rotate, in order to record images of the experiments it is necessary to synchronize the triggering of the camera with the passage of the encapsulation cell and also with the overdriving pulses of the light source, so as the cell passes by the observation window of the camera, a top signal is generated indicating to the camera to start capturing images and to the LED panel lighting intensity to overdrive simultaneously, the top signal is adjusted manually through a delay by trial and error. Finally, one has to make sure that at each turn, one has enough images to determine the speed of a drop at a given position with a good precision.

The frame rate of the camera is between 1380 frame per second (fps) for a full resolution (1920\*1200 pixels) and 19600 fps for a resolution 384\*288 pixels, Table 13 shows the

maximum frame rate (FPS) for each resolution. The maximum shutter speed of the camera is  $1/10^6$  s, which corresponds to an exposure time  $t = 1 \mu\text{s}$  permitting able to capture sharp images until  $N = 3600$  rpm thanks to the increased intensity of lighting, above this rotation speed, the images quality won't be excellent. The optimum magnification which permits to visualize the injection and crossing of the droplets with their micrometric size range has an observation window of  $12^\circ$  out of the  $360^\circ$  complete turn of the injection cell (Figure 59). So, we are able to observe the phenomenon in the cell only for  $1/30$  of each turn, so in order to increase the probability of observing each event (formation, rising, crossing...), we need to inject droplets continuously and as much as possible.

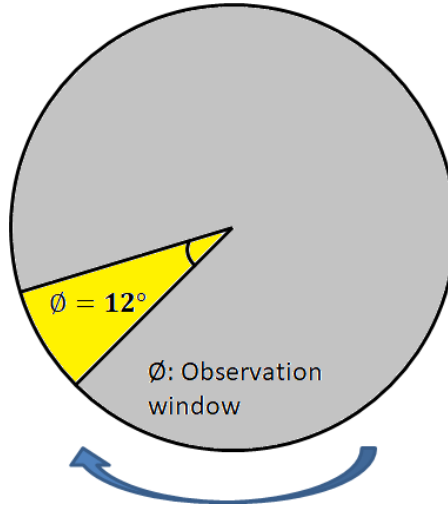


Figure 59: The complete tour with the observation window accessible by the camera colored in yellow.

Moreover, for a fixed observation window ( $12^\circ$  in our case), and at a certain speed of rotation, a higher resolution permits a better observation of the cell and better quality, yet lower resolutions increase the maximum frame rate of the camera. This means that in the passage time of the cell by the observation window, the camera is capable of capturing more images at a reduced resolution. However, at a fixed resolution the higher the speed of rotation, the shorter the passage time of the cell by the observation window, and therefore, less number of images captured per turn. Table 12 illustrates the relation between the **resolution, image quality, and frame rate, and number of images per turn** alongside with the relation between the **speed of rotation, passage time, and number of images per turn**. In order to find the optimum acquisition condition, a compromise must be searched between the resolution and the speed of rotation in order to save enough number of images per turn with a good quality.

For example, at the full resolution ( $1920 \times 1200$ ), the maximum frame rate of the camera is 1380 fps equivalent to  $\Delta t \approx 725 \mu\text{s}$  as a time between two consecutive images. For a rotation speed of 2750 rpm, the passage time by the observation window  $t_{\text{obs}}$  becomes smaller than the time between two consecutive images, so that only one image can be taken

per turn, which is not enough to access to the velocity of the droplet. Table 14 shows the number of images per turn for different speeds of rotation.

Resolution increasing				
<b>Constant speed of rotation</b>	Constant passage time	+ Quality	- Maximum Frame rate	- images/turn

Speed of rotation increasing				
<b>Certain Resolution</b>	Constant Maximum frame rate	Constant Quality	- passage time	- images/turn

Table 12: The relation between the resolution, image quality, the frame rate, and the number of images per turn alongside with the relation between the speed of rotation, passage time, and number of images per turn.

Resolution	FPS
1920*1200	1380
1920*1080	1540
1152*1152	2250
1024*1024	2780
1280*800	2960
1280*720	3280
640*480	8490
512*512	9330
384*288	19600

Table 13: The maximum frame rate per second (FPS) corresponding to different image resolutions.

Starting from a resolution of 384\*288 and less, the observation of the whole cell becomes impossible, even with the higher magnification of the microscope, a small part of it only appears instead. We look, to find an optimum resolution which has a maximum frame rate permitting to take the most possible number of images per turn at 3600 rpm (optimum case for the constraint of exposure time), while observing the whole cell. Finally, we propose the resolution 512\*512 as an optimum resolution where its maximum frame rate permits the acquisition of 4-5 images per turn at 3600 rpm, which is the highest number of images for a resolution permitting the visualization of the whole cell. With this resolution, the final spatial resolution of the image will be 43.83 pixel/mm.

Resolution	FPS	Images/turn				
		600 rpm	1200 rpm	2400 rpm	3600 rpm	5400 rpm
1920*1200	1380	4.6	2.3	1.15	0.77	0.51
1920*1080	1540	5.1	2.57	1.28	0.85	0.57
1152*1152	2250	7.5	3.75	1.875	1.25	0.83
1024*1024	2780	9.26	4.63	2.32	1.54	1.03
1280*800	2960	9.86	4.93	2.47	1.64	1.09
1280*720	3280	10.93	5.47	2.73	1.82	1.21
640*480	8490	28.3	14.15	7.075	4.71	3.14
512*512	9330	31.1	15.55	7.775	5.18	3.45
384*288	19600	65.3	32.67	16.33	10.9	7.26

Table 14: The maximum number of images per turn as a function of the resolution at a speed of rotation 3600 rpm



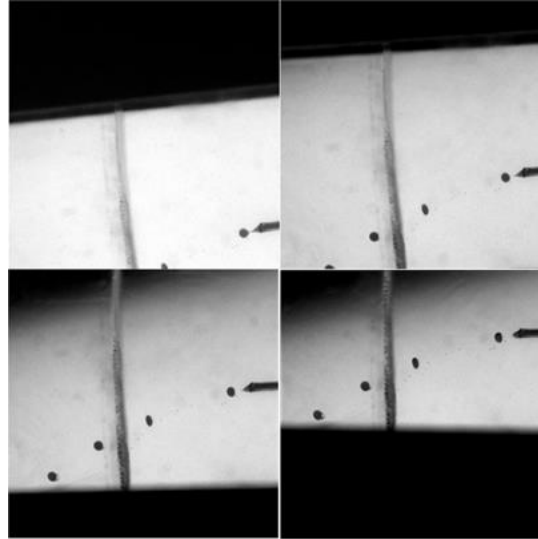


Figure 60: The four different positions of the cell visualized during one tour. From right to left then up to down:  $n_{pos}$ : 1, 2, 3, 4.

## 5.2. Image Processing Methodology

With the aim of process development and determining the operating parameters for size control, interfacial crossing, and film entrainment, it is indispensable to determine the injected droplet size, form, trajectory, and velocity. These information are accessible through image processing, where the droplets center of mass can be detected by **Hough transform**, which gives the precise Cartesian coordinates of the droplet in the camera frame of reference which we call reference (IM) with point O(0,0) being its origin (Figure 61). Figures of experiments shown in this descriptive part correspond all to the same experimental example which has the parameters shown in Table 15.

Phase 1	Phase 2 (Drop)	Phase 3	N (rpm)	d ( $\mu\text{m}$ )
<b>Silicone oil</b> $\mu=0.005 \text{ Pa}\cdot\text{s}$ $\rho=913 \text{ kg}\cdot\text{m}^{-3}$	<b>Sucrose in Water solution <math>[\eta]_m= 25\%</math></b> $\mu=0.0024 \text{ Pa}\cdot\text{s}$ $\rho=1081 \text{ kg}\cdot\text{m}^{-3}$	<b>Water with SDS surfactant</b> $\mu=0.001 \text{ Pa}\cdot\text{s}$ $\rho=997 \text{ kg}\cdot\text{m}^{-3}$	3600	367

Table 15: The parameters of the experimental example appearing in the figures of this part.

The detection of the same droplet in different image positions during the same tour allows to calculate the droplet displacement, and consequently its velocity at a given position. This droplet displacement is calculated precisely through the **cross-correlation function**. **Contour Processing** allows to detect the form of the droplet which is probably deformed and can be fixed by an ellipse in order to determine its equivalent diameter. The interface position in each turn is detected by analyzing the variation on grey level profile along the capillary axis.



Figure 61: The centers of mass of droplets detected by Hough transforms with their corresponding coordinates in the reference of the image shown on top of the image.

In the following sections we will discuss the details of the different techniques used in the image processing procedure, in particular: Hough transform for center of mass, cross-correlation function to calculate the droplet speed, Contour treatment, and the detection of interface position.

### 5.2.1. Trajectory Detection: Hough transform and frame of reference

The Hough transform, initially invented by Paul Hough in 1962 (US patent: US3069654A) is a feature extraction technique with applications in image analysis, computer vision, and digital image processing. The classical Hough transform was used first to determine lines in the image, but then it was extended to other arbitrary shapes, such as circles or ellipses. The “Generalized Hough transform” as it is universally used today was invented by Richard Duda and Peter Hart in 1972. Reader can refer to the patent of Paul Hough and the paper of Ballard published in 1981 for further information (Ballard, 1981).

The Hough transform used in our methodology returns the coordinates of the droplet centroid in the image reference, with an estimation of the equivalent diameter corresponding to a sphere. The detection of all droplets in all tours allows us to trace a trajectory for each capillary or cell position. Figure 62 shows the positions of the center of mass of all droplets in each image position of the example shown in Figure 61.

In order to plot a unique trajectory for all droplets detected in different positions, the fixed frame of reference must be transformed into a rotating frame of reference, with change of origin from O to capillarity tube outlet called O' with reference axis x' collinear with the capillarity tube axis. So, we need first to detect the coordinates of the capillarity tube outlet in each image position reference.

In order to detect the position of the capillary, a simple method is applied, the first step is to choose manually the position of its vertex in image position 1. This chosen point is cross-correlated (the explanation of the cross-correlation function can be found in the next section) with the next image position, in order to calculate its displacement. With this displacement, the coordinates of the capillary tube vertex is precisely detected in the next position, and in the position after in the same manner. The same procedure is repeated for the second vertex of the capillary tube outlet, and the midpoint of the two detected vertices in each image is the new origin of the coordinate system  $O_i$   $i=1, 2, 3, \dots, n$  with  $i$  being the image position (Figure 64). The origin of the coordinate system is changed from point O to  $O_i$  and all coordinates of droplet centers of mass are translated with changing the direction of the x-axis. Now, the four trajectories detected in Figure 62 have the same origin, yet in order to obtain a unique trajectory of the droplets, a rotation of the axis must be performed to have a common frame of reference for all image positions. The change of axis to be done is demonstrated in Figure 64, so the final step of rotation will be to detect the angle between the two frames of reference. The two transformations: the translation to bring the points to the same origin, and the rotation of the coordinate are summarized in the following equation (3):

$$X' = R_i \cdot (X_i - X_{O'_i}) \quad (3)$$

With  $i=1, 2, 3, \dots, n$ , where:

- $X' = \begin{pmatrix} x' \\ y' \end{pmatrix}$  is the matrix of the coordinates in the new common frame of reference.
- $X_i = \begin{pmatrix} x_i \\ y_i \end{pmatrix}$  is the matrix of the coordinates in the frame of reference (IM).
- $X_{C_i} = \begin{pmatrix} x_{O'_i} \\ y_{O'_i} \end{pmatrix}$  is the translation matrix with  $x_{O'_i}$  and  $y_{O'_i}$  are the coordinates of point  $O_i$ .
- $R_i = \begin{pmatrix} -\cos \delta_i & \sin \delta_i \\ \sin \delta_i & \cos \delta_i \end{pmatrix}$  is the rotation matrix.

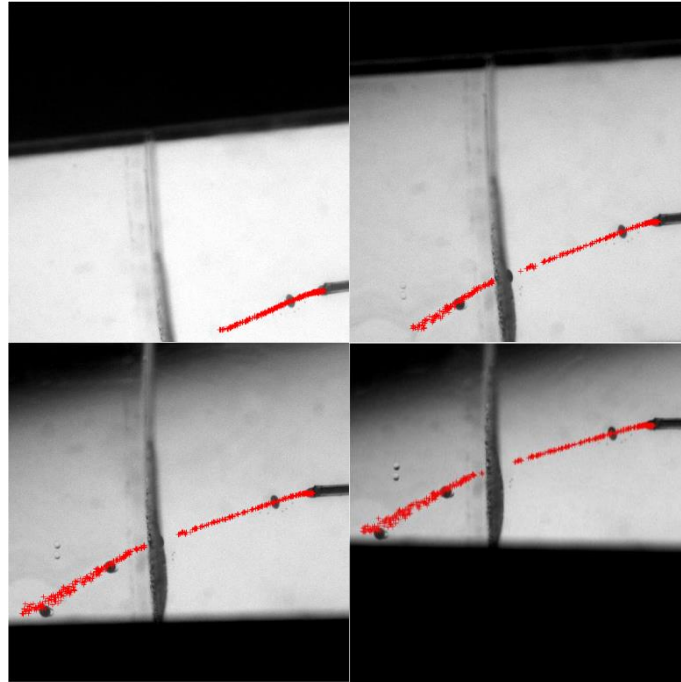


Figure 62: The position of the centers of mass of the detected droplets in all tours for each image position. The resultant of all the positions detected forms an envelope of the droplet trajectory.

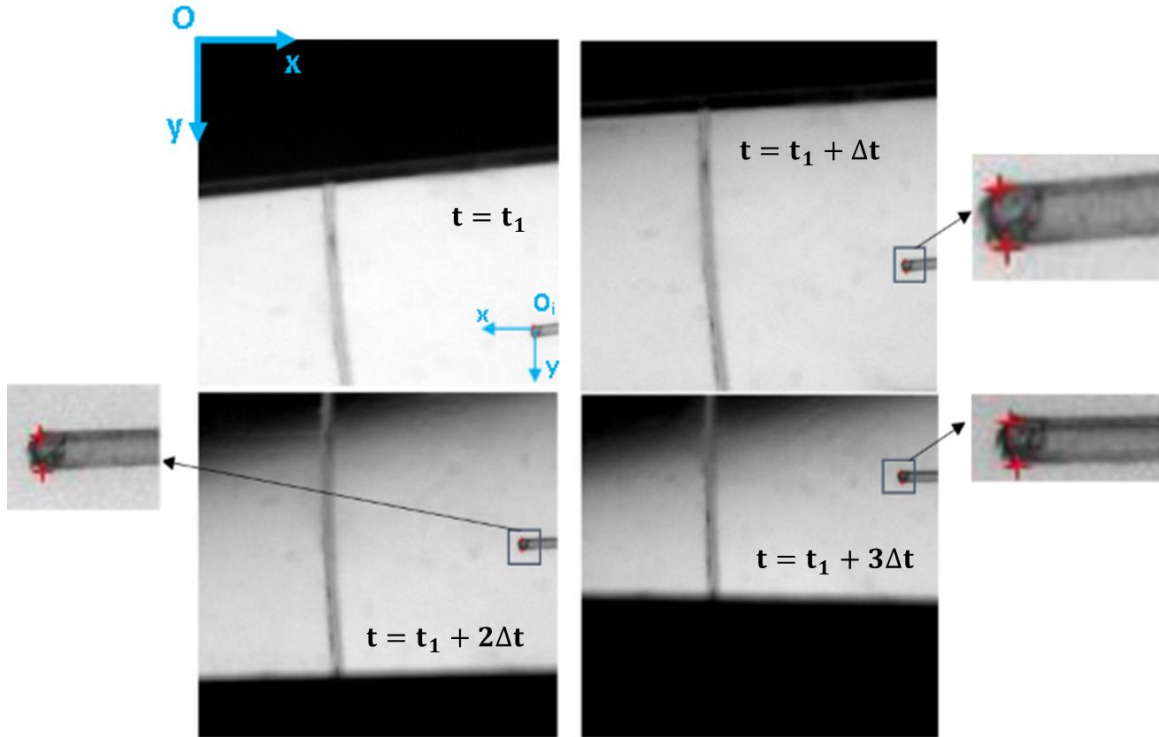


Figure 63: The detection of the capillary tube vertices in the four consecutive image position. The midpoint of the two vertices will be the origin of the new reference which will put the four detected trajectories on one plot.  $\Delta t = 107.58 \mu s$ .

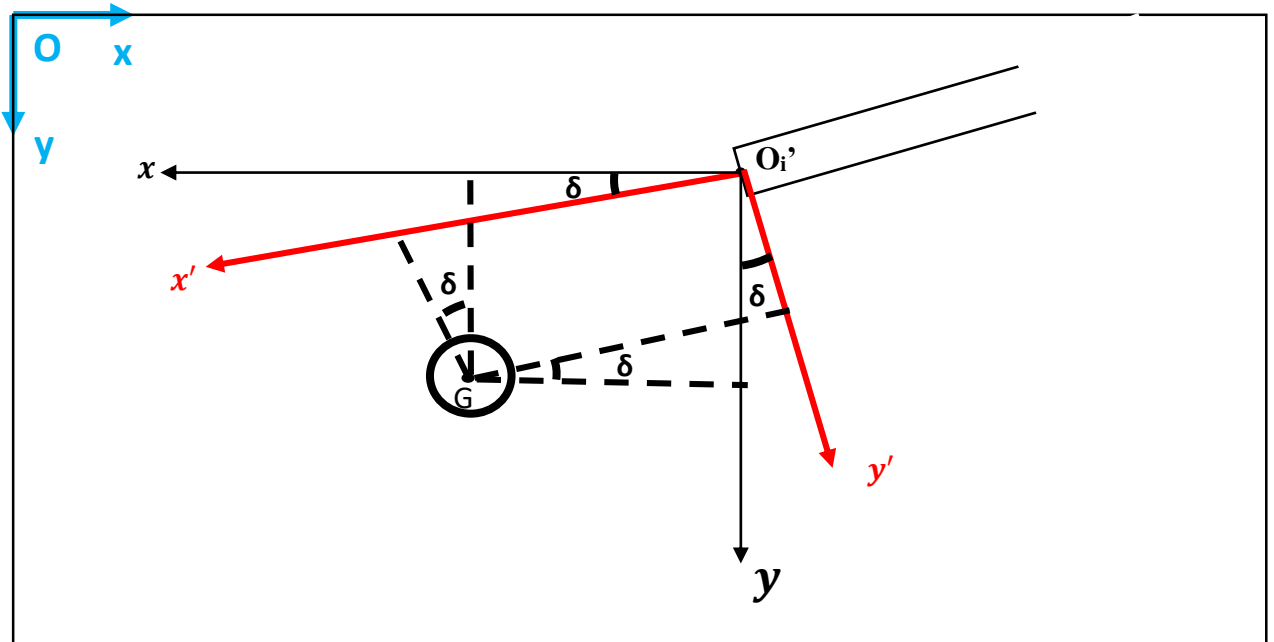


Figure 64: A scheme of a droplet in a certain image position where the black frame of reference is the translated camera frame of reference and the red one is the frame of reference corresponding to the capillary axis, and the angle  $\delta$  being the angle between the two references.

After the transformation of the frame of reference, one trajectory is plotted in Figure 65.

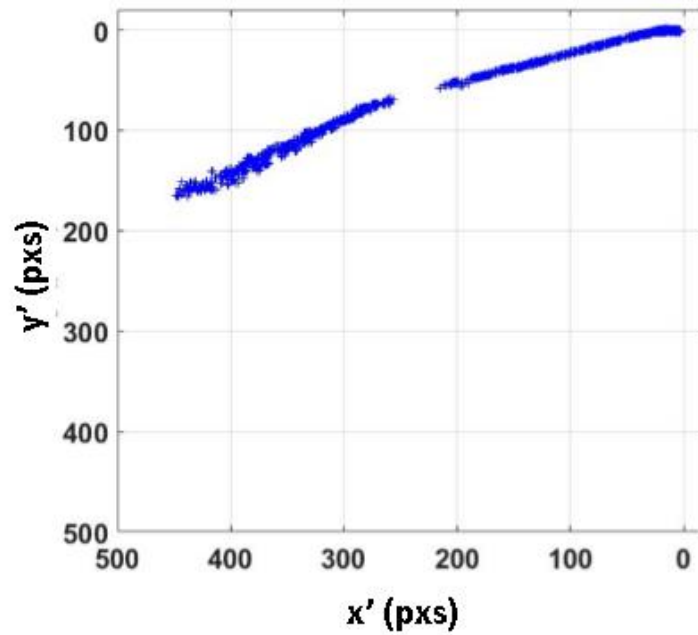


Figure 65: The coordinates of all droplet centroids in the frame of reference ( $x'Oy'$ ) found on a single envelop of trajectory.

### 5.2.2. Contour Processing: Size and Form Determination

The Hough transform returns a precise position of the center of mass of the droplet with an estimation of its equivalent diameter in pixels. We perform automatically a square crop around the detected droplet, the center of the square is the center of mass detected by Hough transform, and the size of its sides is 2 times the equivalent diameter returned by the Hough transform (between 12 and 70 pixels). Figure 66 shows an image with a detected droplet and the result of the square crop around the droplet.

Now, we consider the cropped image, and we implement an active contour segmentation method in order to detect the foreground and background (respectively the droplet and the first continuous phase in our case) regions inside the cropped image using level sets and active contours (Figure 66). It is a MATLAB function code named “active contour” which implements the well-known Chan-Vese segmentation algorithm from the paper "Active Contours without Edges" (Chan & Vese, 2001). This technique deforms an initial curve so that it separates foreground from background. The technique is very robust to initialization and gives very good results when there is a difference between the foreground and background means. Images of our results are 8-bits images, and the difference of grey level between the droplet region and the first phase is around 150.

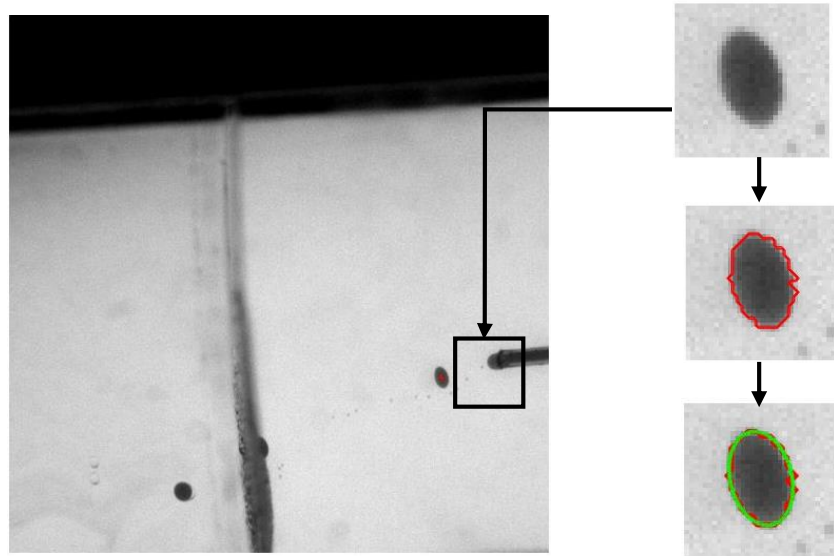


Figure 66: The detection of one droplet in a certain captured image and the crop around it, with a cropped image showing the contour detected by the active contour segmentation method around the droplet (in red), and finally this contour is fixed by an ellipse (in green).

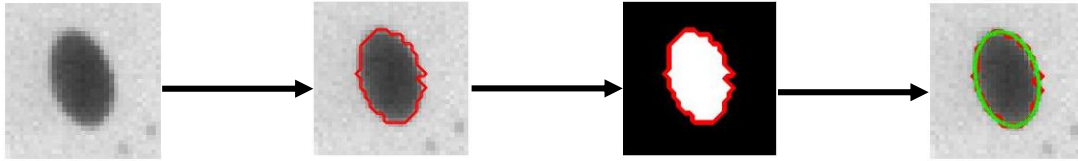


Figure 67: The transformation of the image to a binary image, above which we plot the detected contour in this figure and finally the fixed ellipse.

The contour is finally detected and traced around the droplet as shown also in figure 15 and 16. The image type is changed from a greyscale to a binary image, where inside the contour the value of grey level is 1 (white), and outside is 0 (black) as shown in figure 16. Finally, the MATLAB function “regionprops” is implemented in order to fit the white region contoured in red by an ellipse, and returns its properties, what concerns us out of the properties returned are the followings:

- **Equivalent Diameter ( $D_{eq}$ ):** Diameter of a circle with the same area as the region of the ellipse, computed as  $\sqrt{\frac{4A}{\pi}}$ , where A is the area of the ellipse.
- **Major Axis Length (a):** Length of the major axis of the ellipse that has the same normalized second central moments as the region.
- **Minor Axis Length (b):** Length of the minor axis of the ellipse that has the same normalized second central moments as the region.
- **Orientation angle ( $\beta$ ):** Angle between the x-axis of the image and the major axis of the ellipse that has the same second-moments as the region. This angle can be also transformed to the reference X’.

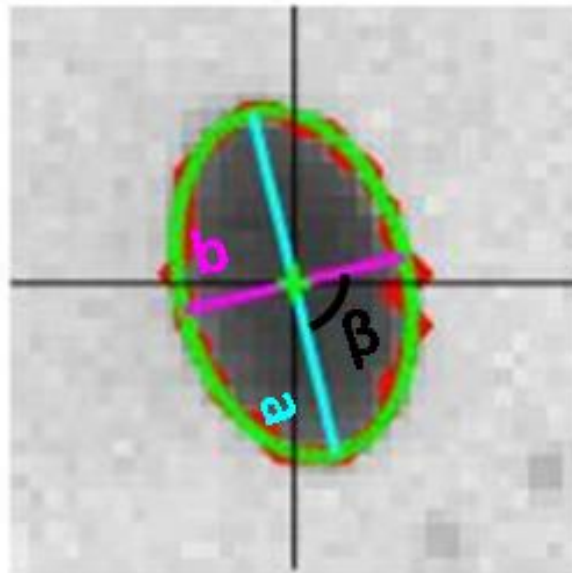


Figure 68: The detected contour with the fixed ellipse and the properties presented.

The Equivalent Diameter is supposed to be the size of the injected droplet, and the shape of the droplet is determined by the aspect ratio ( $\chi$ ) defined as the ratio between the Major axis length and the Minor axis length. Figure 16 shows the image of the detected droplet with the fixed ellipse and the properties mentioned above.

$$\chi = \frac{a}{b}$$

### 5.2.3. Velocity Calculation: By Image Cross-correlation function

Cross correlation function in image processing can be used for template matching defining a reference image (the template), in order to find an occurrence (or at least a similar enough occurrence) of the template in a targeted image. The correlation coefficient is a parameter of the correlation function which measures the similarity between the template and the targeted image for every pixel point (x,y). The result will be maximum for locations where the template have correspondence (pixel by pixel) to the sub image located at (x,y). Normalized cross-correlation function usually implies subtracting the mean pixel value then dividing by the standard deviation for the two regions of interest.

In our case, the template is the square cropped image around droplet inside image position  $i$ , which will be cross correlated with a following recorded image in the same tour ( $i+1$ , or  $i+2$ , ..., or  $i+n-1$ , with  $n$  is the number of images per tour). So, the cross-correlation function is between the cropped region and a whole following image, the correlation coefficient is calculated for every (x,y) position in the targeted image, the maximum correlation coefficient corresponds finally to the position of the droplet in the targeted image. This position is determined with sub-pixel interpolation and a maximum error of 0.2 pixels. Performing a parabolic interpolation of the correlation peak allows to increase the resolution of the measurement to sub-pixel values. So, we can calculate the displacement of the droplet in the abscissa and ordinate directions between two images, and by knowing the time between the two images, it will be possible to calculate the velocity of the droplet at a given position. Calibration of the image and thus the transformation from pixel to metric systems is done by referring to the capillary tube size. Figure 69 explains the velocity calculation procedure and presents the droplet positions in a series of images corresponding to same tour according to the calculated displacement.

However, the displacement is calculated in the image frame of reference, so it must be transformed to the frame of reference ( $x'O'y'$ ) which is common for all image positions. Now we take the example shown in figure 9, and we apply the procedure explained above to calculate the radial displacement of all detected droplets in the frame of reference ( $x'O'y'$ ) between image position 1 and image position 2 ( $V_{1-2}$ ) and so for image positions 2 and 3, and 3 and 4 ( $V_{2-3}$  and  $V_{3-4}$  respectively). Figure 18 shows the profile of  $V_{1-2}$ ,  $V_{2-3}$ , and  $V_{3-4}$  as a function of  $x'$  both in pixels.



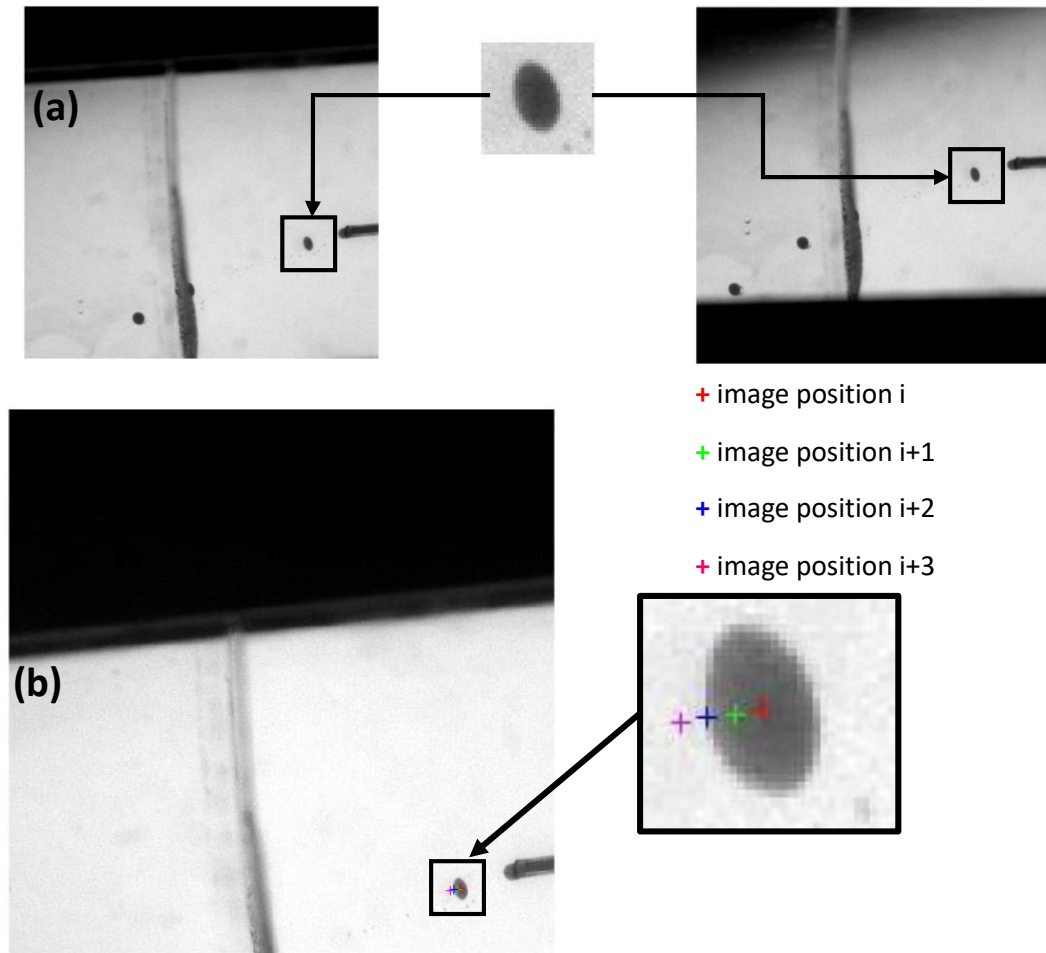


Figure 69: A scheme describing the procedure of cross-correlation function. (a) From left to right hand side, image position  $i$  with a droplet detected, the template which is a square cropped image around the droplet (center: droplet center of mass, and size:  $2 \cdot d_{eq}$ : equivalent diameter of droplet), and finally image  $i+2$  where the template is detected. (b) The droplet position at different image positions corresponding to the same turn according to the displacement calculated by the cross correlation function.

For the same curve of displacement of Figure 70, the variation of the calculated displacement ( $V_{1-2}$ ,  $V_{2-3}$ , or  $V_{3-4}$ ) for two different droplets detected at the distance from the injector is around 0.2 pixels ( $\approx 4.5 \mu\text{m}$ ). Moreover, when comparing  $V_{1-2}$ ,  $V_{2-3}$ , and  $V_{3-4}$  for the same detected droplet at the same position, the dispersion is also around 0.2 pixels  $\approx 4.5 \mu\text{m}$ . The total dispersion for a certain position (not necessarily same droplet) is  $4.5 \mu\text{m}$  in addition to  $4.5 \mu\text{m}$  due to different intervals of calculations ( $V_{1-2}$ ,  $V_{2-3}$ , and  $V_{3-4}$ ) making finally the relative error around  $9 \mu\text{m}$  for a certain droplet position and calculation of displacement between two consecutive images, equivalent to 2.4% of a droplet diameter 10% of the calculated displacement. Finally, we note that in the case of  $V_{1-2}$ , the displacement of droplets located after the interface position is not possible since this part is not captured in image position 1 (Figure 62).

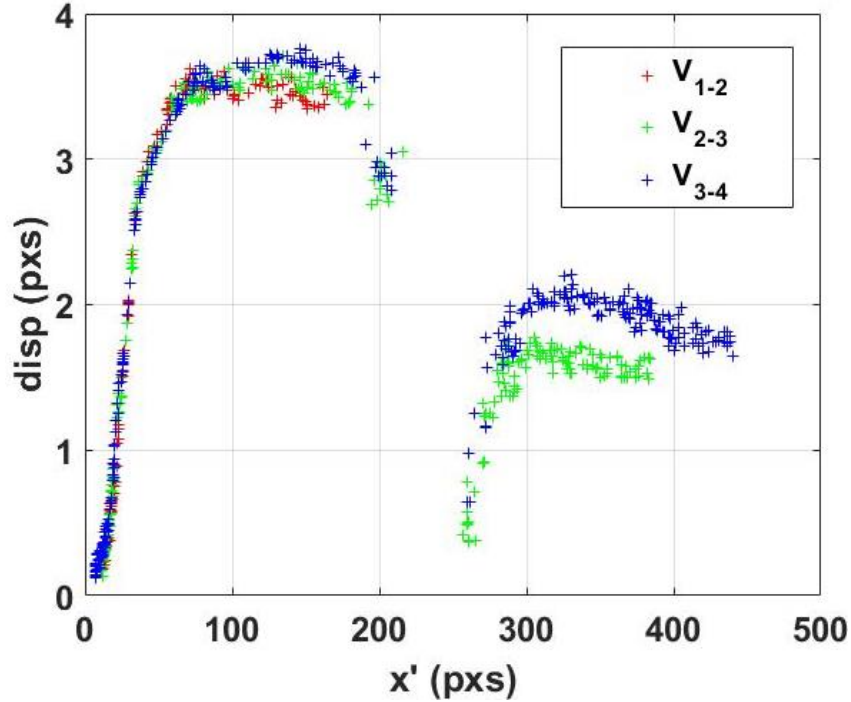


Figure 70: The displacement between two consecutive images  $V_{1-2}$ ,  $V_{2-3}$ , and  $V_{3-4}$ . In the three cases the droplet accelerates in phase 1 and decelerates upon arriving at the interface ( $x'$  between 200 and 250 pixels), then reaccelerates.

An idea to reduce the error on displacement is to calculate the displacement on a larger time interval, increasing the displacement of droplet and thus reducing the relative error. So, the cross correlation function is between an image position  $i$  and image position  $i+2$  to calculate a displacement on a doubled interval of time. For present example, the displacements to calculate are  $V_{1-3}$  and  $V_{2-4}$ , and results are finally shown in Figure 71. Now, the error presented on the displacement and velocity is reduced to around 5% by increasing the displacement of the droplet. This error can be reduced to 3.5% if we take  $V_{1-4}$  where image position  $i$  is correlated with position  $i+3$ . This is possible only for the part before the interface (Figure 72). Finally, the calculation of velocity for the part before the interface can be calculated with an error of 3.5% in the best case and after the interface with an error of 5% at the best case.

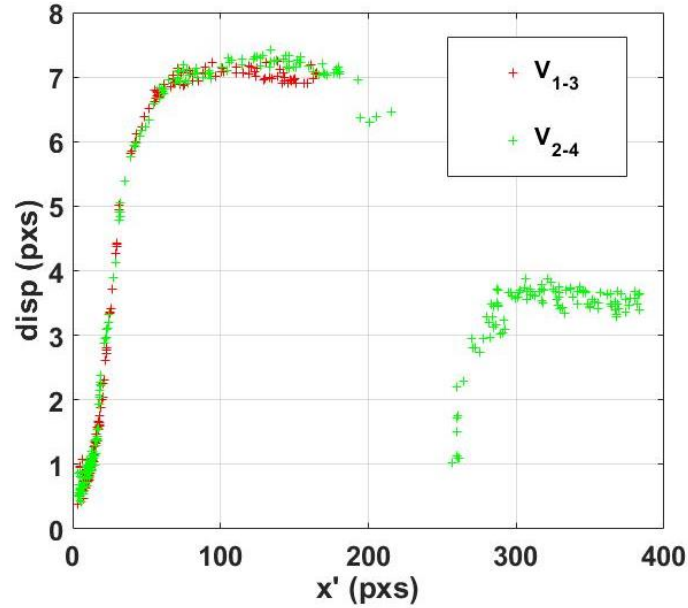


Figure 71: The displacements  $V_{1-3}$  and  $V_{2-4}$  as a function of droplet center of mass position.

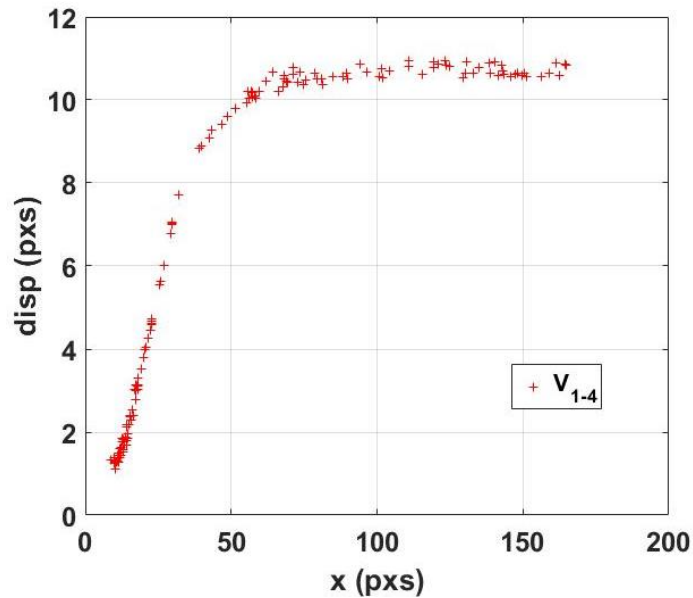


Figure 72: The displacement  $V_{1-4}$  as a function of droplet center of mass position.

#### 5.2.4. Calculation of droplet frequency

The droplet frequency is the inverse of the time needed to form a droplet of a certain volume from a capillary tip under the effect of a flow of speed  $u_c$ . To measure the droplet frequency we follow the procedure demonstrated in Figure 73. First, we measure the distance ( $x_{12}$ ) between two consecutive droplets denoted drop 1 and drop 2 rising inside the first phase with nearly the same velocity. Next, we calculate the mean velocity ( $u_{\text{mean}}$ )

of the two instantaneous velocities of the two droplets:  $u_{mean} = \frac{u_1 + u_2}{2}$ . Finally, the frequency of the droplets is given according to the following expression:  $f = \frac{u_{mean}}{x_{12}}$ .

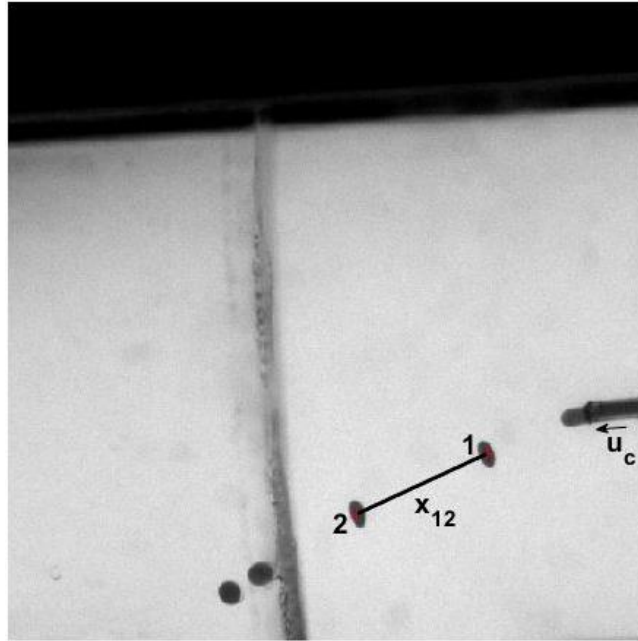


Figure 73: The scheme explaining the procedure to calculate the droplet frequency through the distance between two consecutive droplets: drop 1 and drop 2 separated by a distance  $dis$ .  $V_c$  is the fluid velocity within the capillary tube.

The above steps are applicable if the two droplets before the interface are separated by an observable distance on the same image as in Figure 73. Yet, it is not applicable when the frequency of the droplet is less than 1 drop per tour. In such conditions, the frequency is measured by counting the number of tours needed to form one droplet, so the precision of this measurement will be overestimated by one tour.

Multiplying the frequency of the droplets by their corresponding volume gives the injection rate  $Q_c$  in  $m^3/s$ , and dividing the injection rate by the surface of the capillary tube orifice gives the velocity  $u_c$  inside the capillary tube.

### 5.2.5. The detection of Plane Interface position

The last part of this processing methodology, is the detection of the interface position in each tour. This position is sometimes shifted due to continuous injection as mentioned before. In order to calculate the position of the interface, the procedure starts by considering the point  $O_i'$  of only one image position per turn (take image position 2 for this instant), then plotting a horizontal line (H) with respect to the image frame of reference as shown in Figure 74. Starting from point  $O_i'$  to the end of the horizontal line, the objective is to search for the abrupt variation in the grey level (more than 80 in our 8-bits images),

which indicates the presence of the plane interface which has a less grey level value. Given  $S_i$ , the point at which the grey level value strongly changes, the distance  $O_i'S_i$  defines the horizontal distance between the injector and the interface in the image frame of reference, which is transformed to the frame of reference  $(x'O'y')$  by the following equation:

$$D_{int} = \frac{O_i'S_i}{\cos \delta_i}$$

Where  $\delta_i$  is the angle between the two frames of reference and  $D_{int}$  is the perpendicular distance between the injector and the plane interface.

In this method, the thickness of the interface is not taken into account, the first point of change in the grey level values is only taken into account. Thus, the precision of the method is equivalent to the thickness of the interface which is between 10 and 20 pixels which represents 4 to 13% of the distance between the droplet and the plane interface, which varies between 150 to 250 pixels depending on the chosen experiment.

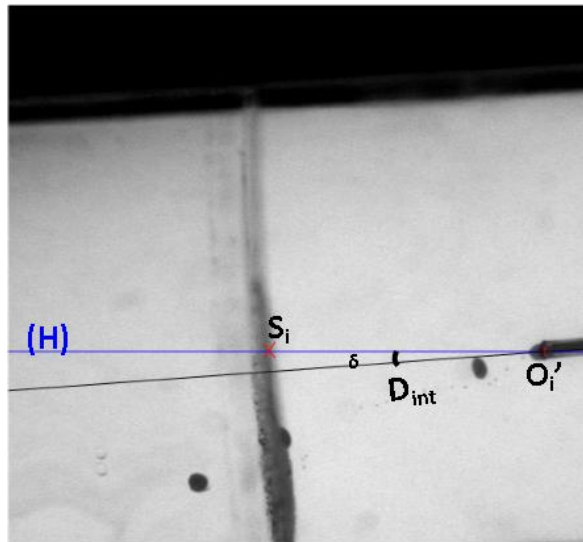


Figure 74: The detection of the interface, where  $S$  corresponds to the point of change of the grey level values along the horizontal line  $(H)$ , and  $D_{int}$  being the distance between the injection position and the interface position.

### 5.2.6. Calculation of the maximum column length

The maximal column length forming behind the droplet after crossing is measured experimentally. As defined in the previous chapter, the maximal column length  $L_{max}$  is the distance between the position of pinch-off close to the interface and the droplet center of mass. Due to the Coriolis force, the shape of the column is curvilinear with a deviation with respect to the perpendicular line to the interface. So, to measure  $L_{max}$ , we take the image at the instant of column detachment, we manually plot points along the column with

small distance  $dl$  (less than 3 pixels) between them as shown in figure . The maximal length of the column  $L_{max}$  is the sum of  $n$  small distances  $dl_{i,i+1}$   $i=1,2,3,\dots,n-1$ .

$$L_{max} = \sum_{i=1}^{n-1} dl_{i,i+1}$$

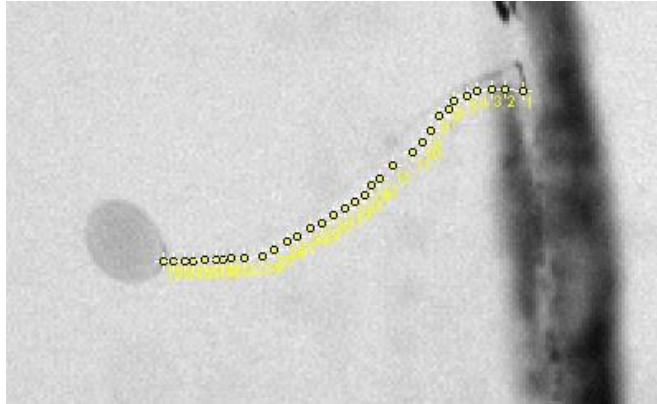


Figure 75: An image of the column forming behind the droplet with consecutive points plotted manually. The distance between point  $i$  and  $i+1$  is  $dl_{i,i+1}$ .

### 5.3. Chemical Products

To develop and scale-up the encapsulation process, the main challenge is to determine the optimal operating physical parameters of the system components, given the setup dimensional characteristics. Three liquids are to be selected for phases 1, 2 and 3 (Figure 76). Phase 2 and 3 are aqueous, whereas phase 1 is immiscible with water. The products are chosen so as to respect certain operating constraints of the encapsulation device studied, and also so as to be able to explore a wide range of hydrodynamic conditions. Recall that phase 1 consists of an organic phase which will coat the drops (phases 2). Once coated, the drops will remain in a new continuous aqueous phase (phase 3). The centrifugal device therefore imposes the following constraint on the densities of the three phases:  $\rho_2 > \rho_3 > \rho_1$ . Phase 3 must be lighter than phase 2, so we choose to add sucrose to phase 2 (percentage retained: 25% by mass), phase 3 simply consisting of water.

In Table 16, we present the chemical products used in our experiments for phases 1, 2, and 3 with their respective physical parameters (densities and viscosities) and the physicochemical parameters (surface tensions  $\gamma_{12}$  and  $\gamma_{13}$ ). We used Silicone oil for phase 1, with different viscosities  $\mu_1$ . Phase 2 is a 25% w/w aqueous solution of sucrose, and Phase 3 is water. In the following, prepared samples are denoted  $E_i$ . Their densities and viscosities are respectively measured with a densimeter DMA 38 supplied by Anton Paar and with a rheometer AR2000ex supplied by TA instruments at 25 °C. For more details on the measurements tools reader can refer to Appendix A. To improve image quality, we colored

phase 2 with Resazurin or Rhodamine supplied by Sigma Aldrich. For some experiments, phase 1 contains a silicon co-polymer, the dimethylsiloxane-(25-30% ethylene oxide) block copolymer (DBE-224) supplied by Gelest. In some experiments, phase 3 contains surfactants, either sodium dodecyl sulfate (SDS) or Tween 80, at a concentration given both in mM (mmol/L) and as a function of the critical micelle concentration (CMC). Table 17 shows different surfactants used in our experiments with their corresponding supplier's name, their CMC in mM and in which phase they have been dispersed (phase 1, 2, or 3). Generally, the CMC of this silicone co-polymer dispersed in phase 1 is on the order of  $10^{-3}$ - $10^{-2}$  mM (Rheingans et al., 2000). In a sample of Silicone oil, we dilute 25 mg of this surfactant, so the concentration is 0.047 mM fairly more than the CMC value. In Table 18, we present the surface tensions between samples of this chapter measured by the pendant droplet method, using the Tensiometer KRUSS.

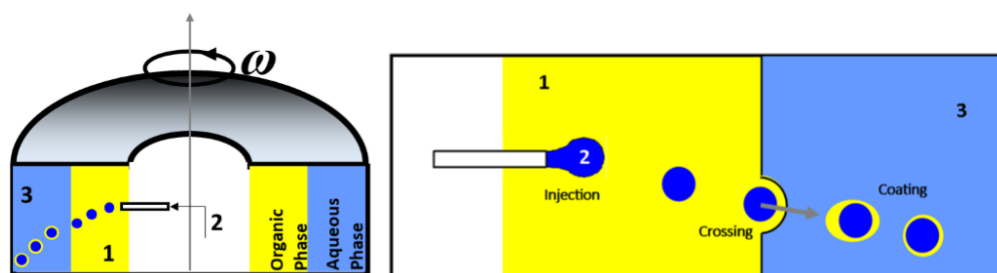


Figure 76: Left, a scheme of the centrifugal cell where droplets are injected and encapsulated. Right, the three-phase system with their labels and numbers.

The Silicone block co-polymer DimethylSiloxane (25-30% Ethylene Oxide) is provided by Gelest has a chemical structure shown in Figure 77 and molar mass  $M = 10^4$  g/mol. This surfactant is non-soluble in water and highly soluble in Silicone oil. The surfactant Sodium dodecyl sulfate (SDS) provided by Sigma Aldrich is a synthetic organic amphiphile  $\text{CH}_3(\text{CH}_2)_{11}\text{SO}_4\text{Na}$ , with a molar mass  $M = 288.372$  g/mol, used in domestic cleaning, personal hygiene, cosmetic, pharmaceuticals, and food applications. The hydrophilic head is an anionic sulfate group and the hydrophobic tail is a hydrocarbon of 12-carbon chain. Tween 80 is a non-ionic surfactant purchased from Sigma Aldrich that we test here at CMC concentration, used in food and cosmetics with the formula  $\text{C}_{64}\text{H}_{124}\text{O}_{26}$  and a molar mass  $M = 1310$  g/mol. The hydrophilic head is polyether and the hydrophobic tail is oleic acid. The critical micelle concentration above which micelles form and the surface tension does not decrease anymore is 0.012 mM.

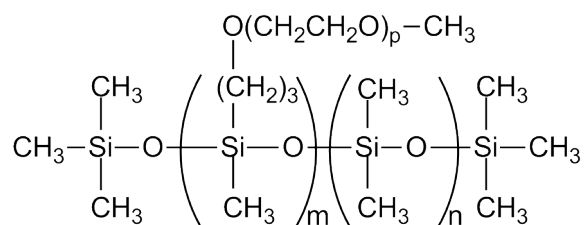


Figure 77: The chemical structure of the Silicone co-polymer used as surfactant inside phase 1.

	Density [Kg.m <sup>-3</sup> ]	Viscosity [Pa.s]	Surfactants Concentration
<b>Phase 1</b>			
Silicon Oil S5	913	0.005	0
Silicon Oil S10	930	0.01	0
Silicon Oil S20	950	0.02	0
Silicon Oil S50	960	0.05	0
Silicon Oil S100	960	0.1	0
S10_DBE: Silicon Oil S10+ DBE-224	930	0.01	0.047 mM
<b>Phase 2</b>			
E <sub>2</sub> : Sucrose	1081	0.0024	0
E <sub>3</sub> : Sucrose + SDS	1081	0.00232	0.5*CMC
E <sub>4</sub> : Sucrose + SDS	1081	0.00225	1.22*CMC
<b>Phase 3</b>			
W: Water	997	0.001	0
E <sub>5</sub> : Water + SDS	997	0.001	1.22*CMC
E <sub>6</sub> : Water + SDS	997	0.001	0.73*CMC
E <sub>7</sub> : Water + SDS	997	0.001	0.5*CMC
E <sub>8</sub> : Water + Tween 80	997	0.001	1.13* CMC

Table 16: Viscosities, Densities, and surfactant concentration for each sample used in our experiments.

Surfactant	Diluted in	CMC [mM]
SDS	Phase 2 and/or 3	8.2
Tween 80	Phase 3	0.0106 ± 0.0007
Silicon Co-polymer (DBE 224)	Phase 1	0.001-0.01 (Rheingans et al., 2000)

Table 17: Characteristics of the surfactants used in our experiments.

	$\gamma_{12}$ [mN.m <sup>-1</sup> ]			$\gamma_{13}$ [mN.m <sup>-1</sup> ]				
	E <sub>2</sub>	E <sub>3</sub>	E <sub>4</sub>	Water	E <sub>5</sub>	E <sub>6</sub>	E <sub>7</sub>	E <sub>8</sub>
<b>S5</b>	37	18	10.5	36	10	-	-	14.5
<b>S10</b>	40	-	-	38	11	13	18	14.8
<b>S20</b>	41	-	-	-	12	-	-	15
<b>S50</b>	43	19	11	38	13	-	-	16.5
<b>S100</b>	44	-	-	-	13	-	-	-
<b>S10_DBE</b>	8	-	-	4	1	-	-	3

 Table 18: The surface tension  $\gamma_{12}$  and  $\gamma_{13}$  between different samples at equilibrium.



# Chapter 6:

Experimental Approach:  
Results

# Chapter 6: Experimental Approach: Results

## 6.1. Introduction

The objective of the experimental study is to evaluate and quantify the relevant parameters during all the steps of the encapsulation process, from droplet injection to the coated droplet. The experimental approach focuses on single droplet events, disregarding interactions in between successively injected droplets. Our observation chamber is designed for this purpose and the production frequency is kept as low as possible. The first objective is to inject droplets with controlled size and frequency and to determine their trajectory, velocity, and shape while rising inside a continuous phase submitted to a centrifugal field. Another objective is to determine the conditions for successful crossing as a function of the relevant non-dimensional parameters, and to compare them with theory or numerical predictions. These conditions together with the crossing time will be crucial to design and appropriately use a future pilot. Finally, the crossing dynamics and the volume of the film coating the droplet has been investigated in this study. In order to reach these objectives, the experimental centrifugal device, presented in chapter 5, is monitored with a high-speed camera in order to observe, and analyze each step of the process:

- The **injection** of aqueous droplets (phase 2)
- The **rise** towards the interface between phase 1 (organic) and phase 3 (aqueous)
- The **crossing**, bouncing, or accumulation at the interface
- The **film entrainment and droplet coating**.

Note that this experimental study is complementary to the numerical one in terms of the range of parameters investigated, with some overlaps in a few cases that will be discussed in this chapter. A strong interest of the experimental study lies in the characterization of the surfactants influence on the drop dynamics, as well as the effect of the Coriolis force on the drop motion, both phenomena being disregarded in the numerical study of chapter 5. In experiments, the role of surfactants is necessary for two reasons: it allows to adjust the interfacial Bond number for common oil/water systems to allow the interface crossing and it's a necessary ingredient for the build-up of interfacial films of encapsulated droplets able to resist to external stresses.

As a preamble, we present the range of physical parameters of the experiment and recall the non-dimensional numbers declared in chapter 2. In the next sections, we will present

all experimental results. In particular, we will discuss the relevant parameters influencing the droplet size for a given injection frequency, and the effects of surfactants. We then describe the droplet trajectory, and finally the crossing and coating of drops and the involved physical mechanisms.

**6.2. Range of physical and non-dimensional parameters**

The range of relevant physical and non-dimensional parameters for all experiments are reported in Figure 78, corresponding to the chemical products presented in chapter 4. The rotation speed of the cell corresponds to a range of centrifugal accelerations lying between 24 and 2400g, where g is the gravitational acceleration. The viscosity of phase 1 varies between 0.005 and 0.1 Pa.s, and its density varies between 913 and 960 Kg.m<sup>-3</sup>. The viscosities of phase 2 and 3 are fixed at 0.0024 and 0.001 Pa.s and densities at 1081 and 997 Kg.m<sup>-3</sup> respectively. Interfacial tensions at thermodynamic equilibrium are ranging between 8 and 44 mN.m<sup>-1</sup> for  $\gamma_{12}$  and between 1 and 37 mN.m<sup>-1</sup> for  $\gamma_{13}$ , the lowest values corresponding to CMC values of the surfactants used in this study. This device allows the formation of droplets ranging in size between 100  $\mu$ m to few millimeters. The related range of Archimedes and Bond numbers correspond to a variation from 0.6 to 50 of droplet Reynolds number based on terminal velocity in phase 1, and from 0.5 to 5 for the Weber number  $We_{12}$  corresponding to deformed droplets in inertial regime. Non-dimensional numbers presented in chapter 2 are recalled below.

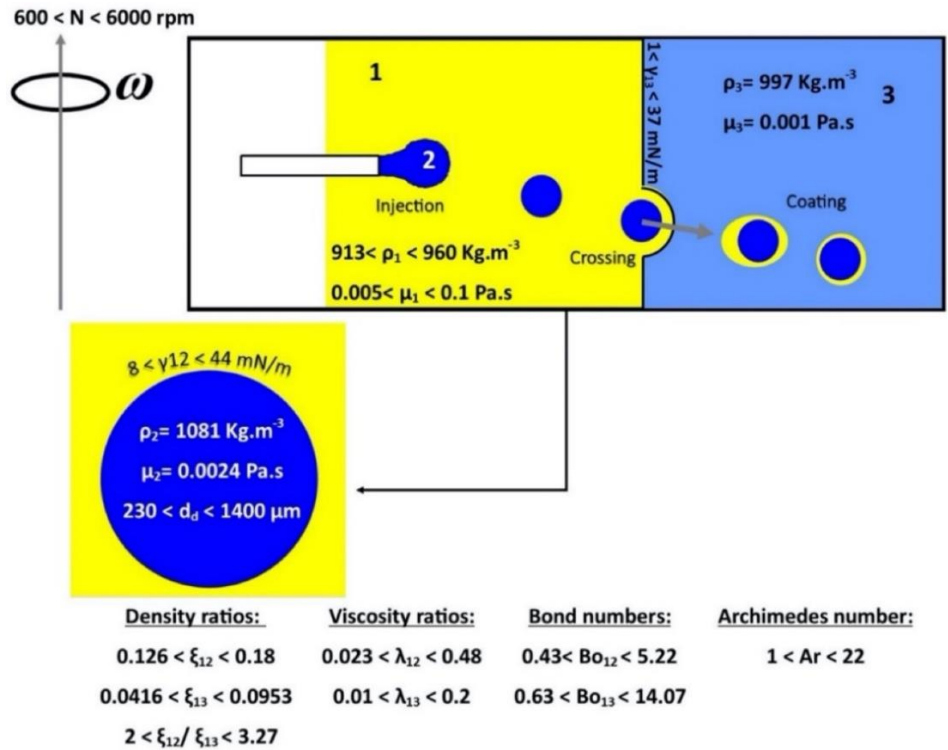


Figure 78: Range of variation of the physical and non-dimensional parameters.

Non-dimensional numbers:

- Density ratio between phase 1 and phase 2:  $\xi_{12} = \rho_2/\rho_1 - 1$
- Density ratio between phase 1 and phase 3:  $\xi_{13} = \rho_3/\rho_1 - 1$
- Viscosity ratio between phase 1 and 2:  $\lambda_{12} = \mu_2/\mu_1$
- Viscosity ratio between phase 1 and 2:  $\lambda_{13} = \mu_3/\mu_1$
- Bond number of the droplet in phase 1:  $Bo_{12} = |\rho_2 - \rho_1| r_0 \omega^2 R^2 / \gamma_{12}$
- Bond number of the interface:  $Bo_{13} = (\rho_3 - \rho_1) r_i \omega^2 R^2 / \gamma_{13}$
- Archimedes number of the droplet rise in phase 1:  $Ar = \rho_1 (\xi_{12} r_i \omega^2)^{\frac{1}{2}} R^{\frac{3}{2}} / \mu_1$
- Droplet Reynolds number in phase 1 based on terminal velocity:  $Re = \rho_1 U_T d / \mu_1$
- Droplet Weber number based on terminal velocity in phase 1:  $We_{12} = \rho_1 U_T^2 d / \gamma_{12}$
- Droplet Ohnersorge number:  $Oh_{12} = \mu_2 / \sqrt{\rho_1 \gamma_{12} d}$
- Liquid film Ohnersorge number of phase 1:  $Oh_{13} = \mu_1 / \sqrt{\rho_1 \gamma_{13} d}$

Experimental constraints impose some limits on the explored range of parameters. Figure 79 presents a graphical illustration of the range of parameter couple  $(Bo_{13}, \frac{\xi_{12}}{\xi_{13}})$  corresponding to our experiments, symbolized by the colored bar on the graph. The Archimedes number has a maximum value of 22 which ensures a stable trajectory of the droplet during its rise in phase 1.

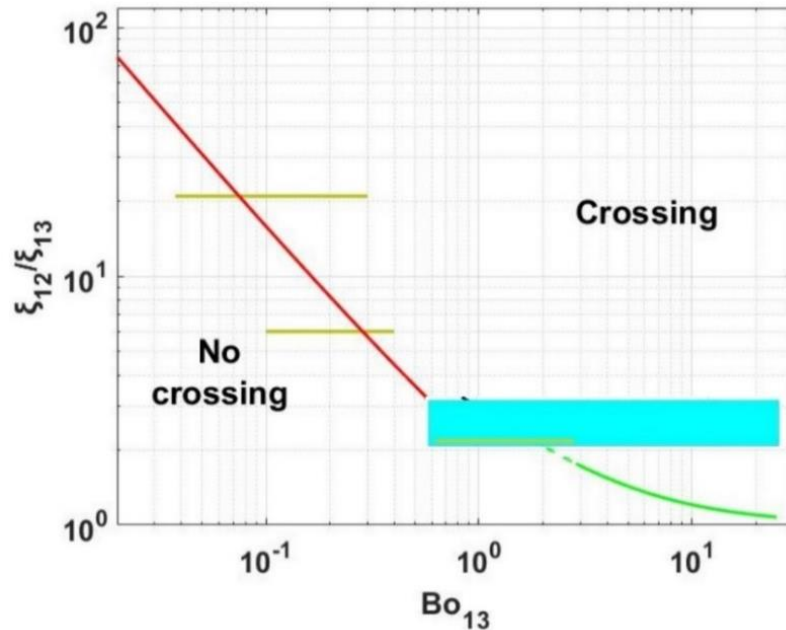


Figure 79: Experimental (blue bar) and numerical simulations (yellow bar) ranges in the plane  $(Bo_{13}, \xi_{12}/\xi_{13})$ . The red and green curves correspond to critical crossing condition respectively for  $Bo \ll 1$  and  $Bo \gg 1$  (Equations 5 and 6 of this chapter).

### 6.3. Droplets injection

The control of the size of the final capsules is highly dependent on the control of the injected droplet size. Droplet injection of phase 2 in phase 1 is performed from the injection capillary in dripping mode (see Figure 80). Phase 2 flows inside the capillary tube at a flowrate  $Q_c$ , adjusted for each experiment thanks to the pressure controller described in chapter 5, and forms a droplet attached to the capillary tip by a capillary force. The droplet grows with time up to a critical diameter above which the centrifugal force exerted on the droplet balances the capillary force. At this critical size, the droplet detaches from the capillary tube and is further moved towards the interface. In this section, the volume of the drops produced has been studied as a function of the system physical parameters, for different inlet capillary diameters ( $D_i$ ), densities of the continuous ( $\rho_1$ ) and dispersed fluid ( $\rho_2$ ), and rotation speeds ( $N$ ). We first define two non-dimensional numbers involved in the physics of droplet detachment from a capillary tube into a viscous fluid:

- The Bond number:  $Bo_D = (\rho_2 - \rho_1)r_0\omega^2 D_i^2 / \gamma_{12}$
- The Ohnesorge number :  $Oh_D = \mu_2 / \sqrt{\rho_2 \gamma_{12} D_i}$

where  $r_0$  is the radial position of the capillary tip with respect to the rotation axis and  $D_i$  is the tube inner diameter.

Table 19 reports the phase properties, operating parameters and average drop size  $\bar{d}_d$  obtained from 27 different experiments, denoted  $M_i$ . Three capillary diameters were tested:  $D_i = 100, 250, 530 \mu\text{m}$ . The number of injected droplets differs between experiments from a 1 to 350. The diameter of the produced drops lies between  $230 \mu\text{m}$  and  $1.4 \text{ mm}$  with a standard deviation varying between  $5$  and  $12 \mu\text{m}$  and a standard error less than  $3 \mu\text{m}$  in all experiments. Except for one experiment, the Ohnesorge number  $Oh_D$  is always of order  $O(10^{-2})$ , varying between  $0.017$  and  $0.05$ . The deformation is thus driven by surface tension and the viscous contribution can be neglected. The external continuous fluid is assumed to be stagnant, so there is no external shear effect. Therefore, drop release is expected to be driven by the equilibrium between the centrifugal and the capillary forces as sketched in Figure 80, reading:

$$F_G = F_\gamma \Leftrightarrow \Delta\rho_{12} \frac{\pi \bar{d}_d^3}{6} r_0 \omega^2 = \alpha \pi \gamma_{12} D_i \quad (1) \Leftrightarrow \left(\frac{\bar{d}_d}{D_i}\right)^3 = \frac{6\alpha}{Bo_D} \quad (2)$$

where  $\alpha$  is an empirical constant expected to be of order  $O(1)$  that regroups effects of drop wettability on the capillary tip, tip geometry and roughness.

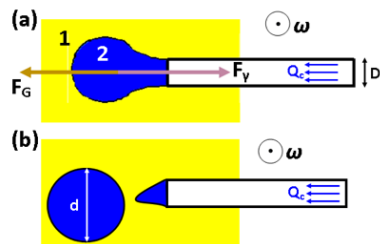


Figure 80: (a) The force balance on a droplet growing from a capillary tube under a flow rate  $Q_c$  in dripping mode.  $F_G$  is the centrifugal force,  $F_\gamma$  is the interfacial tension force. (b) The droplet after detachment.

	Parameters							Results				
	$\rho_1$ [Kg.m <sup>-3</sup> ]	$\rho_2$ [Kg.m <sup>-3</sup> ]	N [rpm]	D <sub>i</sub> [ $\mu$ m]	$\gamma_{12}$ [N.m <sup>-1</sup> ]	Bo <sub>D</sub>	Oh <sub>D</sub>	Q <sub>c</sub> [ $\mu$ L/s]	f [s <sup>-1</sup> ]	$\bar{d}_d$ [ $\mu$ m]	$\sigma_d$ [ $\mu$ m]	$e_{\bar{d}}$ [ $\mu$ m]
M <sub>1</sub>	930	1081	600	250	0.04	0.05	0.023	5	3.3	1406	0*	0*
M <sub>2</sub>			1440			0.32		0.95	4.8	721	4.95	0.93
M <sub>3</sub>			3000			1.37		8.9	177	454	3.773	1
M <sub>4</sub>			3600			1.82		6.1	180	404	3.13	0.61
M <sub>5</sub>			3600			2.02		8	272	380	5.52	0.414
M <sub>6</sub>			4200			2.72		10	427	352	7.7	0.72
M <sub>7</sub>			4800			3.9		0.6	40	306	4.89	1.04
M <sub>8</sub>			5400			4.47		-	-	284	6.94	0.67
M <sub>9</sub>			5400			4.55		5	364	299	11.02	0.938
M <sub>10</sub>	960	1081	3000	250	0.044	1.12	0.022	9.5	119	532	4.992	1.09
M <sub>11</sub>			3600			1.52		0.4	10	422	3.85	0.51
M <sub>12</sub>			4200			2.19		6	212	379	4.31	0.62
M <sub>13</sub>			5400			3.56		3.2	150	346	15.27	4.82
M <sub>14</sub>	913	1081	3600	250	0.037	2.34	0.023	9	347	367	4.09	0.49
M <sub>15</sub>			5400			5.26		0.9	90	268	5.75	0.616
M <sub>16</sub>	950	1081	3600	250	0.041	1.67	0.023	11	310	408	3.575	0.342
M <sub>17</sub>				530		6.69	0.016	15	200	519	5.75	2.75
M <sub>18</sub>	960	1081	3600	250	0.043	1.47	0.022	1.2	30	424	5.19	0.55
M <sub>19</sub>			6000	100		0.66	0.034	-	-	232	11.57	0.84
M <sub>20</sub>	913	1081	2400	530	0.037	4.35	0.016	1.7	20	546	9.09	1.93
M <sub>21</sub>			3600	250		2.38	0.023	1	30	398	4.09	0.49
M <sub>22</sub>			5400	250		5.35	0.023	1.3	90	304	5.75	0.616
M <sub>23</sub>	930	1081	3600	530	0.04	7.49	0.016	11	263	433	12.14	1.49
M <sub>5</sub>				250		2.02	0.023	8	272	380	5.52	0.414
M <sub>5</sub>	930	1081	3600	250	0.04	2.02	0.023	8	272	380	5.52	0.414
M <sub>24</sub>					0.008	10.1	0.052	7	268	366	6.58	0.87
M <sub>25</sub>	960	1081	3600	250	0.012	3.81	0.042	6.5	180	410	4.48	0.56
M <sub>18</sub>					0.043	1.47	0.022	1.2	30	424	5.19	0.55
M <sub>24</sub>	930	1081	3600	250	0.008	10.1	0.052	7	268	366	6.58	0.87
M <sub>26</sub>			1440			1.59	0.052	-	-	652	5.8	1.18
M <sub>27</sub>			1440			1.61	0.052	4.7	24	718	6.31	2.1

Table 19: Flow parameters and phase properties of drop injection experiments.  $\sigma_d$  is the standard deviation and  $e_{\bar{d}}$  is the standard error. As droplets are deformed, diameters values are those of an equivalent sphere. The drop viscosity (phase 2) is  $\mu_2=0.0024$  Pa.s in all experiments. Flowrate is calculated from the injection frequency and the drop volume. Colors indicate varying parameters in each set of experiments. (\*) In M1, only one droplet size was measured.

The influence of flow parameters on the size of injected droplets is first investigated. Those are the speed of rotation (N) and the size of capillary tube (D<sub>i</sub>). Then the effect of surfactants (and of surface tension ( $\gamma_{12}$ )) on the droplet produced is addressed and discussed.

### 6.3.1. Influence of rotation speed

Injection of drops at different rotation speeds for 4 sets of experiments  $M_2$ ,  $M_3$ ,  $M_5$  and  $M_9$  has been studied, corresponding to a single two-phase system detailed in Table 20. In Figure 81, a sequence of images of drop release is presented for each case. The drop grows until it reaches a critical volume at which it detaches after a pinch-off developed, leaving behind a liquid thread at the tip of the capillary. As the speed of rotation increases, the droplet detaches from the capillary tip earlier and at a smaller volume, as illustrated by the image sequences of Figure 81, recorded at different rotation speeds: 1440, 3000, 3600, 5400 rpm.

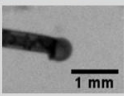
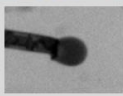
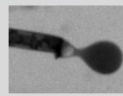
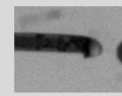

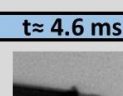
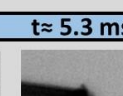
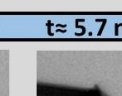
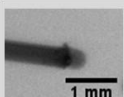
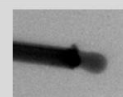
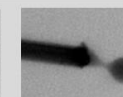
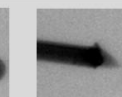
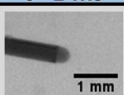
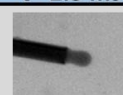
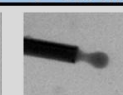
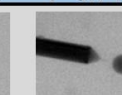
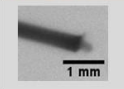
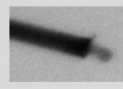
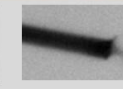
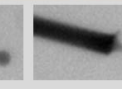
N [rpm]	$t \approx 9$ ms	$t \approx 83$ ms	$t \approx 153$ ms	$t \approx 208$ ms	$\bar{d}_d$ [ $\mu\text{m}$ ]	$\sigma_d$ [ $\mu\text{m}$ ]	f [ $\text{s}^{-1}$ ]
1440					721	4.95	4.8
							
3000	$t \approx 1.8$ ms	$t \approx 4.6$ ms	$t \approx 5.3$ ms	$t \approx 5.7$ ms	454	3.77	177
							
3600	$t \approx 1$ ms	$t \approx 2.5$ ms	$t \approx 3.3$ ms	$t \approx 3.7$ ms	380	5.52	272
							
5400	$t \approx 0.8$ ms	$t \approx 1.8$ ms	$t \approx 2.5$ ms	$t \approx 2.7$ ms	299	11.02	364
							

Figure 81: Image sequence of droplet formation and detachment from the capillary tube for 4 experiments of set 1:  $M_2$ ,  $M_3$ ,  $M_5$ , and  $M_9$  at different speeds of rotation.  $\bar{d}_d$  is the mean droplet diameter,  $\sigma_d$  is the standard deviation and f is the frequency of injection.

Set	Experiments	Phase 1	Phase 2	$\rho_1$ [Kg.m <sup>-3</sup> ]	$\rho_2$ [Kg.m <sup>-3</sup> ]	$\mu_1$ [Pa.s]	$\gamma_{12}$ [N.m <sup>-1</sup> ]	N [rpm]
1	$M_1$ to $M_9$	S10	E <sub>2</sub>	930	1081	0.01	0.04	600 to 5400
2	$M_{14}$	S5	E <sub>2</sub>	913	1081	0.005	0.037	3600
	$M_{15}$							5400
3	$M_{10}$	S100	E <sub>2</sub>	960	1081	0.1	0.044	3000
	$M_{11}$							3600
	$M_{12}$							4200
	$M_{13}$							4500
4	$M_{24}$	S10_DBE	E <sub>2</sub>	930	1081	0.01	0.008	3600
	$M_{26}$							1440
	$M_{27}$							1440

Table 20: Physical parameters of test cases. The droplet viscosity is  $\mu_2 = 0.0024$  Pa.s and the size of the capillary tube is  $D_i = 250$   $\mu\text{m}$ .

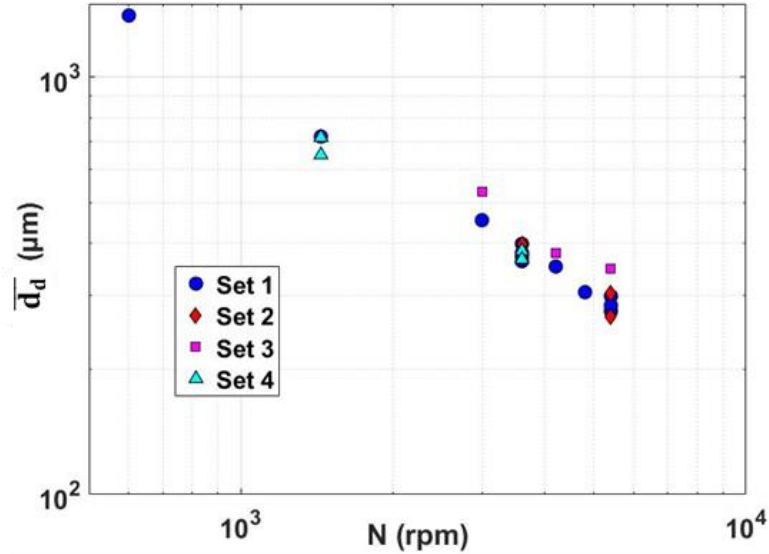


Figure 82: Diameter of injected droplets  $d_d$  as a function of the speed of rotation for 4 phase systems.

In Figure 82, the droplet diameter  $\overline{d_d}$  is reported as a function of the speed of rotation for the 4 sets of experiments of Table 21. The droplet size scales as  $N^{-2/3}$  in all cases where  $N=60\omega/2\pi$ . This result is consistent with equation (1).

### 6.3.2. Influence of capillary diameter

Figure 83 shows an image sequence of droplet injection for a given system of liquids (cf parameters in Table 21) and at a constant speed of rotation  $N=3600$  rpm ( $a_c=850g$ ), for two capillary inner diameters:  $D_i=250 \mu m$  and  $D_i=530 \mu m$  (respectively  $M_{16}$  and  $M_{17}$ ). We observe that the larger the capillary diameter, the larger the droplet size. This is consistent with the fact that the capillary forces increase with the capillary diameter and thus the droplet is expected to detach with a larger volume.

Set	Experiments	Phase 1	Phase 2	$\rho_1$ [Kg.m <sup>-3</sup> ]	$\rho_2$ [Kg.m <sup>-3</sup> ]	$\mu_1$ [Pa.s]	N [rpm]	$\gamma_{12}$ [N.m <sup>-1</sup> ]	$Q_c$ [ $\mu L.s^{-1}$ ]	$D_i$ [ $\mu m$ ]
5	$M_{16}$	S20	E <sub>2</sub>	950	1081	0.02	3600	0.041	11	250
	$M_{17}$								15	530

Table 21: Physical parameters of test cases with different capillary diameter ( $\mu_2=0.0024$  Pa.s).

$D_i$ [ $\mu m$ ]	$t \approx 0.7$ ms	$t \approx 1.2$ ms	$t \approx 2.8$ ms	$t \approx 3.2$ ms	$\overline{d_d}$ [ $\mu m$ ]	$\sigma_d$ [ $\mu m$ ]	$f$ [ $s^{-1}$ ]
250					405	3.57	310
530					519	5.75	200

Figure 83: Image sequence of droplet formation and detachment for cases  $M_{16}$  and  $M_{17}$ .  $\overline{d_d}$  is the mean droplet diameters,  $\sigma_d$  is the standard deviation and  $f$  is the frequency of injection.



### 6.3.3. Influence of surfactants

In order to study their effect on the size of injected droplets, surfactants are added in either phase 1 (Ethoxylated Silicone co-polymer) or in phase 2 (SDS). The addition of Silicone co-polymer surfactant in phase 1 at a concentration 0.047 mM reduces the surface tension  $\gamma_{12}$  at equilibrium from 40 mN.m<sup>-1</sup> to 8 mN.m<sup>-1</sup>. At a concentration of 10 mM (higher than the CMC value 8.2 mM) in phase 2, the SDS surfactant reduces  $\gamma_{12}$  at equilibrium from 40 mN.m<sup>-1</sup> to 11 mN.m<sup>-1</sup>. The effect of surfactants is evaluated with selected test cases detailed in Table 22. We first evaluate the effect of adding surfactant to phase 1 (M<sub>5</sub> and M<sub>24</sub>) and then to phase 2 (M<sub>18</sub> and M<sub>25</sub>), the droplet phase.

Experiment	Phase 1	Phase 2	$\rho_1$ [Kg.m <sup>-3</sup> ]	$\rho_2$ [Kg.m <sup>-3</sup> ]	$\mu_1$ [Pa.s]	$Q_c$ [ $\mu$ L.s <sup>-1</sup> ]	f [s <sup>-1</sup> ]	$\gamma_{12}$ [N.m <sup>-1</sup> ]
<b>Effect of the silicone co-polymer inside phase 1 on droplet size</b>								
M <sub>5</sub>	S10	E <sub>2</sub>	930	1081	0.01	8	277	0.04
M <sub>24</sub>	S10_DBE					7	268	0.008
<b>Effect of SDS inside phase 2 on droplet size</b>								
M <sub>18</sub>	S50	E <sub>2</sub>	960	1081	0.05	1	30	0.043
M <sub>25</sub>		E <sub>4</sub>				6	180	0.012

Table 22: Physical parameters of droplet injection experiments with surfactants ( $\mu_2=0.0024$  Pa.s).

#### Surfactant in phase 1

Figure 84 shows the images of detached droplets in experiments M<sub>5</sub> and M<sub>24</sub>. The average droplet size obtained in the experiment M<sub>5</sub> is 380  $\mu$ m, a value close to that obtained in M<sub>24</sub> (368  $\mu$ m). Contrary to equation (1), the presence of surfactants in phase 1 does not reduce the droplet size. This result suggests that surfactants did not cover the droplet interface during the drop formation and detachment. In order to evaluate the dynamics of surfactant migration to the interface, the characteristic diffusion time across the mass boundary layer of thickness  $\delta$  around the newly created drop interface is estimated. It is scaled as the ratio of the  $\delta$  squared over the diffusion coefficient of the surfactant in the bulk ( $t_{tr} \sim \delta^2/D$ ). The diffusion coefficient of the silicone co-polymer, estimated from the Stokes-Einstein equation, is  $D=3.7 \cdot 10^{-11}$  m<sup>2</sup>.s<sup>-1</sup>. The mass transfer boundary layer  $\delta$  is estimated at 2.5  $\mu$ m, as obtained from a correlation of Sherwood number (Froessling N., 1938) (reader is referred to Appendix B for more details on this calculation). According to this estimate, the transfer time of surfactants is about 180 ms. Eventhough this is an estimaion, it is nearly 50 times larger than the time of droplet formation, defined as the inverse of droplet injection frequency f (reported in Table 22). The interfacial tension between the droplet and phase 1 should thus be only slightly decreased during the formation of the droplet, explaining why the droplet detaches with the same size in M<sub>24</sub> as in M<sub>5</sub> ( $\bar{d}_d$  being slightly higher in M<sub>5</sub> due to a lower  $\gamma_{12}$ ).

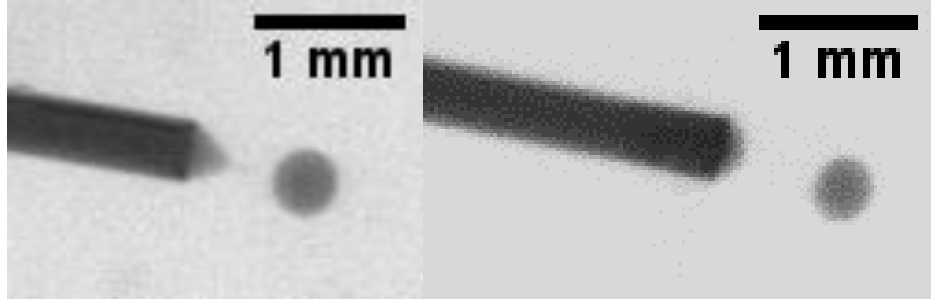


Figure 84: Images of injected droplets. Left: case  $M_5$ ,  $\bar{d}_d = 380 \mu\text{m}$ . Right: case  $M_{24}$ ,  $\bar{d}_d = 368 \mu\text{m}$ .

### Surfactant in phase 2 (droplet phase)

We now evaluate the effect of adding surfactant to phase 2 ( $M_{18}$  and  $M_{25}$ ), the droplet phase. The size of injected droplet for experiment  $M_{18}$  is  $421 \mu\text{m}$ , larger by only 2.6% than the droplet injected obtained for experiment  $M_{25}$  (Figure 85). This suggests that the surface tension  $\gamma_{12}$  is not modified by the presence of SDS surfactant inside the droplet. In order to validate this hypothesis, the mass  $m_s$  of surfactants spread on the droplet interface during its formation is estimated, and based on this calculation, the interfacial tension of the droplet is evaluated according to Henry's adsorption isotherm. In appendix B, we estimate the diffusion coefficient  $\mathcal{D} = 1.3 \cdot 10^{-10} \text{ m}^2 \cdot \text{s}^{-1}$  and the mass transfer flux  $\phi_s \approx 8 \cdot 10^{-12} \text{ kg} \cdot \text{s}^{-1}$ . During the droplet formation, which lasts about 4 ms, the mass of surfactant adsorbed on the droplet interface is  $m_s \approx 3 \cdot 10^{-14} \text{ kg}$ , leading to a very small adsorption density  $\Gamma = 2.23 \cdot 10^{-7} \text{ mol} \cdot \text{m}^{-2}$  as compared to the maximum possible adsorption  $\Gamma_\infty = 5.2 \cdot 10^{-5} \text{ mol} \cdot \text{m}^{-2}$  for a saturated interface. According to Henry's equation of state  $\gamma_{12} = \gamma_0 - k_B T \Gamma$  (valid at low concentration), the surface tension will remain unchanged based on this calculation, explaining the droplet size does not change when surfactants are added to the droplet phase. Reader can refer to appendix B for more details on the calculation.

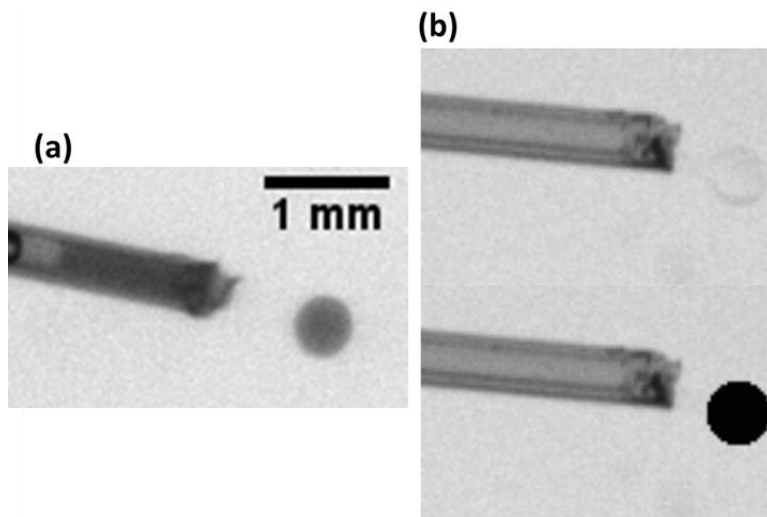


Figure 85: Images of injected droplets (a) case  $M_{18}$ ,  $\bar{d}_d = 410 \mu\text{m}$ ; (b) case  $M_{25}$ ,  $\bar{d}_d = 410 \mu\text{m}$ .

### 6.3.4. Scaling law for droplet size

In Figure 86, the drop reduced volume  $(d_d/D_i)^3$  has been plotted as a function of  $Bo_D$  for all experimental cases of Table 19. For experiments with surfactants either in phase 1 or in phase 2, the Bond number was computed using the value  $\gamma_{12}$  of surface tension between phase 1 and 2 without surfactants given the results described in the previous paragraph. The majority of experiments are performed with a capillary inner diameter  $D_i=250 \mu\text{m}$ , and their corresponding experimental points gather on a master curve equivalent to a linear decreasing power law:  $(\bar{d}_d/D_i)^3 = 8Bo_D^{-1}$ , consistent with equation (2) as shown in Figure 86. This problem was also addressed in the study of Zhang & Stone, 1997 in a more extensive way (taking into account droplet viscosity effect and external flow) under the effect of gravity, and the volume of the injected droplet ( $\sim (\frac{d_d}{D_i})^3$ ) was shown to be proportional to  $Bo_D^{-1}$ , equally  $d \propto Bo_D^{-1/3}$ . Droplets injected with smaller and larger capillary tubes ( $D_i= 100 \mu\text{m}$  and  $D_i= 530 \mu\text{m}$ ) followed also the same trend, with some scattering of the data for  $D_i= 530 \mu\text{m}$  when the drop diameter reaches a size comparable to the capillary diameter. In this case, the static force balance as written in eq. (2) is probably not accurate, probably due to the effect of pinch-off dynamics on the retracting liquid thread, as illustrated in Figure 83. Note that the flow Reynolds number in the capillary  $Re_c = \rho_2 U_c D_i / \mu_2$  varies between 1 and 25 in the present experiments. The frequency of drop injected in phase 1 is an important parameter regarding the interface crossing in continuous mode. From mass conservation considerations, the frequency of drop injection in this range of Reynolds and Bond number therefore scales as  $f^* = 0.18Bo_D$  (The droplets grow from the capillary tip of inner diameter  $D_i$  at a flow rate inside the tube of a velocity  $u_c$ .  $f^*$  is the frequency normalized by the characteristic frequency  $\frac{u_c}{D_i}$ ).

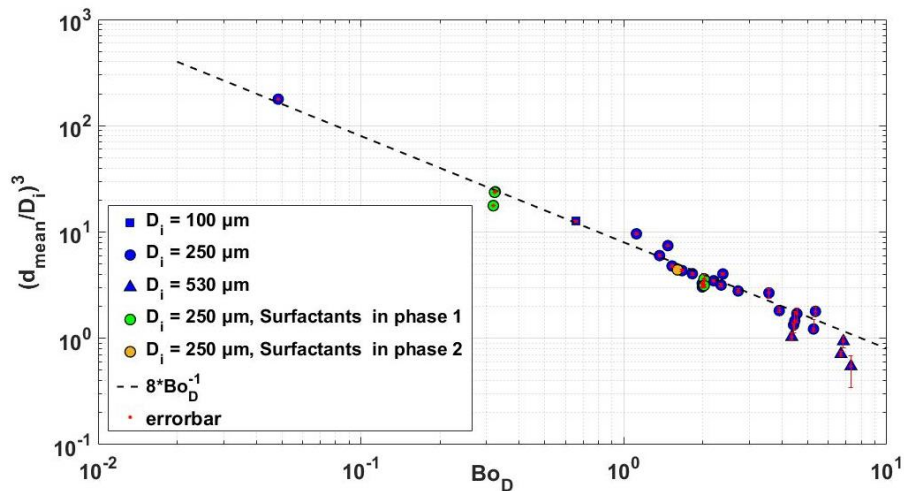


Figure 86: Evolution of drop volume  $(\bar{d}_d/D_i)^3$  as a function of  $Bo_D$  for all experiments.

As a conclusion, the scaling law of Figure 86 allows the determination of the droplet size for a given system of fluids in the present device, when the deformation of the droplet

is controlled by the surface tension ( $Oh_D < 0.1$ , as in our experiments). Due to a short formation time, surfactants present either in the drop or external phase don't have time to migrate to the interface during drop formation and can be disregarded in the drop formation process. Interfacial tension considered in the Bond number is that of liquid-liquid systems without surfactants.

## 6.4. Droplet trajectory before crossing

After detachment from the capillary tip, the droplet rises in phase 1 towards the 1-3 interface. The droplet trajectory is reconstructed through tracking the centroids of different droplets detected by Hough transform analysis (Chapter 5), in all images recorded during different rotations. The coordinates of the droplets in each rotation are then superposed in a single frame. For different systems of fluids at different rotation speeds, the trajectory and velocity profiles of the droplet in phase 1 are modeled by a force balance. Finally, a scaling law is proposed for the droplet shape at steady state of the drop rising in phase 1.

### 6.4.1. Description of droplet motion in the centrifugal cell

For experiment  $M_{14}$ , (cf Table 23 and Table 24), Figure 87 shows the droplet trajectory  $y=f(x)$  and the evolution of the velocity components of the droplets in the Cartesian frame noted  $\{x',y'\}$  in chapter 5. The trajectory corresponds to 216 different droplets detected during 147 cell revolutions at a constant rotation speed  $N=3600$  rpm ( $a_c \approx 850g$ ). The droplet detaches from the capillary tube at  $x \approx 0.08$  cm, so the points of abscissa  $x < 0.08$  cm correspond to the stage when the droplet keeps attached to the capillary tip. The droplet detaches from the tip with a non-zero velocity (Figure 87 (b)). As it rises in phase 1, it takes a linear trajectory with an inclination angle  $\theta \approx 12^\circ$  with respect to the capillary tube axis ( $y=0$ ), as shown in Figure 87 (a). This deviation is due to the Coriolis force  $F_C$  ( $F_C/F_G=0.06$ ), which induces a small drift in the  $y$  direction with a velocity component  $u_y$  of small amplitude. The velocity of the droplet increases until reaching a plateau (quasi-steady state due to the linear increase of centrifugal acceleration with distance  $x$ ) at  $u_{max} \approx 0.78$  m.s<sup>-1</sup> and  $x \approx 0.18$  cm where the droplet wake is developed, leading to a nearly constant drag force. Note that the increase of centrifugal acceleration can be neglected, as the droplet travels a distance of 4 mm inside phase 1, equivalent to an increase in acceleration of only 3%.

Experiment	Phase 1	Phase 2	$\rho_1$ [Kg.m <sup>-3</sup> ]	$\rho_2$ [Kg.m <sup>-3</sup> ]	$\mu_1$ [Pa.s]	$\mu_2$ [Pa.s]	$\gamma_{12}$ [N.m <sup>-1</sup> ]	$D_i$ [μm]	N [rpm]	$\bar{d}_a$ [μm]
$M_{14}$	Silicone oil S5	Sucrose E <sub>2</sub>	913	1081	0.005	0.0024	0.037	250	3600	367

Table 23: Physical parameters of test case  $M_{14}$ .

Experiment	$\xi_{12}$	$\lambda_{12}$	$Bo_{12}$	$Ar$
$M_{14}$	0.184	0.48	1.4	19

Table 24: Non-dimensional numbers of test case  $M_{14}$ .

The droplet trajectory in Figure 87 (a) follows a straight line of equation  $y = \tan \theta x + y_0$ , where  $y_0$  is the ordinate at the instant of detachment, close to zero. The section of the cell is  $(x_L, y_L) = 1 \text{ cm} \times 1 \text{ cm}$  and the distance between the capillary tube axis and the cell walls is 0.5 cm. In order to avoid break up, the droplet should not meet the cell wall before arriving to the interface. Based on the equation of trajectory, a critical position of the interface  $x_{cr} = 0.5 y_L / \tan \theta$  ( $y_L = 1 \text{ cm}$  is the cell length) can be determined above which the droplet meets the cell walls before arriving to the interface. The experimental system is designed in order to prevent such a scenario.

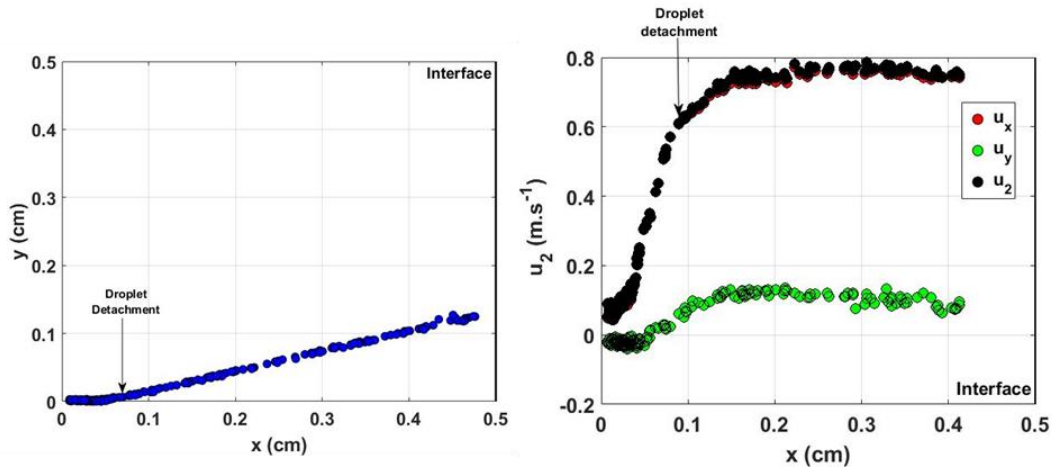


Figure 87: (a) Trajectory of the droplet inside phase 1 in the image frame of reference. (b) The evolution of the velocity components  $u_x$  and  $u_y$  in the image frame of reference with the magnitude of the velocity.

Figure 88 displays the axial profile of the droplet aspect ratio  $\chi$ , starting at  $x = 0.08 \text{ cm}$  (detachment location). The droplet is initially slightly deformed ( $\chi \approx 1.2$ ), and  $\chi$  increases as the drop is rising with an oblate shape. Aspect ratio then reaches a plateau value ( $\chi \approx 1.67 \pm 0.05$ ). Note that a plateau for  $\chi$  is reached at a slightly larger distance than for the velocity plateau, as already obtained in the numerical simulations (chapter 4). This time shift is systematic and dependent on phase 1 viscosity and is a result of the viscous stresses effect on the deformation dynamics.

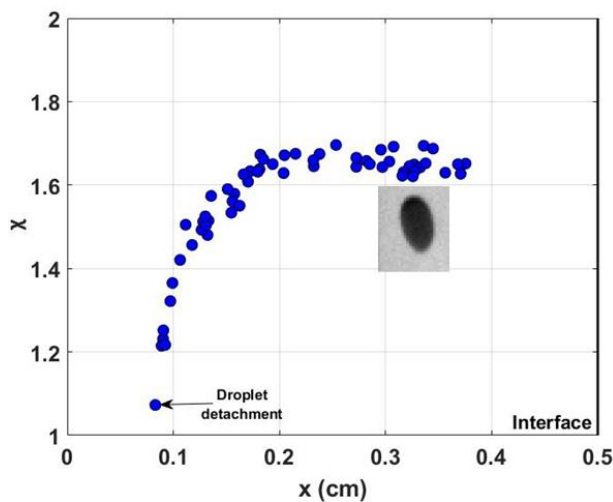


Figure 88: Aspect ratio profile of a droplet rising in phase 1 after injection (case  $M_{14}$ ).

### 6.4.2. Modelling of droplet motion

The droplet trajectory and velocity can be modelled through a force balance on the rising droplet, written in a frame attached to the rotating cell. Forces acting on the droplet are: the centrifugal force  $F_G$ , the Coriolis force  $F_C$ , the drag force  $F_D$  and the added mass force  $F_M$  (Basset force is neglected here). These forces, sketched in Figure 89, are expressed in a polar coordinates system following:

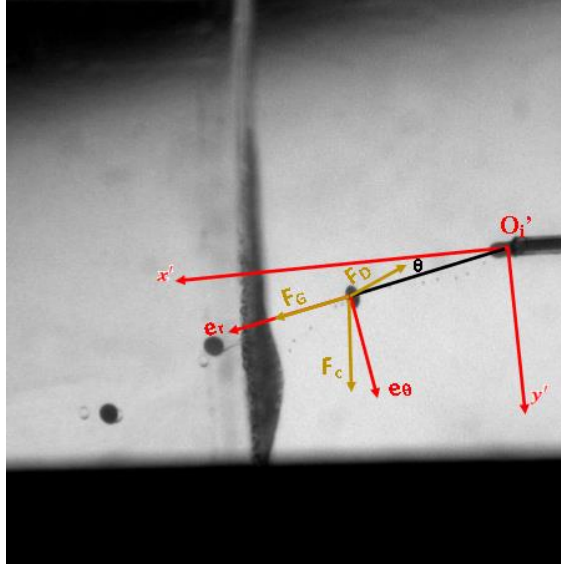


Figure 89: Forces acting on the droplet in the cell, with  $F_G$ : Centrifugal force,  $F_C$ : Coriolis force,  $F_D$ : Drag force.

- **Centrifugal force:**  $\vec{F}_G = (m_2 - m_1)\vec{r} \times \vec{\omega} \times \vec{\omega} = (\rho_2 - \rho_1) \frac{\pi d^3}{6} \omega^2 \begin{pmatrix} r \\ 0 \end{pmatrix}_{\vec{e}_r, \vec{e}_\theta}$
- **Coriolis force:**  $\vec{F}_C = 2m_2\vec{u}_2 \times \vec{\omega} = 2\rho_2 \frac{\pi d^3}{6} \omega \begin{pmatrix} r\dot{\theta} \\ -\dot{r} \end{pmatrix}_{\vec{e}_r, \vec{e}_\theta}$
- **Drag force:**  $\vec{F}_D = -\frac{1}{2}C_D\pi R^2\rho_1 u_2\vec{u}_2 = -\frac{1}{2}C_D\rho_1\pi R^2(\dot{r}^2 + r\dot{\theta}^2)^{0.5} \begin{pmatrix} \dot{r} \\ r\dot{\theta} \end{pmatrix}_{\vec{e}_r, \vec{e}_\theta}$
- **Added mass:**  $\vec{F}_M = -C_M m_2 \vec{a}_c = -C_M \rho_2 \frac{\pi d^3}{6} \begin{pmatrix} \ddot{r} - r\dot{\theta}^2 \\ r\ddot{\theta} + 2\dot{r}\dot{\theta} \end{pmatrix}_{\vec{e}_r, \vec{e}_\theta}$

In these expressions,  $C_D = f(\chi, \lambda_{12}, Re)$  is the drag coefficient,  $C_M$  is the added mass coefficient.  $C_M = 0.5$  for a rigid sphere, whereas for deformable shapes as in the case of droplets and bubbles, the coefficient is correlated to the aspect ratio  $\chi$ , following:

$$C_M = \frac{\alpha_0}{2 - \alpha_0} \quad (3)$$

- $\alpha_0 = 2(\zeta_0^2 + 1)(1 - \zeta_0 \cot^{-1}(\zeta_0))$  for prolate shape droplets
- $\alpha_0 = 2(\zeta_0^2 + 1)\zeta_0 \cot^{-1}(\zeta_0) - \zeta_0^2$  for oblate shape droplets

with  $\zeta_0 = (\chi^2 - 1)^{-\frac{1}{2}}$

The forces involved depend on system parameters and are difficult to vary independently. So, instead of performing a parametric study to investigate the influence of each parameter separately on the trajectory, second Newton's law was developed into a system of 2 non-linear 2<sup>nd</sup> order differential equations, reading:

$$\left\{ \begin{array}{l} -(m_2 - m_1)r\omega^2 + 2m_2\omega r\dot{\theta} - 0.5C_D\rho_1\pi R^2(\dot{r}^2 + r\dot{\theta}^2)^{0.5}\dot{r} = (m_2 + C_M m_1)(\ddot{r} - r\dot{\theta}^2) \\ -2m_2\omega\dot{r} - 0.5C_D\rho_1\pi R^2(\dot{r}^2 + r\dot{\theta}^2)^{0.5}r\dot{\theta} = (m_2 + C_M m_1)(r\ddot{\theta} + 2\dot{r}\dot{\theta}) \end{array} \right\} \quad (4)$$

The resolution of the above system has been achieved with the MATLAB® solver “ode23s” with the appropriate initial conditions. It gives the temporal evolution of the droplet displacement and velocity computed at each instant as  $\vec{u}_2 = \dot{r}\vec{e}_r + r\dot{\theta}\vec{e}_\theta$ . In what follows, we compare the results of the trajectory and velocity obtained by experiments to the solution of equation (4). Results presented correspond to five different experiments reported in Table 25 (physical parameters) and Table 26 (non-dimensional numbers), all at the same rotation speed (N=3600 rpm), but in different flow regimes (1.5 < Ar < 19). Different correlations for the drag coefficient (C<sub>D</sub>) were tested in the simulations and the numerical predictions of this model have been compared to the experimental results.

Experiment	Phase 1	Phase 2	$\rho_1$ [Kg.m <sup>-3</sup> ]	$\rho_2$ [Kg.m <sup>-3</sup> ]	$\mu_1$ [Pa.s]	$\mu_2$ [Pa.s]	$\gamma_{12}$ [N.m <sup>-1</sup> ]	D <sub>i</sub> [μm]	N [rpm]	$\bar{d}_d$ [μm]
M <sub>14</sub>	Silicone oil S5	Sucrose E <sub>2</sub>	913	1081	0.005	0.0024	0.037	250	3600	367
M <sub>5</sub>	Silicone oil S10		930		0.01		0.04			380
M <sub>16</sub>	Silicone oil S20		950		0.02		0.041			405
M <sub>18</sub>	Silicone oil S50		960		0.05		0.043			424
M <sub>11</sub>	Silicone oil S100		960		0.1		0.044			422

Table 25: Physical parameters of trajectory experiments.

Experiment	$\xi_{12}$	$\lambda_{12}$	Bo <sub>12</sub>	Ar
M <sub>14</sub>	0.184	0.48	1.4	19
M <sub>5</sub>	0.162	0.24	1.2	9
M <sub>16</sub>	0.138	0.12	1.19	5
M <sub>18</sub>	0.126	0.048	1.14	2
M <sub>11</sub>	0.126	0.024	1.84	1.5

Table 26: Non-dimensional numbers of the trajectory experiments.

Figure 90 compares the experimental Reynolds profile (based on the instantaneous axial velocity) to the numerical predictions obtained with different drag laws for experiment M<sub>14</sub>, with initial conditions taken from the experiment (drop position and velocity at detachment from the tip). The added mass coefficient C<sub>M</sub> is computed from equation (3), based on the instantaneous value of the aspect ratio  $\chi$ . Four different correlations recapped in Table 27 were tested for the drag coefficient C<sub>D</sub>(t). The first expression was developed by Schiller & Nauman (Schiller & Nauman, 1933) which is valid for a rigid sphere rising

inside a continuous fluid up to  $Re=800$  (with a range of -4 to 5 % deviation, Clift et al., 1978). This expression was corrected by Haywood et al., 1994 to account for droplet deformation, but disregarding internal recirculation. The third correlation evaluated was proposed by Rivkind & Ryskin G., 1976 for a non-deformed droplet with a clean interface up to  $Re=200$ . Finally, a corrected version of the latter is proposed in Clift et al., 1978 and in the study of Helenbrook & Edwards, 2002 to take the effect of deformation into consideration. Note that in the drag force and drag coefficient expressions, the droplet diameter ( $\bar{d}_d$ ) is replaced by the instantaneous value of the droplet major axis ( $2\bar{a}_d(t)$ ).

As shown in Figure 90, the model predictions underestimate the droplet terminal velocity with Schiller & Naumann correlation for rigid spheres. This result suggests that the droplet interface cannot be considered as fully immobile, and that a tangential velocity still exists at the droplet surface, in spite of a possible transfer of contaminants. The correction of the drag coefficient accounting for the deformation of the droplet ( $\chi=1.7$  at steady state, see Figure 92) predicts a much smaller velocity (Haywood & al.). This result is obviously worse, knowing that accounting for the deformation in the model without internal motion only increases the drag of the droplet. If we now consider models of drag coefficients for a clean liquid-liquid interface, for example, the one proposed by Rivkind & Ryskin for non-deformed droplets ( $1 < Re < 200$ ), we find that it predicts  $Re$  over the experimental data by 20%. This difference could be due either to a drop deformation or to the contamination of the droplet interface. The substitution of drop diameter in this correlation by the major axis of the deformed drop leads to the drag coefficient of Clift & al. This model gives a velocity profile nicely fitting the experimental results.

	$C_D$ expression	Reference
1	$C_D(t) = \frac{24}{Re(t)} (1 + 0.15Re(t)^{0.687}); Re = \frac{\rho_1 u(t) \bar{d}_d}{\mu_1}$	Schiller & Naumann
2	$C_D(t) = \frac{24}{Re(t)} (1 + 0.15Re(t)^{0.687}) (1 + 0.06Re(t)^{-0.12} We^{1.4}); Re = \frac{\rho_1 u(t) \bar{d}_d}{\mu_1}, We = \frac{\rho_1 u^2(t) \bar{d}_d}{\gamma_{12}}$	Haywood & al.
3	$C_D(t) = \frac{1}{1 + \lambda_{12}} \left[ \lambda_{12} \left( \frac{24}{Re(t)} + 4Re(t)^{-\frac{1}{3}} \right) + 14.9Re(t)^{-0.78} \right]; Re = \frac{\rho_1 u(t) \bar{d}_d}{\mu_1}$	Rivkind & Ryskin
4	$C_D(t) = \frac{1}{1 + \lambda_{12}} \left[ \lambda_{12} \left( \frac{24}{Re(t)} + 4Re(t)^{-\frac{1}{3}} \right) + 14.9Re(t)^{-0.78} \right]; Re = \frac{\rho_1 u(t) (2\bar{a}_d)}{\mu_1}$	Clift & al. Helenbrook & Edwards

Table 27: Drag coefficient expressions tested in the model.  $a_d$  is the drop major axis radius (oblate shape).

The model prediction using the drag law proposed by Clift et al. or Helenbrooks & Edwards has been further evaluated with four other experiments,  $M_5$ ,  $M_{16}$ ,  $M_{18}$ , and  $M_{11}$ . Reynolds numbers at steady state are respectively 25, 9, 1.6, and 0.6. The droplet undergoes deformation while rising and the aspect ratio profiles are reported in Figure 92. Note that, in these experiments no surfactant was used. The predictions of the model are in very good agreement with the experimental data as shown in Figure 91, validating the drag law for the present experiments, in the range of Reynolds number and drop deformation investigated.



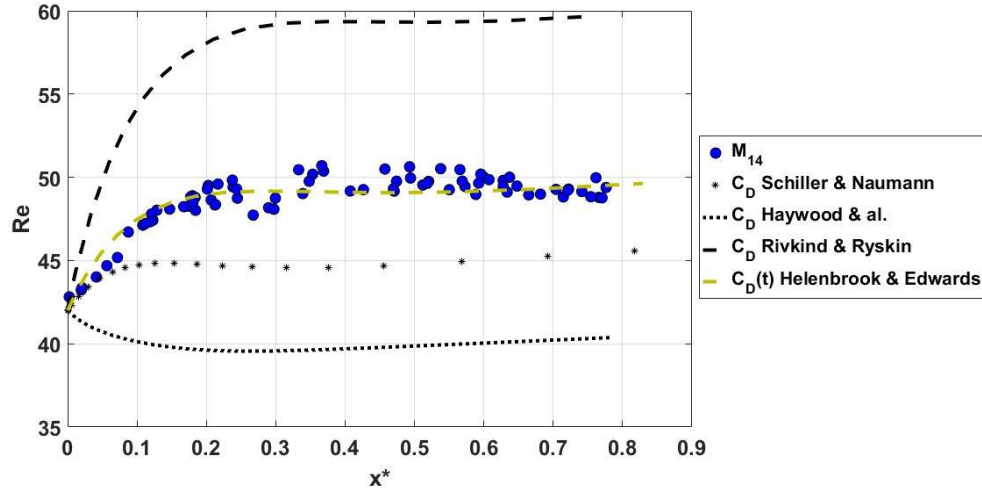


Figure 90: Reynolds number axial profile for case  $M_{14}$  starting from detachment position. Symbols: experiments; Lines: numerical predictions of model (4.11) with different drag laws taken from the literature.

This result tends to validate the assumption of a drag force controlled by deformed droplets with clean interfaces rather than saturated with surfactants. This result suggests that even present, contaminants do not have enough time to get adsorbed at the drop interface during its rising over a time of 10 ms in the centrifugal field.

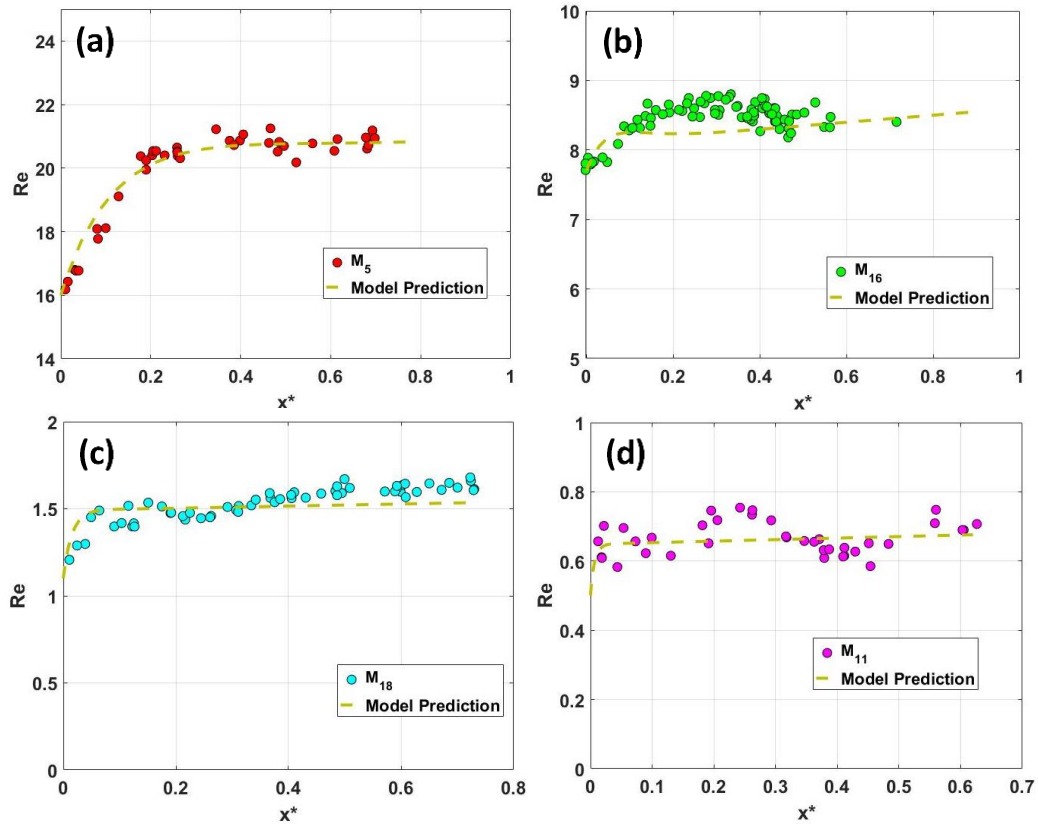


Figure 91: Reynolds number profiles for (a)  $M_{14}$ , (b)  $M_5$ , (c)  $M_{18}$ , and (d)  $M_{11}$ , alongside with the respective predicted velocity by the model.

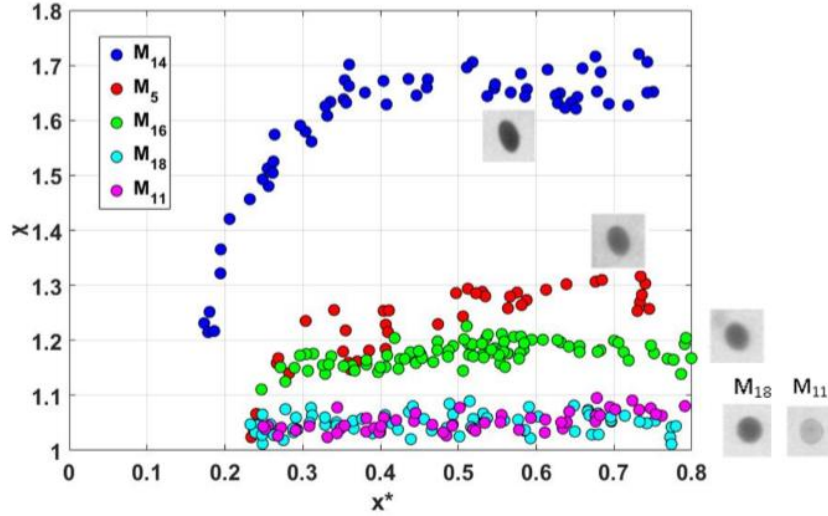


Figure 92: The aspect ratio in the five systems of Table 25 as a function of  $x^*$  with the corresponding screenshots of the droplet.

To conclude on this part, the trajectory and velocity of the droplet in a centrifugal cell can be very well predicted through the resolution of the force balance in the rotating frame, by using the drag coefficient correlation of Rivkind & Ryskin with a correction of the length scale ( $2\overline{a}_d$  instead of  $\overline{d}_d$ ).

### 6.4.3. Droplet shape

The shape of droplets rising in phase 1 are now discussed for experiments of Table 25. In Figure 93, the instantaneous aspect ratio profiles are plotted along with those of the instantaneous Weber number,  $We_{12}(t) = \rho_1 u^2(t) d / \gamma_{12}$ , scaling the droplet deformation in inertial regime. The droplet deforms into an oblate shape as a response to its acceleration. This response, as observed, comes with a delay due to viscous effects. The aspect ratio finally arrives to a quasi-terminal value before the droplet arrival to the interface.

Figure 93 compares the experimental data to the DNS (Direct Numerical Simulations) predictions of  $\chi$  and  $We_{12}$  profiles for cases  $M_{14}$ ,  $M_5$ , and  $M_{16}$ , performed with the code presented in chapter 3. Since implementing an initial velocity in the numerical code would require the knowledge of the initial velocity field, initial conditions in the numerical simulation correspond to a zero velocity field and a drop spherical shape. However, the velocity converges towards the same steady regime as in experiments, even if initial conditions are different. It is recalled that the simulations do not account for the presence of any contaminants or surfactants at the interface (continuity of tangential stresses at the interface). The aspect ratio at steady stage is also observed to be in good agreement with the experimental measurements, with a discrepancy of 5% for the three cases.

The good agreement obtained for both drop velocity and deformation validates that the presence of contaminants can be neglected in the experiments. This comparison confirms also that the drag law proposed by Clift et al. and Helenbrooks & Edwards, is the right correlation to include in the force balance (equation 4). Based on these results, drop deformation of clean droplets at steady state is analyzed.

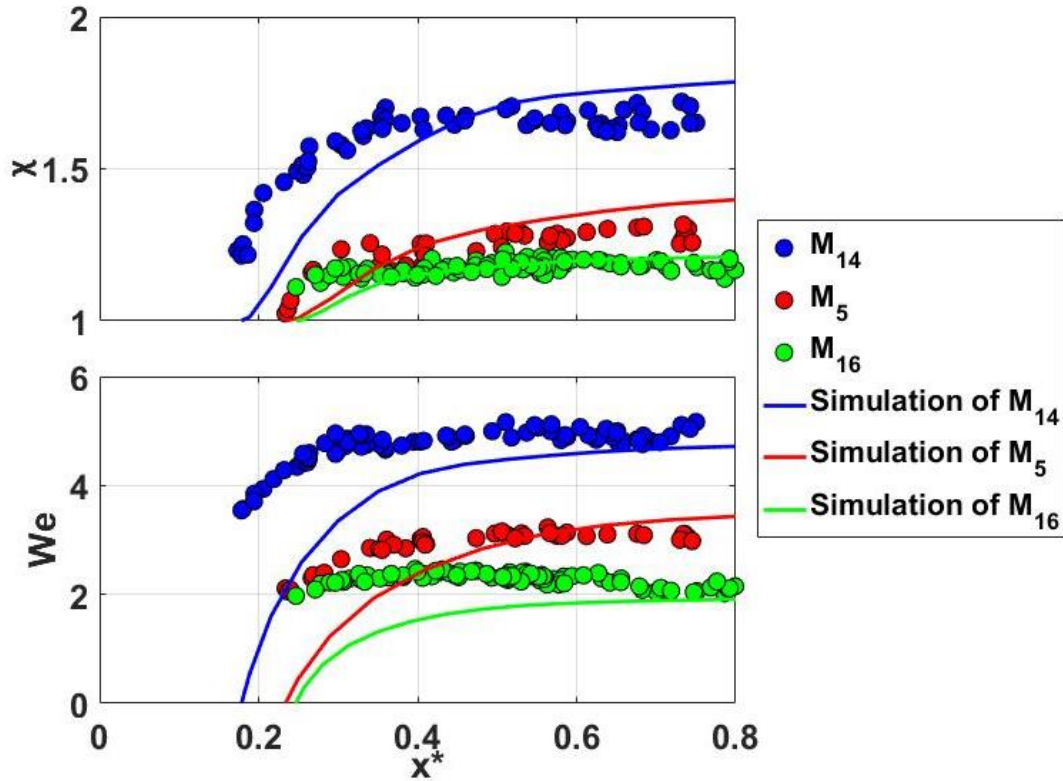


Figure 93: Aspect ratio and Weber number profiles. Symbols: experiments. Lines: numerical simulations of experiments  $M_{14}$ ,  $M_5$ , and  $M_{16}$ .

In order to study the evolution of the drop deformation with inertia, we use numerical simulations from chapter 4, the five experiments of Table 25, the simulations of experimental cases, and former simulation results of drop rising dynamics in a stagnant liquid phase from Lalanne et al., 2015. In Table 28, the values of  $We_{12}$ ,  $Oh_{12}$ , and aspect ratio  $\chi$  at steady state are reported for all these cases.

	$We_{12}$	$Oh_{12}$	$\chi$
<b>Numerical Simulations</b>	7.770	0.1066	3.297
	2.541	1.067	1.371
	2.560	0.92	1.278
	6.690	0.173	2.443
	7.834	0.071	3.271
	9.029	1.067	2.428
	7.381	0.71	2.246
<b>Simulations of experiments</b>	4.764	0.02	1.792
	3.527	0.019	1.42
	1.957	0.019	1.216
<b>Experiments</b>	4.996	0.02	1.726
	3.135	0.019	1.273
	2.438	0.018	1.198
	0.392	0.017	1.051
	0.183	0.0148	1.033
<b>Lalanne &amp; al. Simulations</b>	0.45	0.0142	1.04
	0.81	0.0142	1.0695
	1.8	0.0142	1.175
	2.3	0.0142	1.258
	2.4	0.0142	1.287
	0.86	0.0071	1.074
	1.74	0.0071	1.192
	1.53	0.0071	1.166
	2.9	0.0071	1.439
	1.98	0.0035	1.237
	1.89	0.0035	1.23

Table 28: Non-dimensional numbers and aspect ratio values from experiments and simulations.

As the particulate Reynolds number is large for all these droplets (up to 120), the deformation characterized by  $\chi$ , has been plotted as a function of  $We_{12}$  in Figure 94. It is clear from this plot that a first relevant dimensionless number to describe the droplet deformation is the Weber number: most of the data follow an increasing trend until  $We_{12} \approx 2$ , corresponding to a moderate aspect ratio ( $\chi < 2$ ). For the same limit the correlation of Wellek et al., 1966 (see equation 3 in chapter 2) remains valid. The dispersion, higher for larger  $We_{12}$ , is believed to be due to the internal viscosity because the velocity gradients in the droplet can dissipate a part of the kinetic energy supplied by the outer flow and responsible for deformation. The importance of the internal viscous effects over the interfacial tension that resists to drop deformation can be quantified through the Ohnesorge number  $Oh_{12}$  (values are reported in Table 28), which varies by two orders of magnitude for the cases considered.

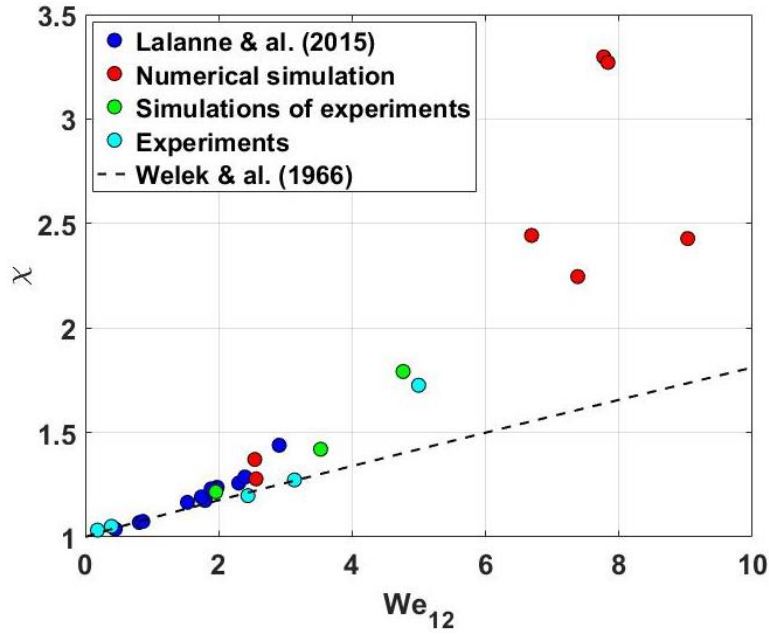


Figure 94: Evolution of  $\chi$  as a function of  $We_{12}$ .

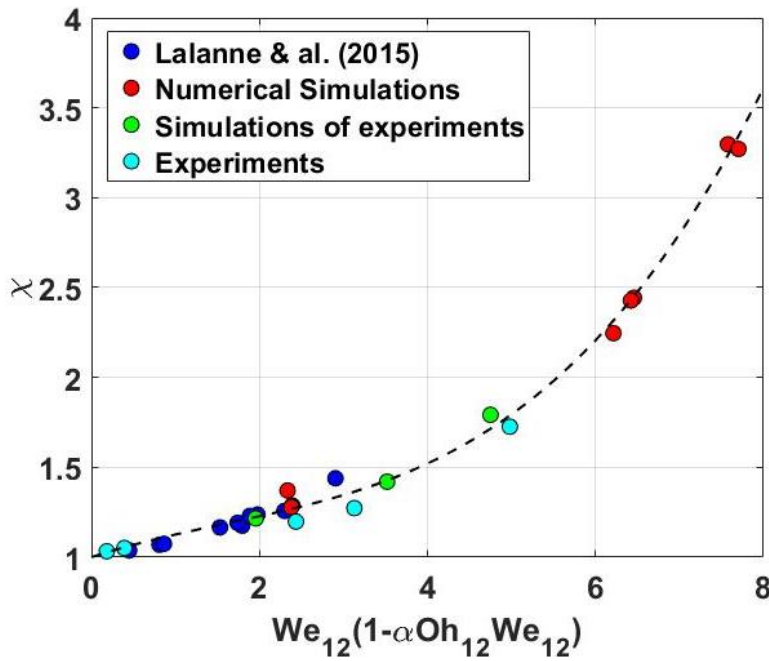


Figure 95: Evolution of  $\chi$  as a function of a function of  $We_{12}$  and  $Oh_{12}$ .

By considering  $Oh_{12}$ , a detailed inspection of the data reveals that the following simple expression of  $\chi$  as a function of both  $We_{12}$  and  $Oh_{12}$  plotted in Figure 95 perfectly predicts the deformation of a droplet with a certain viscosity:

$$\chi = 0.0068 f^3(We_{12}, Oh_{12}) - 0.0326 f^2(We_{12}, Oh_{12}) + 0.1519 f(We_{12}, Oh_{12}) + 1$$

$$f(We_{12}, Oh_{12}) = We_{12}(1 - \alpha Oh_{12} We_{12})$$

where  $\alpha$  is a constant which best fits the data for a value of 0.03. In the latter correlation, the correction due to  $Oh_{12}$  is not constant, but is found to be proportional to  $We_{12}$ , so the correction increases as  $We_{12}$  is increasing.

Note that this correction is different to that obtained with clean bubbles rising in stagnant liquids of various viscosities. In this case, the role of external viscosity is dominant and involves a Morton number (Legendre et al., 2012), the correction being also proportional to  $We_{12}$ .

## 6.5. Interfacial Crossing

This section is dedicated to the experimental conditions allowing interfacial crossing and to the characterization of the different crossing regimes observed. The crossing conditions are first examined in various experimental conditions, then the dynamics of crossing is described: the droplet shape during and after crossing, the mechanism of film formation, and the volume of phase 1 coating the droplet rising in phase 3. As a preamble, it is worth discussing the range of variation of the main non-dimensional numbers governing the crossing a liquid/liquid interface for a droplet in inertial regime, namely, the 1-3 interfacial Bond number  $Bo_{13}$  and the Archimedes number  $Ar$ , as a function of the physical parameters which are experimentally tunable.

The Bond number at the interface  $Bo_{13}$ , compares the buoyancy force of the droplet to the resistive force due to interface surface tension. This parameter scales the crossing criterion in static conditions as seen in previous chapters.  $Bo_{13}$  is proportional to the centrifugal acceleration and to the square of the droplet radius ( $\propto a_c R^2$ ). As previously discussed in section 6.3.4, the droplet radius  $R$  is inversely proportional to the cubic root of the centrifugal acceleration  $R \propto a_c^{-1/3}$  ( $a_c = r_i \omega^2$ ). Therefore, in these experiments, the Bond number scales as  $a_c^{1/3}$ , rather than linearly. As a consequence,  $Bo_{13}$  varies by only a factor of 4.6 when the rotation speed varies from 600 rpm to the maximum rotation speed of 6000 rpm which is the acceptable limit for the present experiment. However, the addition of surfactants in either phase 1 or 3 increases by an order of magnitude the range of  $Bo_{13}$  (from 0.7 to 20 as reported in Table 31).

In the same way, in phase 1, the Archimedes number, describing the flow regime, can be expressed independently from the speed of rotation, substituting in  $Ar$  the droplet diameter dependence with  $\omega$ :  $Ar \propto \frac{1}{\mu_1} \left( \frac{\rho_1 \gamma_{12}}{D_i} \right)^{1/2}$ . In presence of surfactants in either phase 1 or 2, since the diffusion time of surfactants is always much larger than the droplet formation and

rising times, the surface tension  $\gamma_{12}$  is that corresponding to the 1-2 interface at equilibrium without surfactants. In the range of capillary diameter used in these experiments (100-530  $\mu\text{m}$ ),  $Ar$  varies by a factor of 2.3. The viscosity of phase 1,  $\mu_1$ , was thus varied to extend the range of Archimedes number (between 1 and 20, as shown in Table 31). In that aim, silicone oil was chosen for phase 1, with viscosity varying between 0.005 and 0.1 Pa.s.

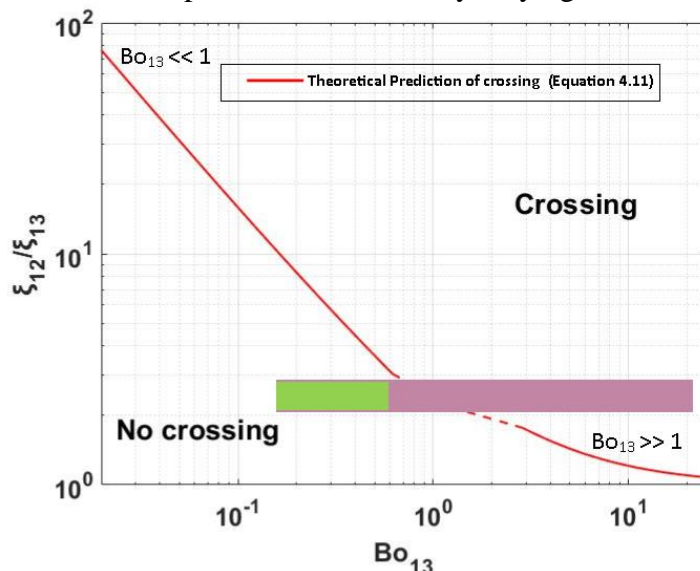


Figure 96: Range of values of  $(\xi_{12}/\xi_{13}, Bo_{13})$  parameters for experiments with (purple) and without surfactants (green).

6.5.1. Conditions for crossing (“Crossing or not crossing?”)

In what follows, crossing condition of the interface is examined for systems, which correspond to fluid combinations presented in Table 29.

System	Phase 1	Phase 2	Phase 3
1	Silicone oil <b>S10</b>	Sucrose <b>E2</b>	Water <b>W</b>
2	Silicone oil <b>S50</b>		Water <b>W</b>
3	Silicone oil <b>S5</b>		Water <b>W</b>
4	Silicone oil <b>S10</b>		Water + SDS at 0.5*CMC <b>E7</b>
5	Silicone oil <b>S10</b>		Water + SDS at 0.73*CMC <b>E6</b>
6	Silicone oil <b>S10</b>		Water + SDS at 1.22*CMC <b>E5</b>
7	Silicone oil <b>S5</b>		Water + SDS at 1.22*CMC <b>E5</b>
8	Silicone oil <b>S20</b>		Water + SDS at 1.22*CMC <b>E5</b>
9	Silicone oil <b>S50</b>		Water + SDS at 1.22*CMC <b>E5</b>
10	Silicone oil <b>S100</b>		Water + SDS at 1.22*CMC <b>E5</b>
11	Silicone oil <b>S20</b>		Water + Tween 80 at 1.13*CMC <b>E8</b>
12	Silicone oil S10 +Silicone co-polymer <b>S10_DBE</b>		Water <b>W</b>
13	Silicone oil S10 +Silicone co-polymer <b>S10_DBE</b>		Water + SDS at 1.22*CMC <b>E5</b>

Table 29: Liquid-liquid systems of crossing condition experiments..

Physical parameters of experimental conditions											Results	
Experiment	System	$\rho_1$ [Kg.m <sup>-3</sup> ]	$\rho_2$ [Kg.m <sup>-3</sup> ]	$\rho_3$ [Kg.m <sup>-3</sup> ]	$\mu_1$ [Pa.s]	$\mu_2$ [Pa.s]	$\mu_3$ [Pa.s]	$\gamma_{12}$ [N/m]	$\gamma_{13}$ [N/m]	N [rpm]	$\bar{d}_d$ [ $\mu$ m]	f [s <sup>-1</sup> ]
C <sub>1</sub>	1	930	1081	997	0.01	0.0024	0.001	0.04	0.036	5400	298	620
C <sub>2</sub>	2	960	1081	997	0.05	0.0024	0.001	0.043	0.037	3600	488	30
C <sub>3</sub>	3	913	1081	997	0.005	0.0024	0.001	0.037	0.01	5400	272	-
C <sub>4</sub>	4	930	1081	997	0.01	0.0024	0.001	0.04	0.018	3600	371	20
C <sub>5</sub>	5	930	1081	997	0.01	0.0024	0.001	0.04	0.013	3600	362	15
C <sub>6</sub>	6	930	1081	997	0.01	0.0024	0.001	0.04	0.011	600	1400	3.33
C <sub>7</sub>	6	930	1081	997	0.01	0.0024	0.001	0.04	0.011	1440	721	24
C <sub>8</sub>	6	930	1081	997	0.01	0.0024	0.001	0.04	0.011	3000	454	171
C <sub>9</sub>	6	930	1081	997	0.01	0.0024	0.001	0.04	0.011	3600	380	272
C <sub>10</sub>	6	930	1081	997	0.01	0.0024	0.001	0.04	0.011	4200	352	427
C <sub>11</sub>	6	930	1081	997	0.01	0.0024	0.001	0.04	0.011	4800	306	40
C <sub>12</sub>	6	930	1081	997	0.01	0.0024	0.001	0.04	0.01	5400	299	364
C <sub>13</sub>	7	913	1081	997	0.005	0.0024	0.001	0.04	0.011	3600	367	347
C <sub>14</sub>	7	913	1081	997	0.005	0.0024	0.001	0.04	0.01	5400	268	90
C <sub>15</sub>	8	950	1081	997	0.02	0.0024	0.001	0.041	0.012	3600	408	310
C <sub>16</sub>	9	960	1081	997	0.05	0.0024	0.001	0.043	0.013	3600	424	30
C <sub>17</sub>	10	960	1081	997	0.1	0.0024	0.001	0.044	0.013	3000	532	119
C <sub>18</sub>	10	960	1081	997	0.1	0.0024	0.001	0.044	0.013	3600	422	10
C <sub>19</sub>	10	960	1081	997	0.1	0.0024	0.001	0.044	0.013	4200	379	212
C <sub>20</sub>	10	960	1081	997	0.1	0.0024	0.001	0.044	0.013	5400	346	150
C <sub>21</sub>	11	950	1081	997	0.02	0.0024	0.001	0.044	0.015	3600	519	100
C <sub>22</sub>	12	930	1081	997	0.01	0.0024	0.001	0.008	0.004	1440	718	24
C <sub>23</sub>	12	930	1081	997	0.01	0.0024	0.001	0.008	0.004	3600	366	268
C <sub>24</sub>	13	930	1081	997	0.01	0.0024	0.001	0.008	0.001	1440	652	8
C <sub>25</sub>	13	930	1081	997	0.01	0.0024	0.001	0.008	0.001	3600	368	268

Table 30: Physical parameters of crossing condition experiments. Colors indicate the parameters which vary between the considered experiments.

In Table 30 and Table 31 physical and non-dimensional parameters are reported for each experiment. In Table 31, non-dimensional parameters ( $Re_T$ ,  $We_{12}$ ,  $I_{ex}$ ) have been also reported. Note that the drop terminal velocity  $u_T$  ( $Re_T$  and  $W_{12}$ ) and the minimal velocity during crossing  $u_{min}$  ( $I_{ex}$ ), defined in chapter 4, were only measured when crossing led to successful encapsulation.



Experiment	Non-dimensional number of experimental conditions											Results			
	System	$\xi_{12}$	$\xi_{13}$	$\xi_{12}/\xi_{13}$	$\lambda_{12}$	$\lambda_{13}$	$Bo_{12}$	$Bo_{13}$	Ar	Oh <sub>12</sub>	Oh <sub>13</sub>	Cross	Re <sub>T</sub>	We <sub>12</sub>	I <sub>ex</sub>
C <sub>1</sub>	1	0.162	0.072	2.25	0.24	0.1	1.54	0.74	10	0.01	0.08	No	-	-	-
C <sub>2</sub>	2	0.126	0.039	3.27	0.048	0.02	2.02	0.86	2	0.017	0.38	No	-	-	-
C <sub>3</sub>	3	0.184	0.092	2	0.48	0.2	1.61	0.87	17	0.023	0.09	No	-	-	-
C <sub>4</sub>	4	0.162	0.072	2.25	0.24	0.1	1.11	1.14	9	0.021	0.12	Yes <sup>(1)</sup>	-	-	-
C <sub>5</sub>	5	0.162	0.072	2.25	0.24	0.1	1.16	1.59	9	0.02	0.15	Yes <sup>(2)</sup>	-	-	-
C <sub>6</sub>	6	0.162	0.072	2.25	0.24	0.1	0.4	0.63	9	0.01	0.08	No	-	-	-
C <sub>7</sub>	6	0.162	0.072	2.25	0.24	0.1	0.72	1.17	9	0.015	0.12	Yes <sup>(1)</sup>	-	-	-
C <sub>8</sub>	6	0.162	0.072	2.25	0.24	0.1	1.22	1.97	10	0.018	0.15	Yes <sup>(2)</sup>	-	-	-
C <sub>9</sub>	6	0.162	0.072	2.25	0.24	0.1	1.2	2.05	9	0.02	0.16	Yes	22	3.33	1.07
C <sub>10</sub>	6	0.162	0.072	2.25	0.24	0.1	1.43	2.3	10	0.02	0.17	Yes	-	-	-
C <sub>11</sub>	6	0.162	0.072	2.25	0.24	0.1	1.55	2.5	9	0.023	0.18	Yes	-	-	-
C <sub>12</sub>	6	0.162	0.072	2.25	0.24	0.1	1.7	2.7	10	0.023	0.18	Yes	-	-	-
C <sub>13</sub>	7	0.184	0.092	2	0.48	0.2	1.4	2.36	19	0.023	0.08	Yes	50	5.14	1.17
C <sub>14</sub>	7	0.184	0.092	2	0.48	0.2	1.57	2.65	17	0.025	0.1	Yes	-	-	-
C <sub>15</sub>	8	0.138	0.049	2.78	0.12	0.05	1.19	1.59	5	0.02	0.3	Yes	10	2.6	1.22
C <sub>16</sub>	9	0.126	0.039	3.27	0.048	0.02	1.13	1.4	2	0.018	0.75	Yes	1.6	0.37	1.3
C <sub>17</sub>	10	0.126	0.039	3.27	0.024	0.01	1.34	1.5	1.2	0.017	1.34	Yes <sup>(2)</sup>	-	-	-
C <sub>18</sub>	10	0.126	0.039	3.27	0.024	0.01	1.85	2.26	1.4	0.016	1.3	Yes	0.7	0.24	1.67
C <sub>19</sub>	10	0.126	0.039	3.27	0.024	0.01	1.84	2.1	1	0.02	1.5	Yes	-	-	-
C <sub>20</sub>	10	0.126	0.039	3.27	0.024	0.01	1.81	2	1	0.02	1.6	Yes	-	-	-
C <sub>21</sub>	11	0.138	0.049	2.78	0.12	0.05	1.77	1.86	6.7	0.017	0.24	Yes	9.8	1.9	1.29
C <sub>22</sub>	12	0.162	0.072	2.25	0.24	0.1	2.9	2.6	8	0.034	0.2	Yes <sup>(1)</sup>	-	-	-
C <sub>23</sub>	12	0.162	0.072	2.25	0.24	0.1	6.25	5.55	9.4	0.045	0.26	Yes <sup>(1)</sup>	-	-	-
C <sub>24</sub>	13	0.162	0.072	2.25	0.24	0.1	3.5	12.5	10	0.033	0.38	Yes	-	-	-
C <sub>25</sub>	13	0.162	0.072	2.25	0.24	0.1	5.7	20.4	9	0.046	0.5	Yes	13	6.6	2

Table 31: Non-dimensional parameters of experiments. <sup>(1)</sup> Crossing observed but the droplets break right after. <sup>(2)</sup> Droplets cross the interface in clusters. Colors indicate the parameters varying between the considered experiments.

Figure 97 displays the crossing conditions of all experiments on a  $(\xi_{12}/\xi_{13}, Bo_{13})$  map. Filled symbols indicate droplets that crossed the interface, open symbols correspond to the cases where crossing was not achieved. The curve on this graph represent the theoretical prediction of crossing/non-crossing transition for solid spheres in static configuration (i.e. without initial motion of the drop at the interface). This curve is represented by two asymptotic behaviors respectively corresponding to the limits of small and high  $Bo_{13}$ , given by following equations (see chapter 2):

$$Bo_{13} \ll 1, \quad \frac{\xi_{12}}{\xi_{13}} = \frac{3}{2Bo_{13}} + \frac{1}{2} + \frac{3}{4} \left( \log \left( \frac{4}{\sqrt{Bo_{13}}} \right) - 0.577 \right) \quad (5)$$

$$Bo_{13} \gg 1, \quad \frac{\xi_{12}}{\xi_{13}} = \frac{3}{2Bo_{13}} \sin^2(k) + \frac{1}{4} \left( 2 + 3 \cos(k) - \cos^3(k) \right) + \frac{3}{4} \left( \frac{2}{Bo_{13}} \right)^{\frac{1}{2}} \sin^2(k)$$

$$\text{with } k = 2(2Bo_{13})^{-1/4} \quad (6)$$

It can be concluded from Figure 97 that this curve is also a good indicator of critical crossing conditions for the experiments (except for exp. C<sub>2</sub>, but in this case, it is also possible that crossing could have taken a very long time, due to the high viscosity of phase 2), suggesting that the main effect which controls the crossing condition is the balance between gravity forces and the surface tension preventing the deformation of the interface, scaled by the interfacial Bond number  $Bo_{13}$  and the shape of the interface in contact with the drop (defined by the pseudo contact angle  $k$  in (5) and (6)). Similar conclusion was obtained with the numerical simulations of solid-like or deformable droplets. In the experiments, the presence of surfactants at the interface is expected to involve additional forces coming at play in the force balance, such as those induced by the concentration gradient along the interface when the droplets is deformed (Marangoni effect). If surfactants probably affect the dynamics of crossing, Marangoni effect does not seem to represent an important contribution in the static force balance. Indeed, regarding crossing conditions, the main effect of surfactants here is to decrease the equilibrium interfacial tension  $\gamma_{13}$  in  $Bo_{13}$ .

### 6.5.2. Droplet crossing configurations:

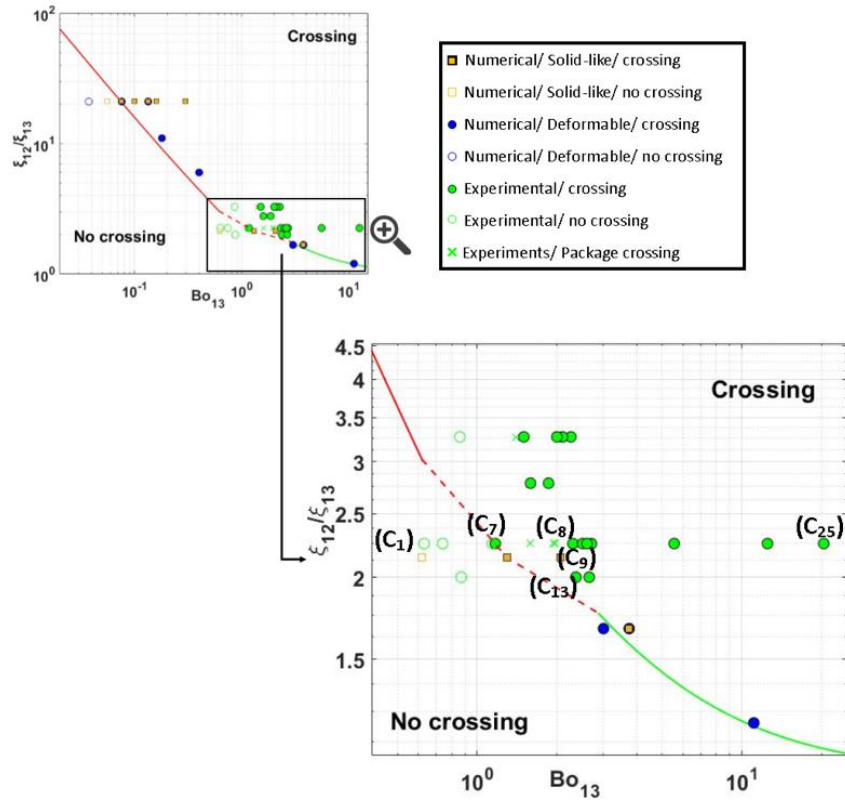
Among the conditions for which droplet crossing is effective, different crossing modes are observed as illustrated on the image sequences of Figure 97 and summarized below:

**Crossing with no film entrained** – For case C<sub>7</sub> (system 6), the drop crosses the interface and immediately coalesces with phase 3, suggesting a complete drainage of phase 1 at the front of the drop and subsequent breakup of this film. In this case, the droplet reaches the interface with a significant velocity, then strongly decelerates at the interface, the velocity even becoming negative. Crossing is hence similar to static conditions but still possible since the droplet weight fulfills the crossing criterion at this interfacial Bond number. However, the thin film drainage rate is higher than the rising time of the drop in phase 3 and coalescence occurs just above the interface.

**Crossing in clusters** – In case C<sub>8</sub> (system 6) the theory predicts interface crossing, but droplets accumulate at the interface and finally cross the interface in clusters. The droplet apparent weight is sufficient to make it cross but within a time larger than the inverse of the injection frequency of the droplets ( $t_f \approx 6$  ms), leading to the formation of a cluster. When clusters form at the interface, the crossing time is larger than the inverse of the drop injection frequency, and smaller when no cluster is observed.

**Crossing with oil entrainment** – Interface crossing with oil entrainment is observed in both experiments C<sub>9</sub> and C<sub>25</sub>, corresponding to the same rotation speed ( $N=3600$  rpm) and to systems 6 and 13 respectively. The difference between C<sub>9</sub> and C<sub>25</sub> is that in case C<sub>25</sub>, a silicon copolymer based on surfactant was introduced in phase 1, which results in a much higher Bond number  $Bo_{13}$  (lower interfacial tension  $\gamma_{32}$ ) and thus an excess of inertia  $I_{ex}$  twice higher than for case C<sub>9</sub>. In both cases, an oil shell coats the droplet but the resulting entrained volume is larger for C<sub>25</sub> than for C<sub>9</sub>. In case C<sub>25</sub>, due to the development of a longer column, the coating volume takes the shape of a liquid thread behind the droplet

(Figure 98). Note that the breakage of the liquid thread was not observed (before the capsule reached the chamber walls). In both cases, the film thickness around the particle is large enough, so film rupture, as it happened in case C7 at a much lower inertia, is not observed.



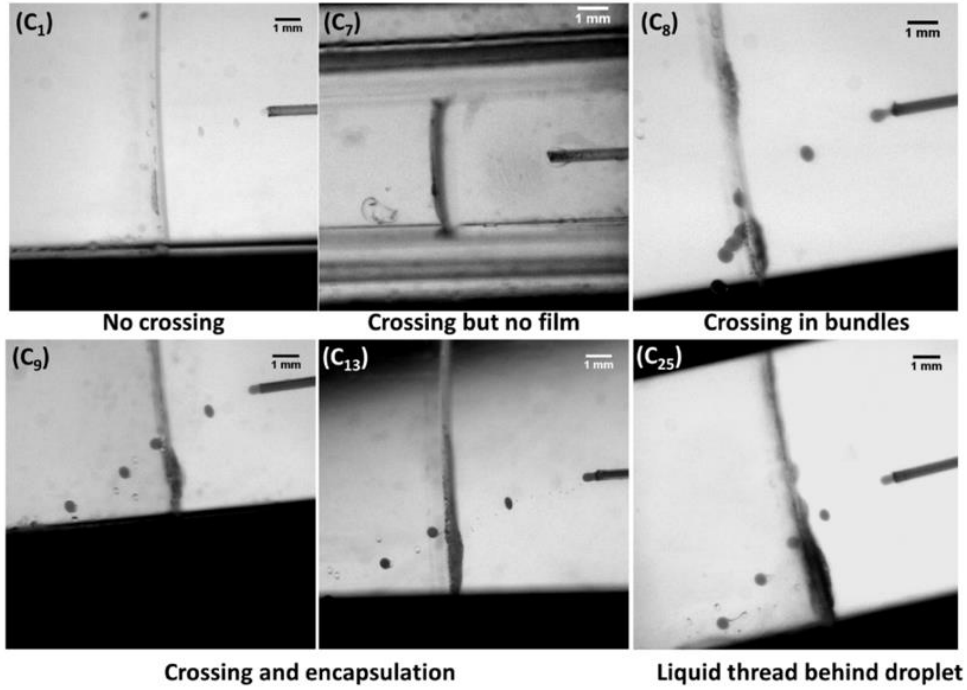


Figure 97: Crossing conditions diagram and images of typical observations of crossing.

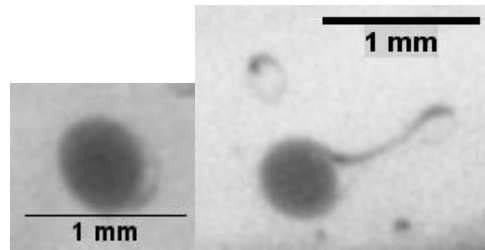


Figure 98: A zoomed image of coated droplets in phase 3. Left: case C<sub>9</sub> ; Right: case C<sub>25</sub>.

The next experiments analyzed are C<sub>13</sub>, C<sub>16</sub> and C<sub>18</sub>, for which crossing with oil entrainment is observed at different flow regimes, respectively characterized by  $Ar=19, 2,$  and  $1.2$  ( $Re_T \approx 50, 1,$  and  $0.6$ ). These three experiments have been carried out at a rotation speed  $N=3600$  rpm, where droplets are injected from a capillary tube of size  $D_i=250 \mu m$ . The physical parameters and non-dimensional numbers of these experiments are reported in Table 32 and Table 33 respectively, including  $I_{ex}$ , the inertia excess rescaled by the criterion for static crossing for a rigid particle, and given by functions of interfacial Bond number ( $Bo_{13}$ ) in eq. (5) and (6).

Experiment	$\rho_1$ [Kg.m <sup>-3</sup> ]	$\rho_2$ [Kg.m <sup>-3</sup> ]	$\rho_3$ [Kg.m <sup>-3</sup> ]	$\mu_1$ [Pa.s]	$\mu_2$ [Pa.s]	$\mu_3$ [Pa.s]	$\gamma_{12}$ [N.m <sup>-1</sup> ]	$\gamma_{13}$ [N.m <sup>-1</sup> ]	$\bar{d}_a$ [ $\mu m$ ]
C <sub>13</sub>	913	1081	997	0.005	0.0024	0.001	0.037	0.01	367
C <sub>16</sub>	960			0.05			0.043	0.013	421
C <sub>18</sub>	960			0.1			0.043	0.013	422

Table 32: Physical parameters of experiments C<sub>13</sub>, C<sub>16</sub>, C<sub>18</sub>.

Experiment	$\xi_{12}$	$\xi_{13}$	$\xi_{12}/\xi_{13}$	$\lambda_{12}$	$\lambda_{13}$	$Bo_{12}$	$Bo_{13}$	$Ar$	$Oh_{12}$	$Oh_{13}$	$Re_T$	$We_{12}$	$I_{ex}$
C <sub>13</sub>	0.184	0.092	2	0.48	0.2	1.4	2.36	19	0.02	0.08	50	5.14	1.17

$C_{16}$	0.126	0.039	3.27	0.048	0.02	1.13	1.4	2	0.02	0.75	1.6	0.37	1.3
$C_{18}$	0.126	0.039	3.27	0.024	0.01	1.85	2.26	1.4	0.02	1.3	0.6	0.24	1.67

Table 33: Non-dimensional numbers of experiments of experiments  $C_{13}$ ,  $C_{16}$ ,  $C_{18}$ .

For the lowest  $Ar$  ( $C_{18}$ ) for which the Reynolds number is less than 1 ( $Re \approx 0.6$ ), Figure 99 shows the image sequence for the droplet crossing the interface. The droplet undergoes a strong deformation into a prolate shape due to the strong reacceleration of the droplet in phase 3. Between images (c) and (e), a column forms behind the rear of the droplet, and as it goes away from the interface the column extends, thins and deforms into a curvilinear shape with two maxima deviated downwards with a non-negligible angle ( $26^\circ$  with respect to capillary axis). This non common shape (i.e. not cylindrical nor conical nor perpendicular to the plane interface as has been described by Manga & Stones, 1995 and Shopov & Minev, 1992 in gravity driven configurations) may be due to the Coriolis force. In image (f), the column thickness decreases to less than 1 pixel, and cannot be resolved. Thus, it is difficult to precisely measure the maximum column length before detachment ( $L_{max}$ ). We thus approximate it by measuring its size on the last image where it is observed. The same mechanism observed for  $C_{18}$  with  $L_{max}/\bar{d}_d \approx 9$  is also observed for  $C_{16}$ , for which  $Re_T \approx 1.7$ , but with a shorter extended column (Figure 100),  $L_{max}/\bar{d}_d \approx 7$ . In both cases, the droplet velocity decreases to zero during crossing, the excess of inertia is then mainly due to the droplet excess weight. The values of  $I_{ex}$  are very close, respectively 1.6 and 1.3 for  $C_{18}$  and  $C_{16}$ , and  $L_{max}/\bar{d}_d$  seems to be an increasing function of  $I_{ex}$ .

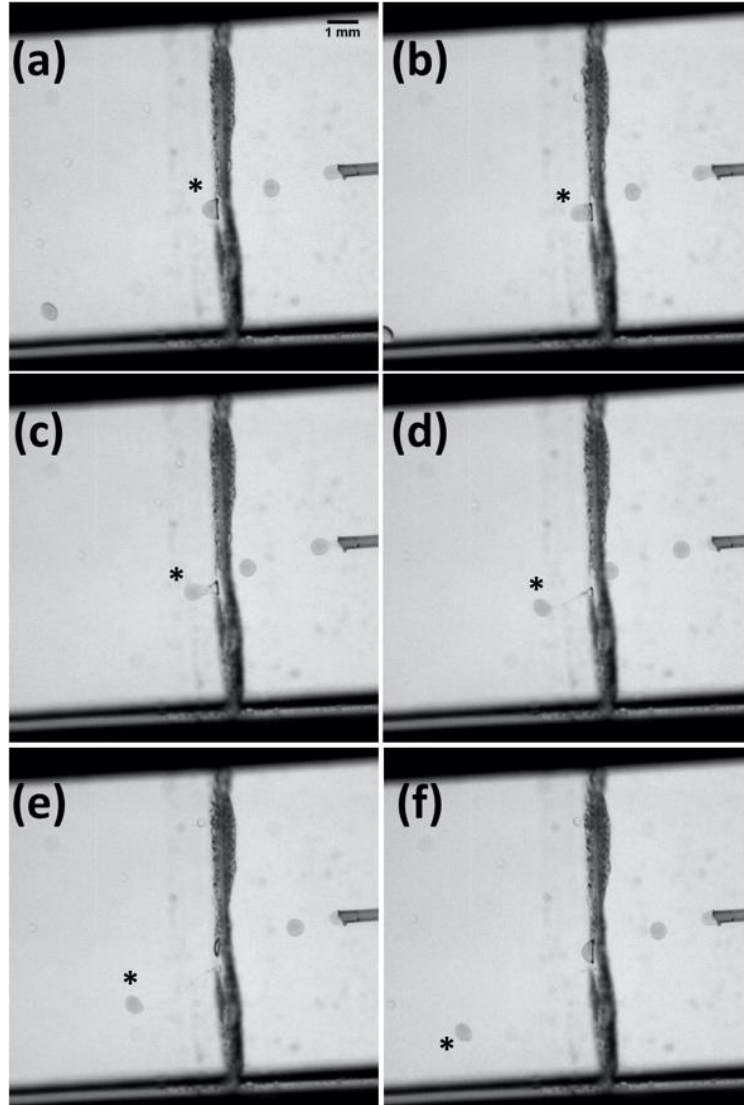


Figure 99: The image sequence of experiment  $C_{18}$ . Tracking the droplet (indicated by \*): (a) Droplet arrival at the interface with an oblate shape; (b) Transition to a prolate shape; (c) Onset of column formation; (d) and (e) column stretching; (f) coated droplet rising in phase 3.

In experiment  $C_{13}$ , the droplet reaches the interface at high inertia with a Reynolds number of 55. Figure 101 presents the sequence of images obtained for this system. In phase 1, the droplets are deformed up to an aspect ratio  $\chi \approx 1.8$ . The droplet thus arrives at the interface with an oblate shape as shown in Figure 101 (a). As the oblate droplet crosses the interface, it recovers a spherical and then a prolate shape (Figure 101 (c)) which is much less prolate than  $C_{16}$  and  $C_{18}$  because  $\lambda_{13}$  is closer to 1 for  $C_{13}$ . The column forming behind the droplet attains a maximal pinch-off length  $L_{\max}$  visibly much smaller than the one obtained for experiments  $C_{16}$  and  $C_{18}$ .  $I_{\text{ex}}$  being also smaller varying from 1.17 for  $C_{13}$  to 1.67 for  $C_{18}$ . The variation of  $L_{\max}$  in these experiments and in other cases will be analyzed extensively with comparison to numerical simulations later in this chapter (section 0). These are the general trends we observe regarding the crossing. We will discuss the effect of surfactant addition on this phenomenology before a more quantitative analysis and comparison to numerical results of chapter 4.

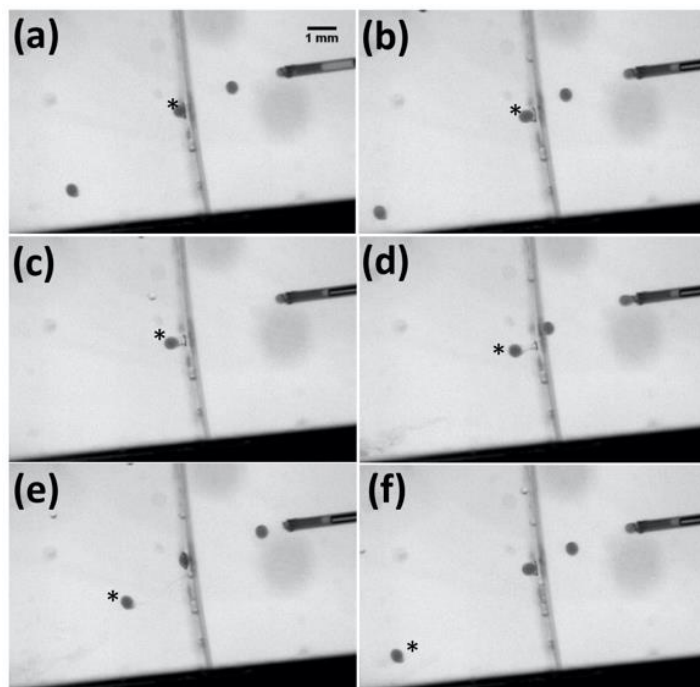


Figure 100: Image sequence of experiment  $C_{16}$ . Tracking the droplet (indicated by \*): (a) Droplet arrival at the interface with an oblate shape; (b) Transition to a prolate shape; (c) Onset of column formation; (d) and (e) column stretching; (f) coated droplets rising in phase 3.

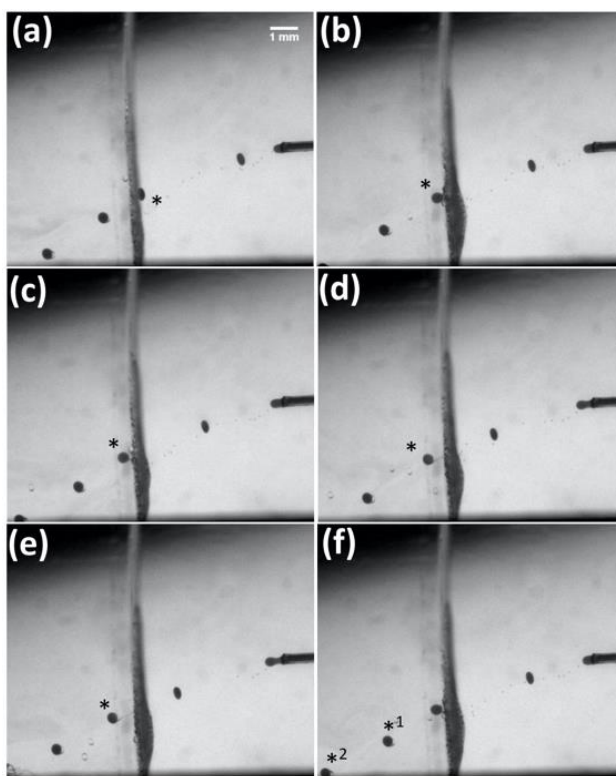


Figure 101: Image sequence of experiment  $C_{13}$ . Tracking the droplet (indicated by \*): (a) Droplet arrival at the interface with an oblate shape; (b) Transition to a prolate shape; (c) Onset of column formation; (d) and (e) column stretching; (f) coated droplets rising in phase 3.

### 6.5.3. Effect of surfactants on crossing

The addition of surfactants in phase 1 or 3 impacts the droplet crossing and coating. First it lowers the surface tension of the interface ( $\gamma_{13}$ ), facilitating interface crossing for a given system at lower inertia. Without surfactant, there is no interface crossing observed up to 5400 rpm with the fluid systems used in study: the droplet floats at the interface. Adding surfactants in phase 1 or phase 3 or in both phases, increases the interface Bond number  $Bo_{13}$  for a given value of  $\xi_{12}/\xi_{13}$ , allowing the drop to cross the interface, as shown in previous experiments. This observation is consistent with the criterion for crossing in static conditions. In addition, surfactants modify the boundary condition at the interfaces, breaking the continuity of tangential stresses on either side of the interface. If a saturated monolayer of surfactants is present on the 1-3 interface, during droplet crossing, the velocity of the film coating the drop (in a frame attached to the droplet) will be close to zero at the interface 1-3, due to a strong Marangoni stress counter-balancing the viscous stress in phase 3, and this independently of the viscosity ratio  $\lambda_{13}$ . As a consequence, the presence of surfactants is expected to slow down the drainage rate of the film coating the droplet as it is rising in phase 3, compared to the case without surfactant. But the main role of surfactants in the encapsulating process is to stabilize the film coating the droplet, due to long-range repulsive forces. If during the droplet rise in phase 3, the film in the front part of the drop is thinned down to the thickness of a black film (molecular size), an unstable hole in the monolayer and lead to coalescence. Hence increasing the concentration of surfactants at the interface increases the film disjoining pressure and stabilizes the film.

In the present system, surfactants can be added either in phase 1 or 3, or in both phases. Two different surfactants added in phase 3 were selected, SDS (Sodium dodecyl sulfate) and Tween 80 (Polysorbate 80) and one surfactant in phase 1, a silicone co-polymer ethoxylated (dimethylsiloxane-(25-30% ethylene oxide) block copolymer)

The influence of the presence of these surfactants in phase 1 or 3 or in both phases, on the crossing dynamics, the coating film volume and its stability have been investigated.

#### Surfactant in phase 3

The influence of the addition of SDS in phase 3 has been studied through 3 experiments,  $C_4$ ,  $C_5$  and  $C_9$ , corresponding to the same liquid-liquid system (system 6 in Table 29) but with increasing concentration of SDS in phase 3, as reported in Table 34. The surfactant concentration is expressed as a fraction of the CMC of SDS which is around 8.2 mM for the present system. In experiment  $C_9$ , this concentration is above the saturation of the interface with SDS, whereas for  $C_4$  and  $C_5$  it ranges below the CMC (respectively 0.5 and 0.73 x CMC). Note that the centrifugal acceleration being the same for these systems ( $N=3600$  rpm), the drop diameter formed in these experiments are close. Non-dimensional parameters are reported in Table 35.



Experiment	$\rho_1$ [Kg.m <sup>-3</sup> ]	$\rho_2$ [Kg.m <sup>-3</sup> ]	$\rho_3$ [Kg.m <sup>-3</sup> ]	$\mu_1$ [Pa.s]	$\mu_2$ [Pa.s]	$\mu_3$ [Pa.s]	$\gamma_{12}$ [N.m <sup>-1</sup> ]	$\gamma_{13}$ [N.m <sup>-1</sup> ]	$\bar{d}_d$ [ $\mu$ m]	[SDS] in phase 3
C <sub>4</sub>	930	1081	997	0.01	0.0024	0.001	0.04	0.018	371	0.5*CMC
C <sub>5</sub>								0.013	362	0.73*CMC
C <sub>9</sub>								0.011	380	1.23*CMC

Table 34: Physical parameters of experiments C<sub>4</sub>, C<sub>5</sub> and C<sub>9</sub> (system 6 in Table 29). The CMC of SDS for this system is taken equal to 8.2 mM.

Experiment	$\xi_{12}$	$\xi_{13}$	$\xi_{12}/\xi_{13}$	$\lambda_{12}$	$\lambda_{13}$	Bo <sub>12</sub>	Bo <sub>13</sub>	Ar	Oh <sub>12</sub>	Oh <sub>13</sub>
C <sub>4</sub>	0.162	0.072	2.25	0.24	0.1	1.15	1.14	9	0.021	0.12
C <sub>5</sub>							1.59		0.02	0.15
C <sub>9</sub>							1.94		0.02	0.16

Table 35: Non-dimensional parameters of experiments C<sub>4</sub>, C<sub>5</sub> and C<sub>9</sub>.

For case C<sub>4</sub>, (lowest SDS concentration) drops do not cross the interface. This observation is consistent with the static crossing criterion for the parameters corresponding to this case (Bo<sub>13</sub>=1.14 and  $\xi_{12}/\xi_{13}$ =2.25). In Figure 102(a) and (b), an accumulation of droplets at the interface can be observed. In image (b), the signature of a drop-interface coalescence can be visualized by the presence in phase 3 of a trace of the dye coloring the injected drops. This coalescence results from the film drainage and breakup of the drop resting below the interface. Hence, a concentration of SDS equal to half of the CMC is not enough to allow crossing and prevent the coating film breakup.

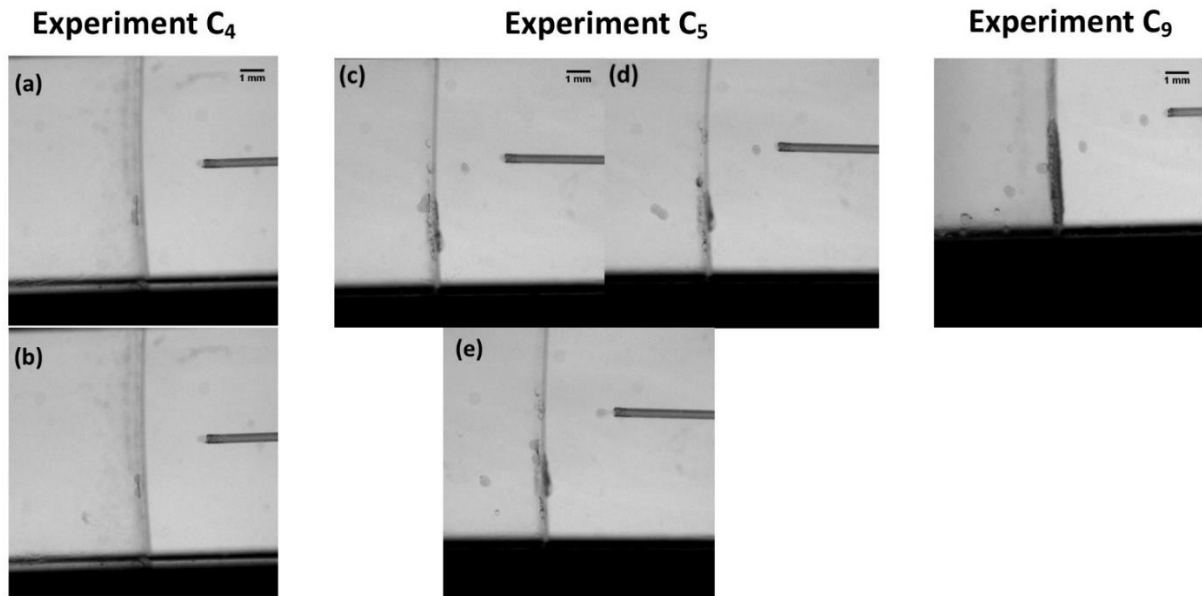


Figure 102: Images sequence for: (a) and (b) C<sub>4</sub>; (c)-(e) C<sub>5</sub>; (f) C<sub>9</sub>.

For experiment C<sub>5</sub>, SDS concentration is 0.75\*CMC and Bo<sub>13</sub>=1.59, corresponding to the critical value of the criterion of static crossing. Figure 102(c) and (d) show that in this case, droplets tend to accumulate at the interface and cross it as a cluster. However, it also happens that a single droplet crosses the interface as shown in Figure 102(e). These observations

suggest that for this experiment, the formation time of the droplet is of same order of magnitude as that of its crossing time. The slightest variation in the time of formation of the drops can shift the single drop crossing mode to the cluster crossing mode and vice-versa. As a consequence, the crossing time for this experiment can be deduced to be of the order of the inverse of the injection frequency (15Hz), i.e. close to 0.067 sec.

At a SDS concentration beyond CMC (experiment C<sub>9</sub>), droplets cross the interface individually and entrain a short column of phase 1 which detaches right above the interface. Then coated drops rise in phase 3 without bursting over several diameters (Figure 102(f)). As the injection frequency is 272 Hz for this experiment, the crossing time is smaller than  $1/272=0.0037$  sec, so more than an order of magnitude smaller than that observed for exp. C<sub>5</sub>. Considering the values of  $Bo_{13}$  of the two experiments, respectively 1.59 and 2.05 for cases C<sub>5</sub> and C<sub>9</sub>, at same density parameter ( $\xi_{12}/\xi_{13}=2.25$ ), this effect is quite significant.

Note however that if increasing the  $Bo_{13}$  allows a fast crossing in case C<sub>9</sub>, formation of oil droplets (phase 1) travelling back in phase 3 is observed, which are accumulating at the 1-3 interface. These oil drops result from the breakup of the film coating the phase 2 droplets when they hit the side walls of the cell. These drops can be visualized on the image sequences of Figure 99(e), Figure 100(c), and Figure 101(e). Then, due to the presence of SDS on the oil drop interface and on the 1-3 interfaces, the drop-interface coalescence is slowed down and oil drops rest on the 1-3 interface in phase 3 (note that they cannot cross it back since the density parameter is  $\xi_{31}/\xi_{31}=1$  in this case). These droplets of phase 1 in phase 3 accumulating on the 1-3 interface, hinder the crossing of subsequent droplets. The presence of surfactants at a concentration higher than CMC results in the formation of O/W emulsions at the interface. Thus, a SDS concentration above the CMC is enough to prevent the oil drop-interface coalescence, i.e. when the external force acting on the interstitial film is very small, but the oil film coating the droplet cannot resist to higher pressure forces as those generated by the centrifugal force on the side walls of the cell.

It can be concluded that increasing the concentration of SDS in phase 3 favors the crossing by increasing  $Bo_{13}$ . It seems however preferable for the process that SDS concentration be smaller than the CMC.

Increasing  $Bo_{13}$  (with respect to the critical value for static crossing) decreases the resistance of the interface and therefore decreases the time for crossing, which is the condition desired in a continuous encapsulation process: the smaller the crossing time, the higher the throughput. At CMC, interfacial tension no longer evolves, so the  $Bo_{13}$  can be increased for a given system and operating parameters. However, the interest of working with a concentration above CMC is to increase the speed of recovery of the saturation condition of the interface 1-3 between successive crossing droplets, keeping constant the interface loading in surfactants.

In order to evaluate the range of these observations, experiments have been carried out with a different surfactant, the polysorbate 80 (Tween 80), a non-ionic surfactant soluble in water. The physical parameters and non-dimensional numbers of this experiment are reported in Table 36 and Table 37 respectively.

Experiment	$\rho_1$ [Kg.m <sup>-3</sup> ]	$\rho_2$ [Kg.m <sup>-3</sup> ]	$\rho_3$ [Kg.m <sup>-3</sup> ]	$\mu_1$ [Pa.s]	$\mu_2$ [Pa.s]	$\mu_3$ [Pa.s]	$\gamma_{12}$ [N.m <sup>-1</sup> ]	$\gamma_{13}$ [N.m <sup>-1</sup> ]	N [rpm]	D <sub>i</sub> [ $\mu$ m]	$\bar{d}_d$ [ $\mu$ m]	[Tween 80] in phase 3
C <sub>21</sub>	950	1081	997	0.02	0.0024	0.001	0.044	0.014	3600	530	519	1.13*CMC

Table 36: The physical parameters of experiment C<sub>21</sub>. The CMC of Tween 80 is 0.012 mM.

Experiment	$\xi_{12}$	$\xi_{13}$	$\xi_{12}/\xi_{13}$	$\lambda_{12}$	$\lambda_{13}$	Bo <sub>12</sub>	Bo <sub>13</sub>	Ar	Oh <sub>12</sub>	Oh <sub>13</sub>
C <sub>21</sub>	0.138	0.049	2.78	0.12	0.05	1.77	1.86	6.7	0.017	0.24

Table 37: The non-dimensional numbers of experiment C<sub>21</sub>.

In experiment C<sub>21</sub>, the concentration of Tween 80 is equal to 1.13xCMC and the interfacial tension  $\gamma_{13}=14$  mN/m, which is close to that obtained with SDS (11 mN/m). At same rotation speed (N=3600), the injected drop diameter is larger than in the former series of experiments (diameter of the capillary is equal to 530  $\mu$ m), leading to an interfacial Bond number Bo<sub>13</sub> of 1.86, well above the critical value of static crossing at  $\xi_{12}/\xi_{13}=2.78$  (cf curve of Figure 97).

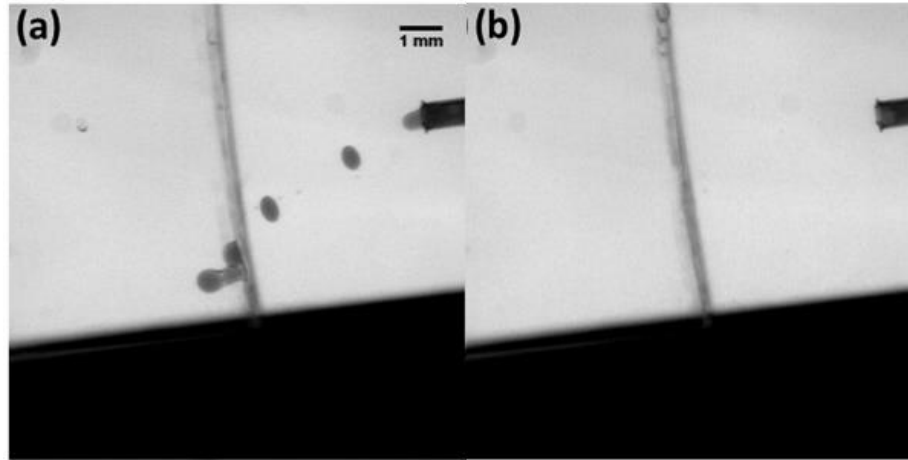


Figure 103: Image sequence of experiment C<sub>21</sub>. (a) Three droplets accumulating at the interface and crossing in a cluster (b) The plane interface after several successive crossings without O/W emulsions forming.

Image sequences of this experiment are displayed in Figure 103(a). Drops are crossing the interface, but at the injection frequency of the experiment (100 Hz), they tend to accumulate and the crossing regime is close to the cluster crossing mode. The time for crossing can be thus estimated to be larger than 0.01 sec, which is at least a factor 3 larger than the crossing time observed for experiment C<sub>5</sub> (0.0037 sec). This result suggests that the concentration of surfactant at the interface and inertia are not the only factors controlling the dynamics of crossing, the nature of the surfactant employed seems also to play a role. This effect is

presumably related to the adsorption time of the surfactant involving its surface concentration at saturation and its bulk diffusion coefficient. However, a rough estimation of these quantities based on published data does not exhibit significant differences between these two molecules. A dedicate study of these quantities on the studied systems seems necessary to conclude on this point.

**Surfactant in phase 1 and in both phases (1 and 3)**

The effect of the introduction of a surfactant in phase 1 was also tested using an ethoxylated silicone co-polymer (DBE 224 supplied by Gelest) at a concentration above the CMC value (0.047 mM) in silicone oil. At this concentration, the water/silicone oil surface tension  $\gamma_{13}$  is reduced by a factor 10, measured at  $4 \text{ mN.m}^{-1}$ . When SDS is added to phase 3 (at a concentration of  $1.22 \times \text{CMC}$ ) in this system, interfacial tension  $\gamma_{13}$  is further decreased to  $1 \text{ mN.m}^{-1}$ . Four experiments corresponding to these 2 systems both with DBE in phase 1 have been carried out (without SDS in phase 3 for experiments  $C_{22}$  and  $C_{23}$  and with SDS in phase 3 for  $C_{24}$  and  $C_{25}$ ), at two different rotation speeds for each system, 1440 and 3600 rpm. Droplets are injected from a capillary tube of diameter  $D_i=250 \mu\text{m}$ . Physical parameters and non-dimensional numbers are reported in Table 38 and Table 39 respectively. For all these cases ( $C_{22}$ ,  $C_{23}$ ,  $C_{24}$  and  $C_{25}$ ), values of the couple  $(\xi_{12}/\xi_{13}, \text{Bo}_{13})$  belong to the crossing regime in static conditions. It can be seen that the significant reduction of the surface tension provides high values of the interfacial Bond number when both SDS and DBE are introduced in phase 3 and 1 respectively (cases  $C_{24}$  and  $C_{25}$ ). Hence the use of this surfactant in phase 1 is expected to facilitate the droplet crossing as it increases  $\text{Bo}_{13}$  up to 20 times the theoretical critical value in static conditions (experiment  $C_{25}$  on Figure 97)

Experiment	$\rho_1$ [Kg.m <sup>-3</sup> ]	$\rho_2$ [Kg.m <sup>-3</sup> ]	$\rho_3$ [Kg.m <sup>-3</sup> ]	$\mu_1$ [Pa.s]	$\mu_2$ [Pa.s]	$\mu_3$ [Pa.s]	$\gamma_{12}$ [N.m <sup>-1</sup> ]	$\gamma_{13}$ [N.m <sup>-1</sup> ]	N [rpm]	$\bar{d}_a$ [ $\mu\text{m}$ ]	[DBE] in phase 1	[SDS] in phase 3
$C_{22}$	930	1081	997	0.01	0.0024	0.001	0.008	0.004	1440	718	0.047 mM	0
$C_{23}$							0.008	0.004	3600	366		0
$C_{24}$							0.008	0.001	1440	652		1.22*CMC
$C_{25}$							0.008	0.001	3600	368		1.22*CMC

Table 38: Physical parameters of cases  $C_{22}$ ,  $C_{23}$ ,  $C_{24}$  and  $C_{25}$ . The reported value of surface tension  $\gamma_{12}$  is taken at equilibrium.

Experiment	$\xi_{12}$	$\xi_{13}$	$\xi_{12}/\xi_{13}$	$\lambda_{12}$	$\lambda_{13}$	$\text{Bo}_{12}$	$\text{Bo}_{13}$	Ar	$\text{Oh}_{12}$	$\text{Oh}_{13}$
$C_{22}$	0.162	0.072	2.25	0.24	0.1	2.9	2.6	8	0.034	0.2
$C_{23}$						6.25	5.55	9.4	0.045	0.26
$C_{24}$						3.5	12.5	10	0.033	0.38
$C_{25}$						5.7	20.4	9	0.046	0.5

Table 39: Non-dimensional numbers of  $C_{22}$ ,  $C_{23}$ ,  $C_{24}$  and  $C_{25}$ .

Figure 104 and Figure 105 show image sequences of successive droplets crossing the interface for case  $C_{22}$  at 1440 rpm and of a single droplet for case  $C_{23}$ . A column of phase 1 is entrained (image (a)) and stretched before detachment (image (b)). However, the droplet bursts just after crossing the interface and coalesce with phase 3. A similar behavior

can be observed with case  $C_{23}$  at  $N=3600$  rpm, as illustrated in Figure 105. In both cases, droplets cross the interface, but the coating film cannot resist the pressure, leading to its rupture and drop coalescence in phase 3. In both cases, the surfactant is soluble in phase 1 and no surfactant is present in phase 3. This observation suggests that during crossing the surfactant concentration at the interface is not maintained close to saturation due to a too slow adsorption rate as compared to film drainage kinetics. During droplet crossing, interface deformation creates a new surface proportional to the droplet surface, so the surfactant concentration decreases by a factor proportional to the surface area increase. The film surface above the drop becomes depleted in surfactants.

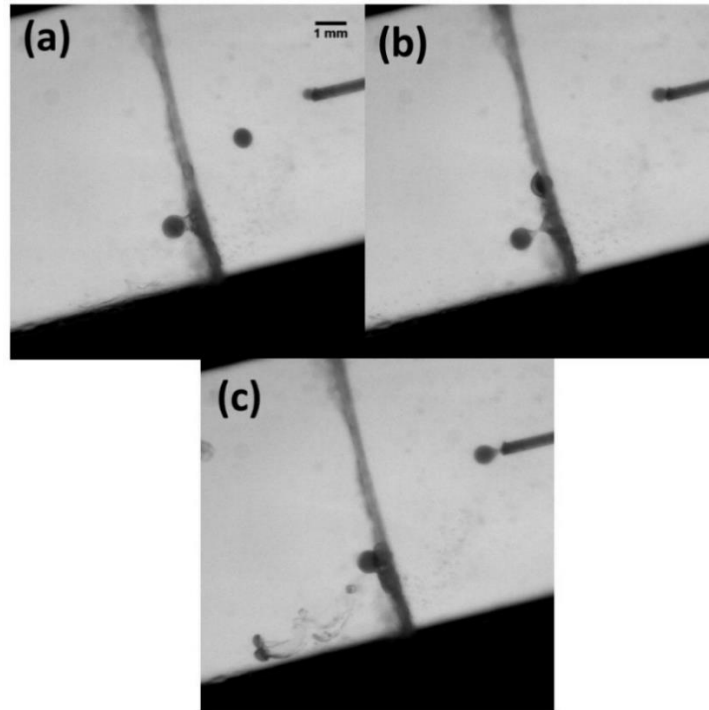


Figure 104: Drop burst during crossing (case  $C_{22}$ ).

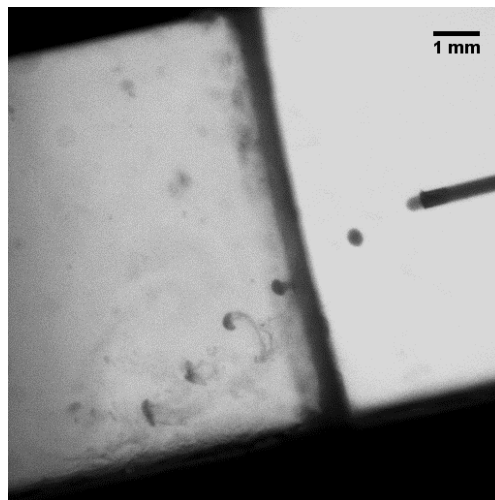


Figure 105: Illustration of drop burst right after crossing (case  $C_{23}$ ).

Now there are two mechanisms susceptible of restoring the surfactant concentration in the front part of the film coating the drop. First is driven by Marangoni effect resulting from the concentration difference arising along the interface between the bottom and the top of the film, second is the adsorption mass flux from the bulk of phase 1 to the film interface. The first is driven by the concentration gradient along the interface and is controlled by a surface diffusion coefficient of the adsorbed surfactant. Even if the drop velocity is significantly damped during the crossing, the interface velocity probably never cancels (difficult to establish) so the interfacial Peclet number is probably high, and the recovery of the surfactant concentration on the top part of the film by this mechanism is likely to be insignificant. The second, assuming the concentration of DBE in phase 1 is in excess and constant, is driven by the adsorption time between the molecular sublayer below the interface and the interface. The thickness of the sublayer is scaled by the adsorption concentration  $\Gamma_{\infty}$  divided by  $C_{TA}$ , the bulk concentration of DBE in the film phase. Assuming there is no potential barrier, the adsorption time can be scaled by the square of this thickness divided by the bulk diffusion coefficient of DBE in phase 1. As the diffusion coefficient of this polymer in the silicone oil was estimated to be two orders of magnitude smaller than that of SDS or Tween 80 in phase 3, it is likely that the adsorption time of DBE is too large in this case to restore the interface loading at saturation during film drainage, in contrast with the case of smaller molecules like Tween 80 or SDS. The oil film will then break right after crossing leading to the coalescence of the drop with phase 3.

In experiments  $C_{24}$  and  $C_{25}$ , SDS was added in phase 3, and results are significantly different as shown in image sequences of Figure 106 (case  $C_{24}$ ) and Figure 107 (case  $C_{25}$ ). Drops are crossing the interface and keep coated by the film in phase 3 as in former experiments  $C_9$  or  $C_{21}$  where no DBE was added in phase 1, confirming that SDS surfactant contribute to the film transient stability after crossing. In both cases, an oil column is stretched and thinned behind the droplet and ends detaching from the interface leaving a clearly visible oil volume surrounding the drop. In experiment  $C_{25}$ , this coating volume takes the form of a long thread, maybe due to a higher Ohnesorge number in the film ( $Oh_{13}=0.5$ ). The coating film volume at the rear of the drop seems also to be larger than that observed in experiments  $C_9$  or  $C_{21}$ , as a result of a higher excess of inertia ( $Bo_{13}=12$  and 20 for  $C_{24}$  and  $C_{25}$  respectively).

The use of DBE surfactant in phase 1 favors the crossing of the interface by decreasing the surface tension by a much higher amount compared to the addition of Tween 80 or SDS in phase 3 alone. However, the coating after crossing is highly unstable without the use of a small surfactant in water phase 3, like SDS. Moreover, even if the coated drop produced is stable right after crossing, the breakage of the column dragged by the drop could occur at a later stage, possibly due to an increase of  $Oh_{13}$  in the film. The resulting thread shape of the coating volume is not convenient regarding the encapsulation process.

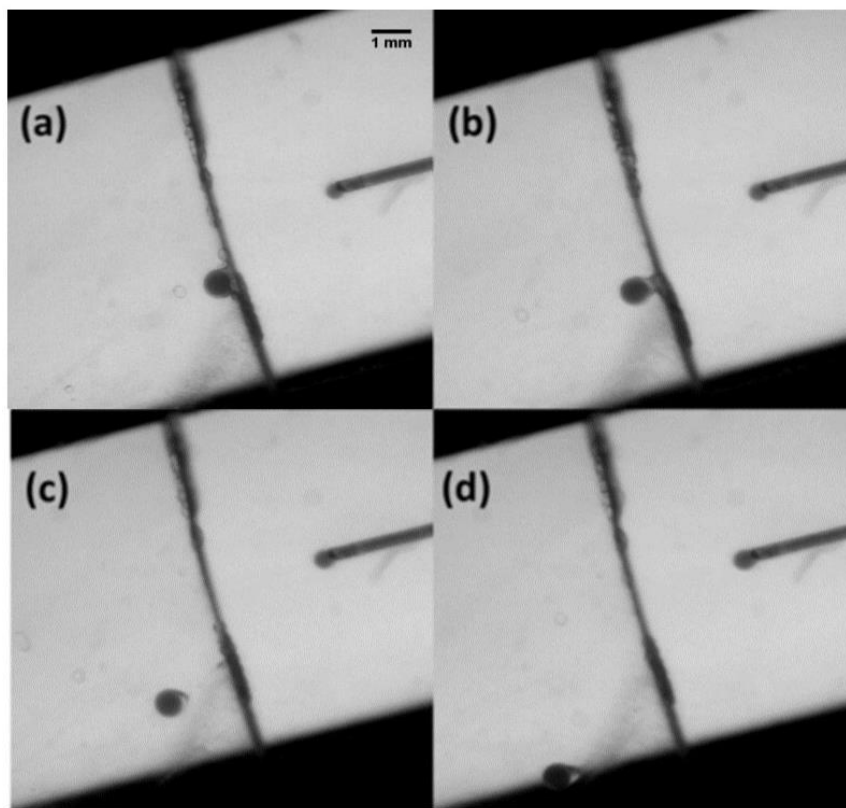


Figure 106: Image sequence of experiment C<sub>24</sub>. (a) Droplet at the interface; (b) film entrainment; (c) stretching and thinning of a phase 1 fluid column; (d) coated droplet.

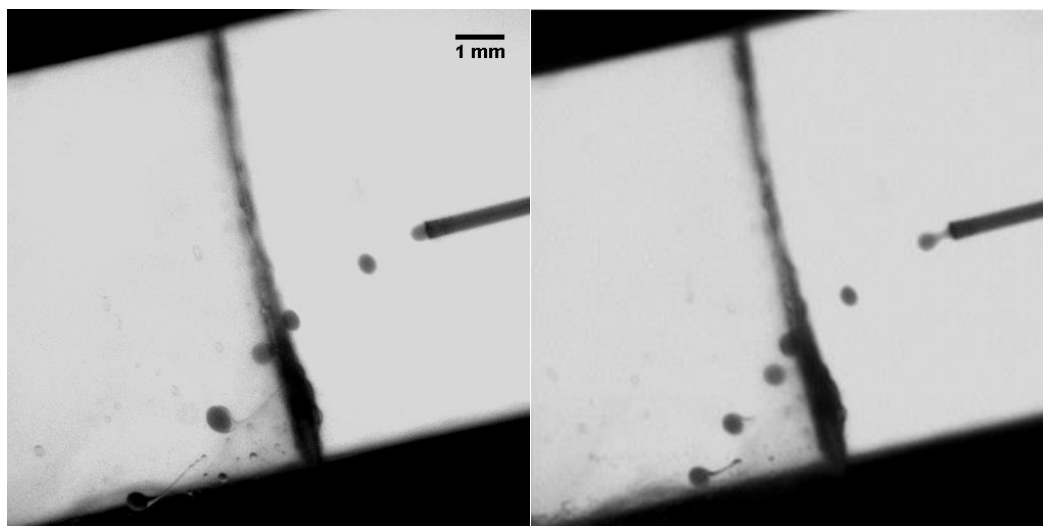


Figure 107: Images of interface crossing in experiment C<sub>25</sub>. Left: entrainment of a long thin column. Right: droplet coated with a liquid thread.

Main conclusions of this section can be summarized as following:

- Surfactants are necessary to allow drop crossing the interface and to ensure the formation of a film coating the droplet.
- Surfactants must be in excess with respect to the CMC in order to optimize the film stability and the speed of recovery of the interface, which should be larger than the film drainage rate. If not, the coating film cannot resist the centrifugal field pressure force and breaks up during crossing or right after. A small surfactants adsorption time compared to the drop formation time is also required to restore the plane interface loading at saturation between successive droplets. The higher the injection drop frequency, the higher must be this rate of recovery.

These experiments have shown that increasing inertia enhances the crossing dynamics (reducing the crossing time) and seem to increase the encapsulated oil volume. However, the nature of the surfactant also seems to influence this dynamic and require further investigations.

- In all experiments, the coated drop ends to coalesce with phase 3 after hitting the cell side walls. This observation suggests that for this process, the choice of surfactants covering interface 1-3 must be first driven by a very high stability of the coating film. Such a property cannot be obtained based on Gibbs elasticity alone; it probably requires the development of a network elasticity at the interface of much higher amplitude. Future investigations will target amphiphilic molecules likely to rapidly develop such a network at an oil-water interface.

#### **6.5.4. Numerical predictions versus experimental data**

In this section, some data and quantities characteristic of the encapsulation process are discussed in the light of both experimental data and numerical simulations presented in chapter 4. One of our objectives is to evaluate the validity of the numerical predictions and of inferred scaling laws for our models that do not account for the presence of surfactants. Even if the comparison is limited to a restricted number of quantities and range of parameters, the two approaches provide complementary information on interface crossing dynamics and this evaluation deserves to be addressed.

We first focus on the droplet trajectory during interface crossing. Numerical simulations of two experimental cases are evaluated. Then, the experimental results obtained for the maximum length of the entrained column of phase 1 and the drop coating volume are discussed for six experimental cases, based on the scaling laws derived from the numerical study.



### Drop trajectory during crossing

The droplet trajectory has been simulated for experimental cases C<sub>13</sub> and C<sub>9</sub> (respectively corresponding to cases D<sub>14</sub> and D<sub>15</sub> in chapter 4) and compared to the experimental data. Physical and non-dimensional parameters of these cases are reported in Table 40 and Table 41 respectively.

	$\rho_1$ [Kg.m <sup>-3</sup> ]	$\rho_2$ [Kg.m <sup>-3</sup> ]	$\rho_3$ [Kg.m <sup>-3</sup> ]	$\mu_1$ [Pa.s]	$\mu_2$ [Pa.s]	$\mu_3$ [Pa.s]	$\gamma_{12}$ [N.m <sup>-1</sup> ]	$\gamma_{13}$ [N.m <sup>-1</sup> ]	$D_i$ [ $\mu$ m]	N [rpm]	$\bar{d}_d$ [ $\mu$ m]	[SDS] surfactant phase 3
C <sub>13</sub>	913	1081	997	0.005	0.0024	0.001	0.037	0.011	250	3600	367	1.22*CMC
C <sub>9</sub>	930			0.01			0.04				380	1.22*CMC

Table 40: Physical parameters of experiments C<sub>9</sub> and C<sub>13</sub>.

	$\xi_{12}$	$\xi_{13}$	$\lambda_{12}$	$\lambda_{13}$	$B_{012}$	$B_{013}$	Ar
C <sub>13</sub>	0.18	0.09	0.48	0.2	1.4	2.36	19
C <sub>9</sub>	0.16	0.07	0.24	0.1	1.2	1.94	9

Table 41: Non-dimensional parameters of experiments C<sub>9</sub> and C<sub>13</sub>.

In the simulations, values of the surface tension are taken at equilibrium and are kept constant. In experiments, the droplet detaches from the capillary tip with an initial speed and a non-zero corresponding velocity field in the liquid which was not measured. In the simulations, the velocity is set to zero in all mesh points of the domain as an initial condition. Drop center of mass trajectories are reported in Figure 108 (for case C<sub>13</sub> on the left graph and for C<sub>9</sub> on the right graph). It can be observed on these curves, that even if initial conditions are different, both experimental and numerical droplet velocity reach the same plateau before the drop interacts with the interface, with a discrepancy of less than 10% for C<sub>13</sub> and less than 1% for C<sub>9</sub>.

When approaching the interface (located at  $x^*=1$ ), the drop drastically decelerates, reaching a minimum velocity much smaller in the experiments than in the simulations. This discrepancy could be an effect of the surfactants which tend to immobilize the 1-3 interface and increase the velocity gradient on both side on the interface of the film pulled by the droplet.

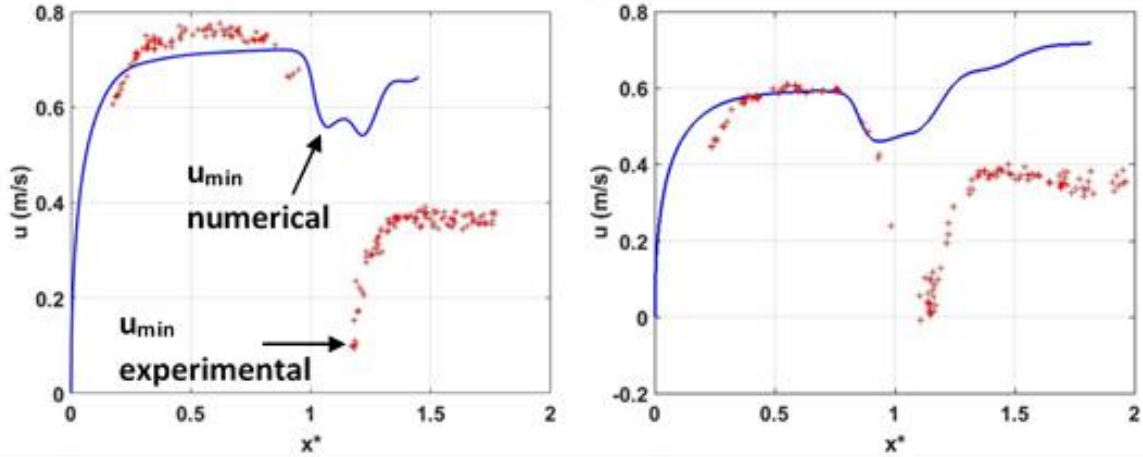


Figure 108: Velocity profile upon the distance travelled in the cell. (+) Experiments and (—) numerical simulations. Left: case C<sub>13</sub>; right: case C<sub>9</sub>. ( $x^*=1$  is the position of the plane interface).

As a result, the drainage rate of the lubrication film between the droplet and the interface is much slower in the experiments than in the simulations, and the amount of energy dissipated during crossing will be higher in experiments, resulting in a much smaller value of the minimum velocity. In chapter 4, this minimum velocity has been identified as a characteristic quantity of the dynamics of interface crossing, scaling the maximum length of the fluid column entrained and the coating volume. It can be anticipated that the influence of surfactants on the minimum velocity will have significant consequences on these two quantities.

After crossing, the droplet reaccelerates in phase 3 where it reaches a much higher velocity in the simulations than in the experiments in both cases considered. The presence of surfactants at the film upper interface tend to increase the production of vorticity increasing the drag exerted on the formed capsule, therefore leading to a much smaller rising velocity in experiments than in simulations.

### Film detachment and coating film volume

The maximal length  $L_{\max}$  of the fluid column entrained by the drop prior to detachment has been measured for different experimental cases whenever those measurements were possible. Physical and non-dimensional parameters are reported in Table 42 and Table 43 respectively. The rotation speed is the same for the six cases considered,  $N=3600$  rpm, and droplets are injected from the same capillary tube of diameter  $D_i=250\ \mu\text{m}$ .

Experiment	$\rho_1$ [Kg.m <sup>-3</sup> ]	$\rho_2$ [Kg.m <sup>-3</sup> ]	$\rho_3$ [Kg.m <sup>-3</sup> ]	$\mu_1$ [Pa.s]	$\mu_2$ [Pa.s]	$\mu_3$ [Pa.s]	$\gamma_{12}$ [N.m <sup>-1</sup> ]	$\gamma_{13}$ [N.m <sup>-1</sup> ]	$\bar{d}_d$ [ $\mu$ m]	$u_f$ [m.s <sup>-1</sup> ]	$e$ [ $\mu$ m]
C <sub>13</sub>	913	1081	997	0.005	0.0024	0.001	0.037	0.01	367	0.173	90
C <sub>9</sub>	930			0.01			0.04	0.011	380	0.098	68
C <sub>15</sub>	950			0.02			0.041	0.012	405	0.1	68
C <sub>16</sub>	960			0.05			0.043	0.013	421	0.061	68
C <sub>18</sub>	960			0.1			0.044	0.013	550	0.049	90
C <sub>25</sub>	930			0.01			0.04	0.001	368	0.1	68

Table 42: Physical properties of experimental cases for the measurement of  $L_{max}^*$ .

System	$\xi_{12}$	$\xi_{13}$	$\xi_{12}/\xi_{13}$	$\lambda_{12}$	$\lambda_{13}$	$Bo_{12}$	$Bo_{13}$	Ar	$I_{ex}$	$L_{max}^*$	$Re_{col}$	Oh <sub>f</sub>
C <sub>13</sub>	0.184	0.092	2	0.48	0.2	1.4	2.36	19	1.17	2.3	2.88	0.09
C <sub>9</sub>	0.162	0.072	2.25	0.24	0.1	1.2	1.94	9	1.06	2.3	0.62	0.16
C <sub>15</sub>	0.138	0.049	2.78	0.12	0.05	1.19	1.59	5	1.22	2.7	0.32	0.29
C <sub>16</sub>	0.126	0.039	3.27	0.048	0.02	1.14	1.37	2	1.3	7.1	0.08	0.69
C <sub>18</sub>	0.126	0.039	3.27	0.024	0.01	1.85	2.26	1.5	1.67	8.7	0.043	1.21
C <sub>25</sub>	0.162	0.072	2.25	0.24	0.1	5.74	20.4	9	2	5.7	0.64	0.54

Table 43: Non-dimensional parameters and  $L_{max}^*$  values.

Figure 109 shows, for each experiment, the image sequence from which the measurement of  $L_{max}$  was performed (cf zoom of the insert on each figure). In some of these images, we can observe the presence of an encapsulated drop in phase 3 preceding the drop on which the measurement of  $L_{max}$  is performed. It means that the fluid column of phase 1 was detached between these two drops, giving an idea of the uncertainty on this measurement. The measurements exhibit a rather large range of variation of  $L_{max}$  between 2 to 9 droplet diameters. In chapter 4,  $L_{max}^* = L_{max}/d$  was found to be a function of the parameter  $I_{ex}$ ,  $I_{ex} = F^*/f(Bo_{13})$ , scaling the inertia excess (due to buoyancy and inertia),  $F^* = \frac{\xi_{12}}{\xi_{13}} \left( 1 + 6 \frac{\rho_2 u_{min}^2}{(\rho_2 - \rho_1) a_{cd}} \right)$ , by the function  $f(Bo_{13})$  (right-hand side of equations (5) and (6)). Two distinct regimes of the evolution of this parameter were observed, both increasing with  $I_{ex}$ , but with contrasted growth rates, which were found to correspond to different flow regime of the fluid column Reynolds number:  $Re_{col} = \rho_1 u_f e / \mu_1$  (where  $e$  is the thickness of the column and  $u_f$  is the drop velocity when the column detaches). These two regimes are represented by the two continuous lines in Figure 110, the higher slope corresponding to small  $Re_{col}$  values and the smaller one to larger  $Re_{col}$ . Experimental values of  $L_{max}^*$  have been reported on this graph for the six cases, exhibiting a sharp increase of  $L_{max}^*$  with  $I_{ex}$ , a trend which corresponds to the regime at low  $Re_{col}$  in the simulations. Indeed, in the experiments the estimation of  $Re_{col}$  showed that it was always smaller than 1 (except for case C<sub>13</sub> where it is equal to 2.88). The numerical prediction of  $L_{max}^*$  for these cases follows the trend at larger  $Re_{col}$  as expected, due to the larger predicted drop velocity in phase 3 (cf Figure 108) and therefore of  $u_f$ , as compared with the experiments. Although the formation of a long thin film behind the drop seems to be related to non-negligible values of the Ohnesorge number in the film (see Table 43), the simulations do not seem to be sensitive to this parameter, because the high predicted value of the drop velocity after crossing. This difference is a probable consequence of the effect of the surfactants on the tangential stress boundary condition at the interface.

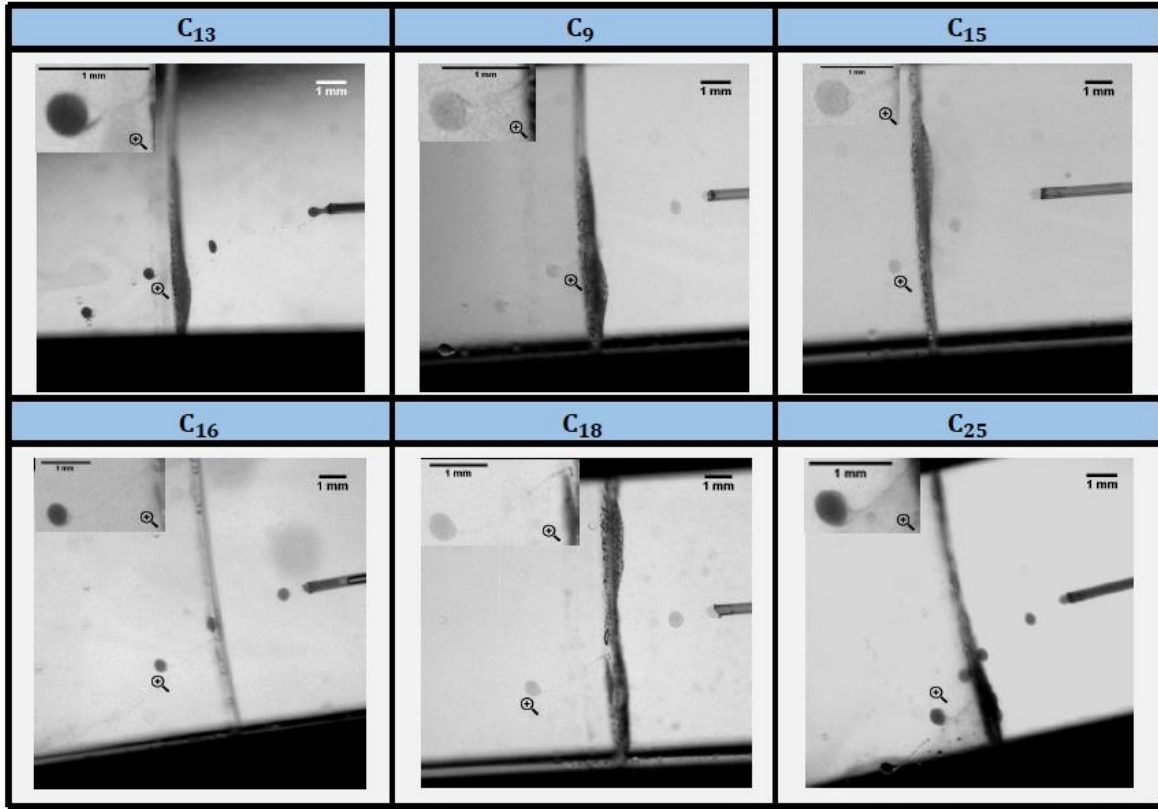


Figure 109: Visualization of column length for experiments of Table 42.

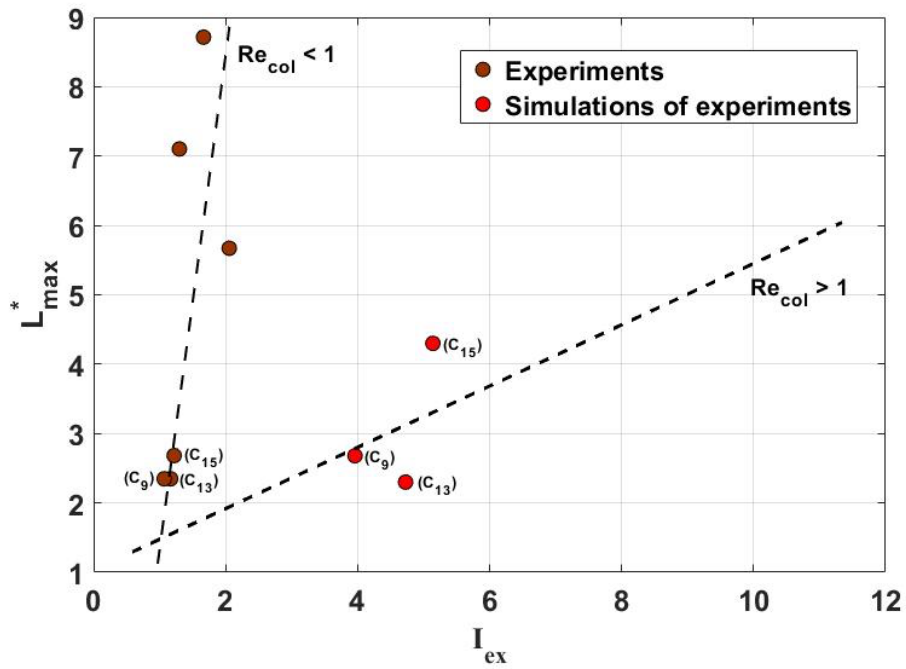


Figure 110: Evolution of  $L_{max}^*$  as a function of  $I_{ex}$ .

The volume of the film coating the droplet in phase 3 after the column detachment was estimated for five experiments. Taking advantage of the systematic drop breakup against the cell side walls, the measurement of the size of the oil droplet resulting from the phase separation gives us the volume of the oil film coating the drop prior to its breakup. Oil droplets travelling back to the interface can be observed in Figure 111. Due to a poor grey level contrast between the oil and water phases, an automatic contour detection couldn't be easily applied for the determination of the size of these droplets. It was preferred instead to measure their size manually, with a relative error on the film volume of the order of 20%. Results are reported in Table 44, Values are ranging between 10 and 24% of the droplet volume.

Experiment	$F^*$	$\lambda_{12}$	$V_f/V$
C <sub>13</sub>	2.24	0.48	0.24-0.28
C <sub>9</sub>	2.25	0.24	0.16-0.2
C <sub>15</sub>	2.84	0.12	0.24-0.28
C <sub>16</sub>	3.27	0.048	0.21-0.25
C <sub>21</sub>	3.27	0.24	0.13-0.17

Table 44: Inertia parameter  $F^*$ , viscosity ratio  $\lambda_{12}$  and film volume  $V_f$  normalized by the droplet volume.

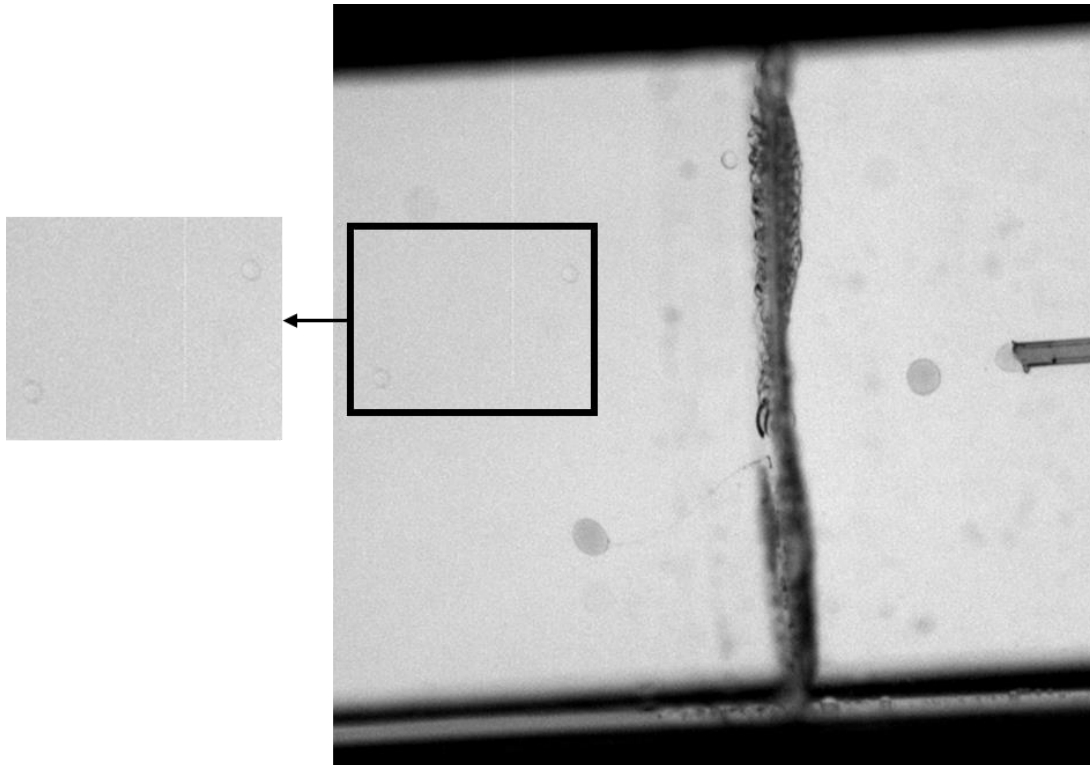


Figure 111: Visualization of oil droplets travelling back towards the interface after droplet breakup.

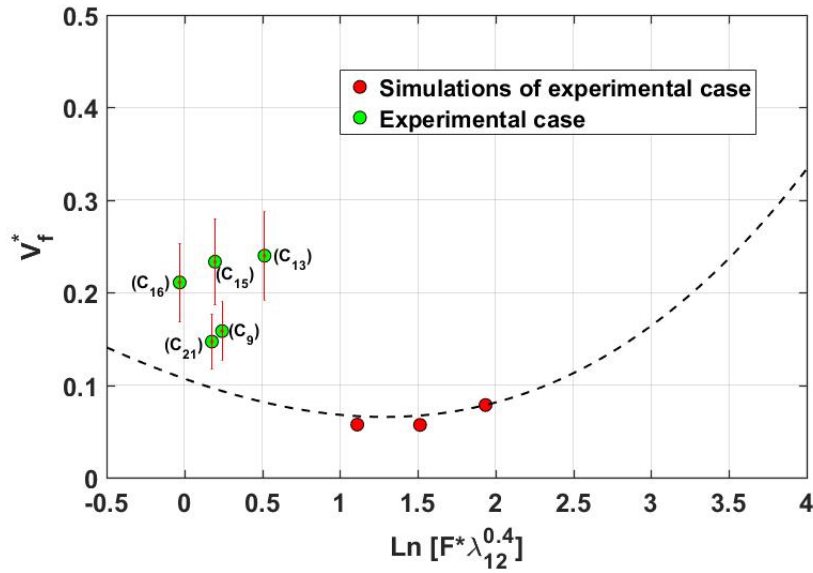


Figure 112: Normalized film volume as a function of  $\text{Ln}(F^* \lambda_{12}^{0.4})$ . Experiments and simulations.

In Figure 112, the normalized film volume is plotted as a function of  $\text{Ln}(F^* \lambda_{12}^{0.4})$ , which was identified as the relevant scaling parameter from the simulations of deformable droplets. The ranges of  $\text{Ln}(F^* \lambda_{12}^{0.4})$ , for the experimental data (C<sub>9</sub>, C<sub>13</sub> and C<sub>15</sub>, red circles) (0-0.5) is shifted to lower value compared to the numerical cases (1-2), because of a much smaller value of the minimum velocity  $u_{\min}$  in the experiments than in the numerical predictions. The numerical trend (dashed line) in a smaller range of  $\text{Ln}(F^* \lambda_{12}^{0.4})$  (between 0 and 0.5) leads to a smaller film volume (by a factor 2). So the effect of surfactants is also clearly visible on these data: experimentally, the condition at the interface due to the surfactant layer leads to a smaller film drainage rate, resulting in a larger film volume at the detachment.

## 6.6. Conclusion

The objective of this experimental study was to visualize the crossing of a liquid-liquid interface by a drop in a centrifugal field, and to characterize the different steps of this encapsulation process: drop injection and rise towards the interface, crossing and phase entrainment, formation of the coated drop. Given the high number of non-dimensional parameters describing this system (7 non-dimensional numbers without accounting for the surfactants), an exhaustive study was not possible, and the number of measurable quantities is limited in such a device. However, a number of conclusions can be drawn from the results of this study which in our opinion, are likely to be relevant for the design of an industrial prototype.

In the range of Reynolds number investigated, the size of the droplets injected in the cell can be simply modelled by a force balance between the centrifugal force and surface tension force at the capillary tip. Provided that drop deformation is controlled by the interfacial tension ( $Oh_D < 0.1$ ), the drop diameter scales as  $Bo_D^{-1/3}$ . In such a centrifugal field, the transfer time of surfactants from the bulk to the drop interface, whether introduced in the external (phase 1) or internal phase (droplet) 1, is always much larger than the drop formation time. As a consequence, it has no effect on the size of the droplets formed and the interfacial tension considered in  $Bo_D$  must be taken as the interfacial tension at equilibrium of the 1-2 interface, without any surfactants. These results guarantee an accurate control of the injection step for encapsulation in a centrifugal microfluidic pilot.

After detachment from the capillary tube, droplets rise in phase 1 with a non-zero initial velocity. In the frame of the rotating cell, their trajectory shows a deviation angle  $\theta$  from the capillary axis. The drop path and velocity inside phase 1 can be accurately predicted by using Newton's second law, accounting for the centrifugal force, the Coriolis force, the force of added mass, and the drag force. It is shown that the correct drag force expression in the force balance must account for the drop deformation (aspect ratio), both in the Reynolds number definition and in the projected surface area offered by the droplet to the flow. During the drop rise, since the drop Reynolds number is moderate or large ( $Re > 1$ ), the droplet shape is mainly determined by the Weber number  $We_{12}$  (deformation due to inertial effects and controlled by surface tension), but a correction involving the drop Ohnesorge number  $Oh_{12}$  is necessary to scale the shape. In the range of investigated parameters, surfactants do not have time to adsorb at the drop interface during the drop rise, which has been verified by comparing DNS calculations with experiments.

Critical crossing conditions observed in the experiments do follow the theoretical criterion for static crossing of a solid sphere. The higher the drop inertia, the faster is the crossing, and thus the larger can be the drop injection frequency in a continuous mode process. An interesting conclusion revealed by this study is that the use of surfactants is a crucial point for the encapsulation process, i.e. the formation of a film coating the droplet. For a given system, surfactants favor the crossing of the interface by decreasing the interfacial tension and increasing inertia forces on the interface. But they are necessary to stabilize the coating film after crossing. Their concentration must be above the CMC in order to ensure:

- a low film drainage rate induced by strong velocity gradients on each side of the interface
- a fast recovery of the interface loading during deformation and between subsequent injected drops
- a high disjoining pressure to resist to the external pressure force during rising in phase 3.

However, it was observed that the coating film could not resist to the pressure force experienced when pushed against the wall of the cell, suggesting that such a process might

require the stabilization of the film via a stronger mechanism such as the use of amphiphilic molecules capable of developing rapidly interfacial networks with an elasticity much larger than Gibbs elasticity, or the cross-linking or solidification of the film itself.

When it was possible, the maximum length of fluid column entrained and coating film volume have been measured and reported as a function of inertia parameters, in the same way as in the numerical study. The entrained fluid of phase 1 forms a long thin column the length of which rapidly grows with inertia from 2 to 9 drop diameters, whereas the coating volume was found to range between 0.1 and 0.25 the drop volume, without any discernable trend as a function of an inertia parameter. The evaluation of the numerical prediction on these quantities highlights the effect of the surfactants on the film drainage kinetics, which impacts both the dissipation of kinetic energy during the crossing and the coating drop volume. As expected, the numerical simulations predict a much higher value of the minimum velocity and a smaller coating film volume than in the experiments. This evaluation is driving the interest of a numerical study including surfactants.



# **Chapter 7:**

Conclusion & Perspectives

# Chapter 7: Conclusion & Perspectives:

In view of scaling up an encapsulation process and designing an industrial pilot, the objective of this study was to understand the physical mechanisms of the crossing of a liquid-liquid interface by a single droplet in a centrifugal field and inertial regime. To this aim, an experimental device equipped with a suitable metrology has been developed, in order to control and monitor the injection, the motion and deformation of droplets crossing a liquid-liquid interface in a centrifugal cell. Crossing conditions were first mapped and analyzed on a wide range of non-dimensional parameters. In parallel, numerical simulations based on the level-set method were carried out and validated in order to simulate the motion and interface crossing of both solid-like and deformable droplets. Both approaches allowed to understand the crossing conditions and dynamics of deformable droplets with and without surfactants, as well as to analyze relevant quantities associated to this problem in inertial conditions (length of the column entrained, the remaining coating film).

## Main results:

Both experimental and numerical approaches have proven to be complementary.

Numerically, crossing conditions for solid-like (non-deformable with a high viscosity ratio  $\lambda_{12}$ ) and deformable droplets were first characterized in dynamic regime. Results showed that the critical conditions for crossing could be predicted by the theoretical criterion already developed in the literature for spherical particles in static conditions. The droplet velocity before, during, and after crossing the interface was characterized and the phenomenology of crossing was described. During crossing, the droplet velocity reaches a minimal value ( $u_{\min}$ ) which was found to be a scaling parameter in dynamic regime of following quantities: crossing time, maximal column length, and volume of coating film. The length of the column entrained by the drop during crossing is a growing function of inertia, exhibiting two distinct regimes of stretching which are not fully understood at the moment. After detachment, the film volume coating the drop was found to be scaled by a parameter which is only function of droplet inertia excess (based on the minimum velocity), independently from surface tension. The coating film volume results from a simple balance acting on the film between two opposite forces, one driven by drop inertia entraining the film in phase 3, and one driven by gravity tending to pull back the film towards the interface. For deformable droplets, this parameter needs to be corrected by the viscosity ratio  $\lambda_{12}$ . The minimum velocity was found to be correlated to the maximum

velocity reached by the drop before the interface, based also on the same excess inertia parameter rescaled by the theoretical criterion for static crossing.

Experimentally, the volume of injected droplets was found to scale as the Bond number based on the tip diameter  $D_t$ . Droplet trajectory in phase 1 was measured and modeled by the fundamental principle of dynamics accounting for drag, added mass, centrifugal and Coriolis forces. The latter was found to be non-negligible as it deviates the droplet trajectory. It was found that the drop deformation modified drag law of Rivkind V. and Ryskin G., 1976 was best fitting experimental data.

Effect of surfactants contained in phase 1 or phase 2 on droplet formation as well as on their rising motion in phase 1 was also investigated. Surfactants did not have any effect on the droplet formation and on the rising motion of the drop over the distance travelled towards the interface. This conclusion was confirmed through comparisons with simulating the drop rise in phase 1 without surfactants, for which velocity and deformation match with the experimental measurements. This result is due to the fact that in the range of flow parameters investigated, the time of transfer of surfactants towards the interface is always larger than the formation time of the drop and of its trajectory time. These experimental results can therefore be used to validate computational codes which simulate liquid-liquid interfaces without surfactants.

Regarding crossing, addition of surfactants in phase 1 and/or phase 3 facilitated the crossing of the interface through decreasing its surface tension. However, the adsorption time of surfactants must be always smaller than the film drainage rate, in order to restore the interface loading at saturation during the drop crossing.

Concerning crossing conditions, experimental results were consistent with numerical results. The limitations of both approaches were discussed in details. The comparison of results between the two approaches showed an additional effect of surfactants. In the experiments, the droplet was strongly decelerated ( $u_{\min}$  being lower than in the simulations) and the film drainage was slower, which results in an entrainment of larger amount of volume coating the droplet.

We summarize in Table 43 the relevant non-dimensional numbers and physical parameters which were found to be relevant for each step of the process. Note that the effect of surfactants is only included in this table through the interfacial tension and the value of  $u_{\min}$  in the crossing step.

		Non-dimensional numbers	Physical parameters
Injection	Droplet size ( $d_d$ )	$Bo_D$	$\rho_1, \rho_2, \gamma_{12}, N, D_i$
	Droplet frequency ( $f$ )	$Bo_D$	$\rho_1, \rho_2, \gamma_{12}, N, D_i$
Droplet rise	Droplet rise terminal velocity ( $u_T$ )	$\xi_{12}, \lambda_{12}, Bo_{12}, Ar$	$\rho_1, \rho_2, \mu_1, \mu_2, \gamma_{12}, N, d_d$
	Droplet minimum velocity ( $u_{min}$ )	All	All
Crossing	Crossing time ( $t_{cr}$ )	-	$u_T$ and $u_{min}$
	Crossing condition	$\xi_{12}/\xi_{13}, Bo_{13}$	$\rho_1, \rho_2, \rho_3, \gamma_{13}, N, d_d$
	Maximal column length	$I_{ex}$ and $Re_{col}$	$\rho_1, \rho_2, \rho_3, u_{min}, N, d_d, e$
	Droplet volume	$F^*$	$\rho_1, \rho_2, \rho_3, u_{min}, N, d_d$

Table 43: Relevant non-dimensional numbers and physical parameters involved in each step of the process.

The scaling-up of such a process requires the design of a multiple injector system to ensure an industrial scale rate of production. For this purpose, a preliminary design of a prototype with two concentric cylinders is proposed: the first is a reservoir of the droplet phase and the second contains the two liquid phases 1 and 3 (Figure 1). Steps of the scaling-up, given a fluid system are the following: (i) choose a suitable injector diameter to provide the targeted size of capsules, (ii) adjust the rotation speed to allow droplet crossing, (iii) adjust the droplet injection frequency ( $f$ ), in a such a way that formation time ( $1/f$ ) is maintained higher than the crossing time, in order to avoid crossing in bundles or clusters, (iv) adjust the distance between two neighboring injectors ( $r_{ij}$ ) to account for Coriolis force induced droplet deviation.

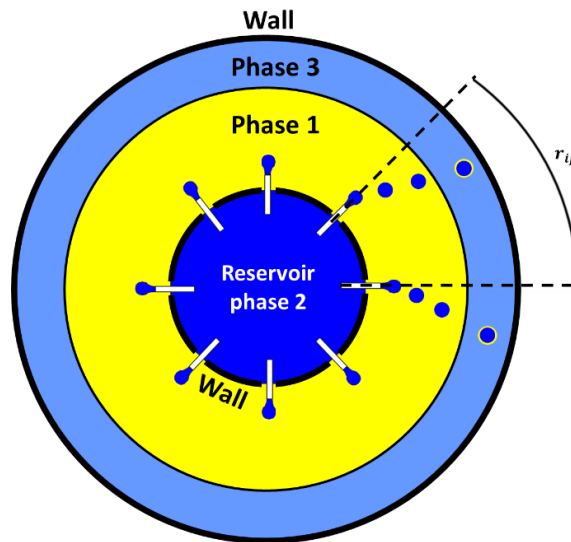


Figure 113: Scheme of an industrial prototype.

### Perspectives:

In order to better understand the role of surfactants in the crossing dynamics and in the lifetime of the coating film, an interesting prospect to this study will be to include the effect of surfactants in the numerical modelling. An example of numerical simulations of rising droplets in the presence of surfactants can be found in Piedfert et al., 2018 for a two-phase flow system. In our case, it would be require to increase the special resolution in order to quantify the effect of surfactants on the film drainage kinetics and its consequences on  $u_{min}$ . Regarding the film volume, the scaling law differentiates between solid-like droplets and deformable droplets where it accounts for viscosity ratio  $\lambda_{12}$  effect. Other simulations with non-deformed crossing droplets are necessary to understand the transition between the behavior of solid-like and deformable droplets.

Concerning the experiments, the limitations of the present system for image acquisition of such a rapid process is possible to overcome with two or more synchronized high-speed cameras imaging at different angular positions in one revolution, allowing the capture of a trajectory at a higher frequency and with a better resolution.

Thanks to the breakage of the capsule, it was possible to measure the encapsulation volume manually by classic image processing tools with an error percentage around 20% (contour detection was not possible due to small difference in greyscale levels). However, it seems more convenient to measure this volume without relying on the breakage of the capsule. A suggestion could be the use of a Fluorescence-lifetime imaging microscopy technique, already tested for the measurement of the thickness of block co-polymer vesicles (Handschuh-Wang et al., 2017).

In an encapsulation process, the remaining step is the solidification of the membrane. This process can take place directly when the droplet is suspended in phase 3, or after collecting the film volume and solidifying it in another device. For an in-situ solidification, several techniques may serve the goal such as the membrane polymerization. If capsules have to be collected, this constitutes also a pending problem. An idea could be to suck them back close to the rotation axis where centrifugal acceleration is lower, keeping the idea of a continuous process. Another solution would consist in collecting the capsules after stopping the rotating motion. In this case, it is necessary to ensure the stability of the emulsion constituted with all these capsules. This requires to make a relevant choice on the surfactant(s) to use which has to prevent coalescence of the capsules before their film solidification. In all cases, this will need further investigation and experiments based on the results of this work.

# **Appendix A:**

Experimental device and  
measuring methods.

# Appendix A: Experimental device and measuring methods

## A1. A 3D scheme of the experimental device

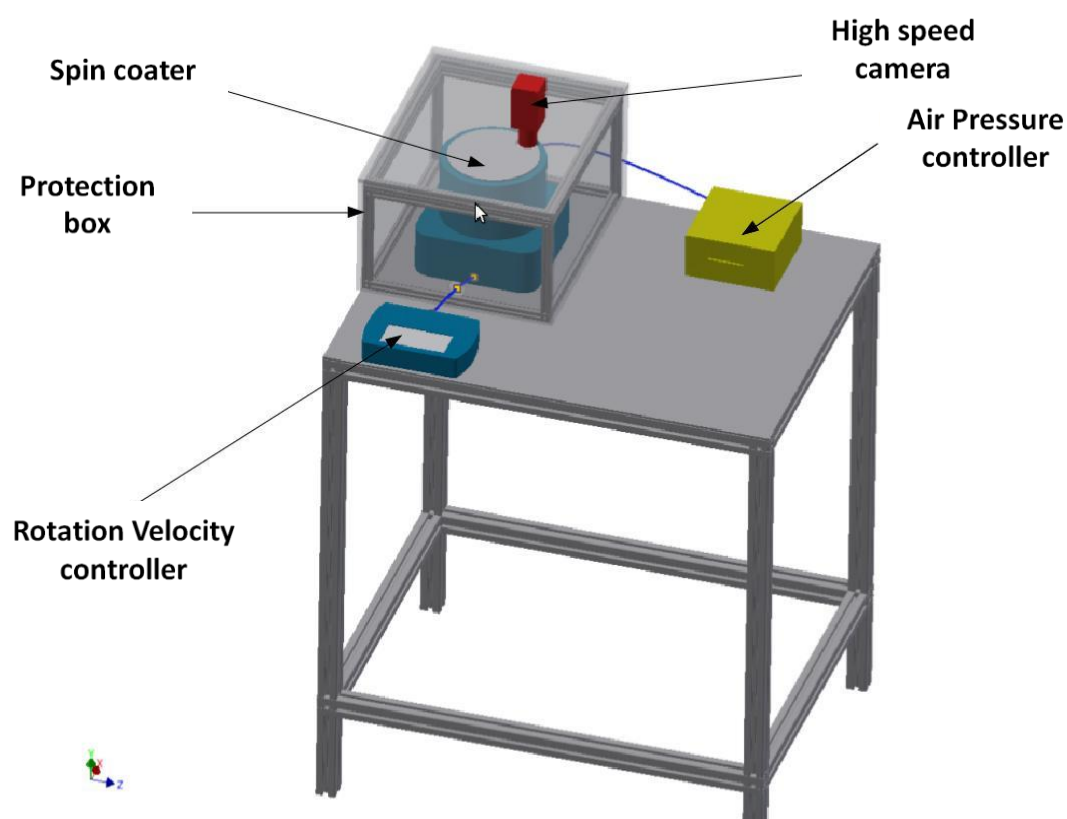


Figure 114: A 3D scheme showing the principle elements of the experimental apparatus.

## A2. Spin Coater and its modifications

### A.2.1. The Spin Coater

The experimental device is built inside the spin coater (SPIN150i) provided by the supplier SPINCOATING with the specification in Figure 116. The mandrel was replaced by an assembly presented in the following subsection.



Figure 115: The image of the spin coater from the website of supplying company.

Specifications	
Available number of programs	Unlimited *
Steps per program	Unlimited *
Spin speed*	1 - 12,000 rpm ** $\pm$ 1rpm steps
Spin speed accuracy	$\pm$ 0.1 rpm **
Spin rotational direction	Clockwise, Counter clockwise, Puddle
Max. acceleration	30,000 rpm/sec **
Spin time	Unlimited*, $\pm$ 0.1 seconds steps
Free programmable outputs	3 dry relays, nominal switching capacity 0.5A /125 VAC - 0.3A / 60DC
System data	
Housing material	Natural Polypropylene (NPP) ***
Process chamber material	Natural Polypropylene (NPP) ***
Interface	Detachable, full-size touchscreen, glove-friendly, IP52, chemical resistant
External connection	1 USB Port in the controller
Max. substrate diameter	160mm round or 4 $\hat{E}$ <sup>2</sup> x 4 $\hat{E}$ <sup>2</sup> square
Max. process chamber diameter	202 mm
Dimension (desktop version)	274 (w) x 250 (h) x 451 (d) mm
Shipping weight	14 kgs
Shipping dimension	600 x 380 x 360 mm
Requirements	
Voltage	100 - 120 VAC / 200 - 240 VAC 50/60 Hz (auto select)
Power consumption	Max. 500 W
Max. current	5A / 2.5A
Vacuum	- 65 kPa (-19 inchHg), $\geq$ 80 lpm Tube OD $\hat{O}$ 8mm
Motor purge gas	20 - 50 kPa, 2-5 l/min, Tube OD $\hat{O}$ 6mm
Drain connection	1" M-NPT
* Considering additional capability of standard unit such as USB backup, recipe cycling, PC software etc.	
** Measured without substrate, limitations may apply depending on chuck used and substrate specification.	

Figure 116: The specifications of the spin coater.



A.2.2. The Assembly replacing the Mandrel

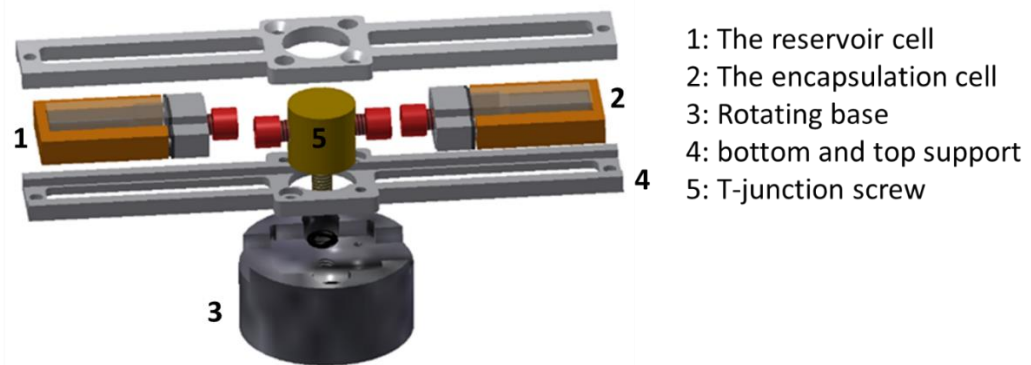


Figure 117: The assembly replacing the mandrel of the spin coater.

A.2.3. The bottom and top supports

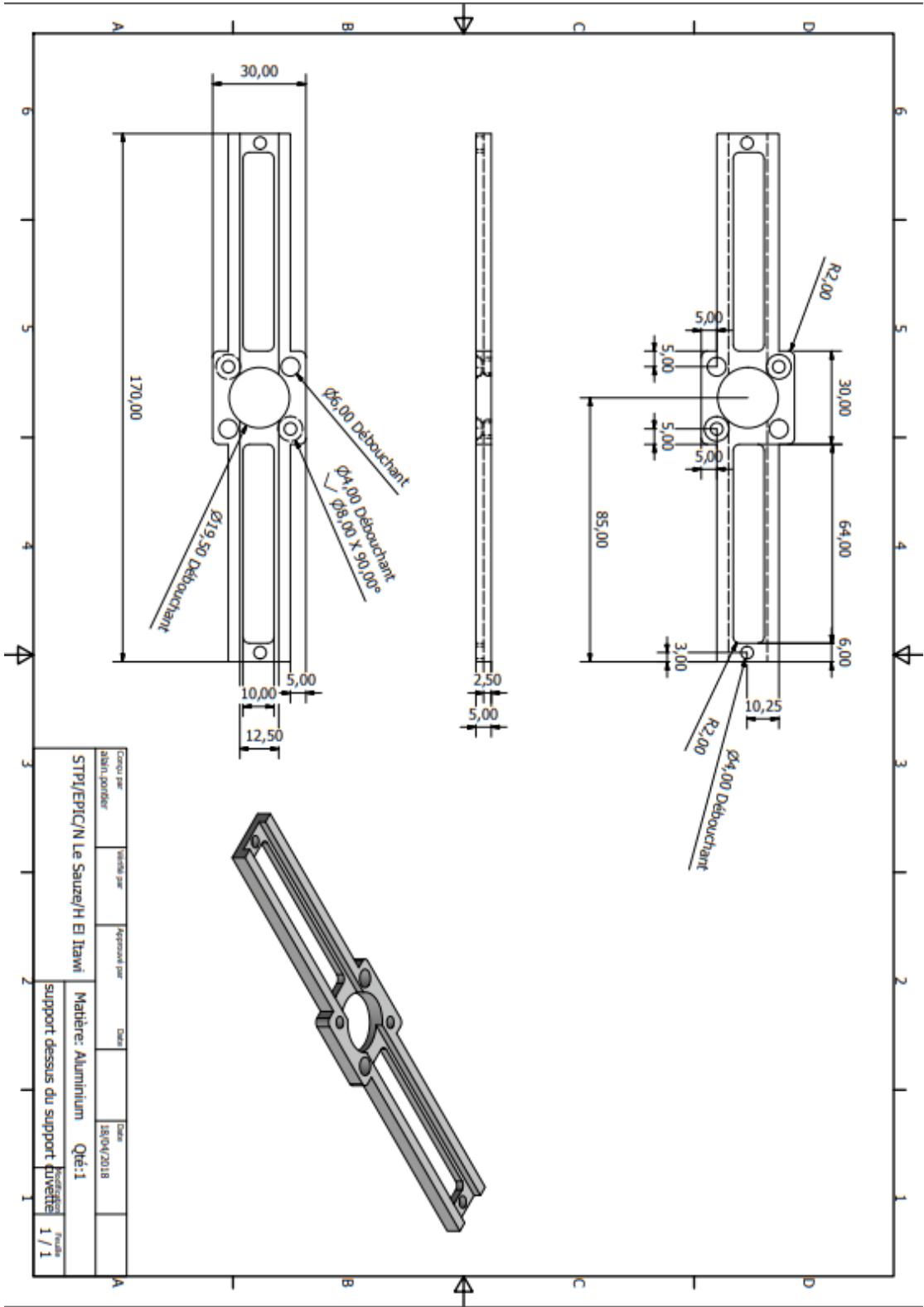


Figure 118: The dimensions of the top and bottom support.

A.2.4. The rotating base

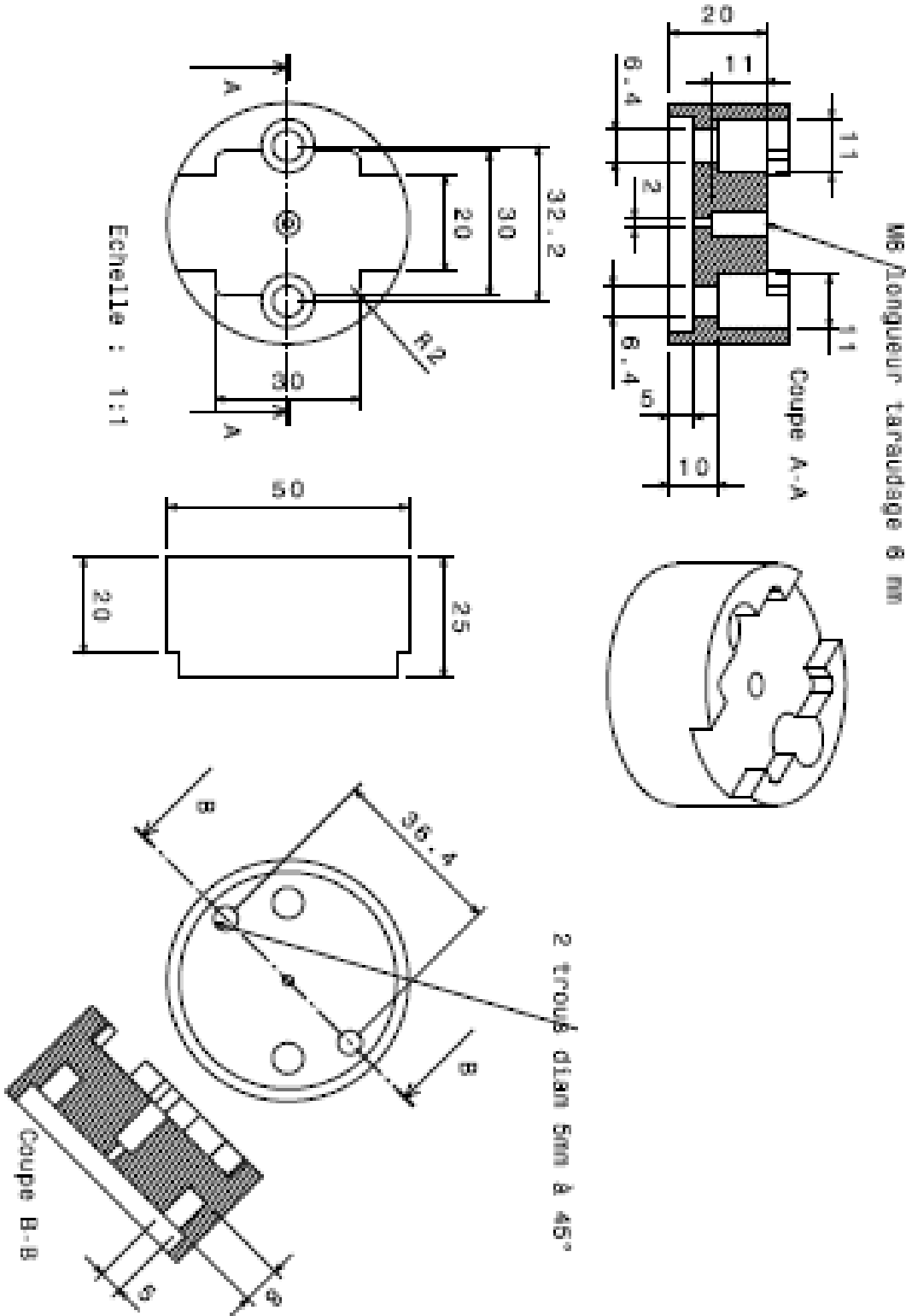


Figure 119: The scheme of the rotating base.

A.2.5. The cells



Figure 120: The reservoir and encapsulation cell. In yellow: an aluminum support which will touch the screw connecting the two rectangular supports (top and bottom), in blue: the cells which contains the liquids, in black: a joint to prevent leakage, in grey: a plug to be screwed with the support at its two sides with a hole in the middle permitting the passage of the connecting capillary tube.

**A3. High-Speed Camera: Phantom Miro 320**



Figure 121: The image of the camera.

<b>Resolution</b>	<b>1920*1200 pixels</b>
<b>Shutter speed</b>	1380 fps at full resolution
<b>Maximum shutter speed</b>	325000 fps at reduced resolution 64*8 pixels
<b>Minimum exposure rate</b>	1 $\mu$ s

Table 45: Principle characteristics of the camera.

**A4. Microscope: LEICA M651**



Figure 122: An image of the microscope ensuring a good quality of the image and holds the camera..

**A5. Pressure Controller: ELVEFlow OB1 MK3**



Figure 123: An image of the pressure regulator.



Figure 124: The outlet channel of the pressure regulator where air exits at a controlled pressure.

**A6. PHLOX LED Panel**

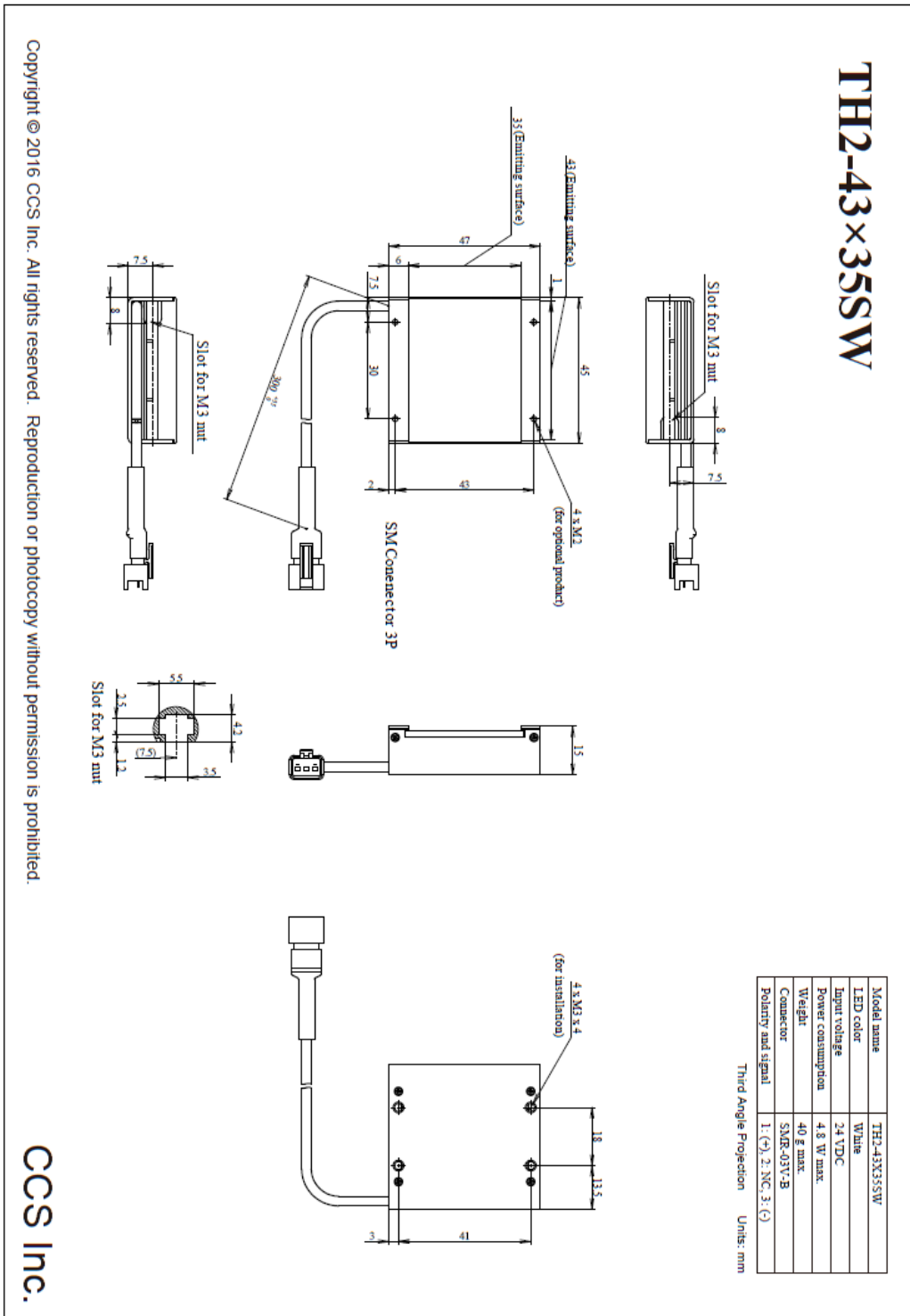


Figure 125: A scheme of the LED panel which supports backlight for the device.

**A7. Gardasoft RT 200-20**



Figure 126: The gardasoft lightning control technology which allows an overdrive in the lightning intensity.

**A8. Anton Paar DMA 38 Density Meter**



Figure 127: The image of the denismeter used to measure the densities of the samples in this work.

Characteristics:

<b>Dimensions (L x W x H)</b>	<b>280 x 210 x 270 mm</b>
<b>Minimum amount of sample</b>	Approximately 0.7 ml
<b>Measuring range</b>	0 to 3 g/cm <sup>3</sup>
<b>Accuracy on Density</b>	±0.001 g/cm <sup>3</sup>
<b>Accuracy on Temperature</b>	±0.3 °C
<b>Repeatability on Density</b>	±0.0002 g/cm <sup>3</sup>

Table 46: The characteristics of the densimeter.

**A9. TA instrument AR 2000ex Rheometry**



Figure 128: An image of the Rheometer used to measure the viscosities of the samples.



# **Appendix B:**

Surfactants mass transfer  
calculation

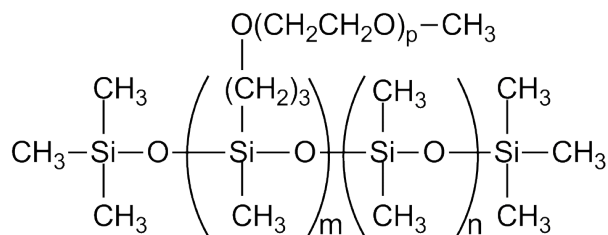
# Appendix B: Surfactants mass transfer calculation

## B.1. The transfer of surfactants from phase 1 to the droplet interface

The droplet interface is newly created during injection. So we calculate in this part the transfer time of surfactants found in phase 1 to the droplet interface in order to compare it to the droplet formation time. The following table presents physical parameters for the experiment:

Experiment	Phase 1	Phase 2	$\rho_1$ [Kg.m <sup>-3</sup> ]	$\rho_2$ [Kg.m <sup>-3</sup> ]	$\mu_1$ [Pa.s]	$Q_c$ [ $\mu$ L.s <sup>-1</sup> ]	$f$ [s <sup>-1</sup> ]
M <sub>24</sub>	S10_DBE	E <sub>2</sub>	930	1081	0.01	7	268

The chemical Structure of the Silicone co-polymer Dimethyl-Siloxane:



The transfer time of surfactants dissolved inside phase 1 to the droplet interface is computed by considering that the resistance of transfer is mainly diffusive across the mass boundary layer around the droplet (which has a thickness determined by the importance of convective effects), then the transfer is estimated by a diffusive time given by dividing the square of the mass transfer boundary layer thickness ( $\delta$ ) by the diffusion coefficient of surfactants  $\mathcal{D}$ .

$$t_{tr} = \frac{\delta^2}{\mathcal{D}}$$

The diffusion coefficient is calculated by the Stokes-Einstein law:

$$\mathcal{D} = \frac{kT}{6\pi\mu_1 R_H}$$

Where k is the constant of Boltzmann, T is the temperature (ambient in our case), and  $R_H$  is the hydrodynamic radius of the surfactant molecule.

It is assumed that the silicone oil is a good solvent for silicone co-polymer and the hydrodynamic radius  $R_H$  is equal to the gyration radius:

$$R_H = R_G = \frac{1}{8} \left( \frac{3\pi}{2} \right)^{1/2} b D_p^{0.6} = 0.594 \text{ nm}$$

Where  $b = 0.163 \text{ nm}$  is the length of bonds holding the groups of polymer chains, in this case, it is the bond between Silicone and Oxygen, and  $D_p = 76$  is the degree of polymerization calculated from the molecular weight and mass fraction of repetitive units of the polymer and its total molar mass.

Therefore, the diffusion coefficient of this surfactant is estimated to  $\mathcal{D} = 3.7 \cdot 10^{-11} \text{ m}^2 \cdot \text{s}^{-1}$ .

The mass transfer boundary layer thickness can be calculated from the film theory, with  $k_L$  being the mass transfer coefficient around the droplet of diameter  $d$  moving at a velocity  $u_0$  in a stagnant liquid

$$\delta \sim \frac{\mathcal{D}}{k_L}$$

By assuming an immobile interface,  $k_L$  is computed by using the correlation on the Sherwood number defined as the ratio of the convective mass transfer to the rate of diffusive mass transport:

$$\text{Sh} = 2 + 0.552 \text{Re}^{1/2} \text{Sc}^{1/3} \text{ (Froessling N., 1938)}$$

$$\text{Sh} = \frac{k_L \bar{d}_d}{\mathcal{D}}$$

$\text{Re} = \frac{\rho_1 u_0 \bar{d}_d}{\mu_1}$  is the Reynolds number of the droplet with  $u_0$  being the velocity of droplet detachment and  $d$  is droplet diameter.

$\text{Sc} = \frac{\mu_1 / \rho_1}{\mathcal{D}}$  is the Schmidt number defined as the ratio of momentum diffusivity (kinematic viscosity) and mass diffusivity.

Based on these calculations:

$$\begin{aligned} \text{Re} &\approx 16 \\ \text{Sc} &\approx 30000 \end{aligned}$$

$$\begin{aligned} \text{Sh} &\approx 150 \\ \mathbf{k_L} &\approx 5.1 * 10^{-6} \text{ m. s}^{-1} \\ \delta &\approx 2.5 \mu\text{m} \end{aligned}$$

Based on this calculation, the transfer time of surfactants is found to be:

$$\mathbf{t_{tr}} \approx 177 \text{ ms}$$

## B.2. The transfer of SDS from the inner part of droplet to the interface

The physical parameters of this experiment:

Experiment	Phase 1	Phase 2	$\rho_1$ [Kg.m <sup>-3</sup> ]	$\rho_2$ [Kg.m <sup>-3</sup> ]	$\mu_1$ [Pa.s]	$Q_c$ [ $\mu\text{L.s}^{-1}$ ]	$f$ [s <sup>-1</sup> ]
M <sub>25</sub>	S50	E <sub>4</sub>	950	1081	0.05	6	180

We calculate  $m_s$ , the mass of surfactants spread on the droplet interface during its formation:

$$\mathbf{m_s} = \varphi_s t_f$$

Where  $\varphi_s$  is the flux of mass transfer and  $t_f$  is the droplet formation time.

The diffusion coefficient of SDS at a concentration higher than CMC (11.8 mM) inside a sucrose solution of concentration 0.001 M was measured by Ribeiro et al., 2001 in their study:  $\mathcal{D} = 3.11 * 10^{-10} \text{ m}^2 . \text{s}^{-1}$ .

Assuming that the viscosity of the solution does not change at this small concentration ( $[\eta]_m = 0.03 \%$ , so  $\mu_2 = 0.001 \text{ Pa.s}$ ), and applying Stokes-Einstein formula, we determine the hydrodynamic radius of an SDS molecule  $R_H \approx 0.7 \text{ nm}$ .

Taking this value of  $R_H$ , and applying again the Stokes-Einstein law, but with properties of the sucrose solution E<sub>4</sub>, knowing that this sample is more viscous than that reported in Ribiero & al., we obtain a diffusion coefficient of the same order of magnitude:

$$\mathcal{D} = 1.3 * 10^{-10} \text{ m}^2 . \text{s}^{-1}$$

Moreover, for this case of internal mass transfer, the Peclet number defined as the ratio of advection rate to the rate of diffusion driven by an appropriate gradient ( $Pe = \frac{u_0 \bar{d}_d}{\mathcal{D}}$ ) is very high, precisely  $Pe \approx 830000$ .

Colombet et al., 2013 showed in their study that starting from  $Pe=1000$  the Sherwood number is constant for a given Reynolds number in the case of mass transfer inside a gas bubble (in this study the interface was not immobile).

We assume that the internal transfer in our case is similar to the case of an air bubble so that at  $Re= 10$ ,

$$\mathbf{Sh} = \mathbf{17.71} \text{ with } \mathbf{Sh} = \frac{k_L \bar{d}_d}{D}$$

Consequently, the coefficient of mass transfer  $k_L$  is computed:  $k_L= 6*10^{-6} \text{ m.s}^{-1}$ .

We calculate the mass transfer flux:

$$\boldsymbol{\varphi}_s = \mathbf{S_d} \mathbf{k_L}[\mathbf{SDS}] \approx \mathbf{8 * 10^{-12} Kg/s}$$

Where  $S_d$  is the surface of the droplet and  $[SDS]= 10 \text{ mM}$  is the concentration of SDS inside the droplet phase.

During 3.7 ms of formation time, the mass spread on the droplet interface is  $m_s \approx 3*10^{-14} \text{ Kg}$ .

This value of  $m_s$  implies a very small adsorption density  $\Gamma= 2.23*10^{-7} \text{ mol/m}^2$  ( $\Gamma=n_s/S_d$ , with  $n_s$  being the the number of moles of surfactants spread on the interface) as compared to the maximum possible adsorption  $\Gamma_\infty= 5.2*10^{-5} \text{ mol/m}^2$  for a saturated interface.

Based on  $m_s$ , we evaluate the surface tension of the droplet according to Henry's model of isotherm adsorption (equation of state):

$$\boldsymbol{\gamma}_{12} = \boldsymbol{\gamma}_0 - \mathbf{kT}\boldsymbol{\Gamma}$$

Where  $\gamma_0= 40 \text{ mN.m}^{-1}$  is the surface tension before diffusion of surfactants, and  $\Gamma$  is the adsorption density given in  $\text{mol.m}^{-2}$ .

According to Henry's equation of state, we found that  $\gamma_{12}$  will remain unchanged based on this calculation, due to the very small amount of adsorbed surfactants during the drop formation time, even if they are present inside the droplet phase.

**B.3. The stagnant cap regime at interface mentioned in section 2.2.3**

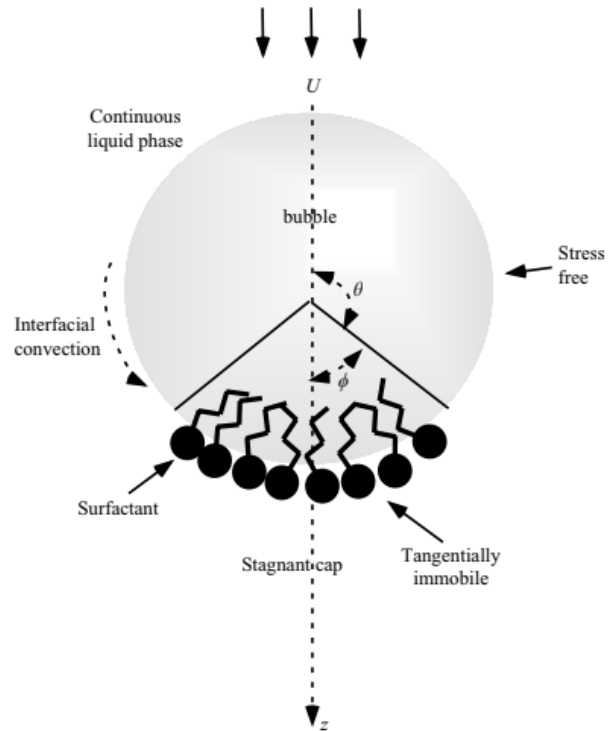


Figure 129: A scheme of the stagnant cap regime due to surfactants presented at the droplet interface. Extracted from (Palaparthi et al., 2006).

# References:

- Abkarian, M., Loiseau, E., & Massiera, G. (2011). Continuous droplet interface crossing encapsulation (cDICE) for high throughput monodisperse vesicle design. *Soft Matter*, 7(10), 4610–4614. <https://doi.org/10.1039/c1sm05239j>
- Aristoff, J. M., & Bush, J. W. M. (2009). Water entry of small hydrophobic spheres. *Journal of Fluid Mechanics*, 619, 45–78. <https://doi.org/10.1017/S0022112008004382>
- Ballard, D. H. (1981). Generalizing the Hough transform to detect arbitrary shapes. *Pattern Recognition*, 13(2), 111–122. [https://doi.org/10.1016/0031-3203\(81\)90009-1](https://doi.org/10.1016/0031-3203(81)90009-1)
- Bel Fdhila, R., & Duineveld, P. C. (1996). The effect of surfactant on the rise of a spherical bubble at high Reynolds and Peclet numbers. *Physics of Fluids*, 8(2), 310–321.
- Bhaga, D., & Weber, M. E. (1981). Bubbles in viscous liquids : shapes , wakes and velocities. *Journal of Fluid Mechanics*, 105, 61–85.
- Bonhomme, R., Magnaudet, J., Duval, F., & Piar, B. (2012). Inertial dynamics of air bubbles crossing a horizontal fluid-fluid interface. *Journal of Fluid Mechanics*, 707, 405–443. <https://doi.org/10.1017/jfm.2012.288>
- Bonometti, T. (2005). Développement d ' une méthode de simulation d ' écoulements à bulles et à gouttes .
- Brackbill, J. U., Kothe, D. B., & Zemach, C. (1992). A continuum method for modeling surface tension. *Journal of Computational Physics*, 100(2), 335–354. [https://doi.org/10.1016/0021-9991\(92\)90240-Y](https://doi.org/10.1016/0021-9991(92)90240-Y)
- Burrill, K. A., & Woods, D. R. (1973). Film shapes for deformable drops at liquid-liquid interfaces. II. The mechanisms of film drainage. *Journal of Colloid and Interface Science*, 42, 15.
- Chan, T. F., & Vese, L. A. (2001). Active Contours Without Edges. 10(2), 266–277.
- Chi, L. G., & Leal, B. K. (1989). A theoretical study of the motion of a viscous drop toward a fluid interface at low Reynolds number. *Journal of Fluid Mechanics*, 201, 123–146. <https://doi.org/10.1021/jp0648011>
- Clift, R., Weber, M. ., & Grace, J. R. (1978). Bubbles, Drops, and Particles. <https://doi.org/10.1017/S0022112079221290>
- Colombet, D., Legendre, D., Cockx, A., & Guiraud, P. (2013). Mass or heat transfer inside a spherical gas bubble at low to moderate Reynolds number. *International Journal of Heat and Mass Transfer*, 67, 1096–1105. <https://doi.org/10.1016/j.ijheatmasstransfer.2013.08.069>
- Cuenot, B., Magnaudet, J., & Spennato, B. (1997). The effects of slightly soluble surfactants on the flow around a spherical bubble. *Journal of Fluid Mechanics*, 339(May), 25–53. <https://doi.org/10.1017/S0022112097005053>
- CW Oseen. (1913). Uber den Goltigkeitsbereich der Stokesschen Widerstandsformel. *Ark. Mat. Astron. Fysik*, 19, 1–15.

- Debrégeas, G., De Gennes, P. G., & Brochard-Wyart, F. (1998). The life and death of “bare” viscous bubbles. *Science*, 279(5357), 1704–1707. <https://doi.org/10.1126/science.279.5357.1704>
- Dietrich, N., Poncin, S., & Li, H. Z. (2011). Dynamical deformation of a flat liquid-liquid interface. *Experiments in Fluids*, 50(5), 1293–1303. <https://doi.org/10.1007/s00348-010-0989-7>
- Dubey, R., Shami, T. C., & Bhasker Rao, K. U. (2009). Microencapsulation technology and applications. *Defence Science Journal*, 59(1), 82–95.
- Emery, T. S., Raghupathi, P. A., & Kandlikar, S. G. (2018). Flow Regimes and Transition Criteria during Passage of Bubbles through a Liquid–Liquid Interface [Research-article]. *Langmuir*, 34, 6766–6776. <https://doi.org/10.1021/acs.langmuir.8b01217>
- Fabre, D., Tchoufag, J., & Magnaudet, J. (2012). The steady oblique path of buoyancy-driven disks and spheres. *Journal of Fluid Mechanics*, 707, 24–36. <https://doi.org/10.1017/jfm.2012.231>
- Fedkiw, R. P., Aslam, T., Merriman, B., & Osher, S. (1999). A Non-oscillatory Eulerian Approach to Interfaces in Multimaterial Flows (the Ghost Fluid Method). *Journal of Computational Physics*, 152(2), 457–492. <https://doi.org/10.1006/jcph.1999.6236>
- Froessling N. (1938). The Evaporation of Falling Drops. *Gerlands Beitrage Zur Geophysik*, 52, 107–216.
- Geller, A. S., Lee, S. H., & Leal, L. G. (1986). The creeping motion of a spherical particle normal. *Journal of Fluid Mechanics*, 169, 27–69.
- Grace, J. R., Wairegi, T., & Nguyen, H. T. (1976). Shapes and sizes of bubbles rising in infinite liquids. *Transactions of the Institution of Chemical Engineers*, 54, 167.
- Green, G. . A., John, C. C., & Michael, T. C. (1988). Onset of entrainment between immiscible liquid layers due to rising gas bubbles. *International Journal of Heat and Mass Transfer*, 31(6), 1309–1317.
- Handschuh-Wang, S., Wesner, D., Wang, T., Lu, P., Tücking, K. S., Haas, S., Druzhinin, S. I., Jiang, X., & Schönherr, H. (2017). Determination of the Wall Thickness of Block Copolymer Vesicles by Fluorescence Lifetime Imaging Microscopy. *Macromolecular Chemistry and Physics*, 218(4), 1–12. <https://doi.org/10.1002/macp.201600454>
- Hartland, S. (1967). The Coalescence of a liquid drop at a Liquid-Liquid interface Part I: Drop Shape. *Trans. Inst. Chem. Engrs*, 45, T97.
- Hartland, S. (1968). The approach of a rigid sphere to a deformable liquid/liquid interface. *Journal of Colloid And Interface Science*, 26(4), 383–394. [https://doi.org/10.1016/0021-9797\(68\)90285-3](https://doi.org/10.1016/0021-9797(68)90285-3)
- Hartland, S. (1969). The effect of circulation patterns on the drainage of the film between a liquid drop and a deformable liquid-liquid interface. *Chemical Engineering Science*, 24(3), 611–613. [https://doi.org/10.1016/0009-2509\(69\)85032-3](https://doi.org/10.1016/0009-2509(69)85032-3)
- Haywood, R. J., Renksizbulut, M., & Raithby, G. D. (1994). Numerical solution of deforming evaporating droplets at intermediate reynolds numbers. *Numerical Heat Transfer; Part A: Applications*, 26(3), 253–272. <https://doi.org/10.1080/10407789408955991>



- Heertjes, P. M., de Nie, L. H., & de Vries, H. J. (1971). Drop formation in liquid-liquid systems-I prediction of drop volumes at moderate speed of formation. *Chemical Engineering Science*, 26(3), 441–449. [https://doi.org/10.1016/0009-2509\(71\)83017-8](https://doi.org/10.1016/0009-2509(71)83017-8)
- Helenbrook, B. T., & Edwards, C. F. (2002). Quasi-steady deformation and drag of uncontaminated liquid drops. *International Journal of Multiphase Flow*, 28(10), 1631–1657. [https://doi.org/10.1016/S0301-9322\(02\)00073-3](https://doi.org/10.1016/S0301-9322(02)00073-3)
- Hirt, C. . ., & Nichols, B. D. (1981). Volume of Fluid (VOF) Method for the Dynamics of Free Boundaries. *Journal of Computational Physics*, 39, 201–225. <https://doi.org/10.1007/s40998-018-0069-1>
- Hodgson, T. D., & Woods, D. R. (1969). The effect of surfactants on the coalescence of a drop at an interface. *Journal of Colloid and Interface Science*, 30(4), 429–446.
- James, D. (1974). The meniscus on the outside of a small circular cylinder. *Journal of Fluid Mechanics*, 63(4), 657–664.
- Jarvis, P. A., Mader, H. M., Huppert, H. E., Cashman, K. V., & Blundy, J. D. (2019). Experiments on the low-Reynolds-number settling of a sphere through a fluid interface. *Physical Review Fluids*, 4(2), 1–17. <https://doi.org/10.1103/PhysRevFluids.4.024003>
- Johnson, T. A., & Patel, V. C. (1999). Flow past a sphere up to a Reynolds number of 300. In *Journal of Fluid Mechanics (Vol. 378)*. Institut National Polytechnique de Toulouse. <https://doi.org/10.1017/S0022112098003206>
- Jones, A., & Wilson, S. (1978). The film drainage problem in droplet coalescence. *Journal of Fluid Mechanics*, 87(2), 263–288.
- Kang, M., Fedkiw, R., & Liu, X.-D. (2001). A boundary condition capturing method for incompressible flame discontinuities. *Journal of Computational Physics*, 172(1), 71–98.
- Lalanne, B., Abi Chebel, N., Vejražka, J., Tanguy, S., Masbernat, O., & Risso, F. (2015). Non-linear shape oscillations of rising drops and bubbles: Experiments and simulations. *Physics of Fluids*, 27(12). <https://doi.org/10.1063/1.4936980>
- Lalanne, B., Villegas, L. R., Tanguy, S., & Risso, F. (2015). On the computation of viscous terms for incompressible two-phase flows with Level Set/Ghost Fluid Method. *Journal of Computational Physics*, 301, 289–307. <https://doi.org/10.1016/j.jcp.2015.08.036>
- Lamb, H. (1932). *Hydrodynamics*. Cambridge University Press.
- Lando, J. L., & Oakley, H. T. (1967). Tabulated correction factors for the drop-weight-volume determination of surface and interracial tensions. *Journal of Colloid And Interface Science*, 25(4), 526–530. [https://doi.org/10.1016/0021-9797\(67\)90064-1](https://doi.org/10.1016/0021-9797(67)90064-1)
- Legendre, D., Zenit, R., & Velez-Cordero, J. R. (2012). On the deformation of gas bubbles in liquids. *Physics of Fluids*, 24(4). <https://doi.org/10.1063/1.4705527>
- Levich, V. (1962). *Physicochemical hydrodynamics*. 689–700.
- Levich, V. G., & Tobias, C. W. (1963). *Physicochemical hydrodynamics*. *Journal of Electrochemical Society*, 110(11).
- Malmazet, E. de, Risso, F., Masbernat, O., & Pauchard, V. (2015). Coalescence of contaminated water drops at an oil/water interface: Influence of micro-particles. *Colloids and Surfaces A: Physicochemical and Engineering Aspects*. <https://doi.org/10.1016/j.colsurfa.2015.06.044>

- Manga, M., & Stone, H. A. (1995). Low Reynolds number motion of bubbles, drops and rigid spheres through fluid-fluid interfaces. *Journal of Fluid Mechanics*.  
[http://journals.cambridge.org/abstract\\_S0022112095000954](http://journals.cambridge.org/abstract_S0022112095000954)
- Maru, H. C., Wasan, D. T., & Kintner, R. C. (1971). Behavior of a rigid sphere at a liquid—liquid interface. *pdf*, 26, 1615–1628.
- Massiera, G., Loiseau, E., & Abkarian, M. (2012). U.S. Patent Application No. 13/384,756.
- Maxworthy T. (1965). Accurate measurements of a sphere drag at low Reynolds numbers. *J. Fluid Mech.*, 23, 369–372.
- Mei, R., Klausner, J. F., & Lawrence, C. J. (1994). A note on the history force on a spherical bubble at finite Reynolds number. *Physics of Fluids*, 6(1), 418–420.  
<https://doi.org/10.1063/1.868039>
- Miller, C. A., & Scriven, L. E. (1968). The oscillations of a fluid droplet immersed in another fluid. *Journal of Fluid Mechanics*, 32(3), 417–435.  
<https://doi.org/10.1017/S0022112068000832>
- Milne-Thomson, L. (1962). *Theoretical Hydrodynamics*.  
<https://doi.org/10.1017/S0022112071210235>
- Mishra, M. (2015). Microencapsulation by Annular Jet Process. In *Handbook of Encapsulation and Controlled Release*. <https://doi.org/10.1201/b19038-13>
- Moore, D. W. (1962). The boundary layer on a spherical gas bubble. *Journal of Fluid Mechanics*, 16, 161–176.
- Moore, D. W. (1965). The velocity of rise of distorted gas bubbles in a liquid of small viscosity. *Journal of Fluid Mechanics*, 23(4), 749–766. <https://doi.org/10.1017/S0022112065001660>
- Myint, W., Hosokawa, S., & Tomiyama, A. (2007). Shapes of Single Drops Rising Through Stagnant Liquids. *Journal of Fluid Science and Technology*, 2(1), 184–195.  
<https://doi.org/10.1299/jfst.2.184>
- O'Brien, S. B. G. (1996). The meniscus near a small sphere and its relationship to line pinning of contact lines. *Journal of Colloid and Interface Science*, 183(1), 51–56.  
<https://doi.org/10.1006/jcis.1996.0517>
- Osher, S. J., & Sethian. (1988). Fronts Propagating with Curvature Dependent Speed. *Computational Physics*, 79(1), 1–5. <https://doi.org/10.1007/s13398-014-0173-7.2>
- Palaparthi, R., Papageorgiou, D. T., & Maldarelli, C. (2006). Theory and experiments on the stagnant cap regime in the motion of spherical surfactant-laden bubbles. *Journal of Fluid Mechanics*, 559, 1–44. <https://doi.org/10.1017/S0022112005007019>
- Peskin, C. S. (1972). Flow patterns around heart valves: a numerical method. *Journal of Computational Physics*, 10(2), 252–271.
- Piedfert, A., Lalanne, B., Masbernat, O., & Risso, F. (2018). Numerical simulations of a rising drop with shape oscillations in the presence of surfactants. *Physical Review Fluids*, 3(10).  
<https://doi.org/10.1103/PhysRevFluids.3.103605>
- Pierson, J.-L., & Magnaudet, J. (2018). Inertial settling of a sphere through an interface. Part 1. From sphere flotation to wake fragmentation. *Journal of Fluid Mechanics*, 835, 762–807.  
<https://doi.org/10.1017/jfm.2017.747>

- Pierson, J. L., & Magnaudet, J. (2018a). Inertial settling of a sphere through an interface. Part 1. From sphere flotation to wake fragmentation. *Journal of Fluid Mechanics*, 835, 762–807. <https://doi.org/10.1017/jfm.2017.747>
- Pierson, J. L., & Magnaudet, J. (2018b). Inertial settling of a sphere through an interface. Part 2: Sphere and tail dynamics. *Journal of Fluid Mechanics*, 835, 808–851. <https://doi.org/10.1017/jfm.2017.747>
- Pierson, J. Lou, & Magnaudet, J. (2018). Inertial settling of a sphere through an interface. Part 1. From sphere flotation to wake fragmentation. *Journal of Fluid Mechanics*, 835, 762–807. <https://doi.org/10.1017/jfm.2017.747>
- Pitois, O., & Chateau, X. (2002). Small particle at a fluid interface: Effect of contact angle hysteresis on force and work of detachment. *Langmuir*, 18(25), 9751–9756. <https://doi.org/10.1021/la020300p>
- Pitois, O., Moucheront, P., & Weill, C. (1999). Franchissement d'interface et enrobage d'une sphère. *Comptes Rendus de l'Academie Des Sciences, Paris*, 11, 605–611.
- Rheingans, O., Hugenberg, N., Harris, J. R., Fischer, K., & Maskos, M. (2000). Nanoparticles built of cross-linked heterotelechelic, amphiphilic poly(dimethylsiloxane)-b-poly(ethylene oxide) diblock copolymers. *Macromolecules*, 33(13), 4780–4790. <https://doi.org/10.1021/ma991985b>
- Ribeiro, A., Lobo, V., Azevedo, E., Miguel, M., & Burrows, H. D. (2001). Diffusion Coefficient of Sodium Dodecylsulfate in Aqueous Solutions of Sucrose and in Aqueous Solutions. *Journal of Molecular Liquids*, 94, 193–201.
- Richard, J., & Benoît, J. P. (2000). Microencapsulation. *Techniques de l'ingénieur*, 2, J2210-1.
- Rivkind V. Ya.M., & Ryskin G. (1976). Flow structure in motion of a spherical drop in a fluid medium at intermediate Reynolds numbers. *Fluid Dynamics*, 11, 5–12.
- Rueda Villegas, L., Alis, R., Lepilliez, M., & Tanguy, S. (2016). A Ghost Fluid/Level Set Method for boiling flows and liquid evaporation: Application to the Leidenfrost effect. *Journal of Computational Physics*, 316, 789–813. <https://doi.org/10.1016/j.jcp.2016.04.031>
- Scheele, G. F., & Meister, B. J. (1968). Drop formation at low velocities in liquid-liquid systems: Part I. Prediction of drop volume. *AIChE Journal*, 14(1), 9–15. <https://doi.org/10.1002/aic.690140105>
- Schiller, A., & Nauman, L. (1933). Über die grundlegende Berechnung bei der Schwerkraftaufbereitung. *Ver. Deutch Ing.*, 44, 318–320.
- Shopov, P. J., & Minev, P. D. (1992a). The unsteady motion of a bubble or drop towards a liquid-liquid interface. *Journal of Fluid Mechanics*, 235(2), 123–141.
- Shopov, P. J., & Minev, P. D. (1992b). The unsteady motion of a bubble or drop towards a liquid-liquid interface. *Journal of Fluid Mechanics*, 235(2), 123–141. <https://doi.org/10.1017/S002211209200106X>
- Shopov, P., Minev, P., Bazhlevkov, I., & Zapryanov, Z. (1990). Interaction of a deformable bubble with a rigid wall at moderate Reynolds numbers. *Journal of Fluid Mechanics*, 219, 241–271.
- Stebe, K. J., & Maldarelli, C. (1994). Remobilizing surfactant retarded fluid particle interfaces: II.

- Controlling the surface mobility at interfaces of solutions containing surface active components. *Journal of Colloid and Interface Science*, 163(1), 177–189.
- Sussman, M., Smereka, P., & Osher, S. (1994). A Level Set approach for computing solutions to incompressible two-phase flow. *Journal of Computational Physics*, 114, 146–159.
- Takagi, S., & Matsumoto, Y. (2011). Surfactant effects on bubble motion and bubbly flows *Mechanics*. *Annual Review of Fluid Mechanics*, 43, 615–636.
- Tanguy, S., Ménard, T., & Berlemont, A. (2007). A Level Set Method for vaporizing two-phase flows. *Journal of Computational Physics*, 221(2), 837–853.  
<https://doi.org/10.1016/j.jcp.2006.07.003>
- Tanguy, S., Sagan, M., Lalanne, B., Couderc, F., & Colin, C. (2014). Benchmarks and numerical methods for the simulation of boiling flows. *Journal of Computational Physics*, 264, 1–22.  
<https://doi.org/10.1016/j.jcp.2014.01.014>
- Taylor, T. Acrivos, A. (1964). On the deformation and drag of a falling viscous drop at low Reynolds number. *Journal of Fluid Mechanics*, 18(3), 466–476.
- Unverdi, S. O., & Tryggvason, G. (1992). A front-tracking method for viscous, incompressible, multi-fluid flows. *Journal of Computational Physics*, 100(1), 25–37.  
[https://doi.org/10.1016/0021-9991\(92\)90307-K](https://doi.org/10.1016/0021-9991(92)90307-K)
- Vella, D., Lee, D.-G., & Ho-Young Kim. (2006). The Load Supported by Small Floating Objects. *Langmuir* 22145979-5981, 22, 5979–5981.
- Wellek, R. M., Agrawal, A. K., & Skelland, A. H. P. (1966). Shape of Liquid Drops Moving in Liquid Media. *A.I.Ch.E. Journal*, 12(5), 854–862. <https://pubs.acs.org/sharingguidelines>
- Zhang, D. F., & Stone, H. A. (1997). Drop formation in viscous flows at a vertical capillary tube. *Physics of Fluids*, 9, 2234–2242.